Investigating methods used to quantify gaseous emissions from vegetation fires using spectroscopic measurements

Tattaris, Maria

Awarding institution:
King's College London

Title: Investigating methods used to quantify gaseous emissions from vegetation fires using spectroscopic measurements

Author: Maria Tattaris

Investigating methods used to quantify gaseous emissions from vegetation fires using spectroscopic measurements

Maria Tattaris

April 2013

A Thesis Submitted To The University Of London For The Degree Of Doctor Of Philosophy Geography Department, King's College London

Abstract

This work investigates the application of ground-based trace gas spectroscopy to determine the chemical makeup and quantity of smoke emitted from vegetation fires. Ultraviolet Differential Optical Absorption Spectroscopy (UV-DOAS) has been infrequently deployed in fire emission studies, yet is potentially a portable, lightweight, inexpensive and simple method. Fourier Transform Infrared (FTIR) spectroscopy has been more commonly used in fire emissions studies, but not generally in the long (> 10 m) open-path ground-based geometry explored here. This research combines these approaches to investigate their ability to quantify trace gas fluxes emitted from open vegetation fires, in part to help validate estimates of fuel consumption rate based on fire radiative power [FRP] measures. UV and IR measurements of the smoke plumes from controlled open vegetation fires (> 4 hectares) were recorded during three field campaigns in Arnhem Land (Northern Australia), Kruger Park (South Africa) and Alberta (Canada). The UV-DOAS was used to quantify NO_2 and SO_2 vertical column amounts (maximum column amounts approx 200 ppmm), allowing the determination of flux-rates when used to traverse the smoke plume and coupled with plume velocity estimates. Horizontal column amounts of the main plume carbonaceous species (CO_2, CO and CH_4) were quantified using FTIR methods and used to calculate emission ratios and emissions factors for the target gases, providing detail on inter- and intra- fire variations that are often available from the current literature. Providing NO_2 and SO_2 are detectable by the FTIR, UV-DOAS flux-rates and FTIR emissions ratios can be combined to calculate flux rates for all FTIR-detectable species. This allows for the determination of the total carbon flux from the fires, and its variation over time. Since vegetation is approximetly 50% carbon, this flux is in theory directly proportion to the fuel consumption rate, and directly comparable to the fire's radiative power output variations as determined by airborne thermal imaging. Hence, in addition to providing the means to estimate smoke plume chemical makeup, emissions magnitude and variability, the simultaneous deployment of the techniques of UV-DOAS, FTIR spectroscopy and airborne thermal imaging enables the validation of FRP derived fuel consumption rates. The FRP method is gaining ground as a tool for improving biomass burning emissions inventories based on satellite observations,

but at present has had relatively little validation. This study therefore contributes to the ongoing evaluation effort.

Findings demonstrate that the UV-DOAS is an effective way to measure column amounts of SO_2 and NO_2 in vegetation fire plumes, providing that the fires are of an adequate size and emit smoke in sufficient quantities. The exact nature of the ability to accurately quantify NO_2 and SO_2 using the method did have a dependence on fuel type, since the combustion of different fuel types (e.g. grasses vs. woody fuels vs.organic soils) appeared to cause more of less of these particular gases to be emitted. There was difficulty in confidently detecting NO_2 via the OP-FTIR approach for the majority of the study cases, due to the relatively weak IR absorption bands used and the relative scarcity of this gas in the plumes in comparison to some others studied. We advocate using the UV-DOAS and FTIR combination in relation to trace gas measurements from vegetation fires, providing SO_2 or NO_2 can be identified by the FTIR in the particular biomass burning situation under study. Where simultaneous FRP measurements are available, the carbonaceous flux rates calculated using the FTIR/UV-DOAS method show a strong correlation with FRP, helping to confirm the relationship between FRP and fuel consumption rate at the scale of these vegetation fires. This is to our knowledge currently by far the largest fires upon which this relationship has been evaluated, prior evaluations being limited to laboratory-scale events only.

Acknowledgements

Contents

List of Figures

14

15

17

20

22

27

List of Tables

Chapter 1

Biomass Burning: Process, Effects and Characterization of Emissions

Contents

1.1 Introduction and Aims and Objectives

The amount of severe fire activity over the last few decades, as well as the realization of the importance of biomass burning, has led to a rise in public interest in biomass burning related issues and, in particular effect of emissions the atmosphere. The Framework Convention on Climate Change and the Kyoto Protocol have emphasized the importance of the relationship between biomass burning and increases in atmospheric concentrations of CO_2 and other green house gases (Innes, 2000). The years of 1997/1998 and 2002/2003 saw particularly severe fire activity in temperate areas and in south-east Asia, south-eastern Australia, western Canada, Mediterranean Europe and southern California. One suggested reason for this is the effects of El Niño, which caused periods of severe drought in many areas. Such "enhanced" fires can be very intense and can burn huge areas very quickly (Lavorel *et al.* 2006). For example, 2009 saw a series of bushfires burn approximately 450,000 hectares in the state of Victoria, Australia between February to March. Also in the same year, many large wildfires burned 20,000 hectares in several areas of Greece, in August.

This chapter shall introduce the importance and main characteristics of biomass burning, including resultant trace gas emissions. Investigations into the quantification of several gaseous species emitted from open vegetation fires via ground-based and airborne remote sensing in the main focus of this thesis. It is widely known that biomass burning emits significant amounts of trace gases and aerosols, which in turn affects atmospheric processes and the Earth's climate. Hence, it is important that accurate data on these emissions are available in order to improve the understanding of how biomass burning contributes to the land-atmosphere interactions and the varying processes that control Earth's atmospheric composition and climate (Akinori and Penner 2004). Remote sensing is a useful and important tool that enables us to better quantify many aspects of biomass burning, including its effects and their variations in space and time. It may allow us to better predict the changes that may occur in the future due to these processes, perhaps enhanced or altered by changing climates, and perhaps also to realize strategies for the mitigation of and/or adaptation to

these changes.

The focus of this research is the investigation of biomass burning smoke plume studies, through the application and synergy of two remote sensing sensing instruments, the Ultra-Violet Differential Optical Absorption (UV-DOAS) Spectrometer and the Fourier Transform Infrared (FTIR) Spectrometer. Ground-based measurements from both instruments have been used to detect the presence of gas species within plumes emitted from open vegetation fires for different types of ecosystems in South Africa, Canada and Australia. To date, research investigating biomass burning emissions is based on a mixture of laboratory experiments and ground-based and airborne field measurements, making it rather difficult to carry out inter-comparisons between some of the research studies. By combining field measurements of the UV-DOAS and FTIR spectrometers, there is potential scope to detect a wide range of species emitted from different types of open vegetation fires in a relatively easy way, thus making it possible to make strong comparisons of emissions from difference types of fuel.

As discussed further on in this chapter, there is much uncertainty associated with the used of the standard method used to calculate emissions (see Equation 1.7 (Seiler and Crutzen, 1980)), particularly due to fuel load and combustion completeness needed for this method (van der Werf *et al.*, 2006). A suggested alternative to eliminate some of this uncertainty is the use of fire radiative power (FRP), which is directly related to the rate of biomass combustion (Kaufman *et al.*, 1996; Wooster *et al.*, 2005). Part of this research shall focus on comparing carbon flux rates derived via the integration of UV-DOAS and FTIR measurements with FRP time series derived from MIR thermal camera imagery in order to investigate the strength of the use of the FRP to estimate biomass combustion rates.

The overall aim is to explore the use of portable ground-based Ultra-Violet Differential Optical Absorption Spectrometry (UV-DOAS) for deployment in vegetation fire assessment and smoke emission studies, including their ability to provide information on trace gas fluxes and their potential for validating variations in fuel consumption rate derived from thermal remote sensing methods during three field campaigns located in:

- Kruger National Park, South Africa

- Banf National Park, Alberta, Canada

- Arnhem Land, Northern Territory, Australia.

For all field campaigns data was collected during several managed open vegetation fires of various sizes and fuel types. For each field campaign, data from at least two different fires were analyzed. Data was not analyzed separately between field campaigns because fires produced varying amount of smoke, allowing for the investigation of how efficient the different instruments and methodologies used here are when too little/too much smoke is emitted by open vegetation fires. Also, even within the different environments analyzed here, there was variations in the biomass burnt, hence analyzing the fires within each field site separately can provide an insight on how varying biomass within the same type of environment can effect the trace gas emissions released from fires.

Within this overall aim, the following objectives will be addressed:

- **Objective**: Inter-compare methods to estimate vertical column amounts of fire-emitted gases from UV-DOAS vegetation fire measurements (key expected species are sulfur dioxide and nitrogen dioxide; which have features in the UV spectral region). **Approach**: Deploy UV-DOAS at a series of vegetation fires showing widely varying characteristics, and develop best method for trace gas retrieval.

- **Objective**: Provide estimates of smoke trace gas emission ratios and emissions factors for vegetation fires, and assess the similarity and complementaries of UV-DOAS and FTIR-based systems. **Approach**: Where possible, deploy simultaneously on a series of vegetation fires the techniques of UV-DOAS and FTIR spectroscopy to retrieve the column amounts of the primary carbonaceous species CO_2, CO and CH_4, and the DOAS-targeted species (NO_2 and SO_2).

- **Objective**: Develop method to determine the flux of carbon from vegetation fires, based on UV-DOAS and FTIR measurement techniques, and use this to evaluate the efficacy of the variations in fuel consumption rate that can be derived from the Fire

Radiative power (FRP) approach. **Approach**: Deploy simultaneously on a series of vegetation fires the techniques of UV-DOAS and FTIR spectroscopy, and airborne IR imaging for FRP assessment.

1.1.1 Global Biomass Burning Activity

Drivers of Biomass Burning

The term 'biomass burning' refers to the open vegetation fires that occur frequently in many vegetated environments, burning living and dead vegetation, including agricultural lands, savannas and forests (Levine, 1994). Fires have been affecting Earth's vegetation for millions of years, with evidence dating back as far as 350-450 million years ago (Parasad *et al.*, 2002). Nowadays, the use of open biomass burning (which excludes the burning of domestic/industrial burning of biomass fuels) as a tool for a wide range of land management purposes is a standard practice in many regions. As well as such anthropogenic ignitions, fires also result from natural ignitions such as lightening, although the former dominates (Blake *et al.*, 1999; Innes, 2000; European Commission, 2002; Lauk and Erb, 2009). In fact, biomass burning has become an increasing practice for management purposes. Lauk and Erb, (2009) estimated 3547-3938 Tg.yr^{-1} of dry biomass is burned around the world during human induced biomass burning. (Innes, 2000).
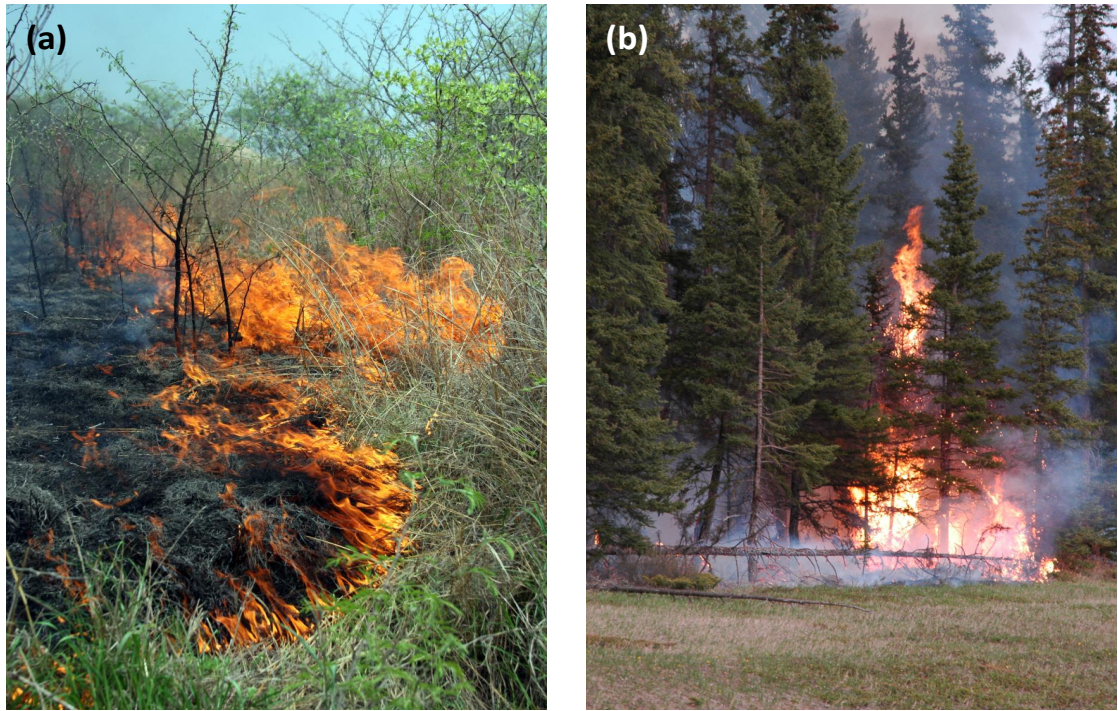
Figure 1.1: *A managed (a) Savannah burn in Kruger National Park, South Africa and (b) pine forest fire close to Banff National Park, Alberta, Canada. These experimental fires were conducted as part field campaigns for this project.*

Extensive deforestation and savannah clearing is conducted to clear land, for example, due to demand for agricultural areas, rising population (more food and living space), increased burning of agricultural waste and domestic fuel fires (wood and biofuels) (Andreae, 1990; Innes, 2000). Looking particularly at savannas, whose fuels consist mainly of grasses, fires are used to create suitable conditions for grazing and hunting, pest control (e.g. insects and snakes), to remove weeds and unwanted shrubs and litter accumulation and to revive the nutrient cycle in the soil using the nutrients that are found in the succeeded vegetation (Andreae, 1990; Andreae, 1991). Due to the large areas involved, savannah fires in total emit up to 3 times as much CO_2 and other trace gases than do fires carried out for land-use change (i.e. deforestation), even though forests boast a much higher biomass density and thus fuel load (Andreae, 1991). Conversely however, the rapid regrowth of savanna vegetation means that the CO_2 released will often be rapidly re-sequested in the former case. Also in some

areas of the tropics such as part of Brazil, a major contributor to air pollution is the burning of sugar cane fields, ignited to clear old crop residues and to help stimulate the growth of this crop in the next growing season. This, and other forms of burning of agricultural waste are believed to form a relatively large proportion of the emissions from biomass burning (Andreae, 1990).

Land clearing for crops is a major contributor to the total amount of biomass burnt globally. Jain *et al.* (2006) estimated that in the year 2000, fires set to clear land made up approximately 43% of total biomass burned, contributing to 25-27%, 25-28%, 20-23% and 28-30% of global biomass burning emissions of CO_2, CO, NO and NMHCs respectively. Biomass burning used to clear land for agriculture is intended either for the purpose of 'shifting agriculture', where after a short time the "natural" vegetation regrows, or the permanent removal of forest vegetation in place of land used for crops or grazing. In both cases, the trees are cut down and left to dry out in order to obtain a greater dryness and thus burning efficiency prior to ignition. In general, in shifting agriculture, after the land has been cleared it is used for several years, until yields fall, and new plots are then cleared in hope of increasing yields once more. Traditionally, the plots used for shifting agriculture are left for around 20 years after yields decline, allowing "natural" vegetation to potentially grow back. When former tropical forests land is intended to be used permanently for agricultural purposes, it can result in poor soil conditions and inefficient land management. Such land management techniques ultimately lead to loss of carbon storage (Andreae, 1991). Lauk and Erb (2009) estimated the percentage of total area burned globally in such shifting agricultural fires as 1052-1442 $Tg.yr^{-1}$, 30% of the total human induced fire activity (Table 1.1). It can be seen that these type of fires occur mainly in the regions of Latin America, Sub-Saharan Africa and South-East Asia.

For some types of managed forests (excluding tropical rain forests), some level of burning is often used to manage the ecosystem, for example, low intensity fires at a regularly frequency prevent a build up biomass which, if left unmanaged, could lead to the destruction of the forest when a fire does occur due to high fuel loads which could create intense, un-

controllable fires. (Innes, 2000). Boreal forest fires are frequently observed across Canada, Russia and Alaska, however it is estimated every year the area involved in savanna fires is almost two times that of boreal fires (Innes, 2000). Even in countries such as the UK, where wildfires are rather insignificant compared to tropical or Mediterranean areas, land managers carry out managed burns. They occur mostly on moorland and peatlands, mainly to promote new growth of strands of *Calluna* (heather), creating a suitable environment for grazing and red grouse management. Hunting red grouse within the UK countryside is economically important, hence particular importance is put on maintaining this source of income. Such regular and controlled fires create a complex and highly artificial landscape pattern.

In boreal areas, lightening is a significant source of fire ignition, and wildfires can burn uncontrollably for weeks in areas where fuel is plentiful. Large wildfires in undisturbed tropical forests are far less common than those in temperate and boreal regions, since these forests tend to often be too moist for the fires to spread significantly (Andreae, 1991). In the tropics, the most common natural source of ignition is lightning, particularly in savannas (Andreae, 1990) with smaller proportion of fires being started by volcanic activities and friction (e.g. falling rocks or landslides) (Stott, 2000).

Spatial/Temporal Patterns and Magnitude

Much of the literature makes reference to a 'burning season' (e.g. Andreae *et al.*, 1988; Stoppiana *et al.*, 2000), but burning occurs outside of this season also (Andreae, 1991). It is true that a great portion of forest and savanna fires take place in the dry season, in particular during November to March in the Northern Hemisphere and from June to September in the Southern Hemisphere. Yet in the tropical regions, burning often happens simply when and where the vegetation is dry enough, which may be outside of the "burning season". For big land clearing operations, fires tend to burn later in the dry season to ensure that the fuel is very dry and hence burns with a greater burning efficiency (Andreae, 1991). For fires that occur with the purpose of shifting cultivation, the whole process begins in November and December, when forests are cleared. By March to May, the cut biomass is dry and burnt, so

that the land is clear for sowing, with harvest occurring in October (Parasad *et al*, 2002).

A general calendar of biomass burning activity was outlined by Langmann *et al.* (2009). Although fires occur throughout the year, it was found that there are generally two emission peaks caused by tropical biomass burning. The first peak is between January and April, mainly from fires in the Northern Hemisphere tropics and subtropics, particularly southeast Asia and Africa. The second peak is from August to November, predominantly from south America and southern Africa. This can be seen from Figure 1.2, presenting the fire hotspots detected by MODIS for days in February and September. This is confirmed by Chuvieco *et al.* (2008), who looked at burned area in the Latin American region. Other high frequency fires occur in Indonesia, central America (April-May) and boreal forests (May-September) in Eurasia and North America (Langmann *et al.*, 2009).

In a study looking at the impact of vegetation fires in Africa, Stroppiana *et al.* (2000) found that generally there is a high frequency of fires at the beginning of the burning season (November-February), when most fires occur in the Northern Hemisphere, with the absolute amount of biomass burned varying from year to year. Stroppiana *et al.* (2000) found there also exists variability in terms of where the fires occur and the amounts of gases emitted. There is a specific monthly distribution of burning, which is due to regional weather conditions. The study identified three periods in which fire activity in Africa can be grouped; November to February, March to May and June to October. Between November to February, most of the burning occurs in the Northern Hemisphere (where the savannas here are dry) and then moves down to the south. The period of March to May sees a fall in fire activity, which increases again from June to October where fires occur in the south then move to the east. The area burned between March and May is less than 38 million hectares, which is around 13% of the yearly total, whereas after June, monthly percentages range from 5% to 9%.
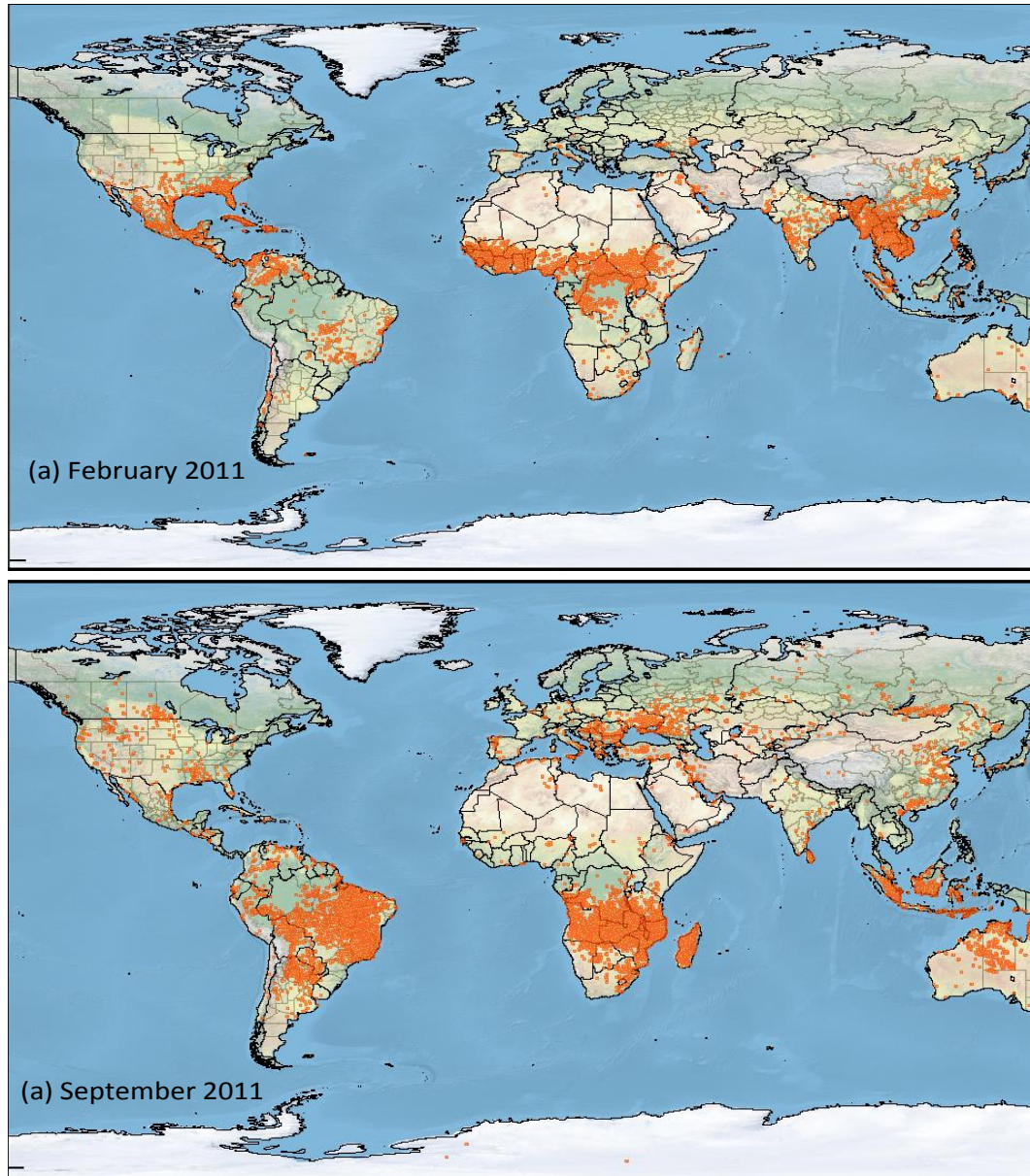
Figure 1.2: *Global maps of fire locations (hotspots) detected by MODIS for the previous 48 hrs on (a) 29-02-11 and (b) 29-09-11. Notice in February most of the fires are located in the Northern Hemiaphere and sub-tropics, whereas in September the fires move south to South America and Southern Africa. Available from the Fire Information for Resource Management System (FIRMS) (http://maps.geog.umd.edu/firms/)*

.

Around 70% of biomass burning is located in the tropics (Andreae *et al.*, 1988), mainly in ecosystems containing tropical forests and savannas. Such ecosystems cover extensive areas: global savanna land cover is around 1530 million ha, and tropical forests 1440 million ha

(Andreae, 1990). Africa is a major biomass burning participant: representing around 50% of global savanna burning (Andreae, 1990), and savanna fires make up nearly 90% of the biomass burning from all forests (Andreae, 1991). Table 1.1 presents a regional breakdown of the amount of dry matter burned ($Tg.y^{-1}$) from large anthropogenic induced fires, taken from Lauk and Erb (2009). It can be seen that Sub-Saharan Africa contributes 70% of total global biomass burned per year, due to the burning of savannas. This is followed by the regions of Latin America, Oceania and Central Asia, although their contribution is much less (5-15%). Van der Werf *et al.* (2006) estimated that for the years 1997-2004, burned area within forest ecosystems made up only 20% of the total burned area, with the majority found in savannas. However, the fuel loads are typically somewhat lower in savanna areas than in forests.

Table 1.1: *The amount of regional dry matter burnt ($Tg.y^{-1}$) from anthropogenic induced fires broken down by region. Note that the burning of agricultural residues is excluded. The term "large fires" refers to fires that are able to be detected by burn scar products. Taken from Lauk and Erb (2009).*

Region	Large Fires Biomass Burned		Total Fires Biomass Burned		Shifting Agricultural Fires Total Burned Area
	Tg dm.yr^{-1}	%	Tg dm.yr^{-1} (min/max)	%	%
N Africa, W. Asia	10	0.4	10/10	0.3	0
Sub-Saharan Africa	1758	70.4	2080/2202	55.9	42
Central Asia	157	6.3	157/157	4	0
E Asia	71	2.8	71/71	1.8	0
S Asia	82	3.3	131/149	3.8	3.2
SE Asia	36	1.4	255/336	8.5	14.8
N America	19	0.8	19/19	0.5	0
Latin America, Caribb	164	6.6	625/795	20.2	40
W Europe	10	0.4	10/10	0.3	0
E, SE Europe	49	2	49/49	1.2	0
Oceania	140	5.6	140/140	3.6	0
Total	2496	100	3547/3938	100	100

1.2 Fire and Smoke Physical and Chemical Characteristics

1.2.1 General Properties of Open Vegetation Fires

The properties of a fire are a complex function of a multitude of variables. Two important variables of open vegetation fires are intensity (which can be considered a measure of the amount of heat released per unit time) and its severity (which can be considered as the amount of heat released per unit area) (Ferguson *et al.*, 2000). These are a product of fuel content (for example moisture), fuel type and how the fire was started. Fire intensity will vary more as the fire lasts longer and has greater spreading rates (Ferguson *et al.*, 2000). Fire intensities tend to be the greatest on fires that are intended to convert forests into other types of land, for example agriculture or urban development. Fire severity can be controlled by changing the fuel bed, carrying out prescribed burns and controlling the ignition pattern. In general, fire durations can range from one hour to a few days. Although landowners tend to prefer the practice of long lasting, low intensity fires that manage to burn light fuels but not the trees, these type of fires tend to have the highest emission factors of many species, and could start additional wildfires (Ferguson *et al.*, 2000).

Short/medium term weather conditions affects fuel availability and flammability, the potential for lightening ignition and the spreading of a fire once it has started (Lavorel *et al.*, 2006). Temperature and moisture levels affect the growth of vegetation; the duration and intensity of dry seasons will have a strong role in how any fires will developed and spread. Hence climate conditions affect the fire as it occurs, but also before it occurs. (Dwyer *et al.*, 2000). As well as climate, fire is also affected by land-cover. Land-covers with different species composition, age and density, micro-climate and soil conditions have different flammability properties. A land-cover that is fragmented is likely to suppress fire propagation. An increase in fire frequency tends to change vegetation cover, usually to grasslands or forests that have a high tolerance of fire and in fact may need it for their regeneration, such that fire has a positive ecological effect (Lavorel *et al*, 2006). Pekin *et al.* (2009) found that, in a study on fires in the eucalyptus forest environment in south-west Australia, may lead to a switch in dominant tree species as well as a rise in small trees and a fall in larger trees.

1.2.2   Fire Chemistry

Combustion is made up of several stages (Andreae and Merlet, 2001), governed by the 'triangle of fire', (see Figure 1.3) which represents the three factors that control combustion; fuel, oxygen (O_2) and heat. If these three elements are combined together correctly, combustion will take place. The heat that is needed for combustion to occur is known as 'activation energy'. When the activation energy is present, it takes part in an exothermic reaction with the O_2 to release the heat stored in the fuel. During this reaction, CO_2 and H_2O are produced, as well as lower concentrations of other species, such as CO, CH_4 and NO. The amount of heat released depends on the calorific value (the amount of heat released per unit of fuel weight) of the fuel, which is quite similar for each fuel type (Stott, 2000).

OXYGEN

HEAT

FUEL

Activation Energy ⟶ Ignition

Drying of fuel

Partial pyrolysis

Flaming Conditions

Volatilization of hydrocarbons

Thermal decomposition of molecules

More energy released to ignite more fuel

~ 400 K

Flaming Combustion

Conversion of intermediate molecular compounds to simple molecules e.g. CO_2, H_2O

Smouldering Combustion

Build up of ash inhibits flames. Less CO2 and more CO released per unit of fuel combusted.

Figure 1.3: *Flow chart outlining the processes involved and the characteristics of the combustion stages. The triangle of fire at the top of the figure represents the three components needed to create fie: heat, oxygen and fuel.*

The first stage of the combustion process, which needs to occur for the fire to start, is ignition. Ignition depends on both the properties of the fuel (size, water content) and environmental factors (temperature, relative humidity, wind speed). During this step, the fuel is dried and partial pyrolysis occurs; the thermal cracking (the breaking down of molecules into smaller molecules) of the fuels. At this stage, small biomass material is combusted fully, whereas larger vegetation is still being heated to its combustion point. For ignition to hap-

pen, all components of the fire triangle have to be present. Vegetation composition usually is usually made up of dry weight, cellulose and hemicelluloses (50-75 %), lignin (15-35%,) minerals (up to 10%) and proteins, nucleic acids, amino acids , alcohols and terpenes. Some fresh vegetation can be made up of around 60%, (or more) of water, therefore in the initial stage of ignition, where heat is applied, the biomass is pre-dried before ignition. If the fire is to carry on by itself, it is necessary that more heat must be released from the fuel so that the biomass in front of the fire-line is dried. Fuel flammability represents how likely it is for fuel to ignite, as well as its ability to sustain a fire after ignition. Wood tends to have quite significant moisture content, hence very substantial external heat is needed to dry living wood (Andreae and Merlet, 2001; Hobbs *et al.*, 1996; Stott, 2000; van Leeuwen and van der Werf, 2011).

Flaming combustion occurs (approximately 1400 K) when the above process frees up enough energy such that the combustion process can move to the part of the fuel that is not ignited and the fire can spread. At the beginning of the flaming stage, the pyrolysis of the cellulose and lignin occurs, where the fuel molecules are broken down by heat. In the breaking down of the fuel molecules, the high molecular weight compounds (typically made up or carbon, hydrogen, nitrogen and oxygen atoms) are decomposed into char (less volatile solids which are high in C), tar (intermediate molecules) and volatile compounds. During flaming combustion, O_2 is involved in rapid reactions with other gases that have originated from the fuel such that the intermediate molecular compounds released during pyrolysis are converted to simple molecules. During this process, C, H, N and S are converted into, for example CO_2, H_2O (water vapor), NO (nitric oxide), N_2O (nitrous oxide), N_2 (molecular nitrogen) and SO_2 (sulphur dioxide). Also, substances such as CO (carbon monoxide), CH_4 (methane) H_2 (molecular hydrogen), C_2H_4 (ethylene), C_2H_6 (ethane), PAHs (polycyclic aromatic hydrocarbons) and soot particles are released. As the fires moves from ignition to flaming, large concentrations of small particles are emitted, which form conglomerates of larger particles (Hobbs *et al.*, 1996; Stott, 2000; Andreae and Merlet, 2001; Akagi *et al.*, 2011; van Leeuwen and van der Werf, 2011).

Glowing combustion may proceed if there is enough O_2 available and the right type of fuel. During glowing combustion, char is oxidized into CO, which in turn is oxidized into CO_2. At the point when the majority of the volatiles have been emitted from the surface of the fuel area, the mix of fuel and air is no longer flammable, open flames will die and stop being produced and pyrolysis will slow down. The fire then moves into smoldering combustion. When this happens, there is a build-up of ash, this contains species such as potassium and silicates, which have the property of inhibiting flames. Temperatures during smoldering combustion are lower than during flaming combustion, around 800-1000 K. At this stage, large amounts of CO are formed when O_2 reacts with carbon. During this process, most of the CO, CH_4, NMHC and organic carbons are released. Less CO_2 is released per unit mass burned, as for this to happen temperatures need to be at least 900-950 K. Note that in forest fires, smoldering phases can have a duration of up to several weeks. The fire eventually stops when the heat produced reaches very low levels, due to the slowing down of pyrolysis. At lower levels of heat, pyrolysis cannot be maintained and the drying of fuel is not possible. The fire comes to a stop usually because of distances between fuel such that it is not possible to prevent heat transfer to additional fuel, rainfall and high moisture content in the fuel. Usually, smoldering and flaming combustion occur at the same time during a fire. (Stott, 2000; Andreae and Merlet, 2001; Akagi *et al.*, 2011; van Leeuwen and van der Werf, 2011).

The emissions of gaseous species found in the smoke of a fire are dependent on the fuel composition as well as the physical and chemical processes occurring during the fire. For most vegetation fuels, the carbon content varies over the range 37%- 54%, (Andreae and Merlet, 2001). Therefore if a species is made up of only carbon, oxygen and hydrogen, the variety in its emitted species relate mainly to the combustion process (Andreae, and Merlet 2001). However, for vegetation species containing significant amounts of elements such as nitrogen, sulphur and halogens, their emissions are related to the fuel composition as well as the combustion process. However, compared with fossil fuel burning, temperatures during vegetation combustion are quite low. During the flaming stage, NO, NO_2, N_2O and molecular N_2 dominate emissions, whereas during smoldering combustion, NH_3, amines and nitriles are predominantly released. Note that it is very difficult to measure the contribution of N_2

made by the smoke plume to atmospheric N_2 in the field since the ambient/atmospheric concentration is so high (Andreae and Merlet, 2001).

McNaughton *et al.* (1998) found that carbon combustion (biomass combustion) occurred at a lower efficiency than nitrogen combustion, hence the fraction of carbon after the fire in the unburnt material was greater than the fraction of nitrogen left in the unburnt material, in most fires apart from those with a low intensity. Hence as the fire intensity increases, the quantity of ash and residual mass decreases, This implies that the nitrogen containing parts of the plant material maybe more flammable than general vegetation.

The relative amounts of smoldering and flaming combustion during a fire can be calculated using the molar modified combustion efficiency, MCE (Yokelson *et al.*, 2008):

$$MCE = \frac{\Delta CO_2}{\Delta CO_2 + \Delta CO},$$ (1.1)

where ΔCO_2 and ΔCO are the elevated mixing ratios (plume mixing ratios minus the background mixing ratios) of CO_2 and CO respectively. It is not advised to measure MCE with satellites as a much higher spatial resolution is needed to identify the changes in CO_2 (that would be induced by fires) over the background (Yokelson *et al.*, 2008). A low ratio of CO to CO_2 emissions indicates that the fuel has a low efficiency, i.e. a large flaming phase (Blake *et al.,* 1996). The mixing ratios can be defined as 'the concentration (volumetric fraction) of a gaseous compound in the atmosphere' (Castro *et al.*, 2007).

1.3 Detailed Chemical Emissions Properties and Magnitude

1.3.1 Main Emitted Gases and Their Impacts

Anthropogenic air pollution dates back thousands of years, when humans first learnt how to use fires. Nowadays, biomass burning still creates pollution. For example, the burning of crop residues in the fields in China has had numerous environmental effects, including the closing down of airports and motorways due to smog (Yan *et al.* 2006). Biomass burning is an important emitter of numerous trace gases, such as CO_2, CO, CH_4, NMHC (non methane

hydrocarbons), CH_3Cl (methyl chloride), CH_3Br (methyl bromide), C_2H_2 , NO_2 (nitrogen dioxide) N_2O, NO, NH_3 (ammonia) and gases containing sulphur (Levine 1996, Blake *et al.*, 1996, European Commission, 2002). Rain forest fires have the potential to release an immense amount of particulate emissions and produce plumes that have the ability to rise very high into the atmosphere and travel a long way, due to large heat release rates (Ferguson *et al.*, 2000). A rise in trace gases is linked with the enhanced greenhouse effect, the production of nitric acid (associated with acid rain) and the tropospheric photochemical production of O_3. The gases emitted can have long term effects, due to the long lifetime of gases, especially for CO_2 and NO_2 (an NO_2 molecule has a lifetime of 150 years) (European Commission, 2002).

Not only is the information on trace gas species and concentration important on an environmental scale, it is also politically important, for example the Kyoto Protocol [1]. When considering developing countries, regional gas emissions are especially important as fires play a significant role in land management, the clearing of land and grazing management. In such countries, greenhouse gas emissions from fires are the major source with respect to total emissions. For example in Africa, the energy created by biomass burning makes up 80-90% of the total energy for the low income population, 55-65% for the middle income population and 30-40% for the high income earners (European Commission, 2002).

The greenhouse effect can be described as the process whereby certain gases ('greenhouse gases') absorb upward moving radiation, hence increasing surface temperature. There are various greenhouse gases in the atmosphere that are very efficient at absorbing infra-red radiation, for example CO_2, CH_4, N_2O SO_2, HNO_3 and NH_3. The concentrations of these gases in the atmosphere maybe low, however their effect on the thermal properties of the atmosphere are strong as they can absorb radiation with the wavenumber range 700-1400 cm^{-1}, which is the atmospheric window in which the majority of the earth's thermal radiation is transmitted from the earth's surface and lower atmosphere (Wang *et al.*, 1976). The

---

[1] The Kyoto Protocol is an international agreement binding (at the moment) 166 countries to reduce their total emissions of greenhouse gases. It was created by the United Nations for the United Nations Framework Convention on Climate Change and negotiated in Kyoto, Japan in December 1997.

gases released from biomass burning are a function of the fuel composition (e.g. carbon, nitrogen, sulphur) and the level of flaming and smoldering within the fire (Potter *et al.*, 2002).

Carbon and its Compounds

Around 45% of dry plant biomass is carbon, with the remaining being mainly hydrogen and oxygen, and small amounts of nutrients. Hence, fire emissions compromise of mostly the oxides of carbon (Andreae *et al.*, 1988). Lobert *et al.* (1990) estimated that 95% of the carbon contained in the burned biomass is volatilized during a fire, with 75% of the fuel weight lost under flaming combustion and the rest during the smoldering phase. Out of all the lost carbon, nearly all was identified in measurements as CO, CO_2, hydrocarbons and within the ash. van der Werf *et al.* (2008) investigated fire emissions from equatorial Asia and calculated an average emission rate of 128 $\pm$51 Tg C.year^{-1} for the years 2000-2006, with a minimum at 2000 during the La Nina of 47 $\pm$ 29 Tg C.$^{-1}$ and a maximum during El Nino in 2006 of 303 $\pm$118 Tg C.year^{-1}. van der Werf *et al.* (2006) calculated that in the years 1997-2004, the majority of carbon emissions from biomass burning came from Africa (49%), followed by South America (13%), equatorial Asia (11 %), boreal areas (9 %) and lastly Australia (6 %). Table 1.2 shows the regional carbon emissions calculated by van der Werf *et al.* (2006) for the years 1997-2004. In the same time period, the average annual emissions were estimated at 2500 Tg C.yr^{-1}.

Table 1.2: *Average carbon emissions from biomass burning during the years 1997-2004. Taken from van der Werf et al. (2006).*

Region	Average Tg C/year	Standard Deviation
Boreal North America	34	0.76
Temperate North America	6	0.39
Central America	68	1.10
Northern Hemisphere South America	26	0.62
Southern Hemisphere South America	88	0.31
Europe	5	0.39
Middle East	0	0.46
Northern Hemisphere Africa	75	0.12
Southern Hemisphere Africa	72	0.12
Boreal Asia	133	0.71
Central Asia	14	0.29
Southeast Asia	90	0.57
Equatorial Asia	349	1.34
Australia	32	0.23
Global	403	0.16

Biomass burning is involved in carbon cycling in the way that it releases CO_2 into the atmosphere (Jain *et al.,* 2006). When there is no burning, the process of photosynthesis and respiration create a closed cycle whereby the amount of CO_2 taken up by the plant during photosynthesis is equal to the amount released into the atmosphere by plants from oxidation during respiration, hence the net CO_2 flux equals zero. It has been suggested that with the existence of biomass burning, when looking at the very long term, this is still the case: CO_2 emitted from biomass burning simply releases into the atmosphere the CO_2 that was taken up by the plants in the past (Andreae, 1990). Yet if this emitted CO_2 is not removed again by the rapid regrowth of plants then it will remain in the atmosphere until it is removed by another process. Hence, in this way, the CO_2 can add to the greenhouse effect and to global climate change (Andreae, 1990). The burning of savannas every few years may make little contribution to the greenhouse effect because the vegetation that grows back after the

fire takes in the CO_2 that was released by these fires. This is not the case for forest fires, as the amount of CO_2 that is released by these fires, in which large amounts of biomass are burnt, cannot fully be taken up by the agricultural type vegetation that have replaced it and sometimes forest regions that will grow in place of the forest, usually grass or crops, as these have a much lower level of biomass (Andreae, 1990; Blake *et al.*, 1996). Hence, when investigating the effect of CO_2 from biomass burning emissions it is important to consider the source of the emissions. Deforestation burning and fires on drained peatlands are net sources of CO_2, whereas for fires in other areas the emitted carbon is eventually taken in by regrowth on decadal timescales (van der Werf *et al.*, 2010). Yet Jacobson (2004) suggested that agricultural/savanna and grasslands may be burned at a frequency shorter than the length of time needed to achieve full regrowth after a fire. Regular burning of such ecosystems, preventing roots of the plants to grow deep and growth of trees/bushes and the collection of dead vegetation will leads to an increase in the level of CO_2 in the atmosphere. However the study projected that removing permanent forest burning will have the greatest effect in reducing atmospheric CO_2 compared with temporary forest burning, savanna burning and agricultural burning. The clearing of tropical forests could lead to around 18-40% of the CO_2 greenhouse effect around the world (Andreae, 1990; Blake *et al.*, 1996). Jain *et al.* (2006) calculated an estimate of the total amount CO_2 emitted by biomass burning carried out for land clearing in the year 2000 as 6564-9093 Tg $CO_2.yr^{-1}$.

Jain *et al.* (2006) calculated an estimate of the total amount CO emitted by biomass burning carried out for global land clearing in the year 2000 as 438-568 Tg $CO.yr^{-1}$. Another estimate of CO emissions is given by Potter (2002), who calculated the annual loading of CO from biomass burning in the Legal Amazon to be 102 Tg $CO.yr^{-1}$. Guyon *et al.* (2005) highlighted the relatively constant ratio of particulate matter emitted per unit of CO for deforestation fires in the Amazon Basin when compared to equivalent values from savanna fires. This is important as CO is relatively easily detected from satellites and therefore used as a tracer for biomass burning events. Hence with this stable ratio, reliable parameterization of aerosols emitted from such fires can be made.

CH_4 is a greenhouse gas, it has a long life and hence is able to enter the stratosphere and affect the O_3 cycle there Blake *et al.*, 1996). Due to this longer lifetime, it is possible to detect CH_4 from biomass burning sources for a longer time compared to other gases (e.g. CO) with shorter lifetimes (Petersen *et al.*, 2010). CH_4 emissions from fires form around 8% of global emissions, however when looking at the increase in CH_4, fire emissions contribute to a much large proportion of this as other sources are remaining stable or getting smaller (for example wetlands) (Blake *et al.*, 1996). Although the atmospheric concentration of CH_4 is around 200 times less than CO_2, it has a much greater ability to trap heat; one CH_4 molecule is 20 times better at trapping heat than a CO_2 molecule (European Commission, 2002). Andreae (1990) estimated that between the years of 1940 and 1980, biomass burning contributed to 21% of the increase in CH_4 emissions. Unlike much of the CO_2 that is emitted during savanna fires,CH_4 does not get sequestered by the vegetation that grows back. Also, CO released during the fire can react with OH to produce CO_2, and hence reducing the main sink of CH_4 (Sinha *et al.*, 2003). Lavorel *et al.* (2006) asserts that in the cases where the land not getting burned leads to an increase in grazing, there will be more CH_4 produced.

Nitrogen Compounds

In experiments with tropical biomass fires, Yokelson *et al.* (2007) quantified the percentage of the fuel nitrogen that was measured in a fire emissions as nitrogen containing trace gases: ammonia; 16 ±8.9%, NO_x (NO_2 and NO); 5.4±2.8%, HCN; 1.3±0.6%, CH_3CN; 1.1±0.5%, propanenitrile; 0.9±0.5%, acryonitrile; 0.5±0.3% and pyrrole; 0.07±0.04%. Andreae (1990) suggests that around 60-70% is released in unknown forms, suggesting that there exists a significant loss of nitrogen from the ecosystems in which burning is a regular occurrence, particularly if the rest is released as molecular nitrogen (N_2). McNaughton *et al.* (1998) suggested that at least 60% of nitrogen in biomass could be left in residual as ash or uncombusted materials after savanna grassland fires. It is very difficult to measure the contribution of N_2 make by the smoke plume to atmospheric N_2 unless in the lab (Andreae and Merlet, 2001).

However, Lobert *et al.* (1990), looking at biomass emissions of nitrogen containing gases, es-

timated that on average, approximately 90% of the nitrogen in biomass was volatilized during burning. Only around 32% of the lost nitrogen was found in the measurements as NO_x NH_3, HCN, CH_3CN, other nitrils, N_2O, amines and HNO_3. The majority of the volatilized species took the form of NO_x, ($\approx$13%), ammonia ($\approx$4%) and HCN ($\approx$2.4%). It is suggested that the biomass burning emissions of some nitriles, such as hydrogen cyanide and acetonitrile may be much higher than industry and auto-mobile emissions and can consequently be used as global tracers for biomass burning. It is suggested that molecular nitrogen accounts for the nitrogen that is undetected. 20% of the undetected nitrogen could be organic compounds that were not measured (but tested with tobacco smoke), produced during incomplete combustion. Hence N_2 could account for the remaining 50% of the undetected nitrogen.

NO_x are released during mainly the flaming phase of a fire (Wang and McElroy, 2004). Biomass burning makes up to around 15% of global NO_x source fluxes each year, making it a reasonably large contributor to overall emissions (Oppenheimer *et al.*, 2004). Jain *et al.*, (2006) estimated the total global NO_x emissions from biomass fires used for land clearing to be 11-16 Tg $NO_x.yr^{-1}$. In areas where biomass burning occurs, emissions of NO_x from fires outweigh those from natural sources, such as soil emissions and lightning. When looking at aged biomass burning plumes, concentrations of NO_x are low, suggesting that most of the NO_x could have reacted with other species within 1 or two days. Hobbs *et al.* (2003) suggested that, in a study investigating emissions from a savanna fire in South Africa, up to 10% of NO_x initially emitted was converted to particulate nitrate in approximately 40 minutes, with much of the rest of the NO_x convert to e.g. PAN and HNO_3. It is unlikely that the NO emitted from fires will reach the stratosphere as before then it will have reacted with NO_2 and HNO_3 (nitric acid) (Crutzen *et al.*, 1979; Andreae *et al.*, 1988; Andreae, 1990; Blake *et al.*, 1996; Andreae and Merlet, 2001; European Commission, 2002; Oppenheimer *et al.*, 2004). NO_y encompasses NO_x as well as the compounds created with its oxidation, including HNO_3, N_2O_5, NO_3 and PAN. The main source of NO_y is emitted NO_x.

The amount of NO_2 contained in the atmosphere is dependent on certain reactions. One is

its reaction with OH, creating nitric acid (Oppenheimer *et al.*, 2004):

$$NO_2 + OH + M \longrightarrow HNO_3 + M, \tag{1.2}$$
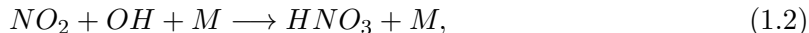
where M represents a general metal. Yet this reaction is not that important close to the plume as here OH reacts with other elements of the plume. When NO reacts with O_3, NO_2 and O_2 are produced (Oppenheimer *et al.*, 2004):

$$NO + O_3 \longrightarrow NO_2 + O_2. \tag{1.3}$$

This reaction is a possible secondary source of NO_2 from the fire.

N_2O, released mainly during flaming combustion, is a greenhouse gas that lives long enough to travel into the stratosphere, influencing the O_3 cycle (Andreae, 1990). It has been claimed that biomass burning may be responsible for about 25% of the total tropospheric increase of this species (Andreae, 1990). However, Lavorel *et al.* (2006) suggests that the N_2O released in the fire, along with the NO_x, is less than the value emitted by soil if it were able to accumulate. N_2O can affect the atmosphere both directly by the greenhouse effect and indirectly through photochemical reactions affect the O_3 layer (Ogawa and Yoshida, 2005).

HNO_3 is another nitrogen compound emitted from the fire, formed mainly during the combustion phase. HNO_3 is created photochemically from NO_x emitted from fires (Blake *et al.*, 1996). As well as from the reaction 3.6, HNO_3 can also be produced through the following set of reactions (Oppenheimer *et al.*, 2004):

$$NO_2 + O_3 \longrightarrow NO_3 + O_2 \tag{1.4}$$

During the day, net production of NO_3 is insignificant (because of strong photo-decomposition of NO_3) , at night however, it reacts with NO_2 (Oppenheimer *et al.*, 2004):

$$NO_3 + NO_2 \longrightarrow N_2O_5 \tag{1.5}$$

$$N_2O_5 + H_2O \longrightarrow 2HNO_3, \tag{1.6}$$

where the NO_2 in Equation 1.4 is from Equation 1.3.

The nitrogen (in oxidized form) that has been emitted from the fires will eventually get deposited on the surface through wet or dry deposition. The form it is in when it gets deposited can be of the form of HNO_3, NH_3, or dissolved in rain water as particulate nitrate and ammonium. The deposited nitrogen can be a source of nutrients to the crops where is has been deposited. but it can also acidify the environment where it has been deposited, in particular rivers and other water bodies (Oppenheimer *et al.* 2004). Acid rain has been reported in the tropics, where organic acids and nitric acids make up most of the acidity, unlike the acid rain found in the industrial regions, where sulphuric acid and nitric acid dominate. Andreae (1991) estimated that biomass burning contributes to approximately 11% of global emissions of NH_3. Figure 1.4 illustrates the cycle of nitrogen released by vegetation fires.

As already mentioned, McNaughton *et al.* (1998) found that at least 60% of nitrogen found in savanna grassland fuels was left as residual matter after a fire, in the ash or in the uncombusted residuals. Hence biomass burning in savanna grasslands may not result in a major fall in nitrogen content within the ecosystem. The nitrogen content can travel down in the soil, sometimes within hours, and can be used by the new re-growth of grass. This new regrowth, coupled with the possible grazing of the new vegetation, may be a key part in the nitrogen cycle in these ecosystems. The study concludes that current estimates of nitrogen emissions due to biomass burning are overestimated and that nitrogen retention is prominent. Romanya *et al.* (2001) emphasizes that the activity of nitrogen after a fire may be strongly dependent on the biomass type, finding that different fuel types (grass and shrubland) had different nitrogen mineralization rates during 6 months after fires.

Lavorel *et al.* (2000) estimated that most of the nitrogen that is emitted from biomass fires in Africa reaches terrestrial ecosystems in Africa, however around one third manages to travel to the ocean, where it is deposited. It is suggested that this may play a major role in

the growth of phytoplankton in the southern Atlantic and Indian oceans. However, there is a sort of cycle, where the fires result in nutrient losses, which leads to more fires to replace these nutrient losses as landowners carry out prescribed burns aiming to enrich the soil with more nutrients for example from the ash.

NO Reacts with $NO_2 \rightarrow HNO_3$
Reacts with $O_3 \rightarrow NO_2$

NH_3, HCN,..+..

NO_2 Reacts with OH $\rightarrow HNO_3$
Reacts with $O_3 \rightarrow NO_3$
Reacts with $NO_3 \rightarrow HNO_3$

NO_2
Reacts with O_3

Acid Rain/Fog

Deposition into lakes/rivers/sea

Atmosphere

Nitrogen

Absorption by plants through rain/fog or by absorption of gases

Uptake through ash
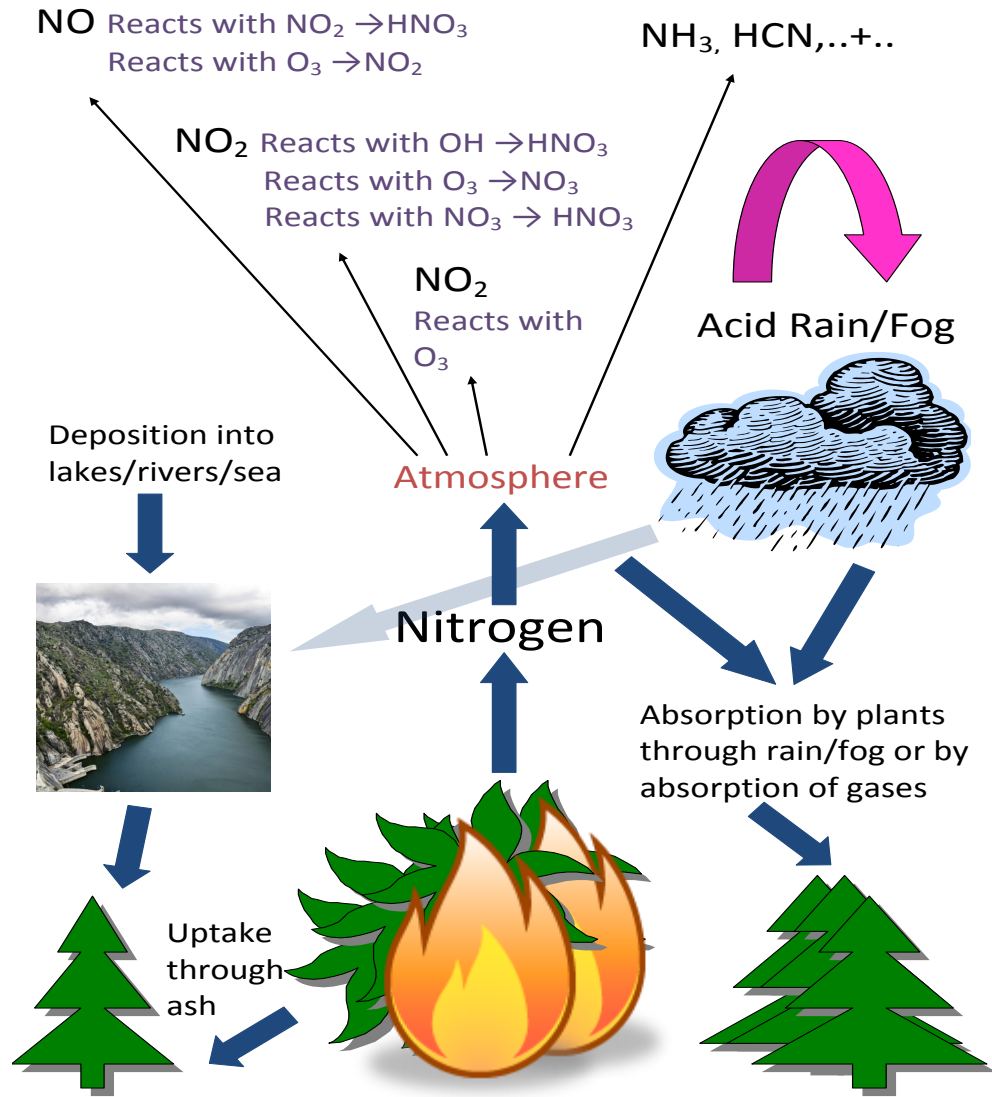
Figure 1.4: *The processes involved in cycle of nitrogen released by biomass burning.*

.

Sulphur and its Compounds

Andreae *et al.* (1988) found that when looking at plumes from biomass fires within the Amazon, levels of SO_2 within the plume were only weakly elevated from background levels. However, levels of sulphate (SO_4) in the plume were high, suggesting that a lot of the SO_2 was oxidized to SO_4 in the atmosphere. This is backed up by Blake *et al.* (1996), who stated that only some sulphur in plants will be converted into volatilized species during combustion, mainly SO_2, but also a small amount of carbonyl sulphide (COS). The remaining sulphur will be pyrolyzed at combustion to sulphate. In a study investigating emissions from a savanna fire in South Africa, Hobbs *et al.* (2003) found that, as much as 10% of SO_2 released was converted to sulphate. Fiedler *et al.* (2011) reported the reaction of SO_2 with OH in aging smoke plumes to produce sulphuric acid. Around 3% of global anthropogenic emissions of sulphur are from biomass burning. Yet as most of the anthropogenic activities that result in sulphur emissions are in industrial, temperate areas, biomass burning makes a more important impact in remote regions such as the Amazon and the Congo Basin (Andreae, 1990). Although biomass burning makes up only a small portion of the global sulphur budget, SO_2 and COS emissions are important as when volcanoes are not active, they are the main species that form sulphate aerosols in the troposphere and stratosphere. The creation of sulphate aerosols could lead to a change in radiative properties locally and regionally. They reflect radiation away from the Earth and also have the potential to act as CCN, changing the reflectiveness of clouds (Smith *et al.*, 2011). Also COS is oxidized to create sulphuric acid aerosol particles, these scatter sunlight and are part of the processes that have created the Antarctic ozone hole (Blake *et al.*, 1999). Also, it is important to understand sources of SO_2 based aerosols due to effects on global energy properties (Potter, 2002).

Tropical areas are known to be lacking of nitrogen and/or sulphur. During a fire, nitrogen and sulphur are released; if deposition in areas nearby occurs then there is no net loss. However, in the case of nitrogen, it is possible that most (up to 70%) (Andreae, 1990) is emitted as molecular nitrogen, resulting in a major loss of nitrogen. But other unburnt areas will receive a rise in nutrient inputs. It has been estimated that in the Amazon Basin, as much as 90% (Andreae, 1990) of all nitrogen and sulphur deposited originates from sources

different from the forest ecosystem, including biomass burning. The affect of this rise in nutrients is uncertain, especially when coupled with the rise in acid deposition (Andreae, 1990). Romanya *et al.* (2001) found that the immediate release of nitrogen into soil after a fire was small compared to other changes in soil nitrogen that would usually take place. However the changes in nitrogen content in the soil proved to be much larger during the next few months following the fire.

Ozone

O_3 is another gas that is efficient at absorbing infra-red radiation, with its reported increase in the troposphere making up around 15% of the total greenhouse effect. The photochemical production of O_3 due to biomass burning emissions makes up about half of the total increase in atmospheric O_3 (Blake *et al.,* 1996; Andreae, 1990). Potter (2002) states that tropospheric production of O_3 occurs in the event of photochemical oxidation of CO and hydrocarbons when NO_x is present. Andreae and Merlet (2001) suggest that O_3 concentrations in dilute smoke from biomass fires in the mid-troposphere carry on increasing until up to 14 days after ignition, with the O_3 emitted from smoke plumes in large areas of tropical forest on savannas forming a large portion of the sources of tropospheric O_3. Hobbs *et al.* (2003) found that levels of O_3 in minute old smoke from a savanna fire in South Africa were below ambient due to reactions in NO, but rose by 9% after just 30 minutes. Elevated concentrations of O_3 in tropical Africa are not unusual during the dry season, when the majority of the biomass burning occurs, with values comparable to that of polluted areas in Central Europe and Eastern United States. (Andreae, 1990). It has been suggested that in temperate areas, pollution in forest regions may occur due to high levels of O_3. In Europe and North America, the observed damage of trees and vegetation has been linked to this. In the tropics, there is an increase in O_3 levels with altitude, hence mountainous regions could be particularly sensitive to pollution (Blake *et al.,* 1996). Granier *et al.* (2000) found that a global increase of surface concentrations of O_3 due to biomass burning to be around 7%, with greater percentages on regional levels. In areas where biomass burning is common, percentages reach up to 17% due to emissions of species that produce O_3. Results showed a net increase of 25% of global O_3 production. Yet increases in the troposphere are smaller than surfaces

increases as O_3 concentrations are already very high there and chemical processes do not have such a prominent affect as near the surface.

Aerosols

Due to high variability in space and time, as well as complex optical and chemical processes, determining the impact of biomass burning aerosols is unclear (Abel *et al.*, 2005). Although the amount of particulate matter emitted during biomass burning is still not that clear, it is known that large amounts are frequently released. For example during the dry season in sub-sahelian of Africa, when agricultural fires are extremely common, a large layer of aerosols is created from the emissions of these fires, reaching from East to West, thousands of kilometers across Africa (Johnson *et al.*, 2008). The greater the age of such biomass burning aerosol, the greater the heights reached, for example fresh aerosols can be observed around 300m while aged aerosols can reach altitudes between 1.5 to 4 km (Johnson *et al.*, 2008). In a study by Blake *et al.* (1996) it was found that particulate organic carbon (POC) made up around 66% of the total amount of aerosol smoke. Black elemental carbon (EC) (soot and charcoal particles) levels in the smoke can vary, depending on whether the fire is smoldering or flaming (Andreae, 1990). However Ferek *et al.* (1998) found that although PM emissions were correlated with smoldering combustion of tropical vegetation fires, it was a weak correlation, suggesting that predicting PM emissions is a complex process and is not directly related to any phase of the fire. It was estimated that biomass burning emits around 90 $Tg.yr^{-1}$ of total particulate matter (TPM), which makes up around 6% of total aerosol emissions around the world. However, many of these are large particles that do not stay in the atmosphere for long, unlike the smaller particles which have longer lifetimes and are more effective in scattering solar radiation (Andreae, 1990).

The effect aerosols have on the climate is very uncertain as they have both direct and indirect effects. Direct effects are those caused by scattering and absorbing the Earth's radiation, hence changing the radiative balance of the Earth. Indirect effects are links with changing the properties of clouds. Cloud condensation nuclei (CCN) are aerosol particles on which cloud droplets form. If there are lots of CCN, more droplets form, which means

a smaller size of the droplets for a given amount of water. The smaller the cloud droplets, the more reflective the clouds and the more sunlight that is reflected back into the atmosphere and the less likely they are to produce rain. Clouds are one of the main variables that control the heat balance of the earth, hence any changes in cloud properties will have a severe effect on the climate. Data suggests that aerosol particles produced by fires are effective CCN. An increase in CCN may lead to a change in precipitation levels. Studies on how well fire induced aerosols act as CCN show that efficiency decreases with age. This adds to the changes in the water cycle in the tropics caused by deforestation and desertification (Andreae, 1990; Blake *et al.*, 1996; Abel *et al.*, 2005; Johnson *et al.,* 2008; Rose *et al.,* 2010).

Acid Rain

Acid rain has been found to be a problem in the tropics, not just in Europe and North America (Andreae, 1990; Blake *et al.*, 1996). However, in the tropics, the acidity comes mainly from organic (mainly formic and acetic acids) and nitric acids, whereas in more cooler regions, it is sulphuric and nitric acid that are the main acidifiers. The organic acids were originally thought to originate from natural emissions, such as plant emissions. Yet there is evidence now that organic acids could be a result of the gases from biomass burning and from photochemical reactions in smoke plumes. Acid containing species found in the atmosphere can be absorbed by plants either through wet deposition (through rain or fog) or by dry deposition (through direct surface absorption of gases and aerosols). In a tropical environment, it is mainly wet deposition that occurs, whereas in savannas it is dry deposition. It is thought that acid deposition in Europe and USA has lead to the damage in forests, either through the deposition of acidic aerosols and gases on leaves or through soil acidification. The gaseous nitric and organic acids emitted from biomass burning are likely to create an environment where fog and dew will be of a pH level that can damage leaves, which in absence of fires is uncommon. Trees in the tropics have leaves that have a longer lifetime compared to other areas in the world, hence they are more sensitive to foliar damage. Most tropical soils are resilient to acidification as they have the ability to absorb high levels of sulphate. Yet there are some areas, such as Venezuela, where soils are sensitive to acidification. In addition, if the more resilient soils are constantly exposed

to acid deposition, acidification will eventually occur. This will lead to a change in the dynamics of the nitrogen cycle as well as microbial processes. In the tropics, many animals, at some stage of their life, live in rainwater that has been collected by plants, and others, like frogs and salamanders, need water to keep their skins moist. Levels of acidity in the water are a risk to such animals (Andreae, 1990; Blake *et al.*, 1996).

Smoke Plume

It has been suggested that the pollution created by biomass fires can in some cases rival the industrial pollution of developed countries, specifically smog. Smog is made up of N_2O, hydrocarbons and CO, which chemically react with each other to create species that contribute to pollution, such as O_3. When looking at global emissions of the species that make up smog, biomass burning is a source to around 20-30% of them, which is around one half of the anthropogenic emissions (Blake *et al.*, 1999).

The chemical reactions that preserve the stratospheric ozone layer involve many of the gases that are emitted from biomass burning (Andreae, 1991). Generally, the plumes that travel high into the atmosphere are likely to affect radiation and O_3 formation, whereas those that stay closer to the surface have more of an effect on human health (Ferguson *et al.*, 2000). Smoke plumes can also have an effect on pressure and wind at large scales. For example gases and particulate matter emitted from biomass burning can alter the cloud average and vertical temperature profile, which has the effect of changing wind velocity and hence pressure at a local level. This local change in pressure must be accounted for elsewhere, which will in turn have an effect on wind speed and cloud cover (Jacobson, 2004). The amounts of trace gas species found in large plumes emitted from open vegetation fires depends on the age of the plume due to chemical reactions between the species. For example Sinha *et al.* (2004) found that after around 45 minutes downwind of a South African savanna fire, NO_2 had depleted yet O_3 had enhanced. It is important to note the age of the smoke plume sampled, as emissions derived smoke smoke measurements are directly used in global atmospheric chemistry models before chemical reactions may occur (Akagi *et al.,* 2011).

Yokelson *et al.* (2007) investigated a 'mega-plume' that was observed over parts of Brazil, Bolivia and Paraguay for around one month, during the TROFFEE research campaign. This sort of plume could perhaps be common in the tropics during the peak of biomass burning. Often plumes from fires do not integrate and hence age alone. However, this 'mega-plume' includes plumes from different fires and sampling showed a dilapidation of reactive gases, such as HCHO, C_2H_4 and C_2H_2. There was also signs of early development of O_3, formic and acetic acids. It was suggested that the mega-plume briefly affected air quality of São Paulo, around 1500 km away from the main burning area, when it was situated directly above the city.

1.4 Quantification of Global Emissions Budgets (from fuel consumption to emissions)

Atmospheric chemistry needs to be modeled to investigate and predict sources, sinks and concentrations of trace gases (Potter *et al.*, 2002). Quantifying emissions helps to evaluate the regional and global effects of biomass burning, with change in atmospheric chemistry due to biomass burning already noted (Andrea and Merlet, 2001). In particular, accurate characterizations of biomass burning impacts in atmospheric transport and atmospheric chemistry models require accurate and up-to-date emission data from biomass burning (Andrea and Merlet, 2001; Wiedinmyer *et al.*, 2006).

The total emission of a gas per annum, $E_{i,j}$ (g) for a type of biomass i within the fuel type j can be characterized as (Seiler and Crutzen, 1980):

$$E_{i,j} = A_{i,j} \times B_{i,j} \times CC_{i,j} \times EF_{i,j}, \tag{1.7}$$

$A_{i,j}$ (m^2) and $B_{i,j}$ (kg.m^{-2}) are burned area and fuel load respectively, for fuel i at j, $CC_{i,j}$ is the combustion completeness of fuel i at j, and $EF_{i,j}$ is the emission factor (g.kg^{-1}) of fuel i at j (Jain *et al.*, 2006).

The combustion completeness, CC, varies between fires that burn under different conditions, even if fuel types are similar, due to its dependence on the combustion process and

fuel moisture. Yet CC can be grouped for different environments, linked with fuel types, fuel loads, fuel configuration and the combustion that happens within these (Jain *et al.*, 2006). The combustion completeness of fine fuels are usually very high, close to 1. The coarser the fuel is, with lower surface to volume ratio, the higher the level of incomplete combustion. Water content also effects the combustion completeness, with twigs having higher values compared to live stem (van der Werf *et al.*, 2006). van der Werf *et al.* (2009) expressed the sensitivity of emission calculations to combustion completeness values. High, medium and low values were used (from a range of published estimates) to investigate sensitivity, with low values reducing emission calculation up to 40% and high values increasing calculations by up to 16%. The combustion completeness can be determined from laboratory studies and from biogeochemical models. Such models can simulate different types of fuels and moisture levels (Langman *et al.*, 2009).

The burned area is usually obtained from satellite burned area products, such as the AQUA/TERRA MODIS burned area product (Korontzi *et al.*, 2004; van der Werf *et al.*, 2006), Landsat data (Korontzi *et al.*, 2003) or the ESA-ATSR (GLOBSCAR) and SPOT-VEGETATION (GBA2000) burnt area data sets (Ito and Penner, 2004; Korontzi *et al.*, 2004; Jain *et al.*, 2006). Using burned area products rather than active fire detection overcomes the problem of gaps due to cloud cover and the fact that active fire detection only reside where the fire is burning at the time of the observation. However, as there has been a lack of multi-year burned area data, active fire detections are also used to estimate burned area. This has the advantage of being at near real time (Langmann *et al.* 2009). Yet, active fire events detected by satellites (such as NOAA-AVHRR and Tropical Rainfall Measuring Mission-Visible, Infrared Scanner (TRMM-VIRS) and the Along Track Scanning Radiometer (ATSR) hotspot systems), can be low due to the timing of the overpass. This is not so much the case for burnt area detections as burnt area can be detected for long periods of time, unlike active fires which may only last for a day or even several hours. Active fire detection is effective in tropical ecosystems where fuel can be very dense and hence burnt areas cannot be detected very efficiently. Yet there exists the problem of detector saturation when a fire burns at a high intensity (Ito and Penner, 2004; Michael *et al.,* 2005). Also there exists a

problem with the size of detectable active fires and burnt areas (Ito and Penner, 2004). For example, the GLOBSCAR and GBA burnt area data sets cannot detect burnt areas below 1 km^2 (Jain *et al.*, 2006). Estimates of individual burn scars derived using ground based and airborne measurements can be accurate but are not readily available (Akagi *et al.*, 2011).

Fuel load is a function of vegetation type, climate, soil, fire frequency and other processes that affect fuel quantities, such as grazing. Fuel load differs from biomass in that not all biomass will be available for burning, for example trees in savannas usually do not get burnt as flames do not reach the canopy. Emission estimates for peat fires have high uncertainties associated with them as these fires will burn at different depths such that the burned volume, not just area, needs to be taken into account (Langmann *et al.*,. 2009). In emission estimates, fuel load is usually obtained from modeling (e.g. Jain *et al.*, 2006) or by fuel sampling. Example models are those based on net primary productivity (NPP) with incorporating satellite driven inputs such as MODIS or AVHRR percent tree cover (Korontzi *et al.*, 2004; van der Werf *et al.*, 2006) or the use of satellite derived (e.g. AVHRR) NDVI (Ito and Penner, 2004). It is possible to use interpolation on a number of field site measurements to derive fuel loading, however the number of measurements may not be sufficient fir accurate estimations. Another method is to combine satellite measurements with plant production models to produce above ground biomass maps (Potter *et al.*, 2002).

The emission factor of a particular species is defined as the amount of species released per unit of dry fuel consumed by a fire (Andreae and Merlet, 2001). Despite considerable research on the determination of emission factors from numerous global projects, there still exists variability with the values found in the current literature. Current literature derivations and uncertainties are discussed in the subsequent sections as the emission factors are a key component in the data analysis of this work as well as in the general investigation of biomass burning emissions. Part of this current project involves quantifying emission factors of numerous species over various biomass types and hence will be described in more detail in the preceding chapters. Andreae and Merlet (2001) stated that one problem encountered while putting together data on emission factors was differing levels of detail available for

each trace gas and fuel type. Calculated average emission factors for the major compounds, for example CO and CH_4 had uncertainties of around 20-30%. Yet greater uncertainties exist when looking at regional and global fire emission due to the problems in measuring total biomass burned. To date, such measurements, per unit area, are rather ad-hoc, and have not greatly improved in line with the improvement of remote sensing instruments.

Another issue in the derivation of emission factors is their expectancy to change over seasons, due to changes in moisture. At times of the year when the fuel moisture content is high, smoldering combustion increases, leading to a change in emission composition. The amount of smouldering and flaming combustion can be approximated using the MCE value of Equation 7.1 (Ito and Penner, 2004). Yokelson *et al.* (2007) examined the variation of emission factors with MCE, with emission factors measured from tropical deforestation and vegetation fires in the Amazon, using airborne instruments. Figure 1.5 shows the emission factors of NO_x, CH_4, C_2H_4, CH_3OH, PM_{10} (particles less than 10 micrometers) and CH_3CN against MCE. NO_x emissions increased with MCE (favoring flaming combustion), while the emissions of the other compound showed a downward trend (favoring smoldering combustion) with MCE, apart from CH_3CN, which showed no relationship with MCE. The steeper the slope of the EFs against the MCE, the greater the dependence on the combustion process. An uncorrelated relationship between EFs and MCE suggests a weak dependence on the combustion process (Sinha *et al.*, 2003). A strong correlation with MCE suggests that EFs are a function of the combustion process taking place and hence it may not be suitable to have just 1 fire averaged for the emission factor of a whole fire but multiple values to represent each of the combustion stages.
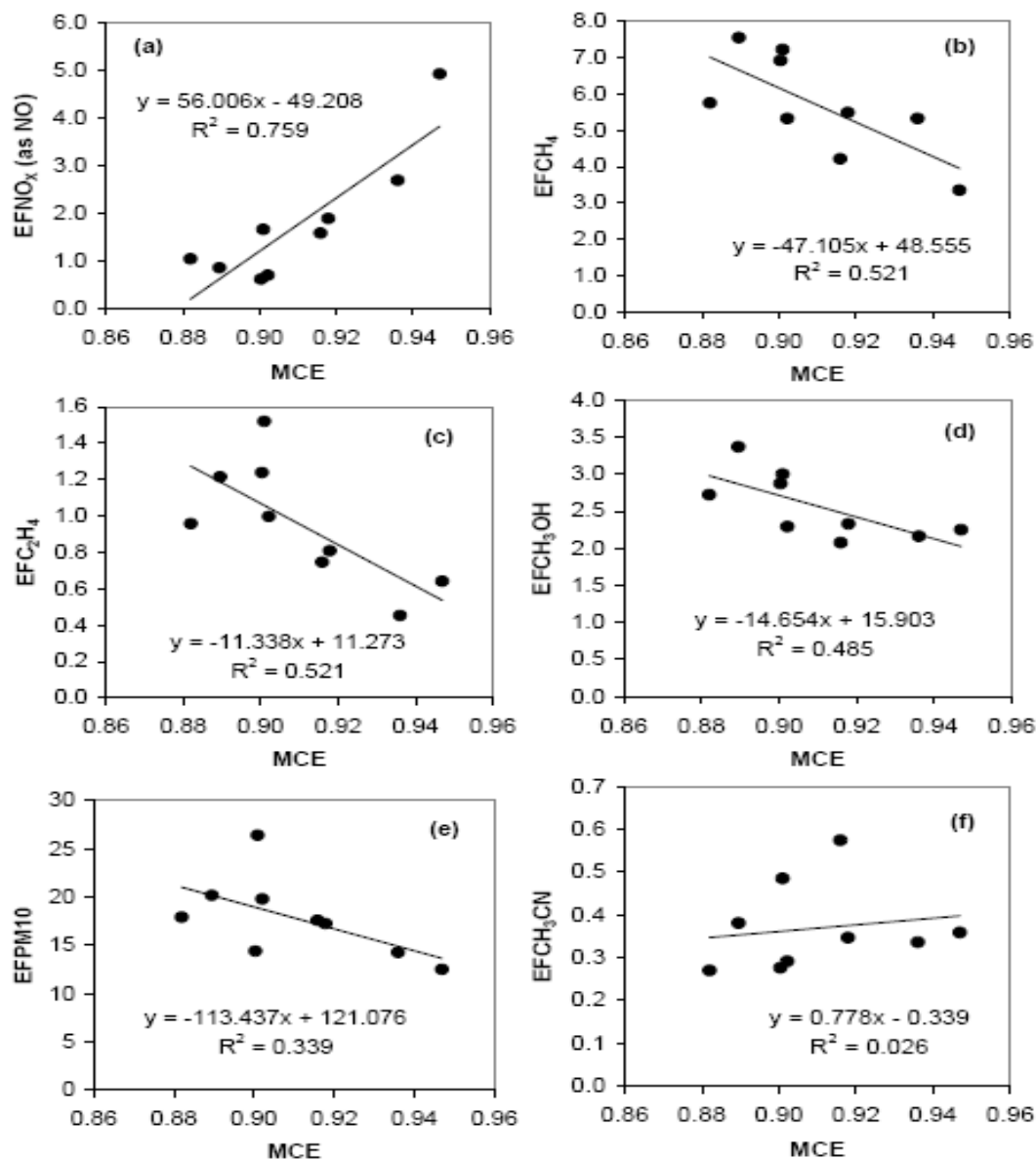
Figure 1.5: *Emission factors of NO_x, CH_4, C_2H_4, CH_3OH, PM10 and CH_3CN and their variation with modified combustion efficiency (MCE), taken from Yokelson et al. (2007).*

Equation 1.7 has much uncertainty associated with it, although the accuracy of measurements of $A_{i,j}$ are improving, the accuracy of the values of $B_{i,j}$ and $CC_{i,j}$ values can be very low, (Wooster *et al.*, 2005). For example, Andreae and Merlet (2001) assumed an error of $\pm 50\%$ in values of biomass consumed when calculating emission estimates of various gases for different fuel types. In addition, Sinha *et al.* (2004) attributed the uncertainty of derived

emissions from woodland and grassland savanna fires in southern Africa to the uncertainty of burned area estimates derived from the SPOT satellite (approximately 30%), which are 55% greater than the MODIS burned area values from Korontzi *et al.* (2003). Combined with uncertainties of approximately 30% and 10% for the combustion completeness and emission factors respectivly, the total uncertainty of the derived emissions of Sinha *et al.* (2004) is approximately 70%. If inter-annual variability of biomass burning emissions are to be compared, then such variability in the combustion completeness and burned area need to be examined also (Sinha *et al.*, 2004).

Following on from the work of Kaufman *et al.* (1996), Wooster *et al.* (2005) has proposed the use of fire radiative energy, which is directly related to the amount of biomass combusted to avoid the inaccuracies of $B_{i,j}$ and $CC_{i,j}$ used to measure amounts of biomass combusted. Fire Radiative Power, (FRP) can be defined as a measure of the radiant energy released per unit of time during biomass burning, due to the rapid oxidation of the fuel, hence relating to rates of fuel combustion and carbon loss. Fire Radiative Energy, (FRE) is equal to the integrated FRP values, with respect to time, over the whole duration of the fire (Roberts *et al.*, 2005). Deriving the fuel biomass combusted during a fire as a function of FRP can allow for the possible substitution of the product $A_{i,j} \times B_{i,j} \times CC_{i,j}$ in Equation 1.7 with this function to eliminate the uncertainties associated with these variables. There has already been a significant amount of research on the quantification of the FRP from biomass burning (e.g. Kaufman *et al.*, 1998; Wooster *et al.*, 2003; Riggan *et al.*, 2004) and specifically the relationship between FRP and biomass consumed by a fire (Roberts *et al.*, 2005; Wooster *et al.*, 2005). Ichoku and Kaufman (2005) investigated the use of FRE measurements from MODIS to estimate emissions from of aerosols emitted from biomass burning. In addition to this, there has been work carried out on the relationship between between FRE and CO_2 and CO from laboratory vegetation fires (Ichkoku *et al.*, 2008; Freeborne *et al.*, 2008). However these methods have not been validated in the field via comparisons with other independent measurements of fire emissions of fuel consumption. Hence there is a need to confirm the ability of the FRP to be used to aid in the estimated of trace gas emissions from open vegetation fires.

Another approach used to estimate trace gas emissions from fires is inversion modeling, a *top down* approach which derives emissions from trace gas concentration measured in the atmosphere (Stroppiana *et al.,* 2010). For example MOPITT has been used to measure CO emissions (Petron *et al.*, 2004). The Model for OZone and Related chemical Tracers (MOZART; Horowitz *et al.*, 2003) was used with *a priori* sources of CO emissions (Stroppiana *et al.,* 2010). For the inverse problem, *a priori* information on the emission structures are used, and subsequently changed such that the model finds the best fit for the measured concentrations.

Figure 1.6: *Images from MODIS on NASA's Aqua satellite: The above is of two large fires in the Okanogan-Wenatchee National Forest in northern Washington captured on the 2nd August 2006. Below is of many fires located in Lake Baikal in south-central Russia on July 10th 2006. Active fires detected by MODIS are shown in red.*

1.4.1 Determination of Emissions

Most experiments carried out to analyze emissions from fires are done by *in situ* gas sampling. Such sampling can be done in the field or by an aircraft, in which continuous or discrete sampling is carried out. The analysis of the samples can be carried out either in the labs or *in situ* (European Commission, 2002). Remote sensing has been used to investigate fire properties within space and time, such as burned area, pre- and post-biomass load and moisture content, fuel distribution, fire characteristics and information on trace gas and aerosol emissions (Stroppiana *et al.*, 2000; European Commission, 2002; Akinori and Penner, 2004).

The information from field and laboratory studies can be used in models to calculate emissions of aerosols and trace gas emissions at different spatial resolutions (European Commission, 2002). Yokelson *et al.* (2008) discussed the advantages and disadvantages of obtaining chemical emission data from the field and from the laboratory. Measurements made of fires in the field have the advantage examining the fires that are considered to have a "global" impact. However, in the case of laboratory work, it may be that is it possible to examine more species due to the fact that smoke uncertainties tend to be higher. In addition, equipment of considerable size, weight or complexity is easier to use in the lab compared to the field. Laboratory work permits measurements of the smoke from the whole fire, unlike in the field where most of the smoke goes unsampled. Airborne measurements tend to overestimate flaming emissions whereas ground based measurement tend to underestimate them (due to the former rising higher in the atmosphere due to their thermal buoyancy). Ground based instruments tend to be better for measuring smoldering emissions (e.g. from logs) that do not rise to high altitudes. A large quantity of these emissions is then pushed upwards either by thermal or frontal properties, yet in general their lifetimes maybe shorter than those species that initially rise to high altitudes through rapid plume injections. Residual smoldering combustion (RSC), combustion phase during an open vegetation fire in which the smoke is not lofted to high altitudes, are usually not sampled during aircraft measurements. Not much data exists on the components of RSC smoke (Sinha *et al.*, 2004).

A major problem with laboratory experiments is that emissions chemistry may differ to those in the field, in particular for tropical vegetation as it is not easy to burn large tropical logs in the lab. McNaughton *et al.* (1998) examined vegetation fires both in the field and in the lab of the same biomass type (tropical grasses) and found that the fire length and total energy released were greater in the laboratory experiments. Hence species emissions and volatilization not only vary according to biomass type, but also with factors such as wind speed, moisture, temperature etc.., which will more than likely differ in the field and laboratory. McNaughton *et al.* (1998) suggests that it is inefficient to use laboratory derived emissions and multiply them by estimated fuel load to determine global and regional budgets. In particular, it is not reliable to assume that a particular fraction of biomass is combusted, as combustion is very sensitive to fuel load, so estimates of average fuel loads and combustion efficiencies have errors. Dhammapala *et al.* (2007) reiterated this by suggesting that combustion experiments carried out in burn chambers are not effected by the same conditions as fires that occur in the field, such as the climate, terrain, burning conditions and fuel moisture. Guyon *et al.* (2005) suggested that as measurements by aircrafts are biased to flaming combustion and ground based measurements are biased towards smoldering emissions, the two methods should ideally be used together to get accurate emission estimates.

Satellite sensors are commonly used to investigate fire properties (for example burnt area or trace gas emissions). MODIS on the NASA Aqua and Terra satellites and SEVIRI on the MSG satellite have both been used for the purpose of active fire detection (e.g. Giglio *et al.*, 2006; Amraoui *et al.*, 2010). However data is measured at a given location at most a few times a day. However when cloud cover and instrumental orbit are taken into account, this becomes more like a few times a week. Hence satellite data can possibly produce limited temporal trends for a given fire compared to ground based or airborne remote sensing techniques. Also there is a trade off between spacial and spectral resolution. The greater the spatial resolution, the more coarse the spectral resolution is, which means large regions can be examined at a time however it will be difficult to detect small fires. However for the case of fine spectral resolution, small fires can be detected yet not at a large regional

coverage (Eva and Lambin, 1998). Yet the use of satellite instruments allows for the tracking of biomass burning plumes in space and time, which is important when investigating the transportation of pollution (Coheur *et al.*, 2009). Also such measurements have the benefit of global covarage (Wagner *et al.*, 2008). The use of nadir viewing spaceborne instruments has recently been used to retrieve gaseous emissions from biomass plumes, for example Coheur *et al.* (2009) used the Infrared Atmospheric Sounding Interometer (IASI) on MetOp-A to investigate the concentrations of several species (e.g. NH_3, CH_3OH and C_2H_4) in biomass burning plumes. Other such examples include the global ozone monitoring experiment (GOME) on ERS-2 and the Scanning Imaging Absorption Spectrometer for Atmospheric Cartography (SCIAMACHY), with the ability to measure gases such as CO_2, CH_4, N_2O and CO (Wagner *et al.*, 2008).

1.4.2 Existing Emissions Budgets and Rates

There have been numerous studies in the past carried out in order to put together to estimate emissions factors of the main gaseous species emitted from open vegetation fires across the globe. The most widely used data set is that of Andreae and Merlet (2001), who brought together available data on fire emission factors. Emission factors, split into categories in terms of fuel types, were used to calculate global emissions of certain species during the last part of the 1990s.

The Tropical Forest and Fire Emissions Experiment (TROFFEE) was a 2004 field campaign using ground based and airborne data collection methods, combined with laboratory work, to examine emissions from tropical deforestation fires in the Amazon. Tables 1.3 - 1.5 show the emission factors estimated using airborne measurements (Yokelson *et al.*, 2007) and laboratory measurements (Yokelson *et al.*, 2008). The emissions of CO_2 and CO from deforestation fires in the Brazilian Amazon Basin were studied as part of the Large Scale Biosphere Atmosphere Experiment (LBA-SMOCC) (Guyon *et al.*, 2005).

Sinha *et al.* (2003) used an airborne FTIR and gas chromatography to calculate emission ratios and emission factors from savanna fires in South Africa, Zambia, Mozambique and

Botswana. EF for numerous species that had at the time not been previously reported as emitted from biomass burning of savannas in southern Africa were reported. These species include DMS, methyl nitrate, several hydrocarbons and particulate matter. Several EFs calculated in this study differed quite strongly with those listed in Andrea and Merlet (2001), for example HCHO and hydrogen cyanide (by factors of 3 and 20 respectively) and ammonia (by a factor of 4). The emission ratios and emission factors from shifting cultivation prescribed burns in tropical deciduous forests in India were calculated by Prasad et $al.$ (1999).

Tables 1.3, 1.4 and 1.5 present a summery of the EF calculated in the studies detailed above. They reflect the inter-species variation between studies and ecosystems. For example the CO EF derived by Andreae and Merlet (2001) for tropical forests (104 g.kg^{-1}) is 5 times greater than that given by Prasad et $al.$ (2000) for Indian tropical deciduous forests (21.4 g.kg^{-1}). However Sinha et $al.$ (2003) and Andrea and Merlet (2001) presented CO EF of similar values for African savannas (68 and 65 g.kg^{-1} respectively). The EF for CO_2 and CH_4 do not exhibit too much of a variation, particularly CO_2 as this makes up the vast majority of the emissions from vegetation fires. NO_2 is usually included as in estimations of NOX EF, not on its own. This is the case for NO too. Yokelson et $al.$ (2007) and (2008) present NO_2 EF for tropical forests in the Amazon, with the former 3 times bigger than the latter, probably due to the difference in measurement techniques discussed above. There is a noticeable lack of literature values of SO_2 EF, perhaps due to the difficulty in measuring this species in biomass burning plumes.

Other work aimed towards the measurement of emission ratios and emission factors includes Castro et $al.$ (2007), who investigated emissions from low temperature biomass burning. Emission ratios of CH_4 and ammonia were calculated from laboratory based infra-red spectroscopy of shrub fires representative of shrubland fires in Spain. Prasad et $al.$ (2002) computed emission ratios and emission factors from ground based sampling methods of shifting cultivation forest fires in India. A significant amount of infer-fire variability was noticed in terms of the emission ratios, which was put down to local site conditions, topography, environmental parameters and fuel characteristics. The CO to CO_2 ratio was linked with

the duration of flaming combustion, with higher values of this ratio implying shorter lengths of flaming combustion. Andreae *et al.* (1988) carried out aircraft sampling and *in situ* measurements of biomass burning in the Amazon Basin as part of the Amazon Boundary Layer Experiment (ABLE 2A). The paper noted that the calculated emission ratios would be biased towards the larger fires generating more heat as emissions from these fires are transported to greater altitudes.

Table 1.3: *Emission factors of CO$_2$, CO and CH$_4$ from Prasad et al. (2000), Andreae and Merlet (2001), Sinha et al. (2003), Guyon et al. (2005), Yokelson et al. (2007) and Yokelson et al. (2008).*

CO			
EF (g/Kg)	**Type**	**ER (CO/CO2)**	**Reference**
68 (±30 SD)	African Savanna	0.064 (±0.022 SD)	Sinha et al. (2003)
21.4	Indian tropical decidous forests	12.4	Prasad et al. (2000)
101.41 (±23.78 SD)	Amazonian Tropical forests and vegetation	-	Yokelson et al. (2007)
90	Amazonian Tropical forests and vegetation	9	Guyon et al. (2005)
57.46 (±29.74 SD)	Amazonian Tropical forests and vegetation	-	Yokelson et al. (2008)
65 (±20 SD)	African Savannas and grasslands	-	Andreae and Merlet (2001)
104 (±20 SD)	Tropical Forests		Andreae and Merlet (2001)

CO2		
EF (g/Kg)	**Type**	**Reference**
1700 (±60 SD)	African Savanna	Sinha et al. (2003)
1615 (±40 SD)	Amazonian Tropical forests and vegetation	Yokelson et al. (2007);
1677 (±111 SD)	Amazonian Tropical forests and vegetation	Yokelson et al. (2008)

CH4			
EF (g/Kg)	**Type**	**ER (CH4/CO)**	**Reference**
1.7 (±0.98 SD)	African Savanna	0.053 (±0.12 SD)	Sinha et al. (2003)
5.68 (1.38 SD)	Amazonian Tropical forests and vegetation	-	Yokelson et al. (2007)
3.82 (±1.99 SD)	Amazonian Tropical forests and vegetation	-	Yokelson et al. (2008)
2.3 (±0.9 SD)	African Savannas and grasslands	-	Andreae and Merlet (2001)

Table 1.4: *Emission factors of NO_2 and NO from Prasad et al. (2000), Andreae and Merlet (2001), Sinha et al. (2003), Yokelson et al. (2007) and Yokelson et al. (2008).*

NO2		
EF (g/Kg)	**Type**	**Study**
As NOX 3.3 (±0.6 SD)	African Savanna	Sinha et al. (2003)
As NOX 4.15	Indian tropical decidous forests	Prasad et al. (2000)
1.83 (±1.25 SD)	Amazonian Tropical forests and vegetation	Yokelson et al. (2007)
0.59 (±0.25 SD)	Amazonian Tropical forests and vegetation	Yokelson et al. (2008)
As NOX 3.9 (±2.4 SD)	African Savannas and grasslands	Andreae and Merlet (2001)
As NOX 1.6 (±0.7 SD)	Tropical Forests	Andreae and Merlet (2001)

NO		
EF (g/Kg)	**Type**	**Study**
As NOX 3.3 (±0.6 SD)	African Savanna	Sinha *et al.* (2003)
As NOX 4.15	Indian tropical decidous forests	Prasad *et al.* (2000)
0.74 (±0.88 SD)	Amazonian Tropical forests and vegetation	Yokelson *et al.* (2007);
1.284 (±0.83 SD)	Amazonian Tropical forests and vegetation	Yokelson *et al.* (2008)
As NOX 3.9 (±2.4 SD)	African Savannas and grasslands	Andreae and Merlet (2001)
As NOX 1.6 (±0.7 SD)	Tropical Forests	Andreae and Merlet (2001)

Table 1.5: *Emission factors and ratios of SO$_2$ and HCHO from Andreae and Merlet (2001), Sinha et al. (2003), Yokelson et al. (2007) and Yokelson et al. (2008).*

HCHO		
EF (g/Kg)	**Type**	**Study**
68 (±30 SD)	African Savanna	Sinha *et al.* (2003)
1.66 (±2.86 SD)	Amazonian Tropical forests and vegetation	Yokelson *et al.* (2007);
0.66 (±0.51 SD)	Amazonian Tropical forests and vegetation	Yokelson *et al.* (2007);

SO2		
EF (g/Kg)	**Type**	**Study**
0.43 (±0.3 SD)	African Savanna	Sinha *et al.* (2003)
0.35 (±1.6 SD)	African Savannas and grasslands	Andreae and Merlet (2001)
0.57 (±2.3 SD)	Tropical Forests	Andreae and Merlet (2001)

There has been many studies using previously calculated emission factors and emission ratios to investigate biomass burning emissions on a regional and global scale. For example van der Werf *et al.* (2006) used the emission factors from Andrea and Merlet (2001) to estimate biomass burning emissions on a global scale for the years of 1997-2004, using a satellite driven biogeochemical model. van der Werf *et al.* (2009) describe the DEforestation

CArbon Fluxes (DECAF) model, in which satellite data is used to investigate properties of fire emissions over different land covers, including factors that are not usually covered within biomass burning modeling frameworks, such as the timing and duration of deforestation fires. Ito and Penner (2004) used satellite data to estimate global biomass emissions for the year 2000. A number of sources were used to obtain emission factors, the main one being Andreae and Merlet (2001). Potter *et al.* (2002) estimated emissions from biomass burning in the Brazilian Amazon region using satellite observations and ecosystem modeling between 1992-1993. Sinha *et al.* (2003) used calculated emission factors from savanna fires in tropical Africa to estimate emission totals of certain gases for the first time, including formaldehyde, ammonia and hydrogen cyanide (HCN). Ideally, such models would combine suitable resolution burned area data with fuel load modeling of the same resolution. Yet most global models are based on global biogeochemical modeling which have a coarser resolution due to data constraints (van der Werf *et al.*, 2010).

1.5 Previous Field Campaigns on Active Fire Measurement

There have been numerous global and regional projects, investigating factors such as burned area and gas emissions. They have been carried out at different sites around the world and then extrapolated to areas where no suitable data can be obtained. Such projects include

- The Biomass Burning Experiment: Impact on the Atmosphere and Biosphere (BIBEX), part of the International Global Atmospheric Chemistry (IGAC) Project, under the International Geosphere-Biosphere Program (IGBP), which has carried out various experiments on biomass burning in grasslands of southern Africa and Brazil, tropical forests in Brazil and Russian boreal forests.

- NASA carried out the Smoke, Cloud and Radiation (SCAR) experiment in forests in the United States Pacific Northwest. SCAR-C looked at the US pacific fires and the properties and radiative effects of the emitted smoke and trace gases. SCAR-B was carried out over continental Brazil and the southern Amazon Basin to look at chemical and radiative properties of biomass burning smoke.

- One of the programs launched under BIBTEX was the Southern Tropical Atlantic

Regional Experiment (STARE), which had two components: Southern Africa Fire-Atmosphere Research Initiative-1992 (SAFARI-92) and Transport and Atmospheric Chemistry near the Equator-Atlantic (TRACE-A).

- Under BIBEX and the International boreal Forest Research Association (IBFRA), an experiment on biomass burning in the boreal forests of Russia was launched, the first phase of the Fire Research Campaign Asia-North (FIRESCAN).

- The Experiment for Regional Sources and Sinks of Oxidants (EXPRESSO), using ground based and aircraft data methods in the Central African Republic and the Republic of Congo to look at tropical biogeochemistry, remote sensing was also used to investigate location and extent of biomass burning and vegetation type.

- The African Fire Atmosphere Research Initiative (AFARI), was an expansion of the SAFARI project, looking at Kenyan Savanna fires and aerosol, CO and CO_2 concentration.

- The Zambian International Biomass Burning Emissions Experiment (ZIBBEE) was conducted over southern African woodlands, looking at aerosol and trace gas emissions.

- The Tropical Forest and Fire Emissions Experiment (TROFFEE) was set up to investigate emissions from tropical deforestation fires. This included a series of laboratory experiments in conjunction with airborne and ground-based fieldwork. (Levine, 1996; European Commission, 2002; Yokelson *el al.*, 2007).

Instruments and analysis methods that have been used in field experiments, both using *in situ* and remote sensing measurements include (Andreae *et al.*, 1988; Andreae *et al.*, 1994; Levine *et al.*, 1996; Blake *et al.*, 1999; Stroppiana *et al.*, 2000; Praasad *et al.*, 2002; Wooster *et al*, 2003; Riggan *et al.*, 2004; Oppenheimer *et al.*, 2004):

- Airborne lidars (for example to measure O_3 and aerosol distribution)

- Laser absorption instruments (for CO)

- Infrared absorption instruments, for example the imaging spectrometer EDRIS (for CO_2)

- Optical scanner probes (aerosol densities, differential absorption instruments (for CO and NO_2) chemiluminescent instruments (for O_3) grab samples of air and smoke, which are then analyzed, for example, by gas chromatography.

- Spaceborne instruments include the high resolution LandSat TM, the National Oceanic and Atmospheric Administration Advanced Very High Resolution Radiometer (NOAA AVHRR), the Along Track Scanning Radiometer (ASTR) on the European Resource Satellite (ERS-1), the Geostationary Operational Environmental Satellite (GOES), the Moderate Resolution Imaging Spectroradiometer (MODIS), and the Bi-Spectral Infrared Detection (BIRD) satellite.

For TROFFEE project, Karl *et al.* (2007) and Yokelson *et al.* (2007) used an airborne Fourier Transform Infrared Spectrometer (AFTIR) and a Proton-Transfer-Reaction mass spectrometer (PTR-MS) for the aircraft measurements and again an FTIR for ground-based measurements to obtain mixing ratios and consequently emissions of trace gases and volatile organic compounds (VOCs). As part of the same project, Yokelson *el al.* (2007, 2008) explained the laboratory experiment which used an open path FTIR and a PTR-MS to validate field results and to obtain mixing ratios of various trace gases not measured in the field. Guyon *et al.* 2005 made aircraft measurements over pasture and deforestation fires in the Brazilian Amazon Basin using a Licor infrared gas analyzer to measure CO_2, an Aero-Laser for CO measurements, and an isokinetic inlet for aerosol particle sampling. Petersen *et al.* (2010) made use to ground based solar FTIR measurements to investigate CH_4 concentrations in Suriname, including during biomass burning events.

1.5.1 Outline of Thesis

The review of the literature has shown that FRP is becoming more commonly used, however the method for generating smoke emissions fluxes is unvalidated at anything other than lab scale (Freeborne *et al.*, 2008). At the same time, the UV-DOAS methodology suggests a route to obtain plot scale measurements of smoke fluxes for UV active gases (e.g.NO_2, SO_2) and techniques such as OP-FTIR or lab analyses may provide a route to getting the necessary x:SO_2 or x:NO_2 ratios that would be required to combine the fluxes of the UV-active species to those of the more important carbonaceous species, without relying on the uncer-

tain emissions ratios listed in the literature which may not be specific to the environment under study. Below is an outline of the structure of the thesis.

Chapter 2 introduces the main principles of electromagnetic radiation, including the concepts of emission and absorption of radiation by mediums. The chapter then goes into detail about absorption spectroscopy, as this forms the basis of the analysis methods used to retrieve trace gas amounts and mixing ratios from the ground based instruments used in the field campaign of this thesis: the UV spectrometer for differential absorption optical analysis a (UV-DOAS) and the Infra-red Fourier Transform Spectrometer (FTIR). The general instrument design and measurement principles for both the UV-DOAS and FTIR are outlined in this chapter.

Chapter 3 follows into the general methods that can be applied to retrieve trace gas amounts and mixing ratios from the spectroscopic methods measured using the UV-DOAS and FTIR. The concept of forward modeling is introduced and explained. This method can be applied to the analysis of both the UV and IR spectra collected during the field campaigns. In addition, an emperical method that can be applied to the UV-DOAS spectra to return trace gas column amounts is described. Lastly, a comparative analysis of the trace gas retrieval methods described in the chapter is carried out and the methods chosen for the subsequent analysis of the field data are justified.

Chapter 4 outlines the how the trace gas amounts and mixing ratios derived from the UV and IR spectra can applied further. In particular for the UV analysis, this includes the dertermination of fluxes of SO_2 and NO_2 and emission factors and emission ratios for the IR analysis. In addition to this, Fire Radiative Power is introduced and methods on its derivation are outlined.

Chapter 5 introduces the South African and Canadian field campaigns, and in particular, the deployment of the UV-DOAS during these experiments. The specific methods used to derive pathlength averaged column amounts and fluxes of NO_2 and SO_2 from this instru-

ment are given. The results are presented and discussed.

Chapter 6 describes the pilot study of FTIR measurements during the South African field campaign. The specific methods used for the data analysis are described and the results are presented and discussed. This chapter also includes the synthesis of the UV-DOAS and FTIR data from South Africa and comparisons with MIR thermal camera derived FRP time series.

Chapter 7 presents details of the Australian field campaign. This includes the deployment of both the UV-DOAS and FTIR and analysis methods to retrieve and compare data from these instruments. The results are presented and discussed, including an inter-comparison of results from the previous field campaigns presented in Chapters 5 and 6. There is a comparison of trace gas derived fluxes with the FRP time series from the same fires. Results are compared with current work in the literature.

Chapter 8 presents the key findings of the previous chapters and concludes the main outcomes of this research. Also, suggestions for potential future research are outlined.

Chapter 9, the Appendix, details further work that has been carried out after the initial submission of this thesis.

Chapter 2

Principles of Ground Based Atmospheric Spectroscopy in the UV and IR Spectral Regions

Contents

2.1 Basic Principles of Electromagnetic Radiation

The properties of electromagnetic radiation are usually interpreted with respect to either the particle or wave model (Platt and Stutz, 2008). The former describes radiation as if it were a series of photons, with characteristics similar to particles. The latter states that wave-like vectors are released as energy from the vibrations of particles (Barrett and Curtis, 1992). In this latter model, the regions of the electromagnetic radiation spectrum are classified into various sections depending on their wavelength (see Figure 2.1). Wavelength is defined as successive maxima or minima of a wave, and frequency as the number of waves per second. The relationship between the frequency and the wavelength is as follows (Koller, 1965):

$$\lambda = \frac{c}{\upsilon},\tag{2.1}$$

where υ is the frequency, λ is the wavelength and c is the speed of light (299,792,458 m.s^{-1}). The energy level by the photons in the electromagnetic radiation is given by:

$$E = h\upsilon = \frac{hc}{\lambda}.\tag{2.2}$$

Hence the longer the wavelength, the lower the energy intensity.
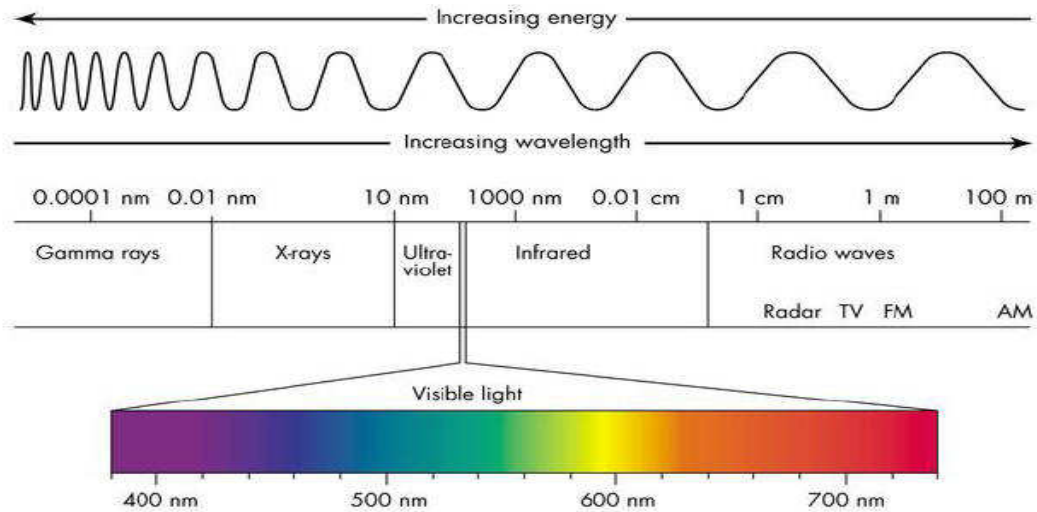
Figure 2.1: *Electromagnetic Spectrum.*

All material above absolute zero (0 kelvin) emits electromagnetic radiation (Barrett and

Curtis, 1992). The Stefan-Boltzmann Law quantifies the energy emitted by a blackbody, a perfect absorber and radiator of radiation (Barrett and Curtis, 1992):

$$M = \sigma T^4,$$

(2.3)

where M is the total radiant energy emitted (Wm^{-2}), σ is the Stefan-Boltzmann constant $5.6697 \times 10^{-8} \text{Wm}^{-2} \text{K}^{-4}$ and T is the absolute temperature (K) of the emitter. From this relationship it is clear to see that the total emitted energy increases rapidly with increasing in temperature. Note that in reality most naturally occurring objects exhibit properties quite close to, but not equal, to those of a blackbody (due their bodies normally not having an emissivity of 1 at all wavelengths). Figure 2.2 illustrates how the shape of the emitted electromagnetic spectrum of a blackbody changes with respect to temperature. The area under each curve is equal to the total energy emitted, M. As temperature increases, the maximum of the energy distribution moves towards shorter wavelengths (Lillesland *et al.*, 2007). This can be described using Wien's displacement law:

$$\lambda^* = \frac{A}{T}.$$

(2.4)

λ^* is the wavelength at which the maximum energy is reached and A is 2898 μm.K (Wien's constant). The sun emits radiation with a spectral distribution of a blackbody at a temperature of around 6000 K and a λ^* in the VIS spectral region as calculated in Equation 2.4. Similarly, the Earth has a mean temperature of around 300 K, with its maximum emitter wavelength around 9.7 μm (well within the thermal infra-red region and not visible with the human eye) (Lillesland *et al.*, 2007).
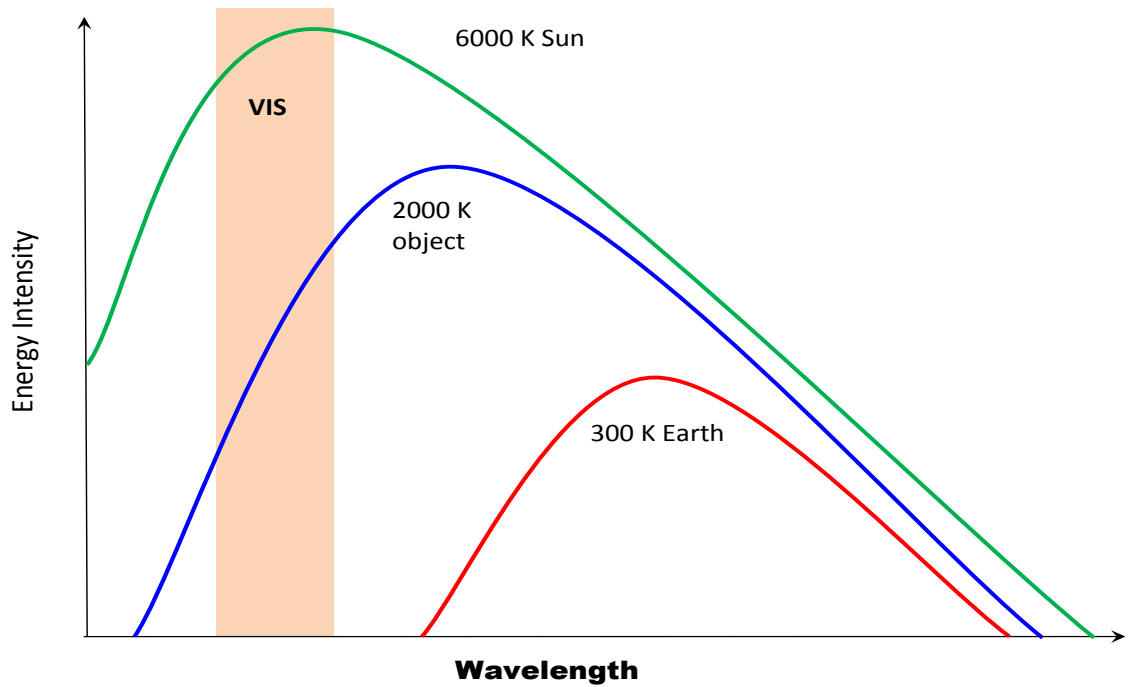
Figure 2.2: *The spectral energy emission distribution of bodies of varying temperatures: 300 K (e.g the Earth), 2000 K and a 6000 K blackbody (e.g the sun). Notice that as the temperature of the body falls, the peak of the energy distribution moves to longer wavelengths, described by Wien's displacement law, Equation 2.4.*

Since real objects are not black bodies, the Stefan-Boltzmann Law is not a true description of the energy emitted. We can relate the total energy that is expected to be emitted by a blackbody (M_b) to the energy (M) that is actually emitted by a body at a given temperature (Lillesland *et al.*, 2007) by:

$$M = \epsilon M_b, \tag{2.5}$$

where ϵ is the broadband emissivity of the actual body. The emissivity is a measure of how 'well' a body is able to emit energy compared to a blackbody. ϵ lies at 0 and 1, with the emissivity of a blackbody equal to 1. A greybody has an emissivity less than 1 and fixed with wavelength. If the emissivity of a of a body is a function of wavelength, it is said to be a selective radiator. Some objects can behave like a blackbody within a certain wavelength range, for example, water has an emissivity close to 1 between 6-14 μm. The wavelength interval 8-14 μm is key as it is the region in which most objects on Earth (with temperature

at approximately 300 K) have their thermal radiation emission peak, hence most thermal remote sensing instruments measure within this spectral range. The emissivity of an object can also be a function of its conditions. For example, soil has a greater emissivity when wet than when dry. From Equation 2.4, as the temperature of a body rises, the wavelength at which it emits radiation at a maximum moves to shorter wavelengths. Hence some remote sensing systems work within the shorter wavelengths to detect hotter objects (such as fires), but this tends to compromise their ability to best detect of objects of lower temperature (Lillesland *et al.*, 2007).

2.1.1   Spectral Lines

Spectral lines are identified at wavelengths where intensity fluctuates 'suddenly' with respect to wavelength, either positively or negatively, in an otherwise continuous spectrum. Such lines are characterized as emission lines (an increase in intensity) or absorption lines (a decrease in intensity), see Figure 2.3.
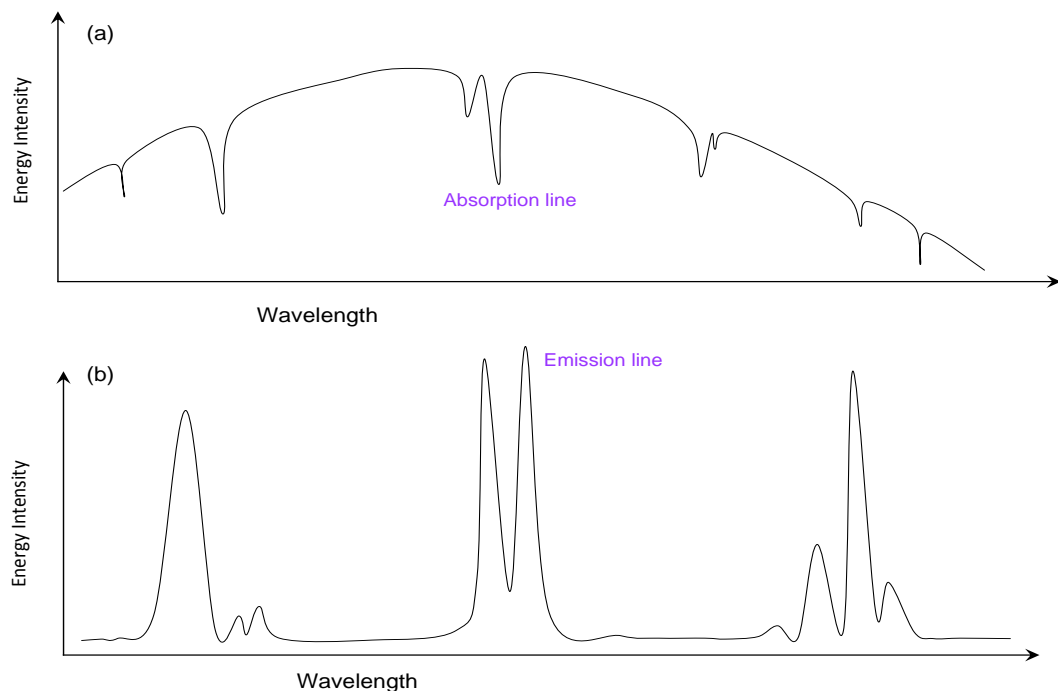
Figure 2.3: *Sketches of (a) absorption and (b) emission spectra. The absorption spectrum exhibits a drop in intensity at the wavelengths where absorption lines occur. Likewise the emission lines appearing on the emission spectrum correspond to an increase in intensity at given wavelength.*

Recall Equation 2.2, the relationship between the wavelength or frequency of the electromagnetic radiation and its photon energy. A change in energy level of a molecule can be of the form of electronic, vibrational or rotational energy, with electronic energy changes needing the most energy and rotational energy changes needing the least. A change of energy level state in the form of electronic energy is known as electronic excitation. This can be thought of as the move of an electron in the outer shell of the molecule to a higher energy level state. The electrons of an atom are negatively charged and situated around the positively charged nucleus. The electrons are kept in orbit due to the opposite charges of the nucleus (positive) and electrons (negative). The electron moves to a higher orbital state during electronic excitation, and a greater energy level is achieved. Rotational excitation can be defined as the rotation of the entire molecule, and vibrational energy as the vibration of the individual atoms within the molecule. The normal electronic energy level of a molecule is known as its

ground state, with greater electronic energy levels denoted as the first and second excited states.

When the energy level state of an electron falls from a higher to a lower state value, energy must be lost and so photons are emitted. This causes spectral emission lines. Conversely, absorption lines occur when photons are absorbed as the energy level of a molecule increases. In the case where the molecule only absorbs a small amount of energy from a photon, e.g. in the far infra-red or microwave region, only a change in its rotational energy will occur. If more energy is absorbed, for example, in the near infra-red region, then the vibrational energy may change as well as the rotational energy. For even greater levels of photon energy, as in the UV region, all three can change: electronic, vibrational and rotational. Note that as only particular energy levels are possible, only particular wavelength photons are absorbed or emitted, causing spectral lines and not broadband features (Rao, 1961; Jensen, 2007; Platt and Stutz, 2008).

2.2 Absorption Spectroscopy

2.2.1 Basic Principles

Radiation is emitted by the sun and arrives at the top of the atmosphere. Radiation is also emitted by the Earth's surface, clouds and water vapor. When electromagnetic radiation passing through the atmosphere it is affected by key main processes, scattering and absorption (see Figure 2.4).

Scattering of radiation by particles in the atmosphere can alter both its direction and intensity and can thus cause attenuation. The main types of scattering are Rayleigh, Mie and non-selective scattering. Rayleigh scattering is caused by particles with diameters smaller than the wavelength of the radiation (Barrett and Curtis, 1992). The effect of Rayleigh scattering is inversely proportional to the 4th power of the wavelength, so shorter wavelengths are scattered more by this process (Lillesand *et al.*, 2007).
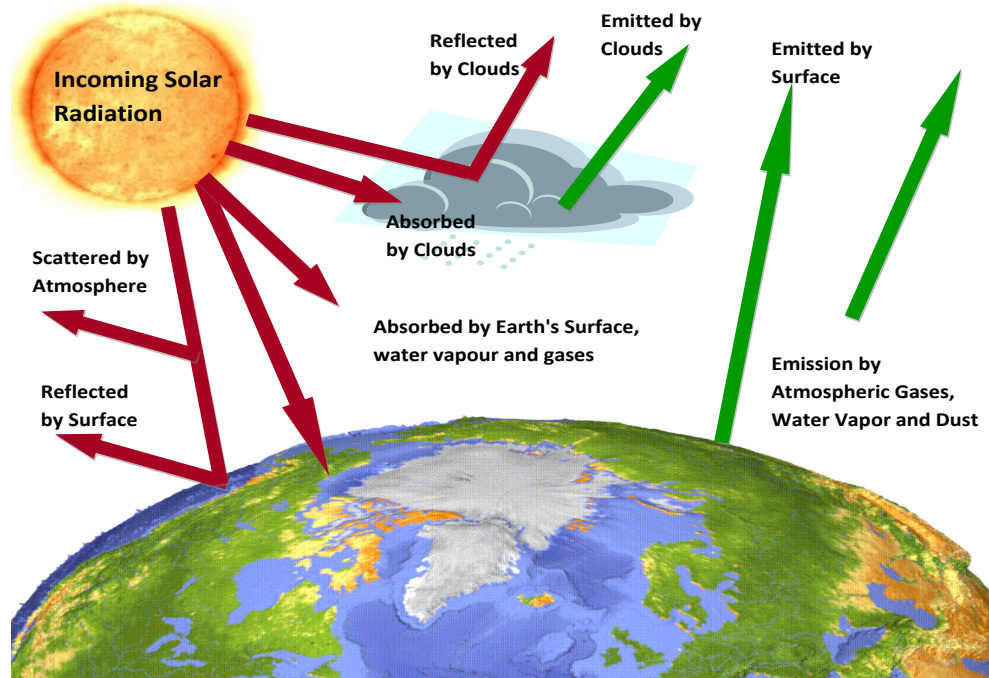
Figure 2.4: *Radiation balance of the Earth and its atmosphere. Electromagnetic radiation is emitted by the sun. This radiation is effected by numerous processes as it passes through the atmosphere and to the surface, such as scattering in the atmosphere, reflection (by clouds and Earth's surface) and absorption (by atmosphere, Earth's surface and clouds). Radiation is also emitted by the Earth's surface, the atmosphere and clouds, albeit at longer wavelengths.*

Rayleigh scattering is the reason why the sky appears blue, as light from the sun at this shorter visible wavelength gets maximumly scattered in the atmosphere (Platt, 1994). Rayleigh scattering is termed "elastic", such that the scattering of a photon changes its direction, but not its energy (Platt and Stutz, 2008). When the particles in question have a diameter approximately equal to the wavelengths of the scattered radiation, the process is defined as Mie scattering. Mie scattering is also elastic and its strength is inversely proportional to wavelength, but to a weaker extent when compared to Rayleigh scattering (inversely proportional to $\lambda^{1.3}$) (Platt and Stutz, 2008). Non-selective scattering occurs when the particles have a diameter much greater than the wavelength of the radiation involved in the scattering process. Water droplets are an example of atmospheric particles that can cause non-selective scattering. With diameters ranging from 500-10000 nm water molecules can scatter all radiation within the VIS and NIR spectral regions, and this type of scattering is not wavelength Dependant (Lillesand *et al.*, 2007).

In contrast to scattering, electromagnetic absorption occurs when part of the incident radiation is converted into heat and later re-emitted as electromagnetic energy, quite possibly at different wavelengths (Barrett and Curtis, 1992). Consider radiation from a continuous source passing through a column of gas, with electrons at a given set of energy levels. The energy of the photons of the radiation are absorbed such that the atoms of the gas move to a higher energy level state. Those photons that do not have sufficient amount of energy to excite the electron level state pass through the gas. The photons that get absorbed by the gas cause absorption lines in the spectrum at the given wavelength where the photons have the necessary energy to cause the electron energy level change that has occurred. The most common gaseous atmospheric absorbers are water vapor, carbon dioxide and ozone (Lillesand *et al.*, 2007). Figure 2.5 illustrates the distribution of solar energy against wavelength at the top of the atmosphere and at sea level and the effect of atmospheric absorbers is clearly seen as a strong decrease in spectral intensity at the particular absorption wavelengths.
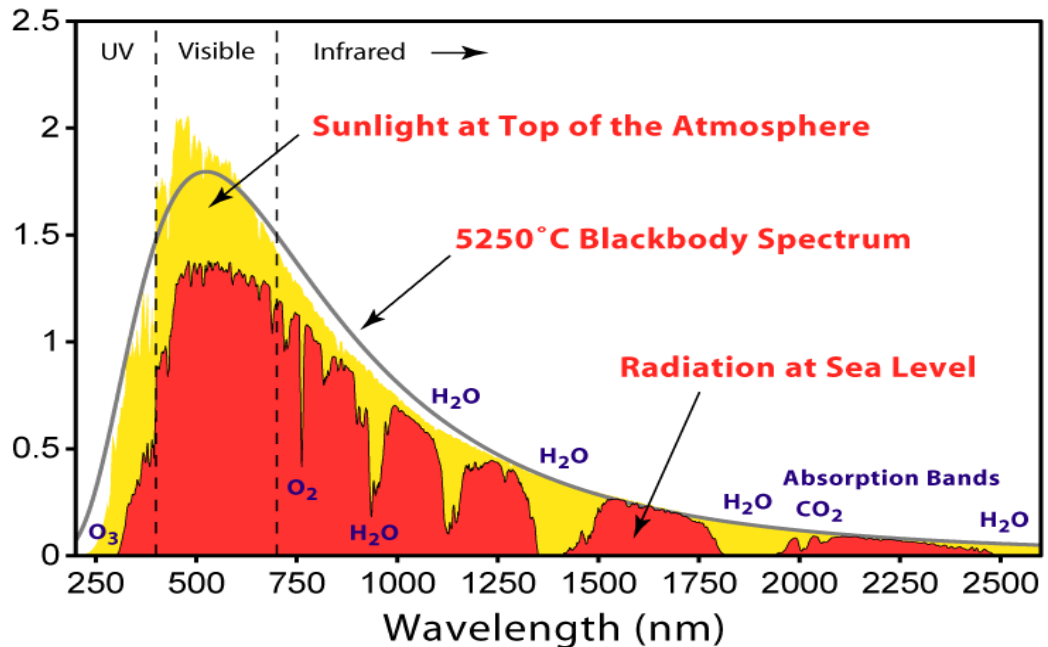
Figure 2.5: *The spectral distribution of radiation at the top of the atmosphere, of a 5250ºC blackbody and at sea-level. The radiation at sea level passes through the atmosphere and hence is effected by the absorption of atmospheric gases such as O_3 and CO_2, decreasing the intensity at the wavelengths in which the absorption occurs. The solar radiation at the top of the atmosphere has a spectral distribution similar to that of a blackbody as there is no decrease in intensity due to atmospheric absorption.*

Note in Figure 2.5 the decrease in radiation intensity due to the main atmospheric absorbers. Also shown is the the blackbody spectrum that quite clearly matches the top of the atmosphere signal, which is that of a perfect absorber and radiator of radiation (Barrett and Curtis, 1992).

Incident solar radiation at the Earth's surface can also be reflected. The way radiation is reflected from a surface is dependent on the surface roughness. The are two types of reflectors; specular and lambertian. The former occurs when the given surface is smooth, i.e. has irregularities that are shorter than the wavelength of the incident energy, causing the energy to be reflected away from the surface at an angle equal to its incidence. Lamberitan surfaces are 'rough' and reflect radiation in all directions in a uniform manner. Most surfaces have properties somewhat in-between the two types. When the wavelength is much shorter than the roughness heights of the surface, Lambertian reflection occurs. The albedo of an

object is the percentage of total incident radiation (over all appropriate wavelengths) that is therefore reflected. A perfect reflector is known as a white body (Barrett and Curtis, 1992; Lillesand *et al.*, 2007).

Transmittance is defined as the percentage of radiation passing through a surface with respect to the original incident radiation. When light passes through a medium and is absorbed, the intensity of the outgoing light falls in relation to that of the incident light (Rao, 1961). Transmittance, T, as defined above, can be expressed as (Thomas, 1996):

$$T = \frac{I(\lambda)}{I_0(\lambda)}, \tag{2.6}$$

where $I_0(\lambda)$ is the intensity of the incident beam that is emitted by the source and $I(\lambda)$ is the transmitted intensity after it passes through the medium, both at wavelength λ. The sum of any absorbed, reflected and transmitted radiation at a surface at any given wavelength must equal that of the incident radiation (Barrett and Curtis, 1992).

2.2.2 Beer Lambert Law

Absorption spectroscopy is defined as the process of analyzing the radiation transmitted through an absorbing medium that is situated between a radiation source and a spectrometer, in order to collect absorption spectra (Rao, 1961). The Beer Lambert law states that the amount of incident light that is absorbed is proportional to the number of molecules along the path, such that the concentration of the material that the light passes through, as well as the pathlength, influences the amount of absorption and transmission (Rao, 1961; Platt and Stutz, 2008):

$$I(\lambda) = I_0(\lambda)e^{(-L\sigma(\lambda)c)}, \tag{2.7}$$

where c (molec.cm^{-3}) is the volumetric concentration of the absorption species, L (cm) is the light pathlength and $\sigma(\lambda)$ (molec.cm^{-2}) is the absorption cross section of the absorbing species at wavelength λ (nm).

$\sigma(\lambda)$ is a characteristic property defining the absorption characteristics of a molecular species

at each wavelength. The cross section is unique to each species, like a fingerprint. By comparing the absorption patterns with the measured spectra, the presence of particular gases and their amounts in the ambient atmosphere or "polluted" plumes can be deduced. Hence the concentration of a species can be calculated using (Platt and Stutz, 2008):

$$c = \frac{log\left(\frac{I_0(\lambda)}{I(\lambda)}\right)}{\sigma(\lambda)L}, \tag{2.8}$$

Defining D as the optical density:

$$D = log\left(\frac{I_0(\lambda)}{I(\lambda)}\right), \tag{2.9}$$

allows us to simplify Equation 2.8 to:

$$c = \frac{D}{\sigma(\lambda)L}. \tag{2.10}$$

However, Equation 2.8 is not fully realistic as it does not take into account all factors that will affect the solar light intensity as it travels through the atmosphere. The greater the atmospheric path (airmass) traveled, the smaller the intensity reaching the surface due to (Platt, 1994):

1. Mie and Rayleigh scattering (for the UV). When such scattering occurs, light is lost from the path and does not reach the detector. Hence this needs to be taken into account.

2. Absorption by other gas species apart from the target species within the light path will cause further reduction in light intensity. There are many gas species within the atmosphere that absorb light. Ozone is a particular issue in the UV and has strong absorption features around 200-300 nm (the Hartley band), as well as weaker absorption bands between 320 and 350 nm (Huggins band) and 450 and 750 nm (Chappius band) (Platt, 1994).

Ideally, all of the above must be taken into account when attempting to derive the amounts of target trace gas atmospheric species via absorption spectroscopy.

2.3 Ultraviolet (UV) and Infra-red (IR) radiation

Most remote sensing instruments tend to focus on measuring energy in the UV/VIS, IR or microwave spectral regions. The choice of region depends on the interactions between radiation and the mediums being measured. In the UV/VIS and near/mid IR properties such as moisture content, pigmentation and mineral content affect the level of energy measured by the instrument. Whereas in the thermal IR, it is heat capacity and other thermal features that control the levels of radiation present (Richards, 1986).

The UV portion of the electromagnetic spectrum ranges from approximately 4 to 400 nm, the exact range depending on the literature as the limits of each of the spectral regions are not well defined. Within the UV regions, two subregions are defined: the near and far UV, from around 300-400 nm and 200-300 nm respectively. The region between 4-200 nm is known as the extreme UV; radiation within this range is strongly absorbed by the atmosphere (Koller, 1965), in particular by stratospheric ozone. Gas species that can be detected using UV spectroscopy due to their absorption features within this spectral region include NO, NO_2, NO_3, HNO_2, NH_3, SO_2, O_3, and OH (Platt, 1994).

The infra-red (IR) spectral region can be found approximately between 700-14000 nm, and can be split into three sections; the near IR (700-1300 nm), the shortwave or mid IR (1300-3000 nm) and the thermal IR (3000-14000 nm) (Lillesand *et al.*, 2007). There is a wide range of molecules that can be detected via their absorption features in the IR spectral regions, including CO_2, CO, CH_4, SO_2, NO_2, and many hydrocarbons. IR radiation has an important role in the greenhouse effect, the process whereby certain gases ('greenhouse gases') absorb and re-emit (partially in the downward direction) upwelling thermal IR radiation, hence increasing Earth's temperature. There are various greenhouse gases in the atmosphere that are very efficient at absorbing infrared radiation, for example CO_2, CH_4, N_2O SO_2, HNO_3, O_3, and NH_3. The concentrations of these gases in the atmosphere may be low, however their effect on the thermal properties of the atmosphere are strong as they can absorb radiation with the wavenumber range 700-1400cm^{-1}, which is the atmospheric window in which the majority of the earth's thermal radiation is transmitted from the earth's surface and lower

atmosphere (Wang *et al.,* 1976).

2.4 Instrumental design and measurement principles

2.4.1 Introduction

For any remote sensing instrument, the specific measurement requirements depend on what the instrument is intended to be used for. For example the light throughput should be maximized to allow for the detection of gas species with low optical densities (Platt and Stutz, 2008). Active measurements are made when the remote sensing instrument uses an artificial light source, whereas in a passive set up the light source is naturally emitted, either by the target itself of an external source, such as the sun (Barrett and Curtis, 1992; Lillesand *et al.,* 2007). The active system set up typically consists of an artificial light source, the spectrometer at the end of the light path and the target medium between the two instruments (Figure 2.10a)). With active measurements, the amount of light reaching the instrument can be controlled by the light source and telescope, however for passive measurements only the telescope can be used. The measurement spectral range is chosen such that the target species can be identified. Obviously a large spectral range allows for the detection of more species, however this can compromise the spectral resolution. The spectral resolution should be narrow enough to detect the absorption structures caused by the target species. The narrower the spectral resolution, the better the detection limit. However, a huge spectral resolution can compromise the size of the instrument and the light throughput (Platt and Stutz, 2008).

2.4.2 UV Spectrometer for Differential Absorption Optical Spectrometry (DOAS) applications

The key components of a DOAS system usually include a telescope, spectrometer, detector, computer and software for analysis and for active measurement also an artificial light source with optics to influence the light path.

Here I shall focus on describing the Ocean Optics USB4000 UV Spectrometer, which is the

instrument used in the current work to measure UV light for use in the DOAS process. The spectrometer, shown in Figure 2.6, has a spectral range of 280-422 nm and spectral resolution of ≈0.05nm. The instrument is portable and lightweight, with dimensions 89.1×63.3×34.4 mm and weight of 190 g. The design of the instrument is based on the asymmetrical crossed Czerny-Turner framework (two mirror system in which the incoming radiation is reflected by the first mirror onto a grating and refocused by the second mirror onto the detector). The focal length is the distance between the mirror and the point where the mirror will focus parallel rays of light. The focal length of the mirrors are 42 mm an 68 mm respectively. The grating is a 2400 mm^{-1} line UV holographic grating that disperses the different wavelengths of light onto the detector array. The detector used is a Toshiba TCD1304AP Linear Charged Coupled Device (CCD) array. The number of pixels (spectral channels) produced is 3648, with pixel dimensions 8 μm×200 μm.
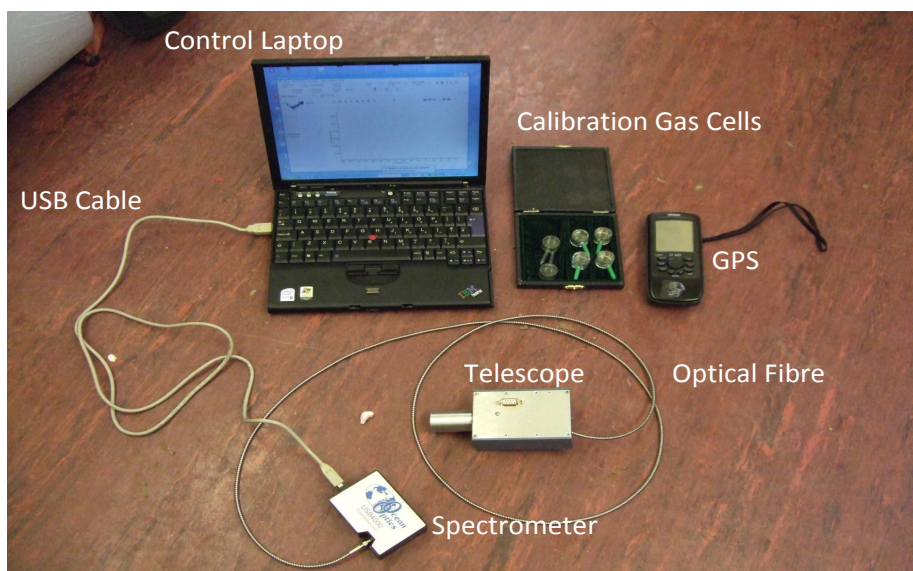
Figure 2.6: *The equipment of the DOAS system used in this work, showing the USB4000 spectrometer connected to the telescope through an optical fiber and the laptop through a USB connection. Also shown is the GPS and gas calibration cells used during data collection.*

For DOAS spectral measurements, scattered sunlight is collect by a 12.7 mm quartz lens

telescope with a 25 mm focal length and 1 degree field of view. The telescope is connected to the 50 μm USB4000 spectrometer entrance aperture by a 2 meter long steel cased 600 micron quartz fiber optic cable. The spectrometer is controlled by a laptop using a USB 2.0 connection at 480 Mbps. The current software used to operate the USB4000 spectrometer is the Ocean Optics SpectraSuite. A 12v battery can be connected to the spectrometer to provide power. As well as a USB 2.0 connection, the spectrometer is operable with a RS-232 connection at 115.2K baud. Most computer operating systems are compatible with the USB4000; Windows 98/Me/2000/XP, Mac OS X and Linux with a USB port and any 32-bit Windows OS with a serial port (Platt, 1994; Galle, 2002). Figure 2.6 shows the entire Ocean Optics UV DOAS system used herein.

During the measurement process of the system shown in Figure 2.6, scattered solar light is collected by the telescope and travels via the optical fiber into the spectrometer entrance aperture (see Figure 2.7) (Galle *et al.*, 2002). Here the light is firstly reflected by a collaminating mirror onto the grating.
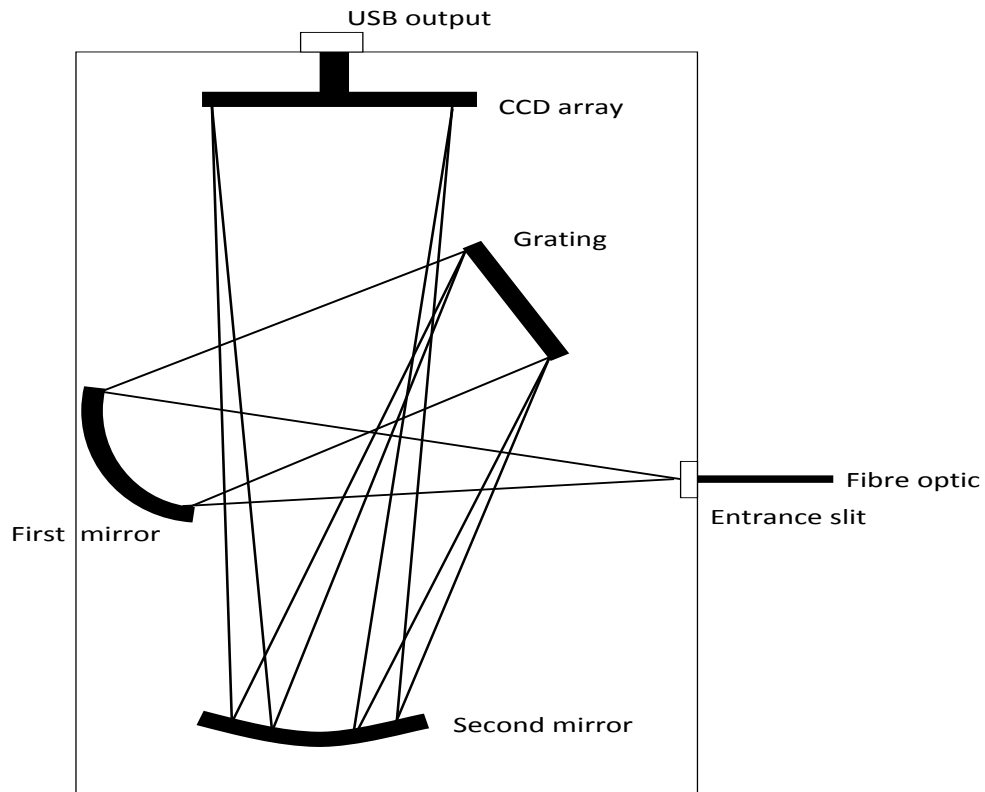
Figure 2.7: *Light path within the USB4000 UV spectrometer, adapted from Galle et al. (2002)*

.

The grating forms the basis of the spectrometer, it separates the incoming radiation into individual wavelengths, such that the intensity at each separate wavelength can be measured. The grating used in the USB4000 system is a diffraction holographic grating, compromising of a group of equally spaced slits which reflect light, whereas the area between the slits does not. Holographic gratings are created by measuring the interference pattern of two light beams, in contrast to ruled grating where the groves are drawn mechanically. All the grooves are created simultaneously, such that there is not much deviation between grove positions and thus small amounts of stray light (Platt and Stutz, 2008). The grating disperses the light into separate wavelengths traveling in slightly different directions using slits that have

a sinusoidal cross section. The 2400cm^{-1} groove density determines the degree of dispersion. After being dispersed, the light is refocused by a final curved mirror onto the CCD detector array. The purpose of the detector is to convert the radiation intensity $I(\lambda)$ into a signal that can be read by the computer, $I'(\lambda)$ (Platt and Stutz, 2008):

$$I'(\lambda) = c.I(\lambda). \tag{2.11}$$

This is done using a linear row of silicon photodetectors (each representing a 'pixel'), that convert the light intensity that reaches the detector into an electrical signal. When the radiation falls on the photodetector, photoelectrons are produced. The number of photoelectrons that are produced is proportional to the intensity of the radiation. This electrical signal is then output through the USB connection to the laptop. A spectrum is formed by combining the signal from each pixel of the CCD array, each one corresponding to light of a different wavelength.

The Czerny-Turner system has a low efficiency associated with it due to the use of two mirrors, as opposed to for example a concave grating spectrometer that consists only of an entrance slit, grating and detector. This is because the extra mirror induces reflection losses (Platt, 1994). In addition, the holographic gratings are considered to be less efficient than the ruled gratings since, whilst they tend to have lower levels of stray light, they have higher levels of light of unused orders, which may increase the stray light of the spectrometer as a whole. The CCD has become recently popular for use in spectrometers, since it is cheap to produce and already being used in camcorders, fax machines, computer scanners etc.. Unlike other detectors, for example the PDA (Photodiode Array) detector, the array of the CCD is two dimensional. This allows for greater pixel height and the possibility to record several spectra at the same time. (Hollas, 1998; Platt and Stutz, 2008).

A DOAS set up similar to that shown here (sometimes called a "mini" DOAS system due to its small size and low cost) has been used in the past to measure trace gas concentrations in the ambient air for the purposes of monitoring pollution. For example Li *et al.* (2007) used the DOAS system to measure tropospheric NO_2 in Beijing, Theys *et al.* (2007) used

the instrument to retrieve stratospheric and tropospheric BrO columns on Reunion Island, while Hendrick *et al.* (2007) did the same for Harestua. Wagner *et al.* (2003) described how the DOAS could be used to get information on atmospheric aerosols and Pisano *et al.* (2003) used the system to measure SO_2 emissions from vehicles. There have also been numerous experiments involving the DOAS to measure SO_2 fluxes from volcanoes, for example Edmonds *et al.* (2002), Galle *et al.* (2002), McGonigle *et al.* (2002; 2003; 2005) and McGonigle (2007). However, to date there have been very few studies in which the DOAS has been targeted at emissions from biomass burning. Platt (2008) put forward the idea that is should be possible to use such systems to gain information on biomass burning plumes whilst Oppenheimer *et al.* (2004) actually employed the instrument to measure NO_2 emissions from sugar cane agricultural fires in Brazil, the only known actual use of the method to vegetation fires.

2.4.3 Fourier Transform Infrared (FTIR) Spectrometer for IR Spectroscopy

As with the DOAS system, the FTIR spectrometer set up typically consist of a light source, telescope, spectrometer and detector. The FTIR has the benefit of measuring the incoming radiation at all wavelengths simultaneously rather than separately like dispersive models with a single detector. The difference with the FTIR instrument is the employment of an interferometer, which is completely unlike the standard monochromator. A monochromator works by singling out the radiation at certain wavelengths and measuring the intensity at these wavelengths. An interferometer measures the intensity at all wavelengths simultaneously. Dispersive models that make measurements from each wavelength separately have a much slower measurement process. In addition to speed, FTIR instruments allow for higher optical throughput due to a larger entrance aperture, therefore allowing for a higher signal to noise ratio (Davis *et al.*, 2001).

FTIR instruments typically use a Michelson interferometer that splits the incident radiation using a beam splitter into two separate paths which are reflected off two mirrors, one fixed and one moving away from the beam splitter, (see Figure 2.8).
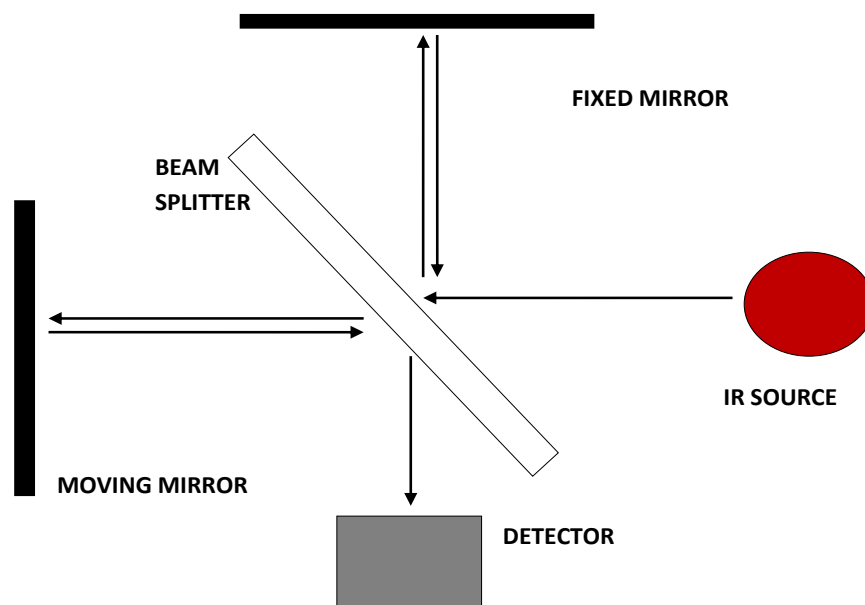
Figure 2.8: *Basic illustration of the the FTIR spectrometer workings. Radiation from the IR source enters the spectrometer and onto the beam splitter, which separates the incoming light into two paths. The light paths are reflected by two mirrors, one fixed and the other moving forward and away from the beam splitter and then meet again at the beamsplitter. The subsequent signal, denoted as the interferogram, is dependent on the optical path difference of the two light paths.*

The two beams subsequently reconvene at the beamsplitter. The resulting signal, a combination of the fixed pathlength and moving pathlength beams, is known as the interferogram. The interferogram is a function of the optical path difference of the of the two beams, with time plotted against intensity, see Figure 2.9.
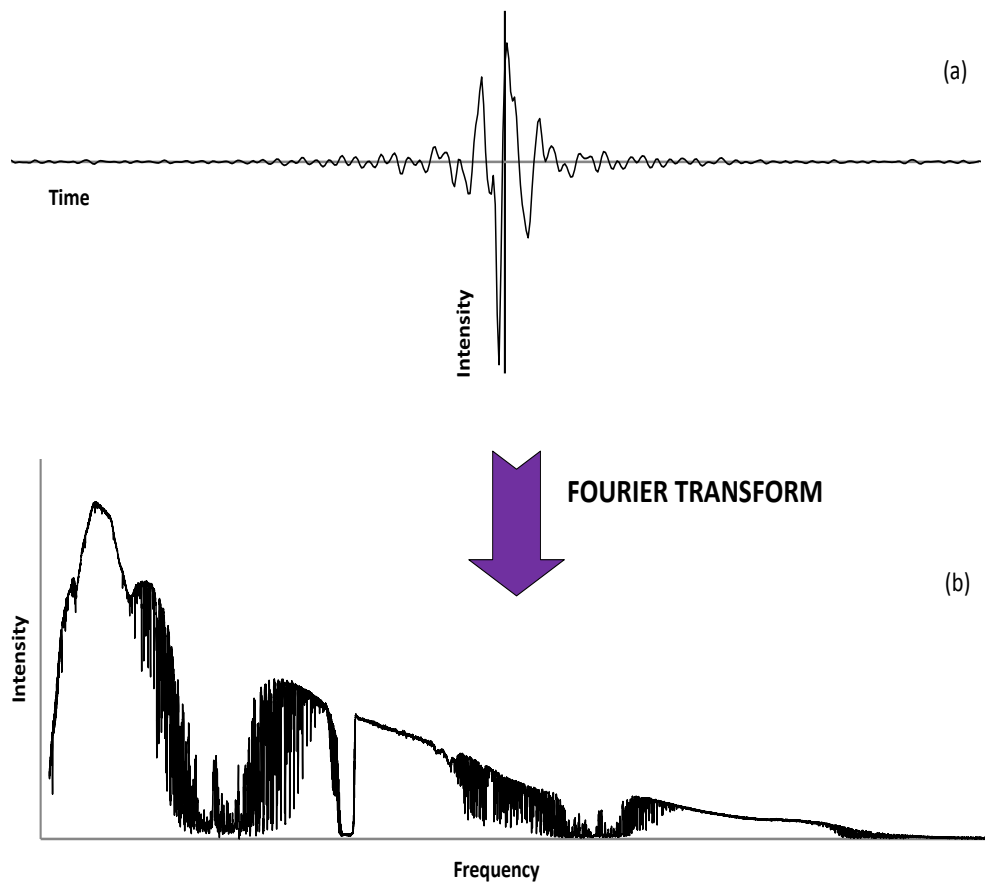
Figure 2.9: *Measurements made by the FTIR. (a) Example interferogram measured by the FTIR spectrometer and (b) its corresponding spectrum. The interferogram, measuring the intensity level of the combined light beams against optical path difference and hence time, is converted to a spectrum of frequency against intensity by applying a Fourier transform.*

To convert the interferogram (Figure 2.9a) to a spectrum of frequency against intensity (Figure 2.9b) a Fourier transform is applied. A Fourier transform allows for the conversion between the time and frequency domains. Suppose that a function $f(x)$ is continuous, it can be represented by a composition of sine and cosine functions (Davis *et al.*, 2001):

$$f(x) = \int_{-\infty}^{\infty} F(\lambda)e^{i2\pi\lambda x}d\lambda, \tag{2.12}$$

where $e^{i2\pi\lambda} = \cos(2\pi\lambda) + i\sin(2\pi\lambda)$ and $F(\lambda)$ is the Fourier transform of $f(x)$ such that:

$$F(\lambda) = \int_{-\infty}^{\infty} f(x))e^{-i2\pi\lambda x}dx. \tag{2.13}$$

Assuming that the interferometer system is linear, the above relationship can be applied to convert an interferogram to a spectrum. Suppose that a beam of light enters the interferogram at frequency λ with intensity $B(\lambda)$. The intensity of the resultant interferogram depends on the optical path difference, x (and hence time) of the two beams as follows:

$$I(x) = \int_{-\infty}^{\infty} B(\lambda)e^{i2\pi\lambda x}d\lambda, \tag{2.14}$$

for all frequencies λ. Taking the inverse Fourier transform of the interferogram gives us the distribution $B(\lambda)$ (Davis *et al.*, 2001):

$$B(\lambda) = \int_{-\infty}^{\infty} I(x)e^{-i2\pi\lambda x}dx. \tag{2.15}$$

Note that the above equations assume linearity. Most systems are not linear, however this simplification allows for the understanding of the basic underlying principles (see Davis *et al.* (2001) for more details on non-linearity). In practice, the interferogram is not able to be measured at infinite times. Hence the end points are truncated, which results in line broadening and peaks. An apodization function is used to remove these errors, by applying a weighting function (Davis *et al.*, 2001).

In this work, a MIDAC Open Path Fourier Transform Infrared Spectrometer was employed to measure IR spectra from which in-plume horizontal column amounts of gases such as CO_2, CO, CH_4, CH_2O, SO_2 and NO_2 are to be retrieved. The instrument is coupled with a 76 mm Newtonian telescope enabling a 9 mrad field of view and using a Stirling cycle cooled mercury-cadmium-telluride (MCT) detector. The FTIR system is placed in a lightweight metal protective case with dimensions $356\times183\times166$ mm. A laptop is used to operate the instrument using a PCMCIA connection and powered with a 12 v battery. The spectrometer receives an IR signal emitted by a 1275 ^{o}C silicon carbide glower inserted on an approximately 50 cm aluminium reflector (Wooster *et al.*, 2011). Spectra are recorded within the range 650-6000 cm^{-1}, with a spectral resolution of 0.5 cm^{-1}. See Figure 6.2 for an example of how the FTIR spectrometer is used in the field.

2.4.4   Active and Passive Spectral Measurements

The most common passive light sources are the sun and moon, and occasionally the stars (Figure 2.10 (b)). The Beer-Lambert law can be applied to retrieve gas concentrations using direct passive measurements, however not directly. This is because the light passes through the whole atmosphere, such that column density (concentration along the light path) is returned, with vertical column densities calculated using radiative transfer models. This set up can only be used when the sun is out (during daylight hours and when the sun is not obscured by clouds). The intensity of direct moon light is much lower than that of direct sunlight, (Platt and Stutz, 2008).

A second type of passive measurements for the DOAS application is scattered sunlight measurements. This is used with the DOAS telescope pointing zenith (Figure 2.10 (c)) or with the telescope scanning through multiple angles, known as multi-axis DOAS (MAX-DOAS), as in Figure 2.10 (d). This cannot be implemented with the FTIR as scattered sunlight by the Mie and Rayleigh processes is not detectable in the IR due to larger wavelengths not being significantly scattered by these processes. Passive spectra measurements using the FTIR spectrometer must directly target the instrument at the sun or moon.
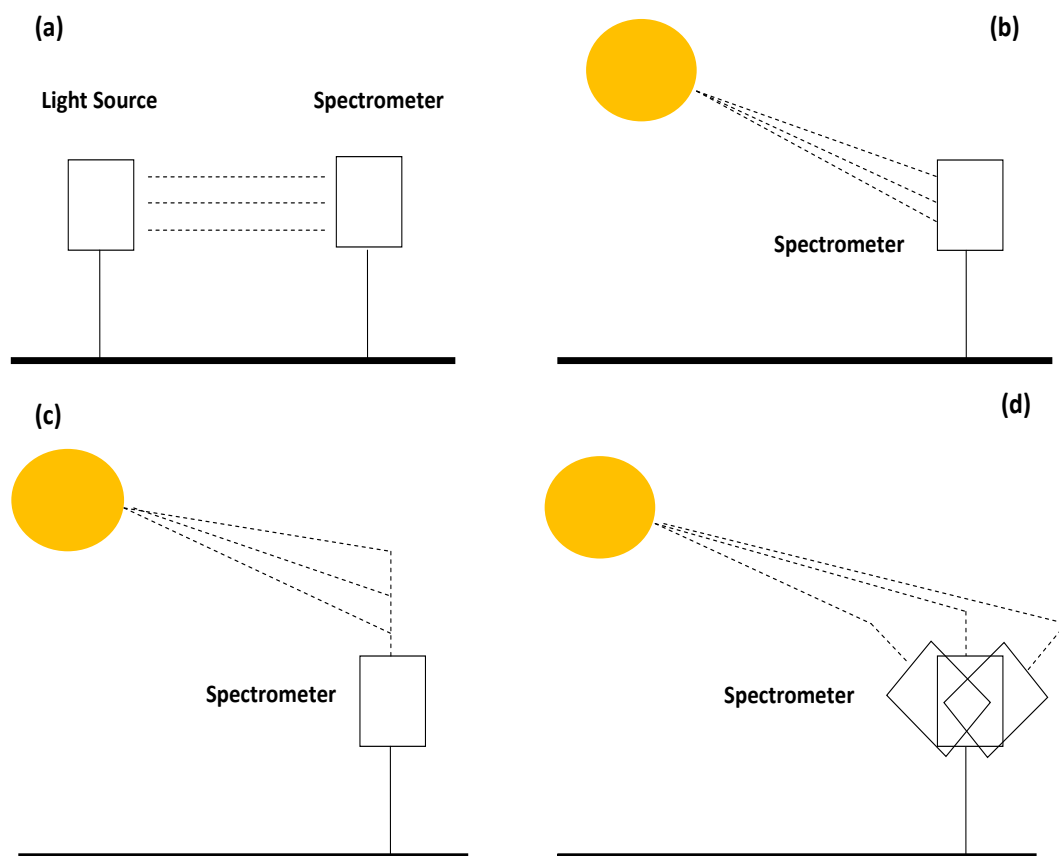
Figure 2.10: *Sketches of the most common set-ups for active and passive spectral measurements of atmospheric constituents: Active measurements with the spectrometer used with an artificial light source (a), passive measurements with the spectrometer directly sampling radiation emitted from the sun/moon (b), passive sampling of scattered sunlight (c) and the multi-axis DOAS (MAX-DOAS) set-up in which the telescope of the DOAS system scans through multiple angles (d). Note that the FTIR cannot be used with the scattered sunlight set-ups ((c)-(d)), because Mie and Rayleigh scattered light is not detectable in the infra-red.*

Scattered sunlight measurements have the advantage of not needed sun following equipment, although the intensity of scattered sunlight is weaker (Platt and Stutz, 2008). Passive measurements have the advantage of not needing a a light source and particularly scattered sunlight measurements usually tend to require only a small telescope. However, light from the sun and moon exhibits complicated spectral structures that need to be taken into account when the retrieval process is carried out, for example Fraunhofer lines (see Chapter

3). These feature mainly in the UV and complicate the retrieval of trace gases due to their narrow structures and large absorption densities. This effect is more prominent in direct sunlight compared to scattered sunlight due to its greater intensity. Another difficulty is the conversion of slant column densities to vertical column densities. Complicated radiative transfer models must be used for this. This is especially complicated for scattered sunlight measurements due to difficulties in determining the length of the light path. An advantage of using the active set up is that usually the light structure is well known such that it can be removed from the measured spectra before evaluation. Other benefits include a well known light path, the ease of making localized measurements and the fact that the light source is always available, i.e. it does not depend on weather conditions or time of day (Kraus, 2006). Also artificial light sources can have an extended wavelength range compared to passive sources, in particular scattered sunlight and tend to be brighter. For example solar energy has to pass through the ozone layer, which consumes the majority of the light below 280 nm. In contrast, the spectral range of artificial light sources can go as low as 200 nm. A disadvantage of the active set up is the inefficiency when looking at atmospheric trace gases due to their low concentrations and hence the requirement of a long light path. (Platt and Stutz, 2008). According to Kraus (2006), the relative short light path and very intense light will result in high photon noise with small absorption activity, i.e. there will be greater levels of noise for weaker absorption levels.

The active DOAS is frequently implemented for the study of the troposphere, as well as laboratory experiments looking at, for example smog and aerosols. Types of UV artificial light sources include halogen and xenon lamps and arcs. Arcs occur when a current of electricity passes through electrodes that are separated by a gas or vapor (Platt and Stutz, 2008). The active set up has been used frequently with the FTIR to investigate pollution plumes using an IR lamp, essentially a heating element at the center of a parabolic reflector.

Chapter 3

Atmospheric Trace Gas Retrieval Methods Using UV-DOAS and FTIR Spectroscopy

Contents

3.1 Introduction

This chapter details the general analysis procedures used to calculate trace gas abundances and mixing ratios from spectra measured using the UV DOAS and FTIR instruments, both of which are deployed in this project. There are two principle methods used to retrieve trace gas column amounts from UV spectra measured with the DOAS instrument, both based on the theory of differential absorption spectroscopy.

The most commonly used is probably the forward model approach, whilst the second is an empirical approach requiring the use of calibration gas cells containing know amounts of the target gas. Both of there methods were investigated for the use in this research, and this chapter gives a comparison of results from both methods whilst Chapters 5 and 7 detail the specific methods used for the full retrieval of NO_2 and SO_2 column amounts collected from the DOAS spectra of vegetation fire plumes studied herein.

This chapter also provides a summery of the various different approaches used for the analysis of atmospheric FTIR spectra. The approach used here is based on forward modeling and the performance of two such methods are compared in this chapter. Chapters 6 and 7 then provide a more detailed explanation of the exact retrieval method finally used for the analysis of the complete FTIR record of the biomass burning plumes studied herein.

3.2 UV Measurement Principles

The evaluation method applied to the spectra is dependent on the light source used for the measurements. Using an artificial light source, such as a UV lamp, offers the advantage that some scattering effects do not need to be taken into account. Scattered and direct light measurements use the sun as the source, hence it is possible to make measurements through the whole atmosphere using just one detector. Whereas direct light measurements view the source directly, scattered measurements use light that has been scattered by Mie

and Rayleigh processes. Scattered light measurements have the benefit of a much longer light path and hence stronger absorptions. This generally means that the detection limit falls for the species of interest, and the measurement accuracy increases (Kraus, 2006). It is possible to calculate the detection limit of a species using Equation 3.6, if the values of the gas cross section, minimum detectable optical density and the path length are known (Platt, 1994). However, with the case of scattered light measurements, the light path is uncertain and strongly dependent on the number of times each photon has been scattered before it reaches the measurement detector. There are numerous Monte-Carlo radiative transfer models that simulate the path of a photon, including any possible scattering events (Kraus, 2006). As the light source used for the project conducted here was scattered sunlight due to the interest being plumes of smoke higher than ground level that were not necessary placed directly between the sun and the instrument. Therefore I shall only describe the evaluation steps to be carried out when using this solar scattered light source.

For scattered sunlight measurements, the telescope of the DOAS instrument does not need to be pointed directly at the sun, but rather can be pointed at zenith where it is able to receive photons that have been emitted by the sun and scattered in the atmosphere, ultimately into the viewing direction of the instrument. The intensity of the received signal at different wavelengths is controlled by the emission intensity from the sun and the degree of scattering, and also by the amount of absorption caused by trace gases at that specific wavelength. By separating the absorption component from the other effects via measurements at two more more closely separated wavelengths we can try to isolate the absorption signal, and thus via the use of Beers law can in theory retrieve the column amount (the total amount of the gas present in the atmosphere column) of the absorbing gas.

3.3 Differential Optical Absorption Spectroscopy

When deploying DOAS instruments in the way used here, attempting to measure the absolute value of the incoming light intensity (I_0) of Equation 2.9 generally proves to be a difficult task. To measure I_0 properly, a measurement of the light source without any atmospheric absorbers would be necessary. However, as already mentioned, when the radiation passes through the

atmosphere and other absorbing mediums, it not only has a reduction in intensity due to the absorption of gases, but also undergoes extinction due to scattering by air molecules and aerosols. Also, the imperfect optical nature of the instrument components (e.g. the mirrors and grating) will cause further reductions in the intensity of I_0. Therefore I_0 cannot easily be determined during measurements of scattered light. Equation 2.7 of the previous chapter can, however, be expanded to take the factors that effect the measured light intensity into account:

$$I(\lambda) = I_0(\lambda)exp[-L\sum_{i=0}^{n}\sigma_i(\lambda)c_i + \epsilon_R(\lambda) + \epsilon_M(\lambda)].A(\lambda), \quad (3.1)$$

where σ_i (molec.cm^{-2}), $i = 1, ..., n$ are the absorption cross sections for the measured species, c_i are the species volumetric amounts c_i (molec.cm^{-3}), $\epsilon_R(\lambda)$ and $\epsilon_M(\lambda)$ are the effects of Rayleigh and Mie scattering respectively and $A(\lambda)$ accounts for any instrumental effects. Note that these last three terms are unitless. To calculate the volumetric amounts of any target gas species using Equation 3.1, it would then be necessary to quantify all the parameters that influence the measured light intensity. This is plausible if done in a laboratory, as the absorbing medium can be removed from the light path. In the open atmosphere however this is not possible (Platt and Stutz, 2008). This issue can be overcome by measuring the 'differential absorption', known as the portion of the total absorption of any molecule that changes rapidly with wavelength. The 'low frequency' (broadband) intensity structures (i.e. those that vary slowly with wavelength) contain information on the scattering and the structure of the light source itself, whereas the 'high frequency' components contain information on the absorption caused by trace gases (Kraus, 2006). Thus, we can say that the absorption coefficient of a molecule can be considered as being compromised of two components:

$$\sigma(\lambda) = \sigma_s(\lambda) + \sigma_r(\lambda). \quad (3.2)$$

Hence, $\sigma_s(\lambda)$ denotes the 'low frequency' part that slowly varies with wavelength, i.e. the cause of broadband structures. This can be thought of as the general slope of the spectrum. Conversely, $\sigma_r(\lambda)$ represents the 'high frequency' part of the absorption whose variation wavelength is fast, i.e. the cause of narrowband features, for example the trace gas absorption lines. Note that the terms 'slow' and 'rapid' are relative to the wavelength interval at the

width of the absorption bands that are being considered. Any effects due to Rayleigh and Mie scattering are put together within $\sigma_s(\lambda)$. Substituting Equation 3.2 into 3.1 gives:

$$I(\lambda) = I_0(\lambda)exp[-L\sum_{i=0}^{n}\sigma_{r_j}(\lambda)c_i].exp[-L\sum_{i=0}^{n}\sigma_{s_i}(\lambda)c_i + \epsilon_R(\lambda) + \epsilon_M(\lambda)].A(\lambda). \qquad (3.3)$$

The first exponential term of Equation 3.3 describes the narrow band structure absorption by the trace gases, while the second exponential term represents the broadband Mie and Rayleigh scattering. $A(\lambda)$ represents the (slow) wavelength-dependent transmission of the instrumental system. Consequently, $I_0'(\lambda)$ can explicitly be defined as $I_0(\lambda)$ without the differential absorption component:

$$I_0'(\lambda) = I_0.exp[-L\sum_{i=0}^{n}\sigma_{s_i}(\lambda)c_i + \epsilon_R(\lambda) + \epsilon_M(\lambda)].A(\lambda). \qquad (3.4)$$

Hence $\sigma_r(\lambda)$ can be inserted into Equation 2.8 and a differential optical density D_r calculated, using the broad spectrum $I_0'(\lambda)$ as the numerator (i.e. the intensity minus the differential absorption) instead of the $I_0(\lambda)$:

$$D' = \log\left[\frac{I_0'(\lambda)}{I(\lambda)}\right]. \qquad (3.5)$$

Figure 3.1 shows the separation of the 'slow' and 'rapidly' varying components of intensity and absorption. From Equation 3.5 and Equation 2.10, the concentration of the species c' can then be calculated using:

$$c' = \frac{D'}{\sigma'(\lambda)L}. \qquad (3.6)$$

L (cm) denotes the light pathlength, and $\sigma'(\lambda)$ is the rapid varying component of the absorption cross section. Note however that this procedure can only work if the target gas species shows narrow spectral absorption features within the wavelength range studied. Also, there are some cases where gas species have very similar absorption features (for example the OH radical and NO_3), such that they may absorb similar amounts of radiation within the same spectral region, which needs to be taken into consideration in any analysis (Platt, 1994).
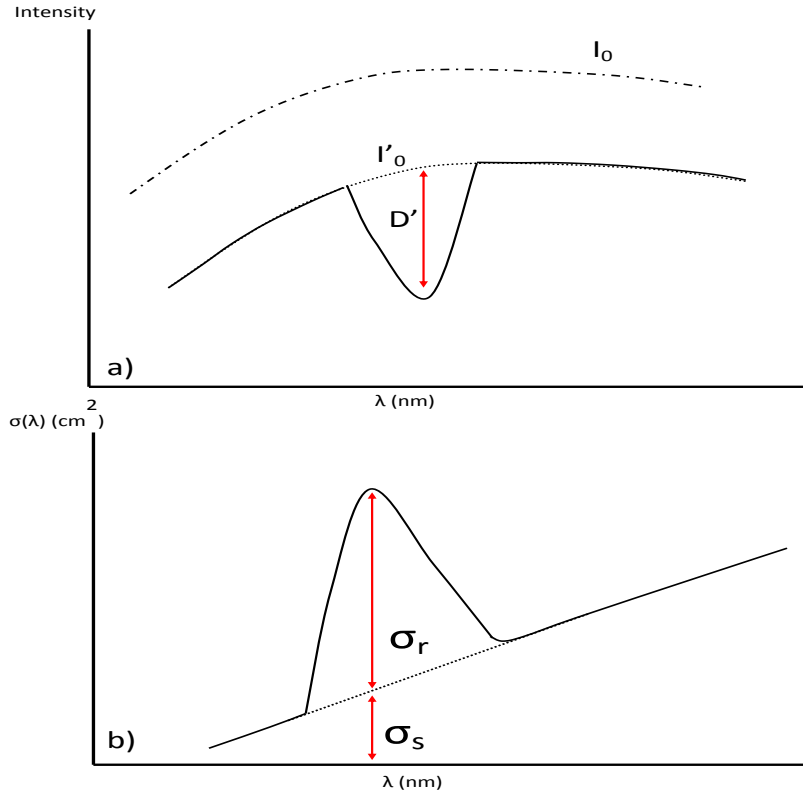
Figure 3.1: *Sketch showing the key principle of the DOAS theory; the separation (by filteringm, discussed further on in this chapter.) of $I_0(\lambda)$ (the incoming light intensity) and σ (the absorption cross section) into the 'slow' (σ_s and $I_0'(\lambda)$) and 'fast' (D' and σ_r) varying structures with respect to wavelength (Platt and Stutz, 2008). a) $I_0(\lambda)$, the intensity of the light beam emitted by the source, is split into the general slope ($I_0'(\lambda)$) representing its slowly varying structures (e.g. those due to atmospheric scattering) and narrow band features (D') due to trace gas absorption. b) the rapid component (σ_r) of the absorption cross section σ caused by trace gas absorption and its underlying broadband structure, σ_s.*

3.4   DOAS Forward Model Method

The DOAS forward model method is based on creating a modeled spectrum using Equations 3.5 and 3.6. For this, it is necessary to use absorption cross sections of the target gases. This modeled spectrum is iteratively matched to the measured spectrum, each time varying the concentration of the target gases until a closest match between the two spectra is given. This type of forward model, as well as the type of algorithms used to fit the modeled to the measured spectrum, are discussed further in this chapter. In the section below, the key

features of the DOAS Forward Model Method are described.

Cross Section

To get the most reliable results from this method, it is necessary that the cross sections used in the retrieval are as accurately as possible. There are two ways in which the cross sections of any target species are obtained. One is through direct measurements using the spectrometer ultimately to be deployed in the field. The advantage of this method is that any sampling and detector noise in the cross section should match those of the field measured spectra (Kraus, 2006). This method has been used for many years for various trace gases, for example SO_2 and NO_2 due the long term stability and accuracy associated with using gas cells containing these gases. However, according to Plat and Stutz (2008), NO_2 has a difficultly associated with it. NO_2 forms a temperature dependent equilibrium with N_2O_4 (nitrogen peroxide), hence the cell concentration of NO_2 will be temperature dependent. Figure 3.2 shows the cross section of O_2, taken using the spaceborne SCIAMACHY Proto Flight Model (PFM) Spectrometer using this technique (Bogumil *et al.*, 2000). As an alternative to new measurements, the cross sections of many trace gases can simply be obtained from the literature, or from one of the various data bases that provide high resolution cross sections of many trace gases.
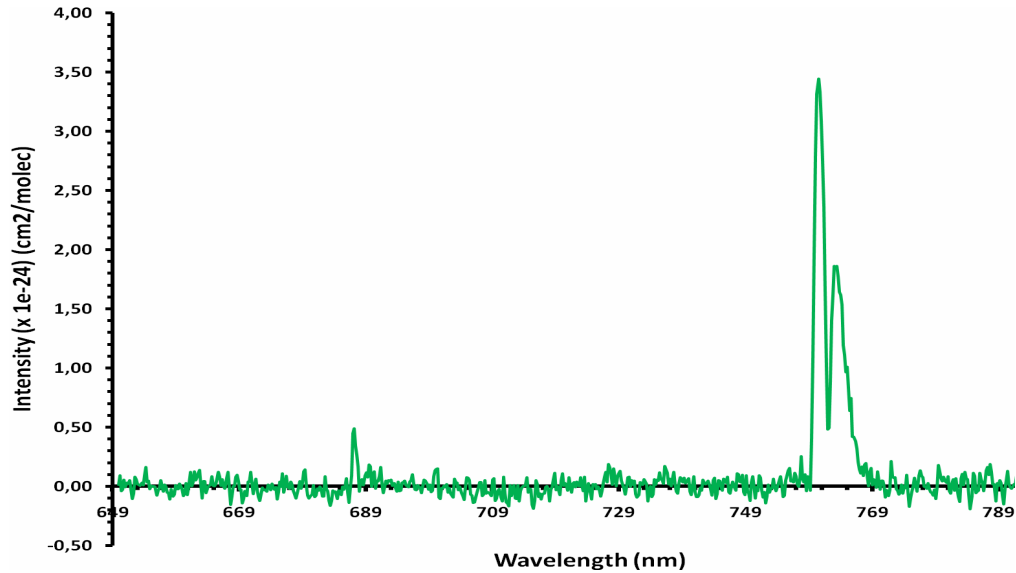
Figure 3.2: *Cross section of O_2 at 293 K measured over the wavelength range 650-799.6 nm. The cross section was taken using the SCIAMACHY Proto Flight Model Spectrometer (Bogumil et al., 2000). Note the strong absorption feature around 750 nm.*

.

The literature published cross sections tend to be of a much higher spectral resolution than the spectra provided by the UV DOAS instrument to be used here since they have been measured with near optimum laboratory instruments. For any accurate evaluation method, the absorption cross section spectral resolution needs to be the same as that of the spectra to be analyzed. Usually therefore, the laboratory cross sections are convolved with the instrument line shape (ILS) of the spectrometer that will be used for the field measurements (Platt and Stutz, 2008). The ILS is defined as the response of the instrument to a monochromatic signal (radiation at one wavelength) of a certain intensity at a certain wavelength (Leigh, 2005). The ILS affects the recording of any narrowband structures measured by the instrument and is sensitive to any movements in the optical system of the instrument. The instrument response will also be spread over more than one pixel, due to entrance slit and diffraction grating properties of the spectrometer. Ideally, the ILS follows a near Gaussian shape, and for most DOAS procedures, the ILS of the spectrometer to be used can be sufficiently accurately determined by the atomic emission lines of a low pressure lamp. The atomic emission line width is much narrower (≈ 10 nm) than the usual spectral resolution

of the field deployed spectrometers, hence the measures of the emission line spectra are a good approximation to the instrument ILS. The lamp is filled with a particular element (e.g. Hg, He,..) at low pressure and two electrodes positioned to electronically excite the element and create an emission signal. The emitted signal consists of many emission lines at well known wavelength locations. The actual spectral shape of the emission lines focused onto the spectrometer is different to their shape of the recorded spectrum due to the relatively low spectral resolution of the spectrometer. In mathematical terms, this can be thought of as the convolution of the original absorption spectrum $I(\lambda)$ with the ILS $H(\lambda)$, to produce the measured absorption spectrum $I_m(\lambda)$:

$$I_m(\lambda) = \int I(\lambda - \lambda')H(\lambda')d\lambda' = I(\lambda) \otimes H(\lambda'). \qquad (3.7)$$

Also, most spectrometer detectors exhibit an overlap between neighboring pixels, for example $x\%$ of pixel i can be a result of the adjacent pixel signal. This again can be expressed as a convolution, between $I_m(\lambda)$ and the detector response function, $G(i, \lambda)$:

$$I'_m(\lambda) = \int I_m(\lambda - \lambda')G(\lambda')d\lambda' = I_m(\lambda) \otimes G(\lambda') \qquad (3.8)$$

It is usually difficult to differentiate the convolution effects of the spectrometer spectral resolution and that of the detector. The measured atomic emission lines thus represent both convolution functions H and G (Platt and Stutz, 2008).

The Ring Spectrum

As mention previously, photons scattered by air molecules in the atmosphere change the signal received by the spectrometer. In the case of inelastic Raman scattering, when a photon is scattered by an air molecule, its resultant energy level is different to that of the incident photon, hence it has lost or gained energy (unlike elastic scattering where the direction of traverse of the photon changes, but not its energy). Because of this, in inelastic Raman Scattering, the wavelength of the photon is changed by the scattering process. In some cases this results in the 'filling in' of absorption lines, in particular the Fraunhofer lines. This is called the ring effect. Sometimes this ring effect can be confused with the signal changes

caused by trace gas absorption, and therefore the effect must be taken into account during analysis. One way to do this is to include a 'ring spectrum', usually calculated using the Fraunhofer spectrum, as an additional cross section for the evaluation process.

The scattered light reaching the DOAS telescope I_{meas} ultimately can be considered to be due to a series of components resulting from the three different scattering processes (Platt and Stutz, 2008):

$$I_{meas} = I_{Rayleigh} + I_{Mie} + I_{Raman} = I_{elastic} + I_{Raman}. \tag{3.9}$$

Taking the logarithms and simplifying:

$$ln(I_{meas}) = ln\left(I_{elastic}.\frac{I_{elastic} + I_{Raman}}{I_{elastic}}\right) \approx ln(I_{elastic}) + \left(\frac{I_{Raman}}{I_{elastic}}\right), \tag{3.10}$$

where the simplification comes from applying the natural logarithm law $ln(ab) = ln(a) + ln(b)$ and the approximation using the Taylor series $ln(1 + a) = \sum_{n=1}^{\infty} \frac{(-1)^{n+1}}{n} a^n$. The ring spectrum can be taken as the ratio of the Raman and elastic portions of the scattered light intensity (Platt and Stutz, 2008):

$$I_{ring} = \frac{I_{Raman}}{I_{elastic}}. \tag{3.11}$$

There are two ways to calculate this ring spectrum. The first method involves the polarization properties of the scattering processes. In brief, a light beam oscillates in all directions perpendicular to its direction of travel. When the light hits a non metallic surface, only the vibration in one direction is completely reflected off the surface. In the case of a bare metallic surface, vibrations in all directions are reflected. The vibrations that strike the non metallic surfaces and do not get reflected are reduced in intensity, or wiped out completely. Hence all the vibration happens in one plane. The vibration that has been reflected is known as polarized light (Jensen, 2007). The process of Rayleigh scattering is strongly polarized at scattering angles close to 90°. However, polarization in Raman scatting is not that prominent. Hence the ring spectrum can be calculated by quantifying the polarized light perpendicular and parallel to the scattering plane and the intensity of light caused

by Raman scattering. However, Mie scattered light also forms part of the light that is unpolarized. Hence clouds and aerosols make using this method to calculate the ring spectrum difficult (Platt and Stutz, 2008).

The second method used to calculate the ring spectrum makes use of two main species in the atmosphere, O_2 and N_2. The energies of the rotational states of these two species are used to calculate the cross section for rotational Raman scattering. This is usually done using the Fraunhofer spectrum. The calculated rotational Raman cross section is then divided by the Fraunhofer spectrum to calculate the ring spectrum. Before this division, any Raman scattering must be removed from the Fraunhofer spectrum such that only elastic scattering is represented (Platt and Stutz, 2008).

3.4.1 Direct Calibration Method

The alternative method used to retrieve vertical trace gas column amounts from the spectra measured by a scattered light DOAS instrument, denoted as the 'direct calibration' method from here on in, relies on formulating an empirical relationship between gas amount and measured absorbance (Elias *et al.*, 2005; Mori and Burton, 2006; Mori *et al.*, 2006; Bluth *et al.*, 2007; Dalton *et al.*, 2009). This method, which is ultimately used for the analysis of the UV spectra in this work, requires the use of calibration cells containing known amounts of the target gases. Gas cell temperatures are at ambient levels and since the smoke emitted from the fire was at low altitudes and most likely mixed with ambient temperatures because it was not close to the flame, it can be assumed that the gas cell temperature and smoke temperature are similar. The difference between the SO_2 gas cells and ambient pressure is negligible, however the NO_2 gas cell pressure is lower than ambient, ranging from 96 to 180 Torr depending on the concentration of the NO_2 gas cell. An increase in pressure broadens the absorption structures of a given target species (Vandaele *et al.*, 2003). This is shown in Figure 3.3, taken from Vandaele *et al.* (2002), in which high resolution NO_2 absorption cross sections were derived using varying pressures and temperatures. It can be seen that higher pressure cause smoothing and broadening of absorption structures, particularly at lower temperatures. Note that the resolution of the spectra in Figure 3.3 is at 0.008 nm.
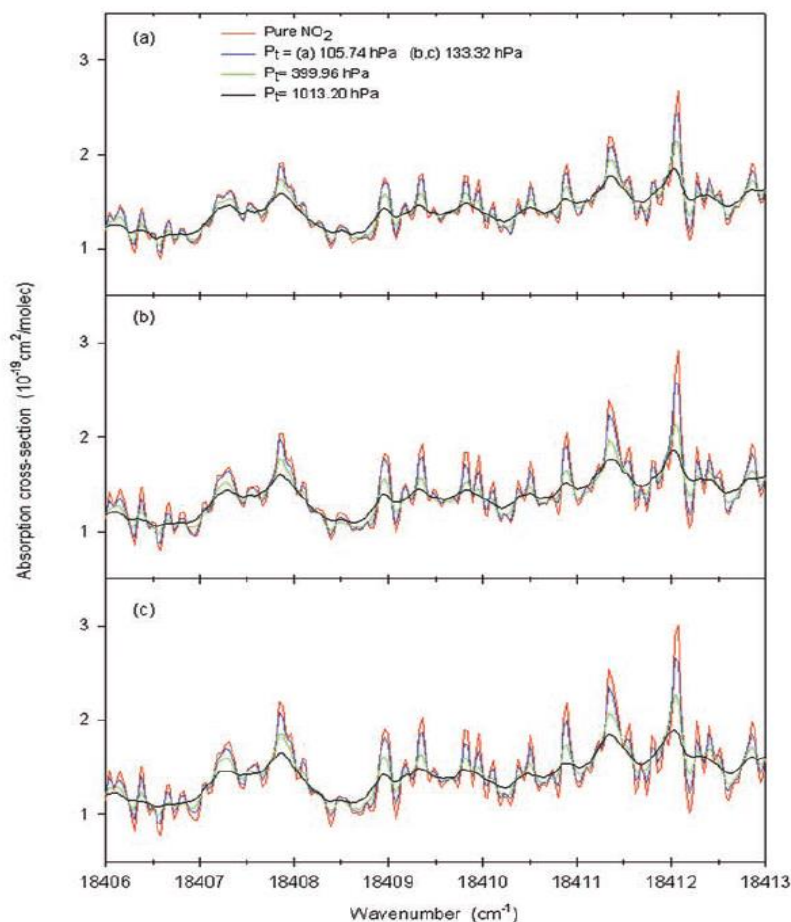
Figure 3.3: *Pressure broadening effect on NO_2 absorption cross section at (a) 294 K, (b)240 K, (c)220 K. Taken from Vandaele et al. (2002), where high resolution NO_2 absorption cross sections were determined using a Fourier transport spectrometer. Here the resolution is at 0.008nm.*

The pressure broadening effect is also presented in Harder *et al.* (1997), in which absorption cross sections were measured at a high resolution of 0.006 nm at pressures between 100-600 Torr. However, Harder *et al.* (1997) and Vandaele *et al.* (2001; 2003) found that measurements from low resolution spectrometers do not exhibit the pressure effect, despite its importance for high resolution spectra. Absorption cross sections of NO_2 at pressures 100 and 1000 Torr (Voight *et al.*, 2002) were convolved with the ILS of the UV-DOAS used in this work, (as detailed above), see Figure 3.4. In accordance with the spectral resolution of the UV-DOAS spectrometers, the resolution of the absorption cross sections are at ≈ 0.05

nm.
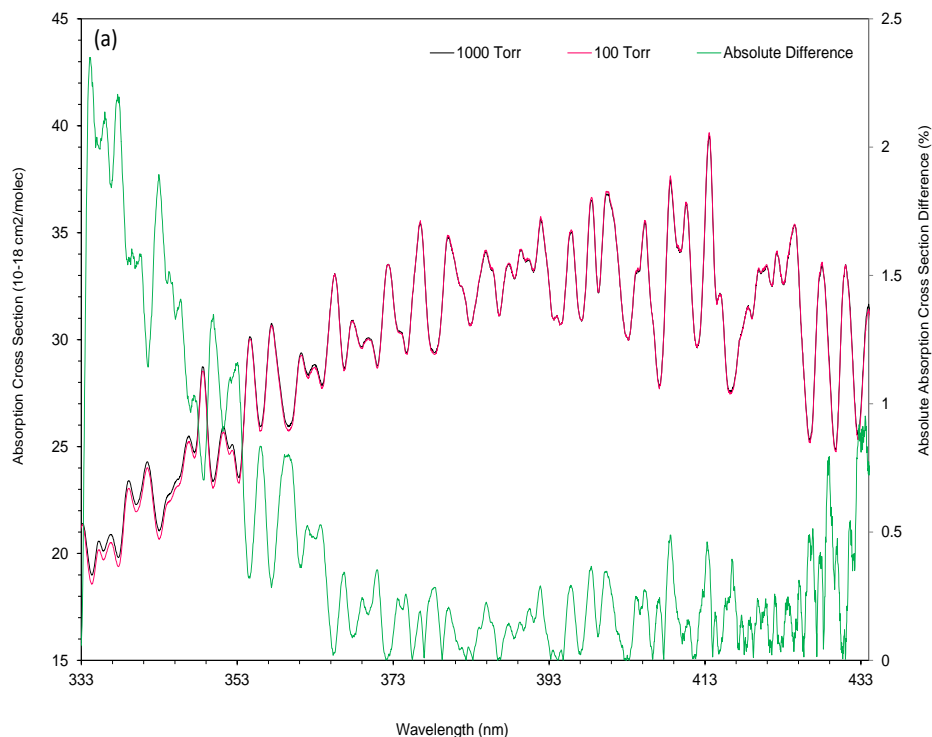
Figure 3.4: *NO$_2$ absorption cross sections from Voight et al. (2002) at pressure of 100 and 1000 Torr iin the spectral region used to retrieve NO$_2$ vertical column amounts of the measured spectra. The absorption cross sections are convolved with the ILS shape of the UV-DOAS spectrometer used for data collection in this work, at a resolution of $\approx$ 0.05 nm. The absolute difference between the two absorption cross sections, expressed as a percentage of the cross section measured at 100 Torr is minimal.*

The absorption cross sections at the two different pressures do not vary by much, this can be seen by the absolute difference of the absorption cross sections expressed as a percentage of the absorption cross section measured at 100 ppmm, shown in Figure 3.4, particularly at 350 nm onwards, the spectral region where most of the retrievals of NO$_2$ from the smoke plume spectra were performed. These absorption cross sections are at a much lower resolution (0.05 nm) than those given in the literature used to show the pressure broadening effect (0.006 nm-0.008 nm). This suggests that the resolution of the spectrometer used in this work is not high enough for pressure broadening effects caused by the difference in the calibration gas cell spectra used during the measurements and the ambient pressure, hence

it will not be taken into account during the analysis method.

UV-DOAS spectra are collected using these gas cells and are converted into absorbance as per the Beer-Lambert Law by taking the negative logarithm:

$$A_\lambda = -\log\left(\frac{I(\lambda)}{I_0(\lambda)}\right), \tag{3.12}$$

where $I_0(\lambda)$ and $I(\lambda)$ are the incoming and measured light intensities respectively, for all wavelengths λ. The absorption features of the target gases (present as peak and troughs in the absorbance spectra, as shown in Figure 3.5) are identified.
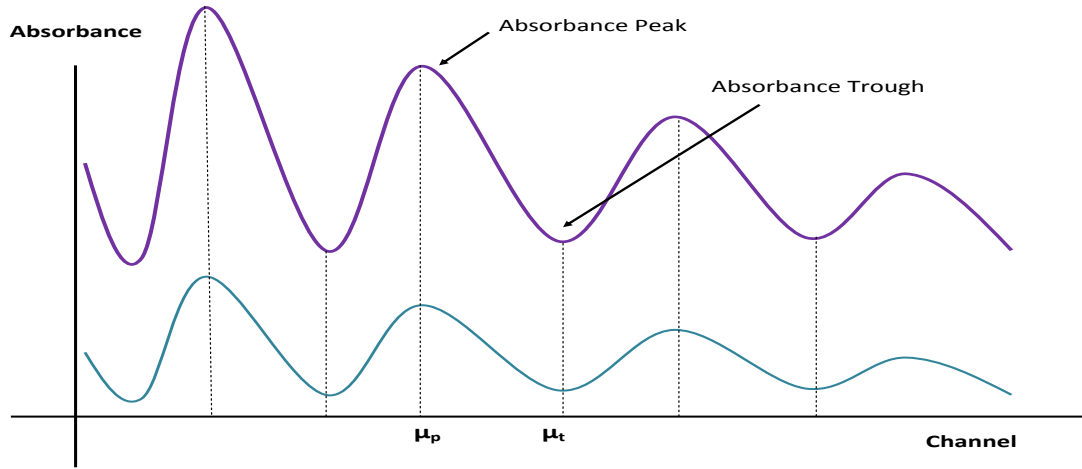
Figure 3.5: *Sketch graph of the absorption structures created by a target trace gases, present as peak and troughs after the measured spectra are converted to absorbance via Equation 3.12. The difference of absorbance at each peak and trough that are of two closely spaced wavelengths (at channels μ_p and μ_t respectively) is calculated as the pseudo absorbance and a linear best fit calculated between this value and the amount of gas contained in the calibration gas cell.*

The difference of each absorbance peak and trough pair is taken to get the psuedo absorbance $\bar{A}$:

$$\bar{A} = -log\left(\frac{I(\lambda)^p}{I_0(\lambda)^p}\right) + log\left(\frac{I(\lambda)^t}{I_0(\lambda)^t}\right), \tag{3.13}$$

for all 'peak' wavelengths λ_p and 'trough' for all wavelengths λ_t. A relationship is derived between these psuedo absorbances derived from the gas cell spectra and their corresponding

gas cell amounts via a polynomial

$$\sum_{i=1}^{n} a_i \bar{A}^i - C = 0, \tag{3.14}$$

where C is the gas column amount (ppmm) of the cell, a_i are the coefficients and n is the order of the polynomial. This relationship is then subsequently applied to the measurement absorbances calculated from the spectra of the actual smoke plumes in order to retrieve the column amounts of the trace gases present in the smoke. The principle of this 'empirical' approach is therefore one of 'calibration', 'measurement' and 'retrieved'. Since all of the other effects (ring effect and so on) are present in both the calibration spectra and the measurement spectra, they are taken into account via this process and hence do not need to be calculated explicitly.

3.4.2   Preprocessing Details

Before the measured spectra are subject to either the DOAS forward modeling method or the direct calibration retrieval method, they need to be preprocessed to isolate the components of the signal necessary for conducting the analysis.

Fraunhofer Lines

Consider the case when the sun is used as the radiation source for measurements. Even if there were no atmosphere in the path of the incoming radiation reaching the spectrometer, there would still exist absorption features, the Fraunhofer lines. Fraunhofer lines occur when the sun absorbs parts of the radiation that it emits itself. The absorption is caused by numerous chemical species (for example Calcium and Nickel) in the outer layers of the sun. To take this into account, a 'clear sky' spectrum is measured, directly looking at the sun, in the absence of the target medium (for example the fire plume). Figure 3.6 shows the Fraunhofer lines on the solar spectrum, where each letter represents a different absorption line caused by a different element. The measured spectra are divided by the Fraunhofer spectrum to get rid of effects caused by the Fraunhofer lines.
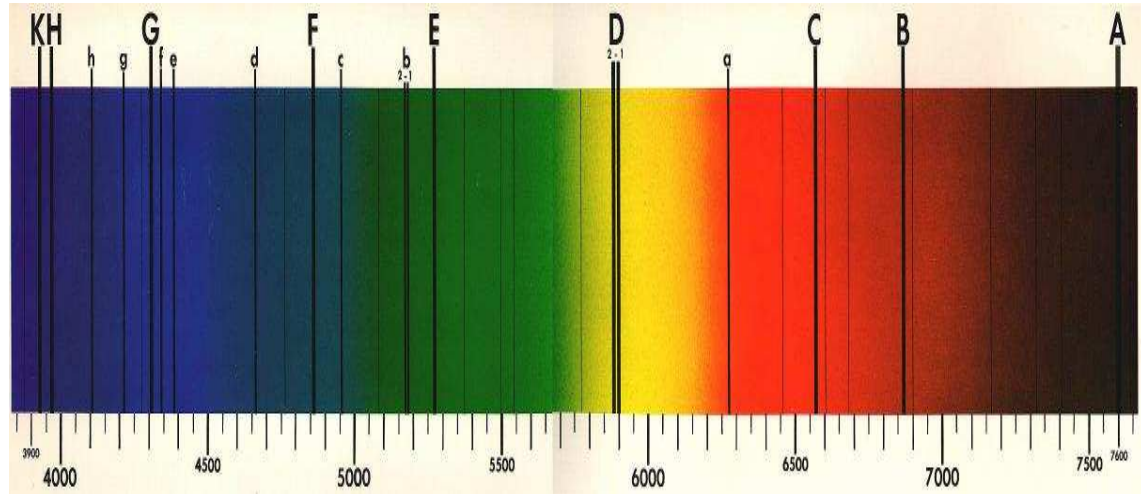
Figure 3.6: *The Fraunhofer lines of the solar spectrum. Each line represents absorption from a particular species (see Table 3.1) (McAteer, 2000).*

Alternatively, the Fraunhofer spectrum could be added as a cross section for the evaluation procedure of the DOAS forward model retrieval method. By including the 'clear sky' spectrum in the evaluation, the aim is that the effects of any absorption structures due to the light source are removed (Kraus, 2006).

Dark current

Even when no incoming light reaches the spectrometer, a signal is still measured, termed the dark current. Dark current occurs when electrons in the detector get thermally excited and are recorded as if they are excited by incoming photons. To asses the effect of this on the measured spectra, a 'dark current' spectrum is recorded by blocking any incoming light coming into the spectrometer. This dark current spectrum can then be subtracted from all subsequent measured spectra prior to any analysis.

Noise and Broadband Structure Reduction

Even when the dark current has been removed, there is still addition 'noise' in the measurement spectra that needs to be removed prior to any analysis. Smoothing can be performed to remove any unwanted 'high frequency' (i.e. changing rapidly with wavelength) structures, using some form of low pass filter. Here, the measured spectra can be filtered with, e.g.

Table 3.1: *Table showing which species are related to the Fraunhofer absorption lines shown in Figure 3.6 (McAteer 2000).*

Fraunhofer Line	Element	Wavelength (nm)
A - (band)	O_2	759 - 762
B - (band)	O_2	687 - 688
C	H	656
a - (band)	O_2	628 - 629
D - 1, 2	Na	590 and 589
E	Fe	5270
b - 1, 2	Mg	518 and 517
c	Fe	496
F	H	486
d	Fe	467
e	Fe	438
f	H	434
G	Fe and Ca	431
g	Ca	423
h	H	410
H	Ca	397
K	Ca	393

a moving average filter. As points measured at neighboring wavelengths are similar, this should not cause much bias, but should help to reduce noise. A standard simple digital or statistical filter is a series of weights that are applied to the data points a number of times, filtering the data such that the new data points are the cumulative product of a range of the original data points. The weights are usually referred to as the filtering function, or the filter. One such filter is the moving average, which simply replaces data point y_i with the average of the n data points before and after it (Platt and Stutz, 2008):

$$y'_i = \frac{1}{2n+1} \sum_{j=-n}^{n} y(i+j). \tag{3.15}$$

The value $2n + 1$ represents the degree of the filter. Too high a degree and broadband structures can be removed. Another filter is the binomial mask, which again replaces data points by a weighted average of the data points next to it. Binomial filters have weights that

are functions of the binomial coefficients (Press *et al.*, 2007; Derpanis, 2005):

$$\binom{N}{n} = \frac{N!}{(N-n)!N!},$$ (3.16)

where $n=0,1,....N$. Alternatively, the binomial coefficients can be found via Pascal's Triangle:

$$
\begin{array}{ccccccccc}
 & & & & 1 & & & & \\
 & & & 1 & & 1 & & & \\
 & & 1 & & 2 & & 1 & & \\
 & 1 & & 3 & & 3 & & 1 & \\
1 & & 4 & & 6 & & 4 & & 1.
\end{array}
$$

Another way to smooth the measurements is to fit some polynomial (of degree n) to the data points. This polynomial will then correspond to the low pass filter. The coefficients of the polynomial can be calculated using a least squares fit. An adaptation of this method is the Savitzky-Golay filter, where a polynomial is fit to a set of n neighboring data points around measurement y_i, not the whole set of data points at once (Kraus, 2006). The basic idea of this filter is to define a moving window of fixed value around y_i, $[n_L, n_R]$, where n_L and n_R are the number of data points to the left and right of y_i respectively. For each y_i a polynomial is fitted around the $[n_L, n_R]$ and the value of this polynomial at point i is used as the new data point y_i'. The calculated polynomial is not used for any other point (Press *et al.* 2007).

Although the DOAS method aims to isolate the (spectrally) rapidly varying absorption features of the measured spectra caused by the trace gases, $I_0'(\lambda)$ in Equation 3.5 also contains slowly varying absorption components caused by atmospheric scattering. One way to take this into account is by low pass filtering the spectra and divided the unsmoothed spectra by their equivalent filtered counterparts (Platt, 1994).

Another high pass filter is the Fourier filter. This transforms the measured spectrum into frequency space, for example via a fast Fourier transform (FFT), where any slow varying absorption features are removed (using cut off frequencies) and another FFT to bring the

spectrum back into normal wavelength space. Any remaining slowly varying spectral components can be accounted for during subsequent analysis by adding a polynomial to the fitting method in the evaluation procedure (Press *et al.*, 2007).

3.4.3 Air Mass Factor and Vertical Column Density

Equation 2.7 provides the amount of absorbing trace gas species in the form of a Slant Column Density (SCD), defined as the amount of the species along the light path (Kraus, 2006). Historically, the SCD has been defined as the integrated concentration over the whole atmosphere (Platt and Stutz, 2008):

$$SCD = \int_0^\infty c(s)ds. \tag{3.17}$$

Here s is the path from the sensor to the sun. In this form, the trace gas amount is not comparable with standard results as it depends on the instrument viewing angle and the solar zenith angle θ (SZA). θ is the angle between zenith (the direction directly above and perpendicular) and the current sun position in terms of the detector position. The higher the value of θ (i.e. the less overhead the sun), the longer the light path and hence the greater the SCD. It is preferred to use a measurement of trace gas amount that is independent of viewing angle, the Vertical Column Density (VCD), i.e. the amount of the species in the column directly above the detector when viewing vertically upward (Kraus 2006). Generally, the VCD is defined as the concentration of a species integrated (vertically) over the whole atmosphere (Platt and Stutz, 2008):

$$VCD = \int_0^\infty c(z)dz, \tag{3.18}$$

where z is the vertical path along the direction of the sun. This definition can be extended for the use of different sections $[z_1, z_2]$ of the vertical atmosphere:

$$VCD = \int_{z_1}^{z_2} c(z)dz. \tag{3.19}$$

The SCD and VCD are related linearly by the Air Mass Factor (AMF) A_i, of species i, at wavelength λ, and the value of θ:

$$VCD_i = \frac{SCD_i(\lambda, \theta)}{A_i(\lambda, \theta)}, \tag{3.20}$$

i.e. AMF is the ratio of the retrieved SCD to the actual atmospheric VCD. As θ strongly affects the SCD, it also affects the AMF. Other factors that influence the AMF include the exact species present in the light path and the wavelength used, due to the fact that scattering effects vary with wavelength (Kraus, 2006). It is possible to calculate AMF from radiative transfer codes, which model the scattering processes, reflection on the Earth's surface, the curvature of the Earth and the distribution of trace gases vertically in the atmosphere (Platt and Stutz, 2008). In the UV, the AMF is dependent on other factors, not just the SZA. For scattered light measurements, in addition to solar position, the elevation angle (ψ) of the DOAS telescope needs to be known. The elevation angle (ψ) is the angle between the horizon and the viewing direction. For telescopes pointing zenith, the elevation angle is 90°.

Light traveling from the sun into the detector is effected by extinction, either by trace gas absorption or by Rayleigh scattering. Rayleigh scattering is the principle factor that affects the direction of light under clear skies, which in turn is mainly dependent on the number of scattering air molecules present. Hence, as air density is greater close to the ground, scattering will occur more at lower heights and decrease with increasing altitude, hence leading to the intensity decreasing as altitude increases. However, the dependence on the AMF (and hence light path) on θ leads to a fall in intensity of the incoming light with a fall in SZA. The Rayleigh and SZA effects the AMF in opposite directions in terms of altitude. This leads to a scattered light distribution in which the intensity of the rays close to the ground are low, increase to a peak then fall with increasing altitude. The peak of this distribution is the most likely height at which the incoming light has come from. For large SZA, the light path increases and the most probable scattering height increases as the intensity reaching the scattering height falls at lower altitudes. For non-zenith viewing telescopes, the most probably scattering height is lower as the elevation angle is smaller, hence the viewing path is closer to the ground. For paths lower than the scattering height,

the AMF is one (Platt and Stutz, 2008).

Hönninger (2004) found that for low altitude trace gas profiles, the AMF of non zenith viewing geometries was well estimated by $\frac{1}{sin\alpha}$, where α is the elevation angle of the instrument. For the UV-DOAS scattered light measurements described in this thesis (which use a zenith viewing geometry and this $\alpha=90^o$), the maximum of the trace gas profiles of the target gases in the plume are assumed to be of a lower height than the most probable scattering altitude, so it can be assumed that the AMF is unity, following Hönninger (2004). Again, as the target trace gas profiles in the smoke plumes studied here are located relatively close to the ground (i.e. < 250 m or lower), it would be suitable to estimate the AMF as $\frac{1}{sin\alpha}$ if a multi-axis DOAS system was used where elevation angle varies.

3.5 Retrieval of Pathlength Averaged Mixing Ratios from the IR Spectra

The most common methods for retrieving trace gas mixing ratios from IR spectra measured with the FTIR spectrometer are based on comparing the sample spectra with either a measured or synthetic reference/calibration spectrum containing absorption features of the target gas of known concentrations (Smith *et al.*, 2011). The reference spectra are usually either measured in the laboratory or are taken from libraries containing information on spectroscopic absorption lines of different gas species. The classical least squares method (CLS) and partial least squares (PLS) method use the Beer Lambert law to find a relationship between calibration the spectra and the gas concentration, which is then applied to the sample spectra (Haalaad and Thomas, 1988). However this approach requires use of a background spectrum, usually taken before or after the sample measurement, within which no absorption features are present (Briz *et al.*, 2006). This can be problematic because of it may not be possible to make such background measurements (i.e measurements without the presence of the target species).

Another method for retrieving trace gas amounts from the measured IR sample spectra is the one line fitting method (Briz *et al.*, 2006). Here the absorption depth is calculated

at a wavelength where absorption of the target gas is strongest, and at two locations where absorption is weakest. The intensity values at the two weak absorption locations are taken to be the baseline of the measurement absorption peak. One disadvantage is that this method does not allow for the detection of interfering of atmospheric gases.

An alternative to these linear approaches described above is the combination of forward modeling (explained below) and non-linear least squares fitting (NLLS), in which a synthetic IR spectrum is created and iteratively matched with the measured spectrum, alternating the assumed gas concentrations until a best match between the measured and modeled spectrum is found. The synthetic spectrum is created using a set of parameters who values are initially defined by the user. These include temperature, pressure, and the *apriori* concentration of the target gases. Some of these other parameters can also be adjusted in the fitting procedure, in addition to the concentration of the target gases.

Two such forward model retrieval methods programmed as computer codes are described by Burton (1998) and Griffith (1996). The former is termed as the Burton method from here on, and the latter the Multiple Atmospheric Layer Transmission (MALT) method. The performance of these methods is compared in Section 3.6, whilst a description of both methods is given below. More emphasis is given to MALT in the description as this is the approach ultimately used for the IR spectral data analysis conducted in this study. As detailed in Chapter 2, the optical depth (D) of the target gas at a given wavelength λ for absorption line k is a function of its absorption coefficient and the pathlength amount (Griffith, 1996):

$$D^k(\lambda) = \sigma^k(\lambda)Lc \tag{3.21}$$

where $\sigma^k(\lambda)$ is the absorption coefficient (molec.cm^{-2}) of the target species at wavelength λ, c is the concentration (molec.cm^{-3}) and L is the pathlength (cm). The Burton computer code makes use of the Atmospheric Radiation Reference Forward model (RFM) (Edwards and Dudhia, 1996) to calculate the optical depths. The RFM is a line-by-line radiative transfer model used to calculate the optical depths of the target gases using the Beer Lambert law and an estimate of the atmospheric state and/or profile (temperature, pressure

and gas concentrations), absorption coefficients taken from the HITRAN spectral database (Rothman *et al.*, 2008) and which takes into account pressure broadening effects using the Voight line shape (see below). MALT convolves line strengths from HITRAN with the FTIR instrument line shape, producing the necessary absorption coefficients. The line strengths for each species taken from HITRAN are corrected to the gas temperature selected by the user since the lower state energy levels of the molecules are dependent on temperature. For each species the line strengths are a series of delta functions at the given wavelengths. The line shape at a given wavelength is taken as the Voigt line shape- the convolution of the Doppler broadening Gaussian line shape function and the pressure broadening Lorentzian line shape function. The former is calculated using temperature and molecular weight and the latter using the temperature dependence information given in HITRAN (Griffith, 1996). At wavelength λ, the overall optical depth D is taken as the sum of all calculated optical depths for all absorption lines k for all species i (Griffith, 1996):

$$D(\lambda) = \sum_i \sum_k D_i^k(\lambda) \tag{3.22}$$

If there is more than one gas layer in the retrieval process (e.g. hot and cold layers of atmosphere), the optical depth for each layer is calculated separately as each layer will then have different pressure and temperature values. With MALT, the optical depth is then converted into a transmission value and convolved with the instrument line shape, resulting in a transmittance or absorbance spectrum (as selected by the user).

The instrument line shape is a function of the apodization function and FOV for the instrument, which again are defined by the user. Recall Equation 3.23 in Chapter (methods) of the transmission T at λ:

$$T = \frac{I(\lambda)}{I_0(\lambda)}, , \tag{3.23}$$

where $I_0(\lambda)$ is the intensity of the incident beam that is emitted by the source and $I(\lambda)$ is the transmitted intensity after it passes through the absorbing medium (the atmosphere),

both at wavelength λ. In theory, the absorbance A at wavelength λ:

$$A(\lambda) = -log(\frac{I(\lambda)}{I_0(\lambda)}) \tag{3.24}$$

should be equal to the optical depth $D(\lambda)$ (Griffith, 1996). However in reality this is not the case, as the spectrometer measurement is the convolution of the actual intensity $I(\lambda)$ with the instrument line shape $G(\lambda)$, producing the measured intensity $I'(\lambda)$:

$$I'(\lambda) = I(\lambda) \otimes G(\lambda) \tag{3.25}$$

If there is no misalignment within the instrument and no phase errors, then the ILS is a convulation of the apodization function and a rectangular line shape which is a function of the FOV. Due to the finite optical path difference present during a measurement scan, however, the interferogram gets truncated. This can result in sharp oscillations around the absorption lines, called ringing, leading to spectral distortions. The application of an apodization function aims to fix this, by smoothing the intensity of the interferogram as it reaches the ends, making it free from noise by reducing the amplitude of the interferogram to values close to/equal to zero at the endpoints, hence eliminating the ringing effect. The trade off is that the apodization function causes line broadening, effectively reducing the spectral resolution (Davis *et al.*, 2001). There are a variety of apodization functions that can be used, but the most common is the triangular apodization function. This will suppresses the extra maxima that are found farther away from the central frequency line, and creates an ILS identical to that of a diffraction limited grating spectrometer.

In theory, the interferogram should be a symmetrical and can be transformed to a spectrum of frequency over spectral intensity using a real (cosine) function and with a phase equal to zero. However, in reality this is not the case due to limitations with the instrument and measurement processes, such as source or detector noise, causing a non zero phase. Hence the measurement interferogram is asymmetrical and requires a complex Fourier transform. If only a real function is used to convert the interferogram to a spectrum in the frequency domain, errors are introduced, for example in the line shapes and positions. Therefore this

phase shift needs to be determined to take into account these errors. The term phase error is used to describe the asymmetry of the interferogram (Davis *et al.*, 2001). Phase errors can possibly affect the absorption line shapes of the trace gases and also the continuum level at the center of the absorption line if there exists any absorption features close by of other species that interfere with the target gas narrow absorption features. This will also effect the zero offset (explained below). Both these will affect the retrieved pathlength averaged mixing ratios (Griffith *et al.*, 2003).

The specific input parameters that the user needs to define when running MALT are:

1. The maximum number of iterations that the fitting algorithm can go through. Usually a successful MALT converges by 20 iterations.

2. The spectral fitting region together with the wavenumber extension in order to take into account absorption wings outside the fitted region.

3. The choice of adding Gaussian random noise to the modeled spectrum, with the rms defined by the user.

4. The choice of y-axis of the modeled spectrum, e.g transmission (0-1), transmission (%) or absorbance.

5. The number of layers in the modeled atmosphere. If more than one layer is defined, then each layer is fitted independently with varying temperature, pressure and trace gas amounts.

6. The atmospheric pressure and its units.

7. The atmospheric temperature and its units.

8. The pathlength and units.

9. The type of broadening that is used for the Lorentzian line shape calculation. There are two choices for this option. Either a weighted combination of air and self broadening, or the air broadening widths can be scaled by a user defined value.

10. How many absorption coefficients of the target species are calculated from the line parameter data.

11. The list of gas species, their *a priori* values and whether these species will be included in the fit or fixed to the *a priori* values.

12. The order of the background polynomial that is included in the fitting process as well as the *a priori* values.

13. The value of any spectral shift and whether it should be fitted. The spectral shift accounts for shifts in the location of the absorption lines due to, for example, photon noise (Davis *et al.*, 2001).

14. The spectral resolution.

15. The apodization function. There is a choice of boxcar, triangle, hamming, NB-wk, NB-med, NB-strong, Blackmann Harris, Cosine or none.

16. An initial guess of the instrument FOV and whether it is to be fitted or not.

17. An *apriori* value for the phase, which takes into account the any asymmetry in ILS due to misalignment of the spectrometer, and whether this will be fitted or not. This is given in degrees and should be close to zero.

18. The zero offset value and whether it should be included in the fit. The zero offset is used to account for non zero spectral intensity when there should be full absorption, for example due to absorption by gases (e.g. CO_2 around 2350 cm^{-1}). This non-zero offset in such regions can be caused by scattering within the instrument, for example due to imperfections with the mirrors (Smith *et al.*, 2011).

The Burton retrieval code does not have such a wide set of input parameters as MALT, offering pressure, temperature, pathlength, spectral fitting region and list of retrieval gases. The order of the background polynomial and the spectral resolution also need to be defined. A separate program in conjunction with the Burton can can be used to calculate the ILS of the instrument, using the FOV and apodization function, both defined by the user. It necessary, a modified version of the Burton method can be used to retrieve the ILS as part

of the fitting procedure.

For both Burton and MALT, the synthetic spectrum is subsequently compared with the measured spectrum and a cost function calculated to represent the goodness of fit. If the new forward model is a better fit than the previous, the new changes in the variables intended to be retrieved are accepted and a second iteration started, with a smaller step size. If the fit is worse, the previous forward model is used for the second iteration along with a larger step size. The process continues until the convergence is reached and the best fit possible (according to previously defined conditions) is reached. The optical depths (D) taken from the best fit forward model are then converted back into the product of pathlength and concentration. The errors are output with the results. The method used for this iterative fitting is the optimal estimated non-linear least squared algorithm Levenberg-Marquardt Method (Levenberg, 1994; Marquardt, 1964).

Note that it is possible to apply both the MALT and Burton method to FTIR spectra collected via solar occulation mode, i.e. with the sun as the IR radiation source for the spectrometer, to retrieve trace gas vertical column amounts. For this, atmospheric layers need to be defined (either by the user or in pre-defined mode from the code), each with corresponding width, temperature, pressure and trace gas amount profiles. In addition to total column amount, it may be possible to retrieve details of the vertical profiles of some species via the investigation of the individual absorption lines. The shape of trace gas absorption lines are are effected by Doppler and pressure broadening, with the former dominating on the stratosphere and the latter in the troposphere, as pressure decreases with altitude (Petersen *et al.*, 2010).

3.5.1 Forward Model

Forward modeling is used in numerous retrieval methods as a way of solving the inverse problem of obtaining values of some parameters from measured data. The theory of the method is detailed in Rodgers (2000). Denote the measurements as a vector $\mathbf{y}$; the measurement vector, and the values of the parameters to be retrieved as $\mathbf{x}$, the state vector.

The way in which the measurement vector is related to the state vector is described by the forward model.

Consider the state vector $\mathbf{x}$, compromising of n parameters x_1, x_2,.....,x_n (of unknown values to be retrieved) representing the state of the atmosphere. $\mathbf{y}$ is the measurement vector, compromising of the parameters that have been observed and are needed for the retrieval of $\mathbf{x}$, with m elements y_1, y_2,.....,y_m. For all $\mathbf{x}$, there exists a $\mathbf{y}$ such that:

$$\mathbf{y} = \mathbf{f}(\mathbf{x}),$$

where $\mathbf{f}(.)$ is the forward function, describing the physics of the measurement. It is unlikely that the physics of a system will be known with full accuracy, and there always exists errors associated with measurements. Therefore the relationship between the state and measurement vector can be written as:

$$\mathbf{y} = \mathbf{F}(\mathbf{x}) + \epsilon, \tag{3.26}$$

where $\mathbf{F}(\mathbf{x})$, the forward model, approximates the physics of the measurement, and ϵ is the measurement error. For simplicity, assume $\mathbf{F}(\mathbf{x})$ is linear and expanding about some reference state $\mathbf{x_0}$:

$$\mathbf{y} - \mathbf{F}(\mathbf{x_0}) = \frac{\partial \mathbf{F}(\mathbf{x})}{\partial \mathbf{x}}(\mathbf{x} - \mathbf{x_0}) + \epsilon = \mathbf{K}(\mathbf{x} - \mathbf{x_0}) + \epsilon.$$

where $\mathbf{K}$ is the $m \times n$ weighting function matrix. Each element of $\mathbf{K}$ is the partial derivative of an element of the forward model with respect to an element of a state vector: $K_{ij} = \frac{\partial F_i(\mathbf{x})}{\partial x_j}$, $i = 1, ..., m$, $j = 1, ..., n$. The act of measurement can be thought of as a mapping from the state space (vector space of dimension n) to the measurement space (a vector space of dimension m). Hence the inverse problem involves finding a correct inverse mapping from the measurement space to the state space.

We can write Equation (3.5.1) in a more general way:

$$\mathbf{y} = \mathbf{f}(\mathbf{x}, \mathbf{b}) + \epsilon = \mathbf{F}(\mathbf{x}, \mathbf{b}) + \mathbf{\Delta f}(\mathbf{x}, \mathbf{b}) + \epsilon, \tag{3.27}$$

where $\mathbf{F}(.)$ is the forward model, $\mathbf{\Delta f}$ represents the error of the forward model in terms of the real physics and $\mathbf{b}$ is a set of parameters that influence the measurement (which are known to some extent, but are not intended to be retrieved). These parameters are known as the forward function parameters, and affect the accuracy of the measurement.

If $\hat{\mathbf{x}}$ is the value that has been retrieved from a retrieval method $\mathbf{R}$, then we can write:

$$\hat{\mathbf{x}} = \mathbf{R}(\mathbf{y}, \hat{\mathbf{b}}, \mathbf{x_a}, \mathbf{c}), \tag{3.28}$$

where $\hat{}$ represents an estimated value. $\mathbf{x_a}$ and $\mathbf{c}$ are not included in the forward function but do affect the retrieval. $\mathbf{x_a}$ is an *a priori* estimate of $\mathbf{x}$, and $\mathbf{c}$ is made up of the retrieval method parameters, compromising of anything else that may be used for the retrieval method, for example convergence details. Substitute eq. (3.27) into eq. (3.28):

$$\hat{\mathbf{x}} = \mathbf{R}(\mathbf{F}(\mathbf{x}, \mathbf{b}) + \mathbf{\Delta f}(\mathbf{x}, \mathbf{b}) + \epsilon, \hat{\mathbf{b}}, \mathbf{x_a}, \mathbf{c}). \tag{3.29}$$

Eq. (3.29) is called the transfer function, representing the whole observing system, including the measuring instrument as well as the retrieval method $\mathbf{R}$.

3.5.2 Fitting Procedures

There are numerous analysis procedures used to fit the forward modeled data to the measured data. An outline of the most common methods is provided below.

Linear least squares fitting techniques aim to minimize the residual between the measured data $y(x_i)$, where $x_1, ..., x_n$ are the independent parameters e.g. cross sections, and a model $F(x_i, a_1, a_2, ..)$, where $a_1, ..., a_m$ are the model parameters to be retrieved (e.g. trace gas concentrations). The function F describes the dependence of $f(x_i)$ on the independent parameter x_i. The model parameters change at each iteration of the fitting procedure until

the best fit for the measured data is obtained. Generally, this involves minimizing χ^2:

$$\chi^2 = \sum_{i=1}^{n}\sum_{k=1}^{m}\left[\frac{y(x_i) - F(x_i, a_k)}{\epsilon(i)}\right]^2, \tag{3.30}$$

where $\epsilon(i)$ is the measurement error, i.e. the standard deviation of the ith measurement point. The model function F has to be linear in the parameters $a_1, ..., a_m$, for example a polynomial (Platt and Stutz, 2008). Note that F can be non-linear in x_i. As F is linear in a_k it is possible to express it as a general linear combination of a_k:

$$F(x_i, a_k) = \sum_{i=1}^{n}\sum_{k=1}^{m} a_k f_k(x_i), \tag{3.31}$$

where $f_k(x_i)$ is a function of x_i, called the basis function. To make the mathematical descriptions easier, matrix notation shall be introduced. Define $\mathbf{A}$ as the $n \times m$ design matrix:

$$\mathbf{A}_{i,j} = \frac{f_j(x_i)}{\epsilon_i} \tag{3.32}$$

for $i = 1, ..., n$ and $j = 1, ..., m$. Let vector $\mathbf{b}$ of length n be defined as

$$\mathbf{b_i} = \frac{y(x_i)}{\epsilon_i}. \tag{3.33}$$

Finally, define $\mathbf{a}$ as the vector of length m as the model parameters $a_1, ..., a_m$. There are several ways to solve Equation 3.30, and the sections below explain two such methods (Press *et al..*, 2007):

1. **Normal equations solution:** Substituting Equation 3.31 into Equation 3.30 and taking the derivative with respect to the parameters a_k gives us:

$$0 = \sum_{i=1}^{n}\sum_{k=1}^{m}\sum_{j=1}^{m} f_j(x_i)\left[\frac{y(x_i) - a_k f_k(x_i)}{\epsilon(i)^2}\right]. \tag{3.34}$$

Equation 3.34 is equivalent to:

$$\mathbf{A^T.b} = (\mathbf{A^T.A}).\mathbf{a} \tag{3.35}$$

146

Equations 3.34 and 3.35 are called the normal equations. There are numerous standard ways of solving these equations for vector **a**, for example LU decomposition and Choleksy decomposition (Press *et al..*, 2007).

2. **Singular value decompositions (SVD)**: SVD is a good technique to use when dealing with equations that are singular or close to singular. It is based on the fact that any $n \times m$ matrix **A** can be expressed as follows:

$$\mathbf{A} = \mathbf{U}.\mathbf{W}.\mathbf{V^T}, \tag{3.36}$$

where **U** is an $n \times m$ column-orthogonal matrix, **W** is an $m \times m$ diagonal matrix with positive or zero elements (the singular values) and **V** is an $m \times m$ orthogonal matrix. Using matrix notation and Equation 3.31, Equation 3.30 can be written as

$$\chi^2 = |\mathbf{A}.\mathbf{a} - \mathbf{b}|^2 \tag{3.37}$$

Denote $\mathbf{U}_i$, $i = 1, ..m$, as the column vectors (of length n) of **U**, $\mathbf{V}_i$, $i = 1, ..m$, as the column vectors (of length m) of **V** and w_i as the singular values of matrix **W**, $i = 1, ..m$. Using these values, the solution of Equation 3.37 can be given as (see Press *et al.* (2007) for proof):

$$\mathbf{a} = \sum_{i=1}^{m} \frac{\mathbf{U_i}.\mathbf{b}}{w_i}.\mathbf{V_i} \tag{3.38}$$

Equation 3.38 says that the values **a** are linear combinations of the columns of **V**, with coefficients as the dot product of the column vectors of **U** and the weighted values of **b**.

An alternative to the least squares method is non linear fitting. Linear methods are preferable as they provide analytical solutions whereas non linear methods involve an iterative process and are consequently somewhat sensitive to the values of the starting parameters. Also, non-linear routines are more computationally expensive, with longer run times and a greater number of parameters needing to be set. However, it is unrealistic to model most problems linearly due to their complex structure. It is more accurate to use non-linear model functions. In general, non linear methods involve the measurements $y(x_i)$, and a nonlinear model

function $F(x_i, b_1, b_2, ..)$ with parameters $b_1, ..., b_m$. Like the linear approach, the process aims to minimize χ^2 in Equation 3.30 (Platt and Stutz, 2008). The approach of non-linear methods is to start with the best approximation of the model parameters, the *a priori* values and to then apply the given method at each iteration until χ^2 ceases to decrease (Press *et al.*. 2007).

1. **The Gauss-Newton method**: This method is based on the fact that the derivative of the minimum of χ^2 with respect to a is zero. Consider the standard multi-dimensional Newton method for optimization for some function $f(x_i)$, $i = 1, ..., n$ (Press *et al.*. 2007):

$$x_{i+1} = x_i - \frac{f'(x)}{f''(x)}. \tag{3.39}$$

   This can be applied to Equation 3.30, using the gradient of χ^2 instead of its first derivative (Platt and Stutz, 2008):

$$\mathbf{a_{k+1}} = \mathbf{a_k} - \mathbf{D}^{-1}\left(\frac{\nabla\chi^2(\mathbf{a_k})}{2}\right), \tag{3.40}$$

   where k is the iteration number, $\mathbf{a_k}$ is a vector of all the model parameters at the kth iteration, $\nabla\chi^2$ is the gradient of χ^2 and $\mathbf{D}$ is the Hessian matrix of the model function $F(x_i, a)$, for $i = 1, .., n$. The Hessian matrix a square matrix with components as the second order partial derivatives of $F(x, a)$ with respect to $\mathbf{a}$ (Press *et al.*. 2007):

$$\frac{\partial^2\chi^2}{\partial a_r \partial a_s} = \sum_{i=1}^{n} \frac{2}{\sigma^2}\left(\frac{\partial F(x_i, \mathbf{a})}{\partial a_r}\frac{\partial F(x_i, \mathbf{a})}{\partial a_s} - [y(x_i) - F(x_i, \mathbf{a})]\frac{\partial^2 F(x_i, \mathbf{a})}{\partial a_s \partial a_r}\right), \tag{3.41}$$

   for $r, s = 1, ..., m$. The iteration will occur until some pre determined convergence condition are met. The convergence condition depends on the problem and the required accuracy. However there is no guarantee that this method will lead to convergence. Best results will be to the minimum of χ^2 (Platt and Stutz, 2008).

2. **The gradient method**: This method is designed to find the minimum of Equation 3.30 by finding the steepest descent of χ^2 in the model parameter space (Platt and Stutz, 2008):

$$\mathbf{a_{k+1}} = \mathbf{a_k} + \lambda \times (-\nabla\chi^2(a_k)), \tag{3.42}$$

where λ is some constant. The method moves from point $\mathbf{a_i}$ to $\mathbf{a_{i+1}}$ along the line from $\mathbf{a_i}$ in the direction of the negative gradient of χ^2 with a width that is chosen through the constant λ. If the constant is small, convergence will be slow as it is likely that there will be many iterations. However there is a chance that the choice of a large constant will lead to the iteration missing the minimum. As with the previous method, the iterations continue until some predefined convergence condition is met. If there is more than one minimum of χ^2, the method depends on the choice of $\mathbf{a_0}$ (Platt and Stutz, 2008).

3. **Levenberg-Marquardt Method**: The Gauss-Newton method is highly dependent on whether the starting values of the model parameters are close to the minimum of χ^2 and the gradient method is likely to converge away from the minimum. Levenberg (1944) took this into consideration and put together the two methods to create a method that is more stable and converges faster (Platt and Stutz, 2008):

$$\mathbf{a_{k+1}} = \mathbf{a_k} + \mathbf{A} \times (-\nabla \chi^2(a_k)), \tag{3.43}$$

where $\mathbf{A}$ is the matrix

$$A = \lambda.\mathbf{I} + \mathbf{D'^{-1}}. \tag{3.44}$$

Here $\mathbf{I}$ is the identity matrix and $\mathbf{D'^{-1}} = \frac{\mathbf{D^{-1}}}{2}$. For large values of λ, this method is more similar to the gradient method, for small values the resemblance is with the Gauss-Newton method and for medium sized values it is a linear combination of both the methods (Platt and Stutz, 2008). Marquardt (1964) suggested that the method follow the procedure below:

- Select values for $\mathbf{a_0}$ and start with a small value for λ, for example $\lambda = 0.001$.
- Solve Equation 3.43 and calculate χ^2 for the new $\mathbf{a_{k+1}}$.
- If $\chi^2(\mathbf{a_{k+1}}) \geq \chi^2(\mathbf{a_k})$ then let $\mathbf{a_{k+1}} = \mathbf{a_k}$, times λ by 10 and calculate the new parameter vector.
- If $\chi^2(\mathbf{a_{k+1}}) < \chi^2(\mathbf{a_k})$ then divide λ by 10 and calculate the new parameter vector.

The iterations stop when pre defined conditions are met, for example if λ is too large such that there does not seem to be any convergence, or if λ is too small, suggesting that convergence has been reached. Another possibility is to set a bound for the change in χ^2, for example if values of χ^2 are not changing very much after each iteration then this suggests that the iterations are close to the minimum. This method will always converge, as the values that do not decrease χ^2 are not used and λ in increased (putting more weight on the gradient method), while conversely the algorithm is trying to reduce λ so that it is more similar to the Gauss Newton method, which provides good estimations for the minimum of χ^2 (Platt and Stutz, 2008).

3.6 Comparative Analysis of Trace Gas Retrieval Methods

This section presents a comparison of available methods for the retrieval of trace gas abundances from the UV and IR spectra collected by the DOAS and FTIR. In the case of the UV spectra, retrievals from the DOAS forward model and direct calibration methods are presented for data of two smoke plumes from fires studied during the South African field campaign described in Chapter 5. Similarly, for the FTIR data, retrievals from the Burton and MALT methods are compared for one plume observed fire from the Australian field trip described in Chapter 7. Chapters 5 and 6 present a more detailed description of the specific retrieval methods ultimately used in the analysis of the full field datasets; the direct calibration method for the UV spectra and MALT for the IR spectra. Here we shows how the use of these particular methods was arrived at, via a comparison to the alternative approach.

3.6.1 UV Spectroscopy Retrieval Method Comparison

As previously mentioned, the DOAS forward model method makes uses of laboratory calculated cross sections of the target gases (here SO_2 and NO_2) to iteratively match a modeled and measured spectrum within a specified wavelength interval using the Beer Lambert law. Conversely, the direct calibration method derives an empirical relationship between target gas column amount and absorbance (Equation 3.14) using spectra of gas cells containing known amounts of the target gases. This relationship is usually a polynomial, with absorbances as the x values and y the gas cell concentrations. For this work, there are three

gas cells containing varying amounts for each target gas, of column amounts 70, 100 and 130 ppmm for NO_2 and 450, 905 and 950 ppmm for SO_2, respectively.

The preprocessing of the measurement spectra, as detailed in Section 3.7, is the same for both the DOAS and direct calibration methods. Below an outline of preprocessing and retrieval details shall be presented from two fires (termed SF1 and SF4), carried out during the South African field campaign that are described in detail later in Chapter 5. Here the aim is simply to compare retrievals made by the two approaches so as to select the retrieval method most appropriate for use in this thesis. Fires SF1 and SF2 were chosen for a comparative analysis because fire SF1 was of a lower intensity than fire SF4 and thus appeared to emit less smoke. It is believed useful to examine how both methods can be applied to different magnitude fires. Measurements were conducted by continuously making transects with the UV-DOAS spectrometer using a vehicle traveling beside the burn plots, perpendicular to the plume direction. More detail on the measurement principles is given in Chapter 5. Again the purpose here is just to test the methods ability to retrieve useful SO_2 and NO_2 column amounts from the measured spectra.

Firstly, preprocessing of the spectra was conducted. A dark current spectrum was subtracted from all spectra to remove any self emitted energy by the spectrometer (see Figure 3.7 a) for an example). This is followed by the division of each measurement spectrum by a clear sky spectrum, which is measured outside of the smoke effected region. An example clear sky spectrum is shown in Figure 3.7 b). High and low pass binomial filters were then applied to the spectra to isolate the target gas absorption features and to smooth out and noisy structures respectively. Absorbances were subsequently calculated by taking the logarithm. See Chapter 5 for examples of calibration gas cell absorbances. After this point, the two different retrieval methods were implemented using the preprocessed spectra.
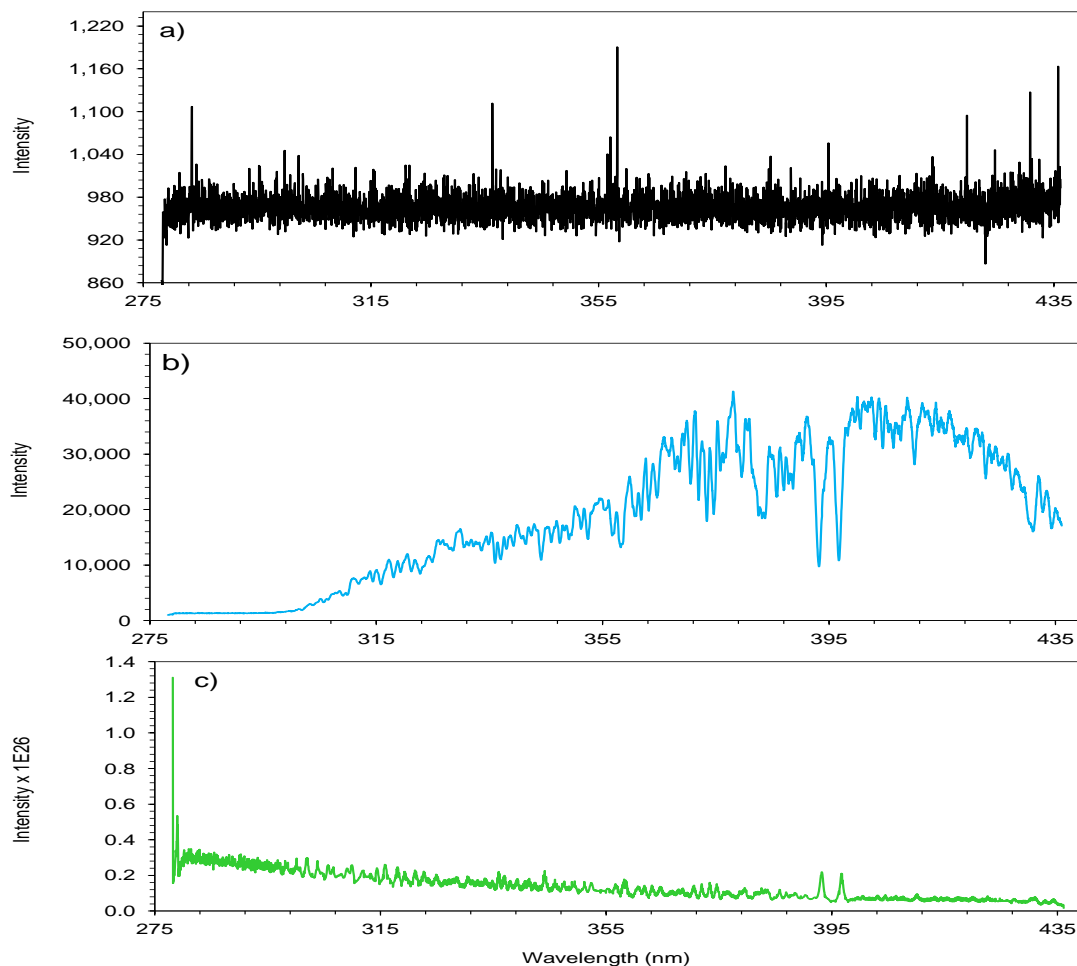
Figure 3.7: *Examples of a) dark, b) clear sky and c) ring spectrum that are used in the retrieval direct calibration and DOAS forward methods to retrieve vertical column amounts of SO_2 and NO_2 from the UV spectra. The dark spectrum is subtracted from all measured spectra in order to remove any signal that is due solely to the DOAS instrument components. Each measured spectrum is then divided by a corresponding clear sky spectrum, measured in ambient conditions in the absence of excess amounts of NO_2 and SO_2. The ring spectrum, used only with the DOAS forward model retrieval method, is used as a cross section that is included in the fitting algorithm along with the absorption cross sections of any gases that have absorption features in the spectral fitting region. The ring spectrum is added to the fit to take into account possible Raman scattering effects that could be confused with the absorption of trace gases.*

For the DOAS forward model method, the ILS of the spectrometer needs to be determined in order that in can be convolved with the trace gas absorption cross sections used in the fitting procedure, since the cross sections were taken at a much higher spectral resolution than that offered by the USB4000 spectrometer used to collect field spectra. The ILS was

152

determined using an Ocean Optics Hg Mercury-Aragon lamp as a light source connected to the spectrometer via the optical fiber. Spectra were recorded of the signal from the lamp and Figure 3.8 shows an example of one such spectrum.
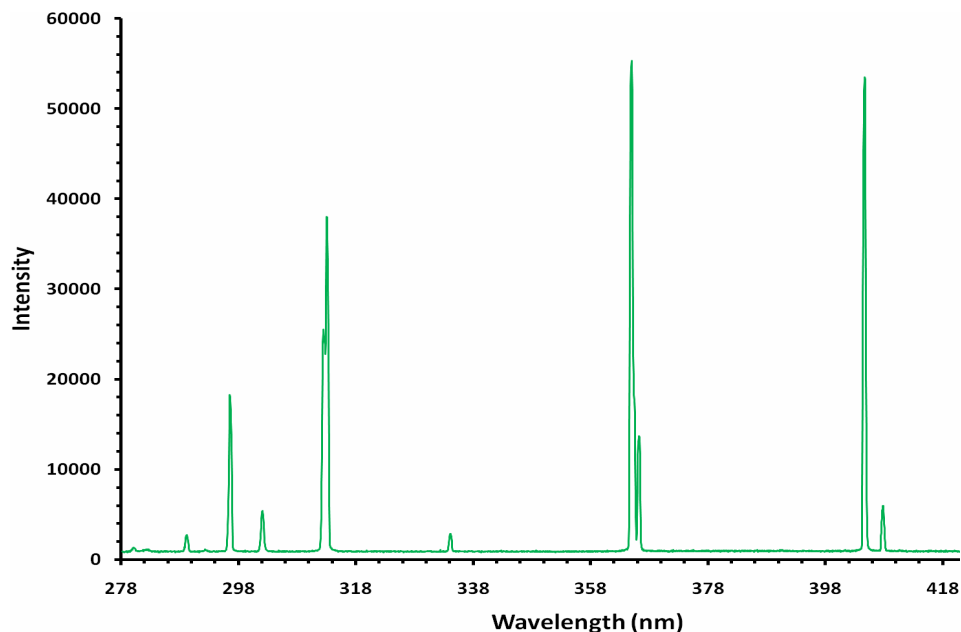
Figure 3.8: *An example of a spectrum collected by the UV-DOAS spectrometer from the signal of the Ocean Optics Hg Mercury-Aragon lamp. Note the strong emission lines.*

The ILS in theory should be Gaussian, a result of the Gaussian shaped emission lines from the Hg-Argon lamp. This is not the case for the mercury emission spectra due to instrument imperfections. Hence for this analysis, a Gaussian curve was fitted for to 334 nm peak for several mercury emission spectra as this was the strongest defined peak. The average of these Gaussian curves was then used as the convolution kernel for use with the trace gas cross sections, in place of the original 334 nm peak from the raw mercury emission spectra. An example of 7 Gaussian curves that were fitted against the 334 nm peak from 7 different emission spectra is shown in Figure 3.9 (along with their average).
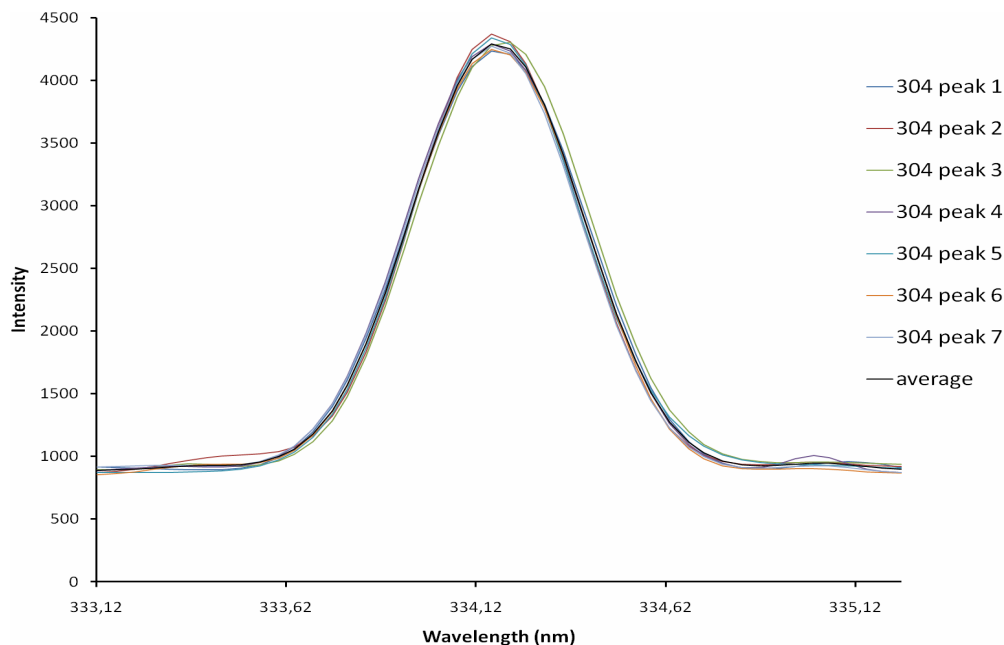
Figure 3.9: *Fitted Gaussian curves of the 334 nm peak from 7 mercury emission spectra (an example shown in Figure 3.8), along with their average. The resulting curve is used as the convolution kernel when attempting to convolve the ILS with the very high spectral resolution gas absorption cross sections obtained from the spectral database.*

High resolution absorption cross sections of the target gas species are needed for the fitting procedure. These cross sections were obtained from the University of Bremen (2007). The absorption cross sections used here were the NO_2 (293 K) 231-794 nm cross section measured using the GOME grating spectrometer, the SO_2 (293 K) 240-395 nm cross section measured from the SCIAMACHY PFM (Proto Flight Model) Spectrometer. In addition, a cross section was obtained for O_3, specifically the (293 K) 230-1070 nm cross section measured with the SCIAMACHY PFM. O_3 is required as it has absorption features in the UV wavelength region used for the retrieval of SO_2 and NO_2, and therefore it needs to be taken into account during the DOAS fitting procedure. Note that the temperature of the gas from which the cross section is measured should be relatively close to that of the temperature of the target gas in the field to the temperature dependence of the absorption cross sections (Platt and Stutz, 2008). Figure 3.10 shows the convolved cross sections for each of the NO_2 and SO_2 target gases along with O_3. Note that the convolved spectra do not need to cover the full wavelength range of the original cross sections, so long as the wavelength range used in the

retrieval process is covered.
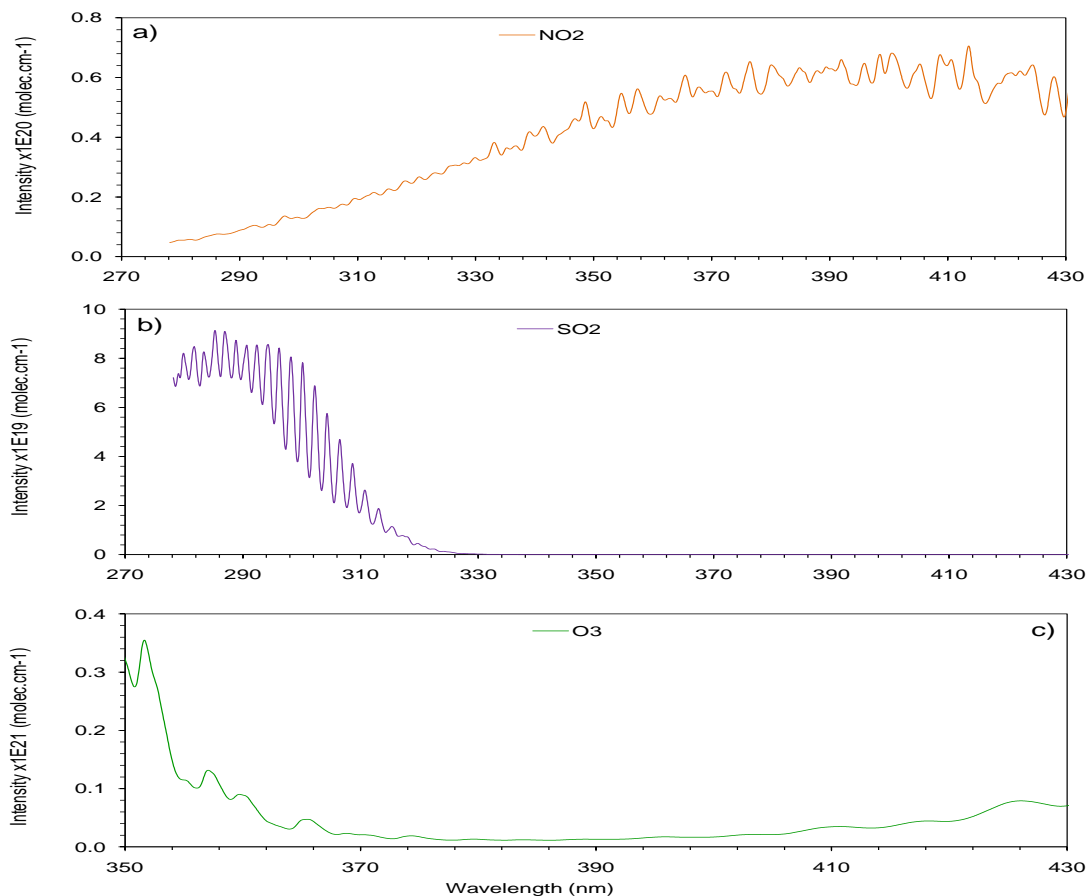
Figure 3.10: *The absorption cross sections of a) NO$_2$ b) SO$_2$ and c) O$_3$ included in the fitting algorithm of the DOAS forward model used to retrieve the vertical pathlength amounts of the target gases SO$_2$ and NO$_2$ The cross section of O$_3$ is included in the retrieval of both target gases as it has absorption features in the spectral fitting windows used for NO$_2$ and SO$_2$ (311-316 nm for SO$_2$ and 426-436 nm for NO$_2$. All three absorption cross sections were convolved with the ILS of the DOAS spectrometer to match the spectral resolution of the measured spectra.*

Along with the absorption cross sections, a ring spectrum is included in the fitting for the retrievals of both gases via the DOAS foward method. This is derived from the clear sky spectrum, an example of which is shown in Figure 3.7 c), using DOASIS (Kraus, 2006). DOASIS is a software package used for the acquisition, mathematical operations and species evaluation of spectral data. The fitting was subsequently carried out using DOASIS, within the spectral region of 311-316 nm and 424-436 nm for SO$_2$ and NO$_2$ respectively. The choice

of the wavelength region was determined by running the DOAS fit on the gas cell calibration spectra using a range of spectral fitting wavelength regions and selecting the region which retrieved vertical pathlength column amounts closest to those of the actual gas cells. Figure 3.11 a) and b) shows the retrieval column amounts of NO_2 and SO_2 calculated using the chosen spectral fitting regions for the gas cell spectra for fire SF4.

For the direct calibration method, the derived polynomial equation relating calibration cell trace gas amounts to the measured absorbances were then applied to the absorbance spectra derived from the actual spectral measurements of the smoke plume. As with the DOAS forward model method, the spectra collected using the gas cells were first used to determine at which wavelengths the equation is most accurate. Chapter 5 shows examples of these calibration equations for both SO_2 and NO_2, along with details of which wavelengths were selected for the derivation of the calibration equations. Figure 3.11 a) and b) show the retrieved trace gas column amounts for SO_2 and NO_2 using this method for fire SF4 at the chosen wavelengths.
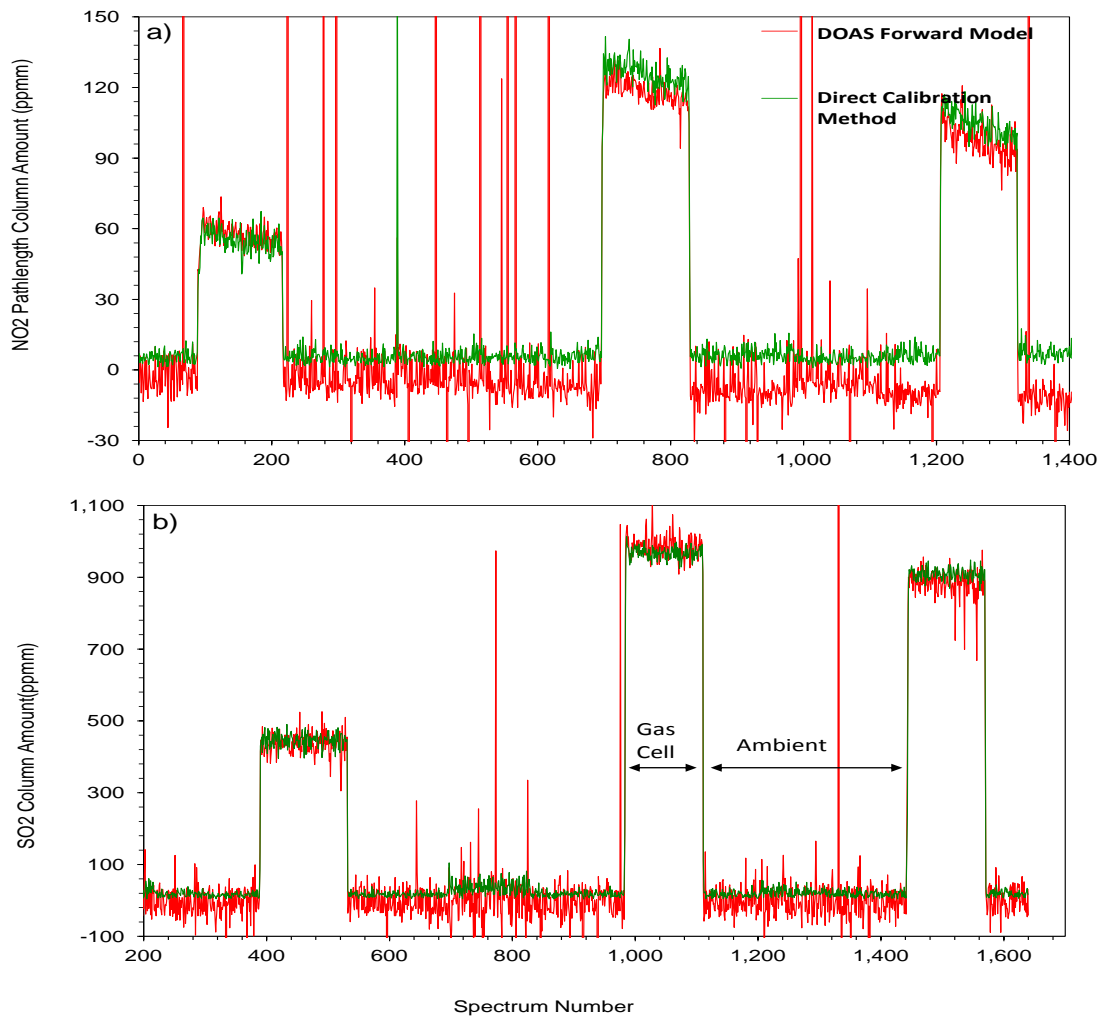
Figure 3.11: *The retrieved vertical column amounts for fire SF4 of NO_2 a) and SO_2 b) by applying the DOAS forward model method (red) and the direct calibration method (green) to the gas cell calibration spectra. Gas cells amounts were of values 70, 100 and 130 ppmm for NO_2 and 450, 905 and 950 ppmm for SO_2. Note the negative amounts for both gases that were retrieved using the DOAS forward model method and, particularly for NO_2, the unrealistically high amounts in the ambient spectra. These features do not appear in the retrieved amounts from the direct calibration method and in general, for both ambient and gas cell spectra retrieved amounts were less nosiey compared to those from the DOAS forward method.*

It can be seen from Figure 3.11 that the retrieved column amounts calculated using the DOAS forward model retrieval method appear much more variable compared to those using the direct calibration method. Since the gas cell amounts in the cells did not vary over the measurement period, any variation seen in the retrieved amounts is viewed as noise.

The DOAS forward model method retrieved results also include negative retrieved column amounts for the ambient spectra in which gas cells were not present (fluctuating between -10 to 10 pppm for NO_2 and -50 to 50 ppmm for SO_2) and also some unrealistically high retrieved column amounts (i.e. much greater than absolute value of 1000 ppmm). Such high values are not present in the retrieved column amounts using the direct calibration method. In addition, the ambient column amounts returned by the direct calibration method do not fall below zero, ranging between 0-10 pppm for NO_2 and 10-30 ppmm for SO_2. These issues are discussed further below. In general, for the gas cell retrieved column amounts, the methods do not differ too much in their averaged retrieved amounts, although for the NO_2 gas cells of 100 and 130 ppmm the results derived from the DOAS method prove to be slightly lower than those from the direct calibration method and more distant from the actual amounts reported the gas cells. The DOAS forward model method has an average variation of 17% from 70 ppmm for the calibration gas cell spectra column amounts of this gas cell, while the direct calibration method results vary on average by 21 % and the averaged amounts from both methods were 6% different to 100 ppmm for this gas cell. For all other gas cells, the column amounts returned by the direct calibration method are on average closer to the amounts quoted for the gas cells compared to those given by the DOAS forward model method (4% cf 9 % for 130 NO_2 ppmm, 3.4 % cf 6 % for 450 SO_2 ppmm, 2% cf 3 % for SO_2 905 ppmm and 2% cf 4 % for SO_2 950 ppmm).

Figure 3.12 shows the retrieved vertical column amounts for the smoke plumes for fires SF1 and SF4 for both target gases. Results from spectra that were saturated by high levels of incoming light intensity or any retrieved values showing an unrealistically high column amount were removed from the data (-100 $< x <$ 300 ppmm). Note that the DOAS forward model method produced a greater number of such unrealistic values, for example for fire SF1, such values made up 8% for NO_2 and 5% for SO_2 of the column amounts retrieved from this method compared with 6% (NO_2) and 1% (SO_2) of the amounts returned from the direct calibration method. The results returned from the DOAS method in general exhibit a higher amount 'noise', particularly for SO_2 (Figure 3.12 b) and d)). This includes negative column amounts and high levels of fluctuations around the ambient level baseline ($\pm$ 60 ppmm).

Also note that for the NO_2 retrieved column amounts, when the direct calibration method exhibits elevated column amounts due to the presence of the smoke plume, the DOAS forward model method at times returns column amounts of an increasing negative value. In general, these large negative values correspond to spectra with a low signal intensity. It may be the case that the accuracy of the DOAS forward model method is compromised down when the clear sky spectrum used for normalization is of a greater intensity than the measurement spectrum, or in fact perhaps simply when the measurement spectra are below a certain intensity. Yet the SO_2 DOAS forward model method results do not exhibit the same pattern, although the spectral region used for the DOAS fitting of SO_2 is always at a lower light intensity than that used NO_2 (see Figure 5.26). However a change in light intensity is seen much more in the NO_2 fitting regions; whilst the light intensity in the spectral region used for SO_2 stays relatively stable. This suggests that NO_2 retrievals made using the DOAS forward model method are more sensitive to differences between the measurement and clear sky spectrum than the SO_2 retrievals. It is difficult to use a clear sky spectrum that will have the same intensity as the measurement spectra for the whole traverse, as the the intensity is constantly changing due to e.g. cloud cover and plume aerosol amount variations, and the choice of clear sky spectrum is limited to times when the instrument is measuring outside of the plume. The derived column amounts from the DOAS forward model method showing very large magnitude (> 1000 pmmm) could be due to a failure in convergence of the fitting algorithm due to poor quality spectra. With more time and effort, it may be possible to increase the accuracy of the DOAS method. However, the direct calibration method appears already robust and produces retrievals that do not contain negative and unrealistic high magnitudes that feature as spikes in the returned column amounts from the DOAS forward model method. Therefore, the direct calibration approach was selected for further use within this thesis.
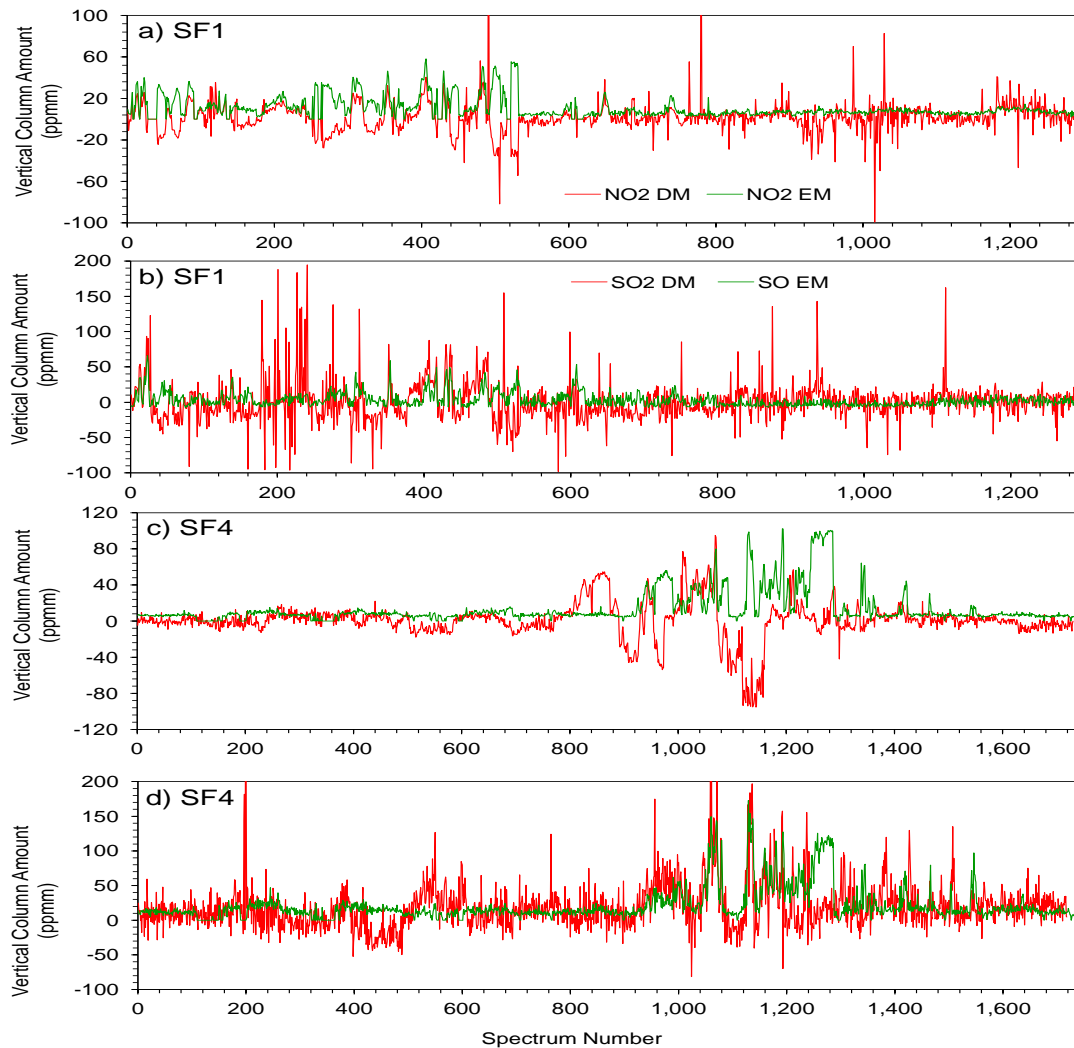
Figure 3.12: *The retrieved vertical column amounts of SO_2 and NO_2 (ppmm) for SF1 a) and b) and SF4 c) and d) using the DOAS forward model (red) and direct empirical method (green). There exist major inconsistencies with the retrieved amounts from the two methods for both gases and for both fires. In particular notice the negative NO_2 amounts retrieved from the DOAS forward model that correspond to elevated amounts retrieved from the direct empirical method. Also note, in particular for the SO_2 results, the amounts retrieved by the DOAS forward model exhibit high levels of noise. Generally, the direct empirical method returned a time series for both fires that corresponding with elevated amounts in the presence of high levels of smoke and low amounts otherwise.*

3.6.2   IR Spectroscopy Retrieval Method Comparison

Here the Burton and MALT methods for trace gas retrievals from the IR spectra are inter compared. The pathlength averaged mixing ratios of CO_2, CO, CH_4 and SO_2 were retrieved

from an example set of IR spectra using both the Burton and MALT methods. The spectra came from a fire carried out during the Australian field trip, denoted as fire AF3 in Chapter 7 (see this chapter for more details of AF3). Spectral measurements were made using the FTIR spectrometer and IR radiation source, with both instruments positioned beside the burn plot, approximately 40 m apart such that the fire smoke plume passed through the optical pathlength between the spectrometer and IR source. See Chapter 6 for more details on the IR spectral measurement principles. The purpose here is only to intercom the retrieval methods.

Table 3.2 shows the spectral fitting windows used for each of the retrieved gases as well as any interfering species that have absorption features in the same spectral regions. 6 gives details on how the spectral regions were chosen, as well as addition details on input data used for the retrievals (e.g. optical pathlength, temperature and pressure).

Table 3.2: *The spectral windows used for the NLLS fitting of gases CO_2, CO, CH_4, NO_2 and SO_2 for both the Burton and Malt method. Also shown are the gases that were also fitted in the chosen spectral regions due to the presence of absorption features in these regions.*

Target Gas	Spectral Fitting Region (cm-1)	Interfering Species
CO_2	2225-2310	N_2O, H_2O
CO	2050-2132	CO_2, H_2O
CH_4	2980-3090	H_2O
NO_2	2910-2940	H_2O, CH_4
SO_2	1120-1200	H_2O, N_2O

Figure 3.13 shows the pathlength averaged mixing ratios retrieved from the IR spectra using the Burton and the Malt methods. Both show a clear elevation of trace gas mixing ratios for all target gases in the presence of the smoke plume. Looking firstly at the CO_2 results, (Figure 3.13 a)), it seems that the Burton method slightly underestimates the mixing ratios compared to the MALT method, at least when using this spectral fitting window, with an average difference of mixing ratios returned by both methods at 6%. This maybe explained by the inclusion of the MALT zero offset, a parameter to take into account the non-zero offset of the spectra in spectral regions in which the intensity is theoretically expected to

fall to zero due to complete absorption of the signal by atmospheric constituents. Such a region is included at the end of the spectral fitting region for CO_2; 2290-2310 cm1^{-1}, due to CO_2 absorption (see Figure 6.7). In theory, a the spectral intensity should fall to zero at wavelengths where there exists total absorption by atmospheric species. However, phase errors may cause a zero offset such that the spectral intensity at these wavelengths will be non-zero (Griffith *et al.*, 2003). If the signal is non-zero then the offset parameter allows for this to be taken into account in the fitting procedure used by MALT. The fitted non-zero value can then subsequently be used as a fixed parameter for the retrievals of the remaining trace gases retrieved in spectral regions where it is not possible to determine any offset.

The returned pathlength averaged mixing ratios for CO and CH_4, Figure 3.13 b) and c), do not show any significant variation between the Burton and MALT methods during the fire (average 1% and 2% respectively). The most significant difference can be seen in Figure 3.13 d), which shows the retrieved mixing ratios for SO_2. Negative pre-fire values are returned from the Burton method (reaching -2 ppmm) and values are higher in the presence of the plume than they are with the MALT code (up to 50% higher). SO_2 does not have strong absorption features in the IR, and amounts for this gas in the smoke are expected to be rather low. Given the importance of the SO_2 retrievals, which is one of the gases theoretically able to be retrieved from both the FTIR spectrometer and the UV-DOAS spectrometer measurements, MALT was therefore selected as the IR retrieval code for the remainder of the work in this thesis. MALT has also undergone a detailed accuracy assessment, reported in Smith *et al.* (2011).
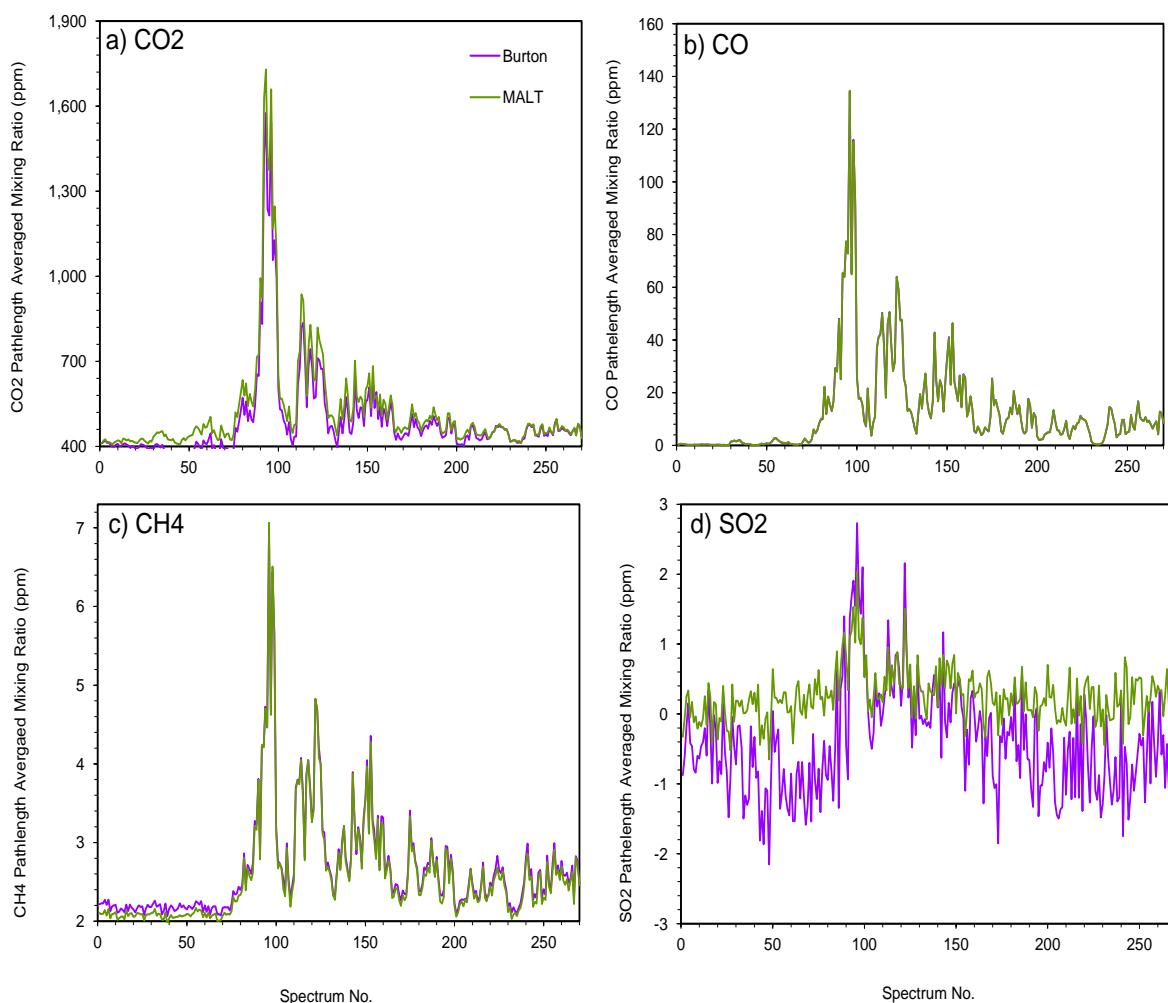
Figure 3.13: *The retrieved pathlength averaged mixing ratios of CO_2, CO, CH_4 and SO_2 for the Burton (purple) and MALT (green) fitting algorithms. There is a slight variation between the returned mixing ratios from both methods for CO_2 and CH_4 while almost no variation for CO. The retrieved mixing ratios for SO_2 show the greatest difference between methods, with the Burton method exhibiting returning negative mixing ratios outside the presence of the plume.*

3.6.3 Conclusion

This section has compared the application of several different methods for the use of retrieving information on trace gas concentrations from both UV and IR spectra collected during measurements of open vegetation fire smoke. The DOAS forward model and direct calibration methods were applied to gas cell and fire smoke spectra collected during two fires SF1

and SF4 from the South African field campaign (see Chapter 5 for more details) to retrieve vertical column amounts of SO_2 and NO_2. The time series of the column amounts returned from the DOAS forward model exhibited negative values and amounts of large magnitude for both the gas cell and fire smoke spectra. In particular, this method did not seem to work efficiently in the NO_2 fire smoke time series when intensity of the fire spectra was low, resulting in negative column amounts. The column amounts returned from the direct calibration method did not exhibit this pattern of negative values and had for of a stable base line around zero in ambient levels without any of the 'spike' features of extremely high/low values found in the alternative method. Hence the direct calibration method was deemed more robust for this research given the time frame and was subsequently applied to the UV spectra collected during the field campaigns for this work to derive the vertical column amounts of SO_2 and NO_2.

Two forward models, the Burton and MALT method, that make use of a non-linear least squares algorithm to estimate the pathlength averaged mixing ratios of trace gases from FTIR collected spectra were compared. Both methods were applied to the same spectra collected during fire AF3 from the Australian field campaign (see Chapter 7 for more details) to retrieve mixing ratios of CO_2, CO, CH_4 and SO_2. In general, the two methods did not show much of a variation for the mixing ratios of the carbonaceous species returned from the fire spectra, an average of 6% for CO_2, 1% for CO and 2% for CH_4. However results differed for SO_2, up to 50% for the fire spectra, with the Burton code returning negative mixing ratios up to -2 ppm. The MALT SO_2 mixing ratios do not fall to such negative values. As SO_2 has weak absorption features in the IR, this may suggest that MALT is more efficient at retrieving mixing ratios of such gases. The retrieval of SO_2 mixing ratios (and NO_2 which also have weak absorption features in the IR) is key to this research as it also has absorption features in the UV and can hence link the trace gas amounts derived from the UV spectra to those derived from the IR spectra. Hence the MALT method is used for subsequent analysis in this work of the IR spectra collected from the field campaigns.

Chapter 4

Approaches to Data Synthesis

Contents

4.1 Introduction

This chapter describes how the trace gas abundances derived from the IR and UV spectra using the methods discussed in chapter 3 can be used to further investigate the properties of open vegetation fire emissions. The general derivation principles of the emission ratio and emission factor metrics outlined in Chapter 1 are presented and their principles of derivation using the horizontal column amounts of the target gases measured using the FTIR spectra. Likewise, an introduction to the estimation of trace as fluxes is provided, since the fluxes of SO_2 and NO_2 are to be calculated using the UV-DOAS derived vertical column amounts of these gases. Finally, these fluxes will be combined with the FTIR emission ratios to return fluxes of all the target species. The aim is to be able to derive smoke flux measurements of the carbonaceos gases being released in the fire plume, and to compare these to the release

rate of radiative energy, the latter being assessed via measurements of fire radiative power provided by the airborne thermal imaging.

A brief introduction to the methods used to derive Fire Radiative Power (FRP) from IR imagery of active biomass burning is also provided in this chapter. Although the FRP data used in this work has been taken from elsewhere and is not explicitly calculated herein, it is compared with the carbon gas flux variations derived from the combined UV and IR spectral observations.

4.2   Emission ratios and Emission factors

Emission factors relate trace gas emissions to biomass burned (Langmann *et al.*, 2009). As explained in Chapter 1, they are used to calculate smoke emissions from burned biomass measurements. An emission factor of a particular gas relates its emission to the fuel load burnt i.e. the amount of a species released per amount of dry fuel burnt, in g Kg^{-1}:

$$EF_x = \frac{M_x}{M_b} = \frac{M_x}{M_C} * [C_b],$$
(4.1)

where M_x is the amount of species emitted during the measured period, M_b is the amount of dry fuel burnt, M_C is the amount of carbon combusted and $[C_b]$ is the carbon content of the biomass. To calculate the emission factor from Equation 4.1, it is necessary to know the amount of fuel burned (or the fuel carbon content and amount of carbon burned), which can prove to be difficult to measure outside of the laboratory. Instead the total amount of carbon emitted during a measurement period is traditionally estimated by summing the measured concentrations of CO_2, CO, hydrocarbons and particulate carbon (Ward and Radke, 1993):

$$EF_x = \frac{[x]}{[C_{CO_2}] + [C_{CO}] + [C_{CH_4}] + [C_{VOC}] + [C_{aeros}] + ...},$$
(4.2)

where $[x]$ is the concentration of the target species x in the smoke and $[C_{CO_2}]$ and so on.. represent the concentrations of the different carbon forms in the smoke. If it is not possible to calculate all individual carbon species concentrations, the carbon budget of the fire can be further estimated by multiplying the measured CO_2 concentration in the smoke by a fixed

factor to take into account the rest of the carbon species. Normally, when this method is used, the total carbon content of fuel is estimated at $50 \pm 5\%$ (by dry weight) (Andreae and Merlet 2001) since vegetation has a reasonably consistent carbon content around all species.

It is difficult to measure the concentration of all the carbon species in the smoke. The method used to calculate emission factors in this work is known as the carbon mass balance method (Delmas *et al.,* 1995) and is described in detail in Chapter 6. One key parameter needed to derive emission factors using this method are emission ratios. The emission ratio of a particular gas describes its emission with respect to that of another gas. Emission ratios can be calculated by dividing the difference between the measured plume and ambient concentrations of the target species by the difference between the measured plume and ambient concentrations of the reference species (also called the 'excess concentrations' of the target reference species):

$$E_{\frac{t}{r}} = \frac{C_t^{plume} - C_t^{ambient}}{C_r^{plume} - C_r^{ambient}},$$

where $E_{\frac{t}{r}}$ is the emission ratio of the target species t with respect to the reference species r, and C_x^{plume} and $C_x^{ambient}$ are the measured plume and ambient concentrations (or mixing ratios) of the two species respectively. Emission ratios are infact usually calculated from the slope of the linear best fit between the target and reference species concentration, or excess concentrations, plotted on a 2D scatter plot (Andreae and Merlet, 2001). Taking the linear regression of the absolute concentrations of the target and base species has the advantage of not requiring any knowledge of the background, which can be difficult when there is a lot of smoke around (Guyon *et al.* 2005). Usually, the species used as references are either CO_2 and CO, but other gases also, such as, CH_4 and C_2H_2. CO and CO_2 are usually used as they are fairly non reactive and make up the vast majority of the carbon released in vegetation fire smoke (Agaki *et al.,* 2011). Different phases of a fire emit different compounds, for example CO is given off at higher ER with respect to CO_2 during smoldering combustion, hence is often preferred as a reference when measuring gases emitted predominantly during the smoldering phase of a fire. In contrast, when looking at gases emitted more predominantly from the flaming phase, CO_2 often makes a more suitable reference. Due to the importance of this $ER_{\frac{x}{CO_2}}$, even smoldering species are linked with CO_2 as reference species, either by

using the regression slope of CO_2 and the target species, or calculating the emission ratio with CO as a reference species, working out the average of the emission ratio of CO to CO_2 and multiplying the two ratios. The use of emission ratios in this way is ideal when it is not possible to measure the fuel load burnt, since all that is needed to calculate the emissions factor of a particular species is in-plume and ambient measurements of the target species with respect to CO_2 and those of other main carbonaceous species (Andreae and Merlet, 2001). Emission ratios and emission factors are important concepts when investigating emissions from biomass burning, as absolution concentrations are just a representation of the level of mixing of the target species in the ambient air (Delmas et $al.$, 1995). However, when investigating the emission ratios of reactive gases, values can be highly variable and if derived from measurements of smoke downwind of the fire, values may not be equal to the actual emission ratios (Akagi et $al.$, 2011) due to chemical reactions occurring within the smoke as it 'ages'.

4.3 Trace Gas Fluxes

The retrieved trace gas vertical column amounts from the DOAS measurements can be used to calculate the fluxes of SO_2 and NO_2, if the DOAS measurements were successful in capturing the full cross section of the plume. The UV-DOAS instrument in this work is set up on a vehicle which then traverses underneath the smoke plume throughout the duration of the experimental burns, hence measuring a cross section of SO_2 and NO_2 emitted from the plume (see Figure 5.10). The UV-DOAS measurement principles conducted during the field campaigns are explained in greater detail in Chapter 5. Emission ratios refer to the amount of the target species that is emitted per unit of the reference species. In contrast, the trace gas flux provides a measure of how much of the target gas passes through a given cross section area per unit time. Along with the retrieved column concentrations, the velocity and distance traveled between each spectral measurement are required for the calculation of these fluxes.

To calculate these flux rates, firstly consider the case in which the measurement traverses are perpendicular to the plume transport direction, as in Figure 5.10 (a). The cross sectional

area of the trace gas column amounts for each traverse are then simply calculated by multiplying each retrieved column total (molec.cm^{-2}) by the distance traveled perpendicular to the plume (m) between the acquisition of one spectrum and the next. These products are summed over the traverse, resulting in the column totals integrated over the plume cross sectional area in the plane defined by the traverse. The values for each traverse are then multiplied by the wind speed at plume height (m.s^{-1}) during the traverse, such that flux values (g.s^{-1}) are obtained. This is summarized by the following equation:

$$F_i = \frac{W_x}{A} \times \sum{}_j (CD_{molec_j} \times d_j) \times P_{s_i} \times 100^2, \tag{4.3}$$

where F_i is the flux rate (g.s^{-1}) for traverse i, CD_{molec_j} (molec.cm^{-2}) and d_j (m) are the column densities and distance for measurement j respectively and P_{s_i} (m.s^{-1}) is the plume speed for traverse i. W_x (g.mol^{-1}) and A are the molecular weight of the target gas x and Avogadro's Constant ($6.02214199 \times 10^{23}$) respectively, used to convert molecules to grams. The molecular weight for NO_2 is 46.0055 g.mol^{-1} and 64.07 g.mol^{-1} for SO_2. 100^2 is for unit conversion.

Now consider the case where the traverses are not perpendicular to the plume, as in Figure 5.10 (b). For this, the distances between measurements calculated as above need to be projected onto the plane perpendicular to the plume direction. Using the plume direction of travel, the angle between the plane perpendicular to the traverse direction and the plume direction, ϕ can be calculated.
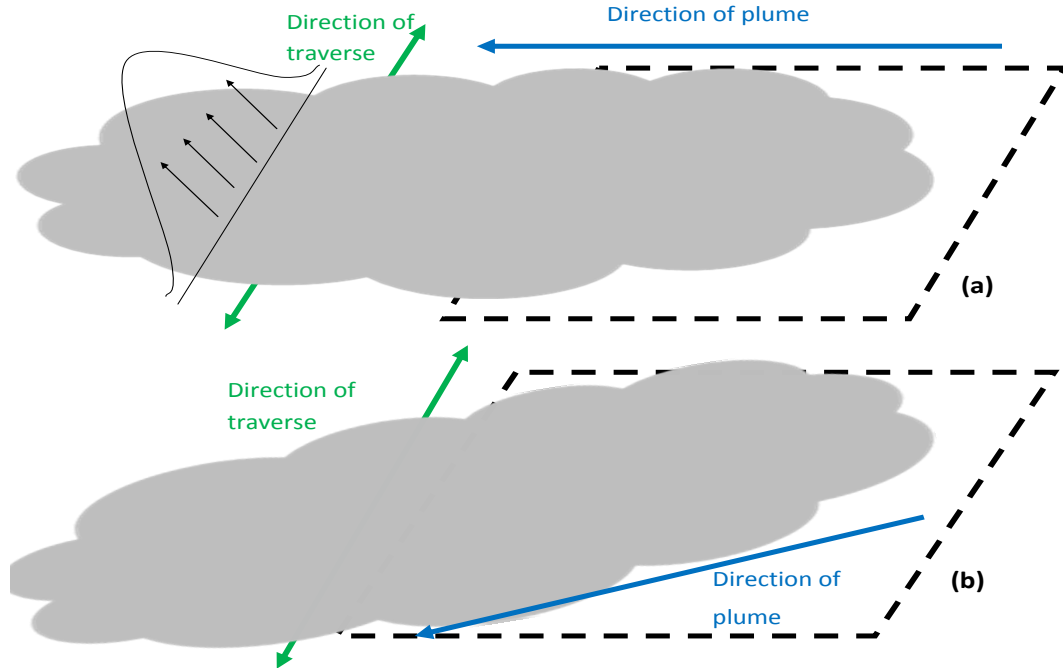
Figure 4.1: *Sketch of the UV-DOAS traverse direction underneath the plume during the experimental burns in relation to the plume direction when the traverse is following a path perpendicular (a) and non-perpendicular (b) to the plume. Traverses are made throughout the duration of the fire, such that a cross section of the emissions of SO_2 and NO_2 from the plume can subsequently be determined. Note that (a) represents the idealized Gaussian plume cross section.*

Knowledge of angle ϕ allows calculation of the projection of the original measurement distances onto the plane perpendicular to the plume direction:

$$|\mathbf{B}| = |\mathbf{A}| \times COS(\phi)$$

where $|\mathbf{A}|$ is the distance between two measurements ($\mathbf{A}$ is the vector form) along the traverse and $|\mathbf{B}|$ is its projection onto the plane perpendicular to the plume ($\mathbf{B}$ is its vector form). $|\mathbf{B}|$ now represents that distance (distance is not a vector) between the two measurements perpendicular to the plume direction (see Figure 4.2 for an example). This approach has been adopted previously in the analysis of volcanic plumes (e.g. McGonigle *et al.*, 2003; Oppenheimer *et al.,* 2004; McGonigle *et al.*, 2005; McGonigle, 2007).
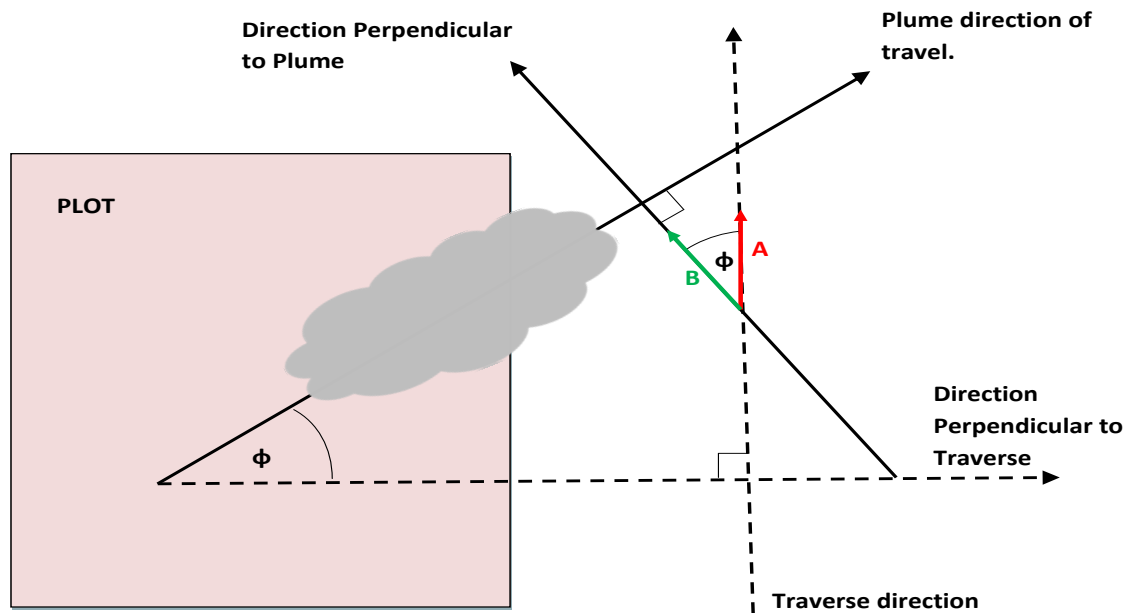
Figure 4.2: *Sketch showing the geometry of the UV-DOAS measurements made in a transect direction that is not perpendicular to the direction of the plume path. The projection B of vector A, representing the distance between two consecutive measurements, can be calculated using the angle between the plume direction and the plane perpendicular to the UV-DOAS traverse, ϕ.*

The flux rates of SO_2 and NO_2 derived using this approach can be used to estimate the flux rates of any of the FTIR detectable species, providing SO_2 or NO_2 can be detected by the FTIR and that an emission ratio of the species of interest can be estimated with respect to SO_2 or NO_2. The UV-DOAS cannot be directly used by itself to estimate fluxes or carbon compounds as these do not have absorption features in the UV. Rather the method can be used to estimate the fluxes of SO_2 and NO_2 that do have UV absorption features, and these fluxes combined with the carbonaceous species emission ratios with respect to these two UV-detectable gases, in order to to calculate carbonaceous gas fluxes. Assuming SO_2 (or NO_2) is detectable during the fire via the FTIR, the emission ratio and any FTIR detectable species x to either SO_2 or NO_2 can be multiplied by the SO_2 (or NO_2) flux rate to get the flux rate of species x.

Currently there has been relatively little work conducted on flux rates from biomass burning compared to the large number of studies on the chemistry and total magnitude of the emissions themselves. The UV-DOAS method employed to estimate SO_2 (and NO_2) flux rates in this work has been traditionally used to estimate flux rates of species emitted from volcanoes, mostly of SO_2 (e.g. Edmonds *et al.*, 2002; McGonigle *et al.*, 2005 and Galle *et al.*, 2002). Very little work has been conducted using the approach to study biomass burning emissions, and subsequent to this, Platt (2008) suggested the use of this method for calculating fluxes from biomass burning, but no analysis was presented. To date, Oppenheimer *et al.* (2004) appears to remain the only study using the UV-DOAS to estimate NO_2 trace gas fluxes from sugar cane agricultural fires in Brazil. No work has been conducted integrating such flux observations for UV detectable species to IR derived emission ratios, in order to estimate the flux of key species such as CO_2, CO and CH_4 and the total carbon emission rate.

4.4 Derivation of Fire Radiative Power (FRP)

The rate at which fire releases energy during the combustion process is related to fire intensity (a measure of the amount of heat released per unit of time during a fire) and hence the amount of fuel burnt per unit of time as fire intensity is a function of available fuel load (Wooster, 2002; Ichoku and Kaufman, 2005). Fire radiative power (FRP) can be defined as the amount of radiant energy released per unit of time from vegetation fires through the rapid oxidation of the carbon fuel, relating to the rate of fuel combustion and carbon volatilization (Roberts *et al.*, 2005). As fuel burnt during vegetation fires is made up of approximately 50% carbon, the rate of carbon emission is also related to the fuel consumption rate and there should therefore be a point of comparison between the FRP of a fire and its rate of carbon emission. A number of smoke forecast schemes are now being developed to use satellite-derived FRP observations to directly estimate smoke release rate (e.g. Kaiser *et al.,* 2011). Yet currently, apart from an early airborne study by Kaufman *et al.* (1996) and a follow-up satellite based study by Ichoku and Kaufman (2005) it is mainly within small scale lab experiments (e.g. Freeborn *et al.,* 2008) that this relationship has been investigated. One aim of the currently work is to further evaluate the nature of the relationship between smoke emission

rate and FRP at real open vegetation fires burning in the natural environment. Currently however, this comparison has not been conducted due to the difficulties with measuring trace gas fluxes (and FRP) of large-scale fires. Fire Radiative Energy, (FRE) is equal to the time integrated FRP, over the whole duration of the fire (Roberts *et al.*, 2005), and thus theoretically proportional to the total fuel mass burned. It should be noted that although radiant energy emission is a major source of energy release in a fire, energy is also released through convection, conduction into the ground and through vaporization of fuel moisture (Zhukov *et al*, 2006). When considering a fire, it is unrealistic to assume that it is made up of one homogeneous thermal component at a single temperature. It is much more realistic to think of a fire as compromising of various flaming and smoldering thermal components (Dozier *et al.*, 1981; Wooster *et al*, 2003), and with this assumption, the FRP is given by the Stefan-Boltzmann law (Wooster *et al.*, 2005):

$$FRP_{TRUE} = \epsilon\sigma\sum_{k}^{n} p_k T_k^4, \tag{4.4}$$

where FRP_{TRUE} is the FRP (W), σ the Stefan-Boltzmann constant
($5.57{\times}10^{-8}$.J. s^{-1}.m^{-2}.K^{-4}), ϵ is the fire emissivity (assumed to be a grey body), n is the number of the thermal components in the fire, p_k is the size of the kth thermal component and T_k is the brightness temperature (K) of the kth thermal component. Using Equation 4.4 in conjunction with satellite or airborne datasets is not an effective way of calculating the FRP however, since the fire may make up only a very small proportion of the pixel and thus the multi-thermal component temperature structure can remain unresolved. If this is the case then, the fire pixel brightness temperature can be much lower than the actual brightness temperature of the fires thermal components since it is averaged together with the brightness temperature of the rest of the non fire background within the pixel (Wooster *et al.*, 2005)

4.4.1   The Bi-Spectral Method

In order to overcome the limitations of Equation 4.4 in retrieving FRP from fires observed from satellite or airborne datasets, Dozier (1981) proposed the Bi-Spectral method, aiming to retrieve the magnitude and subpixel area of the two different thermally radiant compo-

nents within a pixel. The method is based on the idea that warmer pixel components will make a greater contribution (proportionally) to the radiance signal at shorter IR wavelengths than at the longer IR wavelengths.

The radiance of a blackbody emitter at wavelength λ can be expressed using the Planck function:

$$R(\lambda, T) = \frac{a}{\lambda c^5 (e^{\frac{b}{\lambda cT}} - 1)} \times \frac{1}{c}, \tag{4.5}$$

where λ is wavelength (μm), T is brightness temperature, $R(\lambda, T)$ is radiance in $\mathrm{Wm}^{-2}\ \mathrm{sr}^{-1}$ $\mu\mathrm{m}^{-1}$, and a,b,c are constants of values $1.191044024 \times 10^{-16}\ \mathrm{Wm}^2$, $1.4387687 \times 10^{-2}\ \mathrm{mK}$ and 10^6 respectively. Dozier (1981) proposed that when considering a pixel made up of just two such thermal components (the fire and the non fire background), the temperature of the whole pixel can be expressed as an area weighted average of the two individual thermal radiance signals:

$$R_i(T) = pR_i(T_f) + (1-p)R_i(T_b), \tag{4.6}$$

where $i = 1, 2$ represents two wavelengths located, for example, in the MIR and TIR spectral regions, T_i is the brightness temperature of the whole pixel at wavelength i, T_f and T_b are the brightness temperatures of the fire and background components respectively, $R_i(T)$, $R(T_f)$ and $R(T_b)$ are the radiances of the whole pixel, the fire component and the background component respectively at wavelength i and p is the proportion of the pixel's area taken up by the fire. Hence, multi-spectral ($i > 1$) observations of $R(T_i)$ can be used with Equation 4.6 to estimate the fire effective brightness temperature and pixel proportion such that the FRP can be calculated as in Equation 4.4. Observations of a greater number of IR wavelengths in theory allow a greater number of sub-pixel thermal components to be resolved. Dozier (1981) originally used the method with data from the Advanced Very High Resolution Radiometer (AVHRR) instrument onboard the polar orbiting NOAA satellite, using measurements at wavelengths 3.8 μm and 10.8 μm to provide two versions of Equation 4.6 to solve for p and T_f, assuming knowledge of T_b can be obtained from elsewhere (e.g. surrounding 'non-fire' pixels).

The main difficulty associated with the bi-spectral method is however the quantification of the non-fire background signal (i.e. $R_i(T_b)$); there is obviously no way of knowing the exact signal of the background without the fire. One way of determining the background is, as stated above, to take the signal of an adjacent non fire pixel or the average signal of a cluster of non-fire pixels. However, this works best for high spatial resolution instruments where the non fire pixels are spatially close to the fire. For instruments with coarser spatial resolution, the background determination is more difficult due to the likely greater variations of altitude, land cover and the presence of fire scars. If the fire takes up a large proportion of the pixel (i.e. if p in Equation 4.6 is large), the non-fire radiance within the mixed pixel is relatively unimportant as the fire signal dominates. But this is not usually the case for low spatial resolution satellite instruments where pixel areas are large compared to most fires. This is particularly limiting in the TIR region, where the signal for a small or weakly burning fire will not vary dramatically above the background signal and will thus be difficult to accurately quantify (Wooster *et al.*, 2005). Giglio and Kendall (2001) showed only a moderate sensitivity of retrieved fire temperatures (T_f) to errors in the background MIR radiance, but approximately 10 times more sensitivity to errors in the TIR background radiance. Another limiting factor of Equation 4.6 is the assumption that the pixel compromises of only two thermal components and that both these components emit as blackbodies or greybodies and with no atmospheric effects (Eckmann *et al.*, 2008). However the equation can be adapted to include spectral emissivities and atmosphere transmisivity terms, but the problem in isolating the fires contribution to the observed TIR spectral emission signal may remain. Nevertheless, whilst the single subpixel fire temperature and area that is output from the standard Dozier (1981) approach maybe a somewhat unrealistic representation of the true size and temperature structure of the fire, the FRP output from the use of these values within Eqn. 1.4 is a much more representative estimate of the FRP, since errors in retrieved area and temperature act in the opposite direction to one another, and in part cancel one another out to deliver in many cases a reasonable estimate of the true FRP (Wooster et al., 2003). This is only the case though, if the Bi-Spectral method can be appropriately applied, i.e. if the fire signal is strong enough that its signal contribution in the TIR over the background can be adequately assessed.

4.4.2 FRP Estimation: Single Waveband Methods

First proposed by Kaufman *et al.* (1996) for MODIS (The Moderate Resolution Imaging Spectroradiometer), a method for calculating FRP using measurements of just one MIR wavelength was suggested to eliminate some of the uncertainties created by the use of the TIR signal (Wooster *et al.*, 2005). Consider a MODIS fire pixel with brightness temperature T_{MIR} (K), its FRP (W.m^{-2}) can be estimated as follows (Kaufman *et al.*, 1996):

$$FRP_{MODIS} = 4.34 \times 10^{-19}(T_{MIR}^8 - T_{b,MIR}^8), \qquad (4.7)$$

where $T_{b,MIR}$ is the brightness temperature (K) of the neighbouring non-fire pixel in the MODIS MIR channel. The scaling factor 4.34×10^{-19} (Wm^{-2} .K^{-8}) was derived empirically from analysis of modeled sub-pixel fires. With this method, only a single wavelength in the MIR region is used, avoiding the more problematic spectral region (Wooster *et al*, 2005).

Wooster *et al.* (2003) suggested an alternative single-band method, proposing that the radiance of an emitter in the MIR region (as in Equation 4.5) can be accurately approximated by a fourth order power law of the emitter temperature. As with the method proposed by Kaufman *et al.* (1996), only one wavelength in the MIR is required, however in this case emitter radiance is used instead of brightness temperature and the relationship to FRP is linear. This linearity enables any adjustments, for example due to changes in pixel size along the swath or variations on atmospheric transmisivity, to be accounted for after the FRP has been calculated if necessary. Also, this method is directly applicable to other sensors, not just to MODIS as the empiricism of the MODIS method has been removed. Consider a fire with radiance $R_{f,MIR}$. $R_{R,MIR}$ can be estimated according to the following rule (Wooster *et al.*, 2005):

$$R_{f,MIR} = \epsilon_{f,MIR}B(\lambda, T_f) \approx \epsilon_{f,MIR}aT_f^4, \qquad (4.8)$$

where $\epsilon_{f,MIR}$ is the emissivity of the fire in the MIR spectral region, a is a constant (W m^{-4} sr^{-1} μm^{-1} K^{-1}) that is calculated using a best fit relationship and T_f is the brightness temperature of the fire. Wooster *et al.* (2003) calculated values of a as 3.0×10^{-9} for MODIS and 3.3×10^{-9} for HSRS (The BIRD Hot Spot Recognition System). Equation 4.8 exhibits

the same form of power law as Equation 4.4, the Stefan-Boltzmann law. Hence combining Equation 4.4 and Equation 4.8 gives a linear expression for the FRP (Wm^{-2}) independent of emitter temperature (Wooster *et al.*, 2005):

$$FRP_{MIR} = \frac{\sigma \epsilon_f}{a \epsilon_{f,MIR}} R_{f,MIR}, \tag{4.9}$$

where ϵ_f is the emissivity of the fire over the whole spectral range. It is assumed that the fire exhibits the behavior of a grey body, such that $\epsilon_f = \epsilon_{f,MIR}$. As Equation 4.8 is the radiance emitted from the fire, when calculating the FRP of a fire pixel, unless the fire covers the whole pixel (or the vast majority of the pixel), the background radiance still needs to be subtracted from the fire pixel radiance. A key advantage of the single waveband methods over the bi-spectral approach is that the signal from the TIR band, where background and fire signals can be rather similar (Giglio and Kendall, 2003) and where there is more uncertainty in the background signal of the fire pixel, is not considered (Wooster *et al.*, 2003). Also, the MIR radiance method requires data from only one spectral band, making it applicable to e.g. the type of single-wavelength thermal imager used to record the fires conducted as part of the current study.

The times series of FRP of a subset of the fires conducted during the field campaigns conducted here is calculated using the MIR method of Equation 4.9 based on thermal imaging of the fires taken from a helicopter-borne thermal imager (Agema 550 described in Chapter 6). The objective is to allow comparisons of temporal trends in FRP to those of the carbon gas fluxes, since both should vary with fuel consumption rate. The FRP rate relates to fire intensity and hence the rate of combustion of biomass during a fire (Wooster, 2002; Ichoku and Kaufman, 2005; Roberts *et al.*, 2005) while the carbon fluxes are indicative of the biomass consumption rate as approximately 50% of fuel in vegetation fires is made up of carbon. The FRP data was derived from the thermal imagery using the MIR radiance method (Equation 4.9) and the geometric correction approach, which uses a set of spatially fixed 'bonfires' at the corner of each plot to act as ground control points for the geometric correction of the MIR camera imagery.

Chapter 5

Differential Optical Absorption Spectroscopy: Field Campaigns and Data Analysis

Contents

5.1 Introduction

This chapter describes in detail the use of the UV Differential Optical Absorption Spectrometer during the field campaigns in Kruger National Park, South Africa and Alberta, Canada. DOAS spectra were collected by vehicle traverses during several prescribed burns in savanna ecosystems in South Africa and two large managed burns in needle leaf forests in Canada and processed to retrieve vertical column amounts of SO_2 and NO_2 in the same plume. For the case of South Africa, SO_2 and NO_2 flux rates were then derived by combining estimates of the smoke plume parameter estimates (e.g. speed and direction) to the vertical column amounts. Flux rate calculations have been omitted from the results of the Canadian analysis as the extensive size of the smoke plume meant the method was not applicable.

Flux rates from the African fires have been used to estimate of the total carbon flux released by each fire via the synthesis of FTIR derived trace gas emission ratios. These C flux estimates are compared with fuel consumption estimates derived from the fire radiative power FRP time series of the same fires. This will further be discussed in Chapter 6.

An additional field trip was undertaken in Dartmoor, UK, during a heathland controlled burn. DOAS measurements were made, however it proved impossible to retrieve usable NO_2 or SO_2 vertical column amounts from the plume due to the small area and and low fuel loads and thus small size of the smoke plume.

5.2 Field Sites

5.2.1 Site 1: South Africa

The experiments were carried out in Kruger National Park, the largest National Park in South Africa, covering around 18,989 km^2 (Figure 5.1). Since 1954, the park has been subject to an experimental burn plot (EBP) trial, designed to investigate the affects of different

burning frequencies conducted at different times of the year. The trial has changed and developed throughout the years. Currently it compromises of 16 strings of plots each containing four replicates, and covering the four main landscapes found in the park: Lowveld Sour Bushveld of Pretoriuskop, *Combretum collinum/Combretum zeyheri* woodland, *Sclerocarya hirrea/Acacia nigrescens* savanna and *Colophospermum mopane* shrubveld on basalt. There are 12 plots in each replicate, all of which experience different fire regimes to examine the effect of these on landscape ecology (Biggs *et al.*, 2003). The layout of the 'strings' of plots can be seen in Figure 5.2, and this project used one plot in each of the four strings (Numbi, Kambeni, N'waswitshaka and Napi).

The plots at Numbi and Kambeni are both of the category 'Lowveld Sour Bushveld of Pretoriuskop' (Biggs *et al.*, 2003), i.e. they are open tree savannas dominated by certain tree species, for example, Silver Clusterleaf *Terminalia sericea, Bushwillow Combretum collinum*, Paperbark Thorn *Acacia sieberiana, Parinari curatellifolia, Pterocarpus angolensis, Acacia caffra, Ficus thonningii* and *Strychnos madagascariensis*.
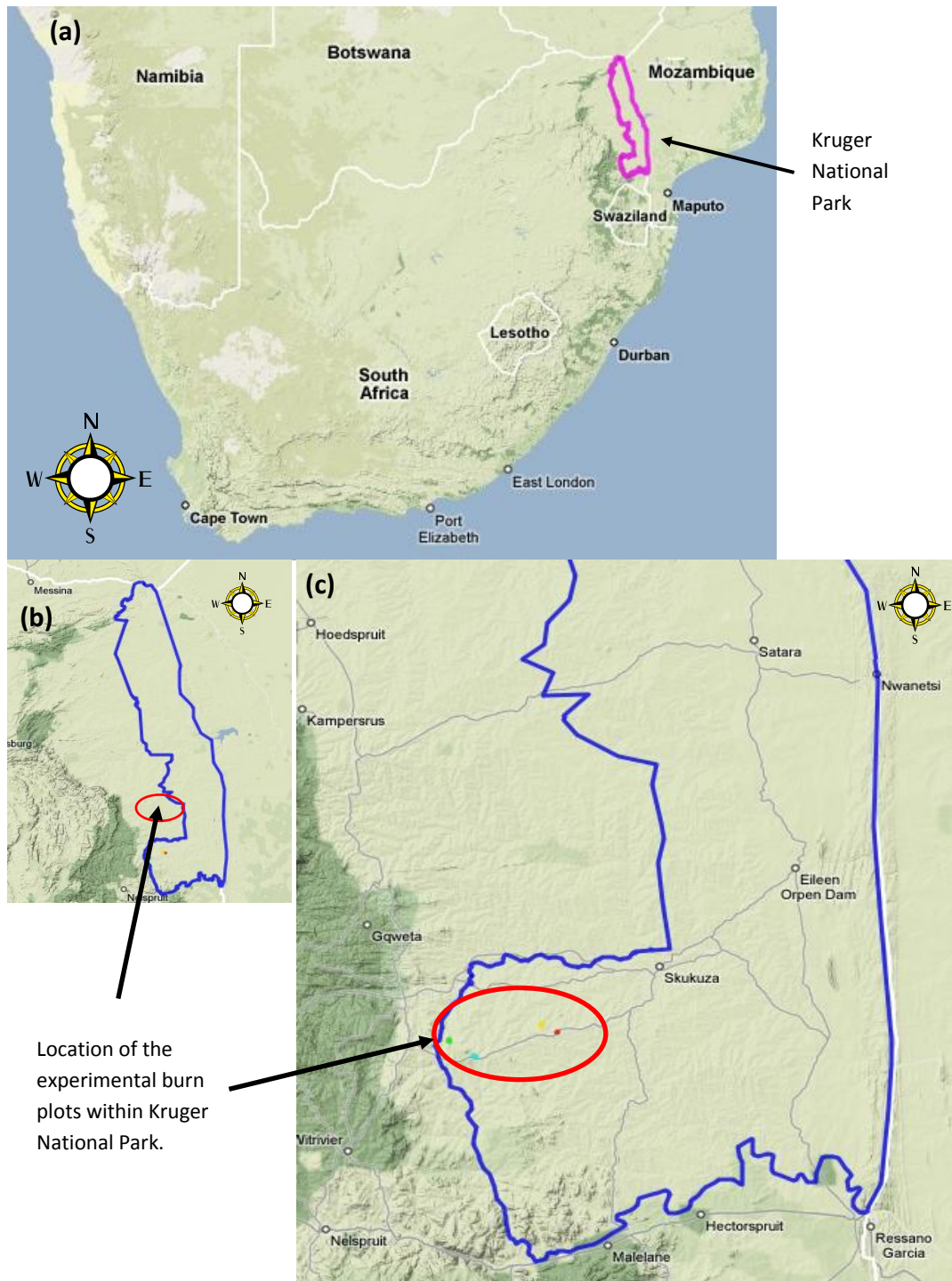
Figure 5.1: *(a): Location of Kruger National Park withing South Africa. (b) and (c): the location of the four experimental burn plots within Kruger National Park (outlined in blue). Location data provided by South Africa National Parks (SanParks) and Kruger National Park Scientific Services GIS Lab.*
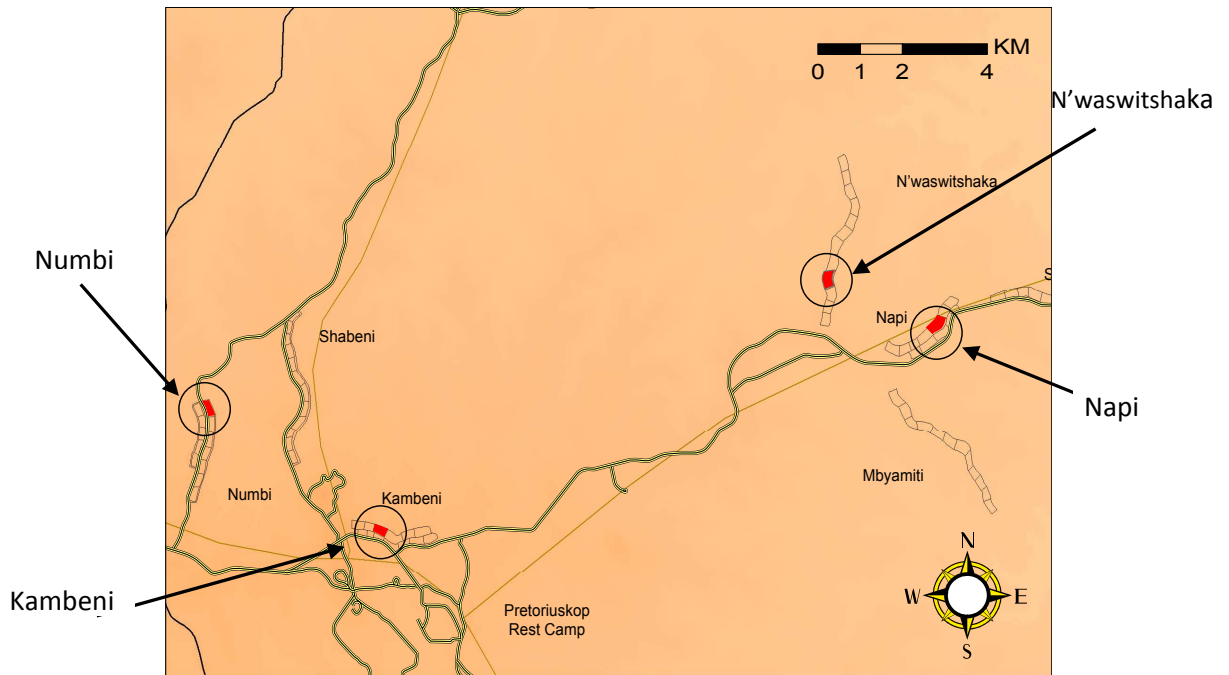
Figure 5.2: *Map showing the location of the four experimental burn plots used in the current experiment. The 'strings' of the plots are shown, and the plots burned for this experiment are coloured red. Map and location data provided by South Africa National Parks (SanParks) and Kruger National Park Scientific Services GIS Lab.*

Shrubs tend to consist of Sickle Bush *Dichrostachys cinerea*, Large Sourplum *Ximenia caffra*, Camel's Foot *Piliostigma thonningii, Antidesma venosum* and *Maytenus heterophylla*. The grass can be dense and tall, consisting of mainly Yellow Thatching Grass *Hyperthelia dissolute*, Wire Grass *Elionurus muticus*, Common Thatchgrass *Hyparrhenia hirta, Setaria sphacelata, Melinis nerviglumis, Cymbopogon excavatus* and *Heteropogon contortus* (Roocroft (a), undated (original source South African National Parks)).

The last plots at N'waswitshaka and Napi are *Combretum collinum/Combretum zeyheri* woodlands (Biggs *et al.*, 2003). Again these are savannas, dominated by the species suggested in the name. The trees range from 1 to 5 m in height and the smaller trees can

be densely packed together, with larger trees generally spread in a less dense manner. The grass and small shrub layer is medium to dense, with typical species including *Pogonarthria squarrosa, Tricholaena monachne, Hyperthelia dissolute, Setaria flabellate, Loudetia simplex, Eragrositis rigidior, Trichoneura grandiglumis, Perotis patens, Brachiaria nigropedata, Digitaria eriantha subpsp. pentzii, Panicum maximum, Aristida congesta subsp. Congesta, A. congesta subsp. Barbicollis, Heteropogon contortus* and *Rhynchelytrum repens* (Roocroft (b), undated (original source South African National Parks)).

The burning studied here took place over two days; the 30th of October and the 3rd of November 2008, with two burns on each day. Figure 5.3 shows pictures from the (pre) burn plots of 30th of October (A) and 3rd of November (B).

Figure 5.3: *Images from the South Africa field campaign plots of Oct 30th (a) and Nov 3rd (b) taken before the fires.*

Figure 5.4 shows several images taken during the experimental burns with in plots (a) and

b))and on the road of the traverse (c).
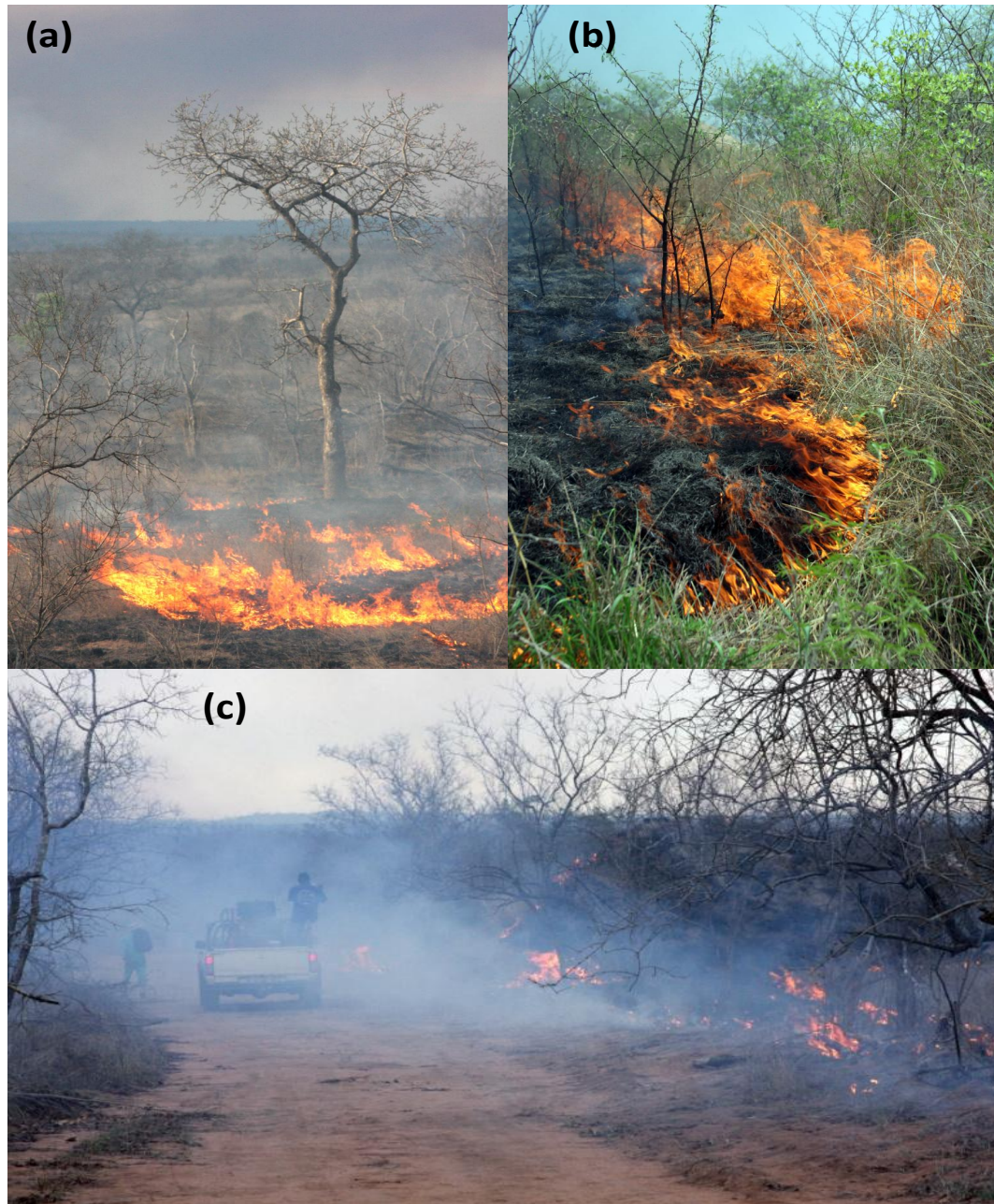
Figure 5.4: *Images taken during fires from the South African field campaign.*

The last two fires were originally planned to occur on October 31st, however rain meant conditions were too wet and consequently they were carried out three days later. Table 5.1 details the timing of each burn.

Table 5.1: *Details of the four plots burnt; length of DOAS measurement traverse, date and time of fire.*

Fire	Plot	Date	Start (UTC/Local)	End (UTC/Local)	Size (m^2)
SF1	N'waswitshaka	30th Oct	10.24 am/12.24 pm	10.58 am/12.58 pm	77385
SF2	Napi	30th Oct	1.46 pm/3.46 pm	2.38 pm/4.38 pm	71465
SF3	Kambeni	3rd Nov	7.44 am/9.44 am	8.11 am/10.11 am	71779
SF4	Numbi	3rd Nov	9.55 am /11.55 am	10.33 am/12.33 pm	87930

The area of each of the 4 plots was measured using a vehicle to drive around the perimeter of each plot and GPS logging waypoints.

5.2.2   Site 2: Canada

The field site in Alberta, Canada is part of the 7900 ha Upper Saskatchewan Unit I prescribed burn experiment, located in the upper area of the North Saskatchewan River on either side of the boundary of Banff National Park, see Figure 5.5. Banff National Park, the oldest national park in Canada, has an area of approximately 6,641 km^2 and is located in the Rocky Mountains. The experimental area is situated between Mount Wilson in the National Park and the Whirlpool point, outside of the park in the province of Alberta. Figure 5.6 shows the location of the experimental area and the burn plots within this area.
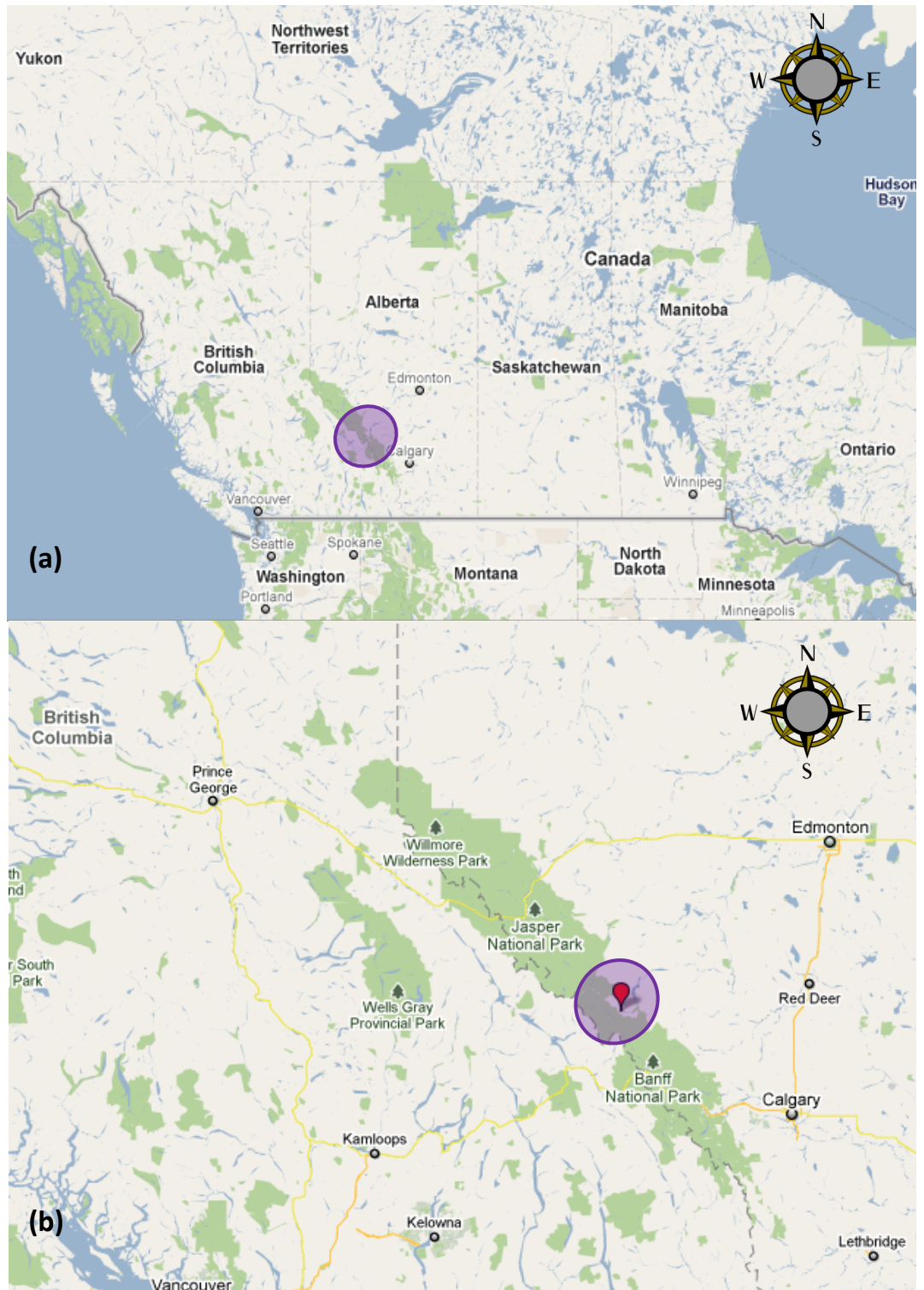
Figure 5.5: *a: The area of the Upper Saskatchewan Unit I prescribed burn experiment within Canada and b: the region of the field site in relation to Banff National Park.*

The project within which the prescribed burns took place had several aims, including the disruption of the spread of the Mountain Pine Beetle. More specifically, the fires aimed to reduce numbers of the lodgepole pine, which has a history of Mountain Pine Beetle infestation. The burning also planned to create a fire break to attempt to reduce damage in future large wildfires. Lastly, the newly burnt area provides an environment that will allow for the continuation of age class groups that has in the past reduced insect and disease levels (Alberta Sustainable Resource Development *et al.*, 2007).

The experimental burn area main tree species are lodge pole pine and white spruce. Other species include engelmann spruce, aspen, whitebark pine, closed shrubs, sub alpine fir and Limber Pine (Alberta Sustainable Resource Development *et al.* (2007).

Figure 5.6: *The location of the burn plots in Banff National Park, from Alberta Sustainable Resource Development et al., 2007*

The majority of the trees in the experimental area date from the years of 1860, 1890 and 1910 when large fires previously occurred. For the past 50 years anthropogenically generated

fires have dominated the area, for example for stand replacement. The most recent wildfire in the area was in 1998, reaching 380 ha and before that in 1974 when 6700 ha was burned.

The UV-DOAS spectrometer was deployed here for two fires on 2nd and 4th July 2009, which shall be denoted as fires CF1 and CF2 respectively. It is difficult to get an estimate of the area burnt for these fire plots as the whole valley was burnt in rapid succession. However, the area is very extensive, and much larger than that of the South African field campaign.

Figure 5.7: *Images taken from the Canadian field campaign. Notice the large size of the plume compared to those of the South African fires in Figure 5.4.*

5.3 UV DOAS Data Collection

For all fires the DOAS UV spectrometer was placed in a small, well insulated cooler (adapted from an in car refrigerator) in order to keep the instrument at an approximately constant temperature, aiming to reduce the instrument noise which is known to be thermally related. The cooler was powered by a connection to the vehicle for the South African field campaign. However due to problems the cooler was not powered during the Canadian field trip, albeit this was not so much of a problem with regards to instrument temperature as ambient temperatures were low compared to those in South Africa (a mean $21^{o}C$ in Canada vs mean of $32^{o}C$ in South Africa). The spectrometer was connected to the laptop and telescope with the a USB cable and optical fiber respectively, as shown in Figure 2.6 Chapter 2. The telescope was positioned on the side of a vehicle, pointing zenith (see Figure 5.8 for South Africa and Figure 2 for Canada), with the optical fiber passing through the car window and into the spectrometer (which was connected to the controlling laptop) inside the vehicle.

Figure 5.8: *Photograph showing how the UV DOAS telescope was positioned on the car during the traverses. Note the optical fiber connecting to the spectrometer inside the car. Photo from the South African field campaign*

During the fire, the vehicle made traverses back and forth along the side of the plot in a direction approximately perpendicular to the wind direction, such that the car traveled repeatedly underneath the smoke plume, with spectra obtained at regular intervals (e.g. every second).

Figure 5.9: *The set up of the DOAS during data collection, with the telescope mounted on the outside of the car and pointing to zenith, connected to the spectrometer inside the car via an optical fibre. The connecting laptop is also kept inside the car. Photos taken during the Canadian field campaign.*

The side of the plot on which the traverses took place was dependent on the wind direction (see Figure 5.10). Multiple traverses were performed during each fire, with each traverse aiming to end with the collection of a clear sky spectrum. However, at times it was not possible to fully exit from underneath the smoke plume, particularly with the Canadian fires, where the plume was very extensive (see Figure 5.7). During each turn, the car traveled back and forth under the plume in this manner until the end of the fire.
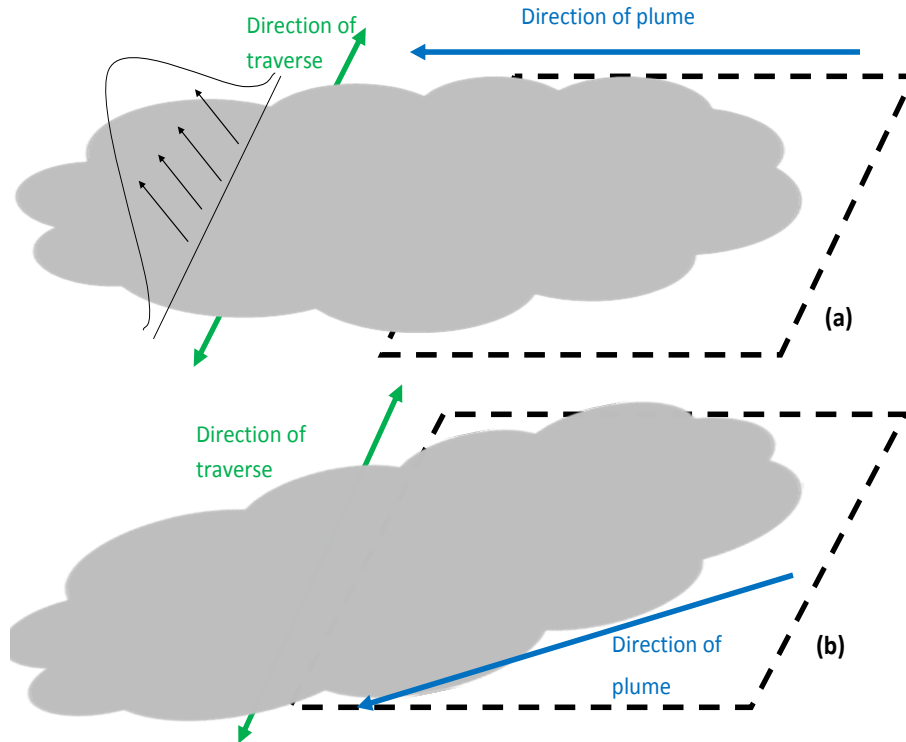
Figure 5.10: *Sketch showing the direction of the DOAS measurement traverse with respect to the predominant wind direction. (a) shows the case where the traverse direction is perpendicular to the plume direction of travel, while (b) illustrates the case where the traverse is not perpendicular to the plume direction of travel. In the upper sketch, vertical pointing arrows indicate potential DOAS zenith views from which total column measurements of the plume can be obtained, and curved line indicates the idealized Gaussian shape of the plume cross section.*

Figure 5.11 shows the vehicle carrying the DOAS during one of the traverses in South Africa.

Figure 5.11: *The vehicle carrying the DOAS during the traverse of a fire of the South African field campaign. This was towards the start of the burn, when little smoke was being generated.*

Figure 5.12 shows the orientation of each of the measurement traverses for the South African fires. The traverses from the Canadian fires are shown in Figure 5.13, with the red line representing that for SF1 and the yellow line representing that for SF2. It can be seen that the traverse for SF1 was much longer than for SF2. This is because the plume was larger in SF1, and hence a longer distance had to be traversed in order to escape the plume and record the clear sky spectra.

Spectra were collected with the UV DOAS instrument continuously throughout the duration of each fire. The integration time of each measurement defines how long the detector is exposed to incoming radiation during the collection of each spectrum; long integration

times result in fewer spectra taken per unit time compared to shorter integration times. The chosen integration times for the fires varied depending on the intensity of sunlight, and were selected to maximize the measurement signal, whilst at the same time avoiding instrument saturation. The integration time had to be changed during some of the fires due to variations in solar radiation intensity caused by changes in cloud cover.
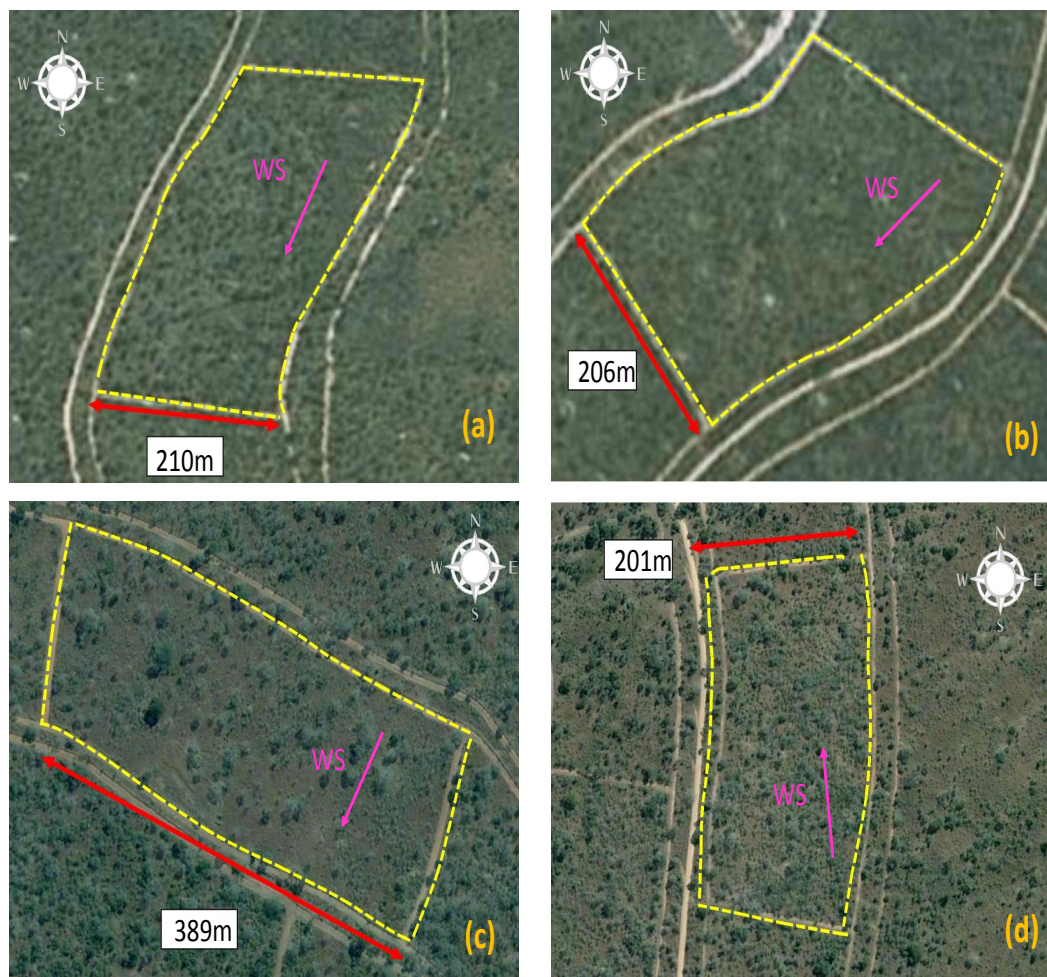
Figure 5.12: *UV DOAS measurement traverses for the four plots of the South African field campaign. a), b), c) and d) are the N'waswitshaka, Napi, Kambeni and Numbi plots respectively. The red line represents the measurement traverse and the yellow the plot outline. Also shown is the wind direction (pink arrow) measured at ground level by anemometer. Background images are taken from Google Earth. The vehicle carrying the UV DOAS spectrometer traveled up and down the measurement traverse repeatedly, until the fire had burned across the entire plot and significant smoke production had ceased.*

Figure 5.13: *The traverses of the DOAS vehicle of fires CF1 (red) and CF2 (yellow), taken from GPS data measured in the vehicle. The traverses of fire CF1 are much larger than those of fire CF2 due to the larger plume of CF1, resulting in more distance to travel to enter clear sky. Background images are taken from Google Earth.*

Spectra from calibration cells containing known amounts of SO_2 and NO_2 were measured before and after each fire, for later use in the retrieval process. There were three different cells of varying amounts available for each gas; 950, 905 and 450 ppmm for SO_2 and 70, 130 and 100 ppmm for NO_2. The calibration cell measurements were conducted before and after each fire, in the absence any smoke plume with the gas cells (shown in Figure 2.6) placed on top of the UV DOAS telescope for around 20 seconds so as to cover its FOV. During these gas cell measurements, 'dark' spectra were also collected where the spectrometer aperture was totally covered so that the instrument dark current could be assessed. These dark cur-

rent spectra are also required during the retrieval process.

During each traverse, a GPS recorded the vehicle location every 5 seconds. For the South African fires, weather stations located alongside and within the plots continuously measured windspeed, atmospheric temperature, pressure and humidity. For fire SF1, the weather station was set up at 1.5 m height, whereas for fire SF2 there were two weather stations at 1.3 and 5.1 m. For fires SF3 and SF4 only a 2 m height weather station data was available. Windspeed and direction from these weather stations are necessary to estimate SO_2 and NO_2 flux rates from the total vertical column amounts retrieved from the measured spectra. There was a weather station set up during fire CF2, but not CF1. The weather station was positioned close to the plot; at 4m height.

5.4   Retrieval of Vertical Column Amounts of SO_2 and NO_2 from Smoke Plumes

As previously mentioned, gas cell spectra were ideally measured using the calibration gas cells before and after each fire. At times it was not possible to record a series of calibration spectra before and after the fire (due, for example to the presence of the smoke plume). The calibration spectra for each gas cell (values of 70, 100 and 130 ppmm for NO_2 and 450, 905 and 950 ppmm for SO_2) were separated into two groups and then the spectra from each group was averaged to produce a single spectrum for each gas cell amount. This separation was carried out so that half of the gas cell spectra could be used to derive the calibration relationship and the other half as a means to test the accuracy of this calibration relationship. Hence, where possible, the calibration relationship was derived from spectra taken before and after the fire to eliminate bias from using just one set of temporal measurements. Also a '0 ppmm' spectrum was derived, which was constructed from a mean series of ambient 'clear sky' spectra that in theory contained no excess SO_2 and NO_2. This 0 ppmm spectrum will from here on in be included in the term 'calibration gas cells'. These averaged calibration spectra (I_μ^c, $\forall$ spectral channels $\mu = 0, ..., 3648$) were then prepossessed as detailed in Chapter 3:

1. Subtract *dark* spectrum (D_μ, $\forall$ channels $\mu = 0, ..., 3648$)

2. Divide by *clear sky* spectrum (S_μ, $\forall$ channels $\mu = 0, ..., 3648$)

3. Apply high and low pass filters, which isolate the gas absorption features and remove the unwanted background absorption structures respectively.

4. Using the Beer-Lambert law, calculate absorbance by taking the negative logarithm.

$$A_\mu = -log\Big(\frac{I_\mu^c - D_\mu}{S_\mu - D_\mu}\Big), \qquad\qquad \forall \mu = 0, ..., 3648. \qquad\qquad (5.1)$$

The preprocessing was carried out using the software package DOASIS 3.2 (Kraus, 2006). The *dark* and *clear sky* spectra are the mean of a series of respective *dark* and *clear sky* spectra taken before/after the relevant fire. A series of different high and low pass filters were tested on the calibration spectra for one fire, such that the combination of filters that produced the most accurate results (i.e. those that were of the closest match to the actual gas cell amounts and exhibited the least noise) were selected for use with the fire spectra themselves. These filters were then used for all the fires as tests show that keeping constant filter values for the series of fires from the same field campaign produced the same level of accuracy. The low pass filter was used for smoothing purposes and the high pass filter for isolating the trace gas absorption features, which is especially important when looking at low amounts of the target gases. The trace gas column amounts for all fires were retrieved using a high pass binomial filter of factor 1000 and low pass filter of 80. For both gases, the peak and trough absorbance features (see Figure 5.14) are identified from the absorbances A_μ. The difference of each absorbance peak and trough pair is taken to get the pseudo absorbance $\bar{A}$:

$$\bar{A} = -log\Big(\frac{I_{\mu_p}^c - D_{\mu_p}}{S_{\mu_p} - D_{\mu_p}}\Big) + log\Big(\frac{I_{\mu_t}^c - D_{\mu_t}}{S_{\mu_t} - D_{\mu_t}}\Big), \qquad\qquad (5.2)$$

for all peak channels $\mu_p \in 0, ..., 3648$ and trough channels $\mu_t \in 0, ..., 3648$. Figure 5.14 shows the absorbances derived from the calibration gas cells that were subsequently used in the retrieval process of both SO_2 and NO_2 from the plume. Note the different wavelength range used for the two gases. This is 298-318 nm for SO_2 and 333-433 nm for NO_2. The exact locations of the peaks and trough (PT) combinations are detailed in Tables 5.2 and 5.3. The same wavelength locations were used for all fires for all field sites.
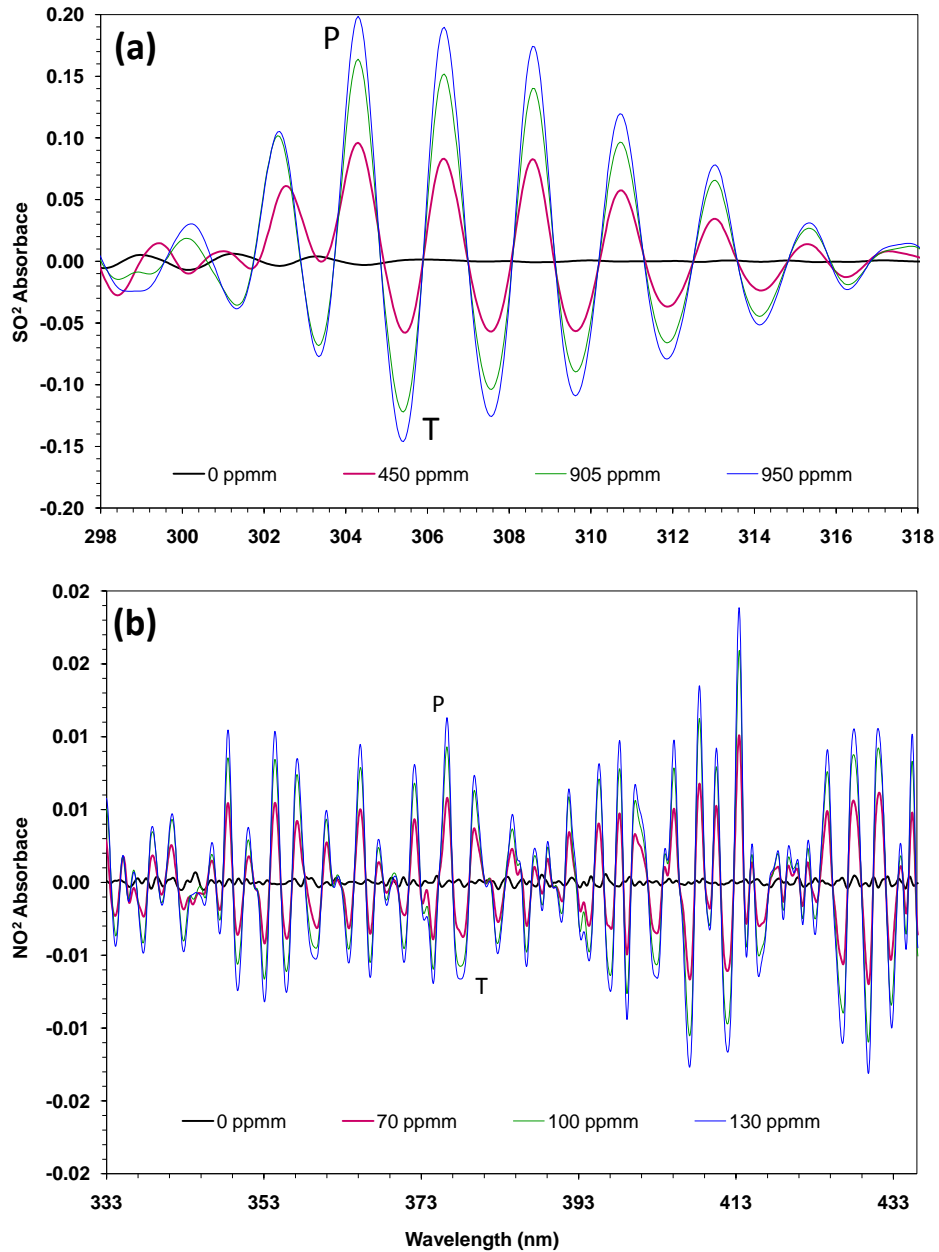
Figure 5.14: *Absorbances of the averaged gas cell calibration spectra for (a) SO$_2$ and (b) NO$_2$ used in the retrieval of the trace gas vertical column amounts for fire SF3. As the gas cell amount of each gas is increased, absorbance features become more prominent. The peak (P) and (T) features are identified in both Figures. These peak and troughs are used for the derivation of the calibration relationship used in the retrieval of the trace gas column amounts.Note the different wavelength range used for the two different gases.*

Table 5.2: *The wavelength locations of the 11 absorbance peak and troughs used for the SO$_2$ retrievals. See Figure 5.14 for the identification of peak and trough features. Also labeled are the PT combinations used for the fire retrievals for each fire. These were selected on the basis of the results of the gas cell calibration retrievals.*

Trough	Channel	Wavelength (nm)	Peak	Channel	Wavelength (nm)
1	319	294.87	1	337	295.80
2 SF1	355	296.72	2	373	297.64
3 SF1	445	301.31	3	468	302.48
4 SF4	485	304.25	4	504	304.30
5 SF3, SF4, CF1	526	305.41	5	546	306.41
6 CF1, CF2	569	307.57	6	590	308.62
7 SF2, SF3, CF1, CF2	610	309.62	7	632	310.71
8 SF2	655	311.86	8	678	313.00
9 SF1	701	314.13	9	725	315.32
10 SF1	745	316.30	10	770	317.53
11	798	318.90	11	815	319.73

Table 5.3: *The wavelength locations of the 29 absorbance peak and troughs used for the NO_2 retrievals of the calibration cells. See Figure 5.14 for the identification of peak and trough features. Also labeled are the PT combinations used for the fire retrievals for each fire. These were selected on the basis of the results of the gas cell calibration retrievals.*

Trough	Channel	Wavelength (nm)	Peak	Channel	Wavelength (nm)
1	1118	334.26	1	1090	332.94
2	1194	337.83	2	1215	338.81
3	1403	347.48	3	1424	348.44
4 SF3	1454	349.80	4	1480	350.98
5	1526	353.05	5	1557	354.44
6	1589	355.87	6	1618	357.16
7	1674	359.65	7	1705	361.01
8	1766	363.68	8	1802	365.25
9	1832	367.5	9	1854	367.50
10 SF1, SF2, SF3	1928	370.68	10	1963	372.18
11	2018	374.51	11	2060	376.28
12	2107	378.25	12	2142	379.71
13	2213	382.65	13	2143	379.75
14	2305	386.42	14	2260	384.58
15 SF3	2416	390.90	15	2436	391.70
16 SF1, SF4, CF2	2568	396.93	16	2534	395.60
17	2623	399.09	17	2601	398.23
18 SF1, SF2, SF4, CF1, CF2	2721	402.88	18	2648	400.06
19 SF1	2831	407.07	19	2781	405.17
20 SF1	2900	409.67	20	2868	408.47
21 SF4, CF1	2958	411.83	21	2920	410.42
22	3025	414.31	22	3001	413.43
23	3076	416.18	23	3045	415.04
24	3222	421.45	24	3240	422.09
25 SF1, SF2, SF4, CF1	3267	423.05	25	3311	424.60
26 SF2	3367	426.56	26	3409	428.02
27	3461	429.82	27	3501	431.19
28	3546	432.72	28	3582	433.93
29	3601	434.57	29	3626	435.41

A relationship is derived between each of these pseudo absorbances and their corresponding gas cell column amount (Elias *et al.*, 2006) via a linear equation of the form $y = mx + c$. The linear best fit is derived using a least squares linear fitting algorithm Reed (1989). The algorithm makes use of York's solution (York, 1966) to solve the linear least squares problem of fitting a straight line function to a series of points, taking into account uncertainties in both x and y. The returned linear function includes uncertainties in both the derived slope and intercept. For each pseudo absorbance $\bar{A}_i$, ($i = 1, ..., 11$ for SO_2 and $i = 1, ..., 29$ for NO_2) derived for each gas cell column amount:

$$\mathbf{y}_i = (M \pm m)\mathbf{x}_i + (C \pm c), \tag{5.3}$$

where M and C are the derived slope and intercept, m and c their respective uncertainties and

$$\mathbf{y}_i = \begin{pmatrix} y_i^1 \\ y_i^2 \\ y_i^3 \\ y_i^4 \end{pmatrix} \tag{5.4}$$

is the vector of column amounts at PT combination i. $(y_i^1, y_i^2, y_i^3, y_i^4)$ equals (0,70,100,130 ppmm) for NO_2 and (0,450,905,950 ppmm) for SO_2

$$\mathbf{x}_i = \begin{pmatrix} \bar{A}_i^1 \\ \bar{A}_i^2 \\ \bar{A}_i^3 \\ \bar{A}_i^4 \end{pmatrix} \tag{5.5}$$

is the vector of the pseudo absorbances $\bar{A}_i^j$ at PT combination i for each of the 4 gas cell amounts ($j = 1, .., 4$). As stated above, the linear least squares algorithm takes into account uncertainties in both x and y, i.e. in gas cell column amounts (ppmm) and in the measured spectra. The uncertainties in the former are taken as 5%, as quoted by the cell manufacturers. For the *background* spectrum of value 0 ppmm, the error is presumed to be negligible as the background level is not assumed to vary. This value is added to the gas cell errors as the

minimal background error is present when the gas cells are measured. The error in the x axis is taken as the standard deviation of the absorbances used to calculate the average gas cell spectra for use in the derivation of the linear calibration relationship. Figure 5.15 shows examples of the lines of best fit derived for fire SF3.
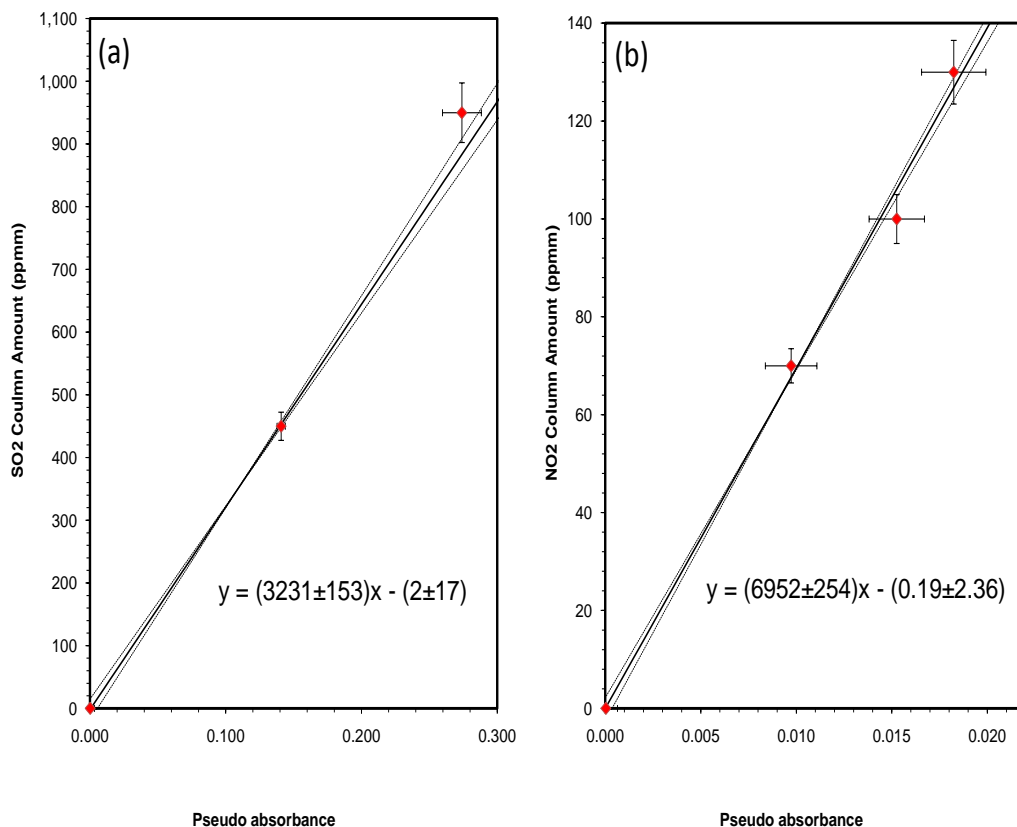
Figure 5.15: *Relationship between the column amount of SO_2 and NO_2 in the calibration gas cell, and the measured pseudo-absorbance. (a) shows results for SO_2 PT combination 4 (PT4) defined in Table 5.2 and (b) for NO_2 PT3 defined in Table 5.3. The data was collected shortly before the fire SF3 (Table 5.1).The linear best fit and uncertainty is also shown. This linear relationship was then used with data collected during the fire to retrieve the column amounts of these gases from the spectra measured during the vehicle traverses.*

The linear calibration equations derived using the calibration gas cells are then applied to the calibration spectra, preprocessed in the usual way, to retrieve the gas cell column amounts in ppmm. The PT combinations that give the closest column amounts to the actual gas cell column amounts and which do not exhibit much retrieval noise are selected for application

to the fire spectra retrievals. Tables 5.2 and 5.3 show the locations of the PT combinations used for each fire. It is not that case that the same PT combinations are used for each fire, reasons for this are discussed in Chapter 7. Subsequently, the fire spectra collected during each traverse were preprocessed according to Steps $1 - 4$ above and the target gas (SO_2 and NO_2) column amounts (ppmm) were calculated for each spectrum based on the derived linear calibration equation and the measured pseudo absorbance at the chosen peak and trough channels μ_p and μ_t. An example of the column amounts retrieved from the calibration cell spectra is shown in Figure 5.16.
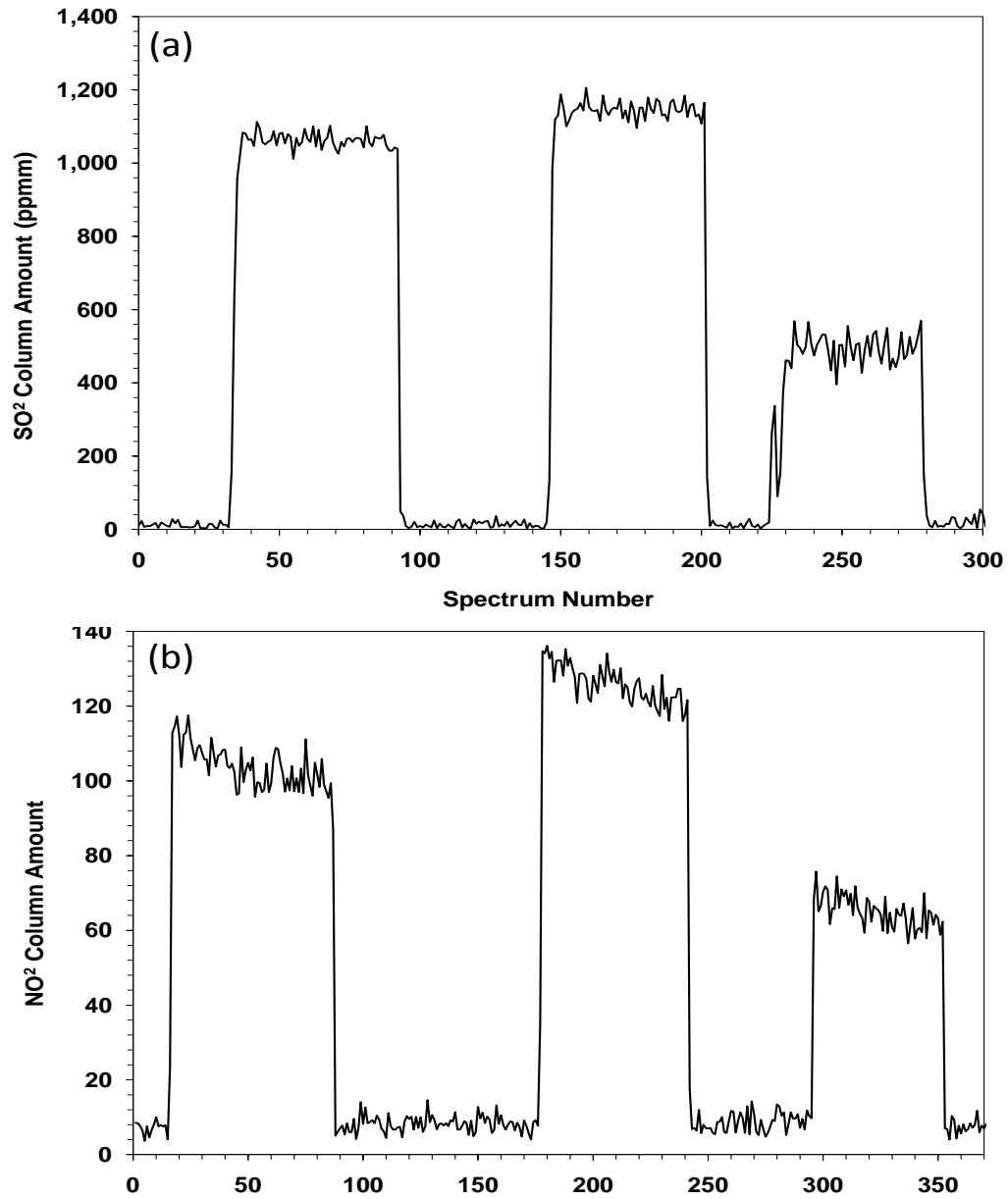
Figure 5.16: *The mean retrieved vertical column amounts based on the spectra of the calibration gas cells of (a) SO$_2$ and (b) NO$_2$ from the 'best' PT combinations from Tables 5.2 and 5.3 respectively, i.e. those that produced column amounts closest to the actual value of the gas cells and those that were the least noisy. These PT combinations were then used for the retrievals, taken during the vehicle traverses.*

Spectra that exhibited saturation (due to high light intensities) in the channels used in the retrieval process were removed from the analysis, as were those that showed excessive noise.

Such spectra made up only $\approx 5\%$ of the total spectra. Results were then averaged to one measurement per second (unless the integration time was such that the frequency of measurement was greater than one second). Further averaging depended on the characteristics individual fire and how variable the retrieval were. Errors for the retrieved column amounts at each of the chosen PT combinations were calculated (see Section 5.4.1 for more details on this). These errors were used to calculate the final returned column amount K for each spectrum as follows (Taylor, 1997):

$$K = \sum_i \frac{k_i}{e_i^2} \times \frac{1}{\sum_i \frac{1}{e_i^2}}, \tag{5.6}$$

for all chosen n PT combinations $i = 1, .., n$. k_i is the returned column amount for PT combination i and e_i is its error. The method hence takes into account the errors of each retrieval when calculating the weighted average. The greater the error, the less weight the column amount from the individual PT combination has in the averaged column amount.

The measurement integration times for fire SF1 alternated between 100 and 200 milliseconds, resulting in the measurement of 5 to 10 spectra per second. The spectra were then averaged (10 each time), leading to a spectra being measured every 1 to 2 seconds. No further averaging was carried out due to low retrieved column amounts. For fire SF2, the integration time was 1000 to 2000 milliseconds, hence spectra were recorded every 1 to 2 seconds. Further averaging of pairs of spectra were carried out; as although the results for this fire also exhibited low column amounts, they were particularly noisy and hence needed additional smoothing. There was still a substantial level of noise, however no more averaging was taken as this would mean a measurement at a frequency longer than 4 seconds, smoothing the data too much. Spectra were collected with an integration time ranging between 200 and 250 milliseconds for fire SF3, such that 4-5 spectra were collected per second. A single integration time of 100 milliseconds was used for fire SF4. Retrieved results for fires SF3 and SF4 were averaged to 1 measurement per second. Figure 5.17 gives a general outline of the steps to be taken for the retrieval of the SO_2 and NO_2 vertical column amounts.

STAGE 1

1) Raw calibration gas cell spectra collected

2) Corrected for non-linearity

3) Subtract 'dark' spectrum

4) Divided by 'clear sky minus dark' spectrum

5) Apply high and low pass filters

6) Take the negative logarithm to calculate absorbance

7) Identify the PT combinations shown in Tables 1.2 and 1.3

8) Calculate psuedo absorbance (peak absorbance minus trough absorbance)

9) Derive linear calibration Equation 1.3 that equates psuedo absorbance with gas cell amount.

STAGE 2

1) Raw fire spectra collected

2) Corrected for non-linearity

3) Subtract 'dark' spectrum

4) Divided by 'clear sky minus dark' spectrum

5) Apply high and low pass filters

6) Take the negative logarithm to calculate absorbance

7) Identify the PT combinations chosen to retrieve vertical column amounts using STAGE 1

8) Calculate psuedo absorbance (peak absorbance minus trough absorbance)

9) Apply the calibration Equation 1.3 dervied from STAGE 1 to return the trace gas vertical column amounts

10) Filter out bad poor quality results (e.g. due to saturation of intrument) and carry out averaging

11) Work out errors and hence total vertical column amount via Equation 1.6

Figure 5.17: *An outline of the process used for retrieval of SO_2 and NO_2 vertical column amounts of the UV-DOAS spectra. (a) details the first stage of the retrieval process, in which a calibration equation is derived using spectra measured from the NO_2 and SO_2 calibration gas cells. The calibration equation is then used in the second stage of the retrieval process (b) to return the trace gas column amounts from the spectra collected during the fires.*

5.4.1 Vertical Column Amount Errors

The formulation of the errors for the retrieved vertical column amounts for NO_2 and SO_2 were based on the the simple formulas given below, and commonly used in error propagation:

$$y = ax, \qquad \Delta y = |a| \, \Delta x$$

$$y = \frac{a}{x}, \qquad \Delta y = \left| \frac{a}{x^2} \right| \Delta x$$

$$y = a \exp(bx), \qquad \Delta y = |bx| \, \Delta x$$

$$y = a \ln(bx), \qquad \Delta y = \left| \frac{a}{x} \right| \Delta x$$

$$y = x \pm u, \qquad \Delta y^2 = \Delta x^2 + \Delta u^2$$

$$y = xu, y = \frac{x}{u} \qquad \left(\frac{\Delta y}{y} \right)^2 = \left(\frac{\Delta x}{x} \right)^2 + \left(\frac{\Delta u}{u} \right)^2$$

where y is a function of variables x and u, Δy, Δx, Δu are the respective errors and a and b are constants. Take k as the linear relationship representing the derived column amounts for each PT combination i at peak channel p_i and trough channel t_i

$$k_i = M_i \bar{A}_i + C_i = M_i \left(-log \left(\frac{I^c_{\mu_{p_i}} - D_{\mu_{p_i}}}{S_{\mu_{p_i}} - D_{\mu_{p_i}}} \right) + log \left(\frac{I^c_{\mu_{t_i}} - D_{\mu_{t_i}}}{S_{\mu_{t_i}} - D_{\mu_{t_i}}} \right) \right) + C_i. \qquad (5.7)$$

Using the relationships above, the error equation formulated for y_i for PT combination i is given as:

$$e_i = \sqrt{ \left(\frac{m_i}{M_i}^2 + \frac{g_i^2}{\bar{A}_i - \frac{C_i}{M_i}} \right) * (\bar{A}_i - C_i)^2 + c_i^2 } \qquad (5.8)$$

for g_i

$$g =_i \left(\frac{\sigma(D)_{p_i}}{I_{\mu_{p_i}} - D_{\mu_{p_i}}} \right)^2 + \left(\frac{\sigma(D)_{p_i}^{err}}{I_{\mu_{p_i}} - D_{\mu_{p_i}}} \right)^2 + \frac{\sigma(S)_i^2 + \sigma(D)_{p_i}^2}{(S_{\mu_{p_i}} - D_{\mu_{p_i}})^2} + \qquad (5.9)$$
$$\left(\frac{\sigma(D)_{t_i}}{I_{\mu_{t_i}} - D_{\mu_{t_i}}} \right)^2 + \left(\frac{\sigma(D)_{t_i}^{err}}{I_{\mu_{t_i}} - D_{\mu_{t_i}}} \right)^2 + \frac{\sigma(S)_{t_i}^2 + \sigma(D)_{t_i}^2}{(S_{\mu_{t_i}} - D_{\mu_{t_i}})^2}.$$

Here $\sigma(D)_{p_i}^{err}$ is the standard error of the dark spectra at peak p_i used to calculate the mean dark spectrum for the retrieval of the fire spectra. This is taken as the error for this variable at p_i as it is an estimate of how the averaged value varies from the mean. Similarly $\sigma(S)_{p_i}$

is taken as the error for the averaged sky spectrum $S_{\mu_{t_i}}$ at p_i. Here the standard deviation is used, since the sky spectra are expected to vary between each measurement and hence a measure of dispersion between individual measurements is needed. $\sigma(D)_{p_i}$, the standard deviation of the dark spectra at p_i, is taken as an estimate for the error of the intensity spectrum $I_{\mu_{p_i}}$ as it provides an indication of the variability of the measurement noise. The same applies to the trough values t_i.

5.5   Flux Calculation

The vertical column amounts of NO_2 and SO_2, calculated from the in-plume measurements of the fires as described above, were used to retrieve the corresponding trace gas fluxes. Chapter 4 explains how the fluxes are calculated. Recall Equation 4.3 (from Chapter 4):

$$F_i = \frac{W_x}{A} \times \sum_j (CA_j \times D_j) \times P_{s_i} \times 100^2, \tag{5.10}$$

where F_i is the flux rate (g.s^{-1}) for traverse i, CA_j (molec.cm^{-2}) and D_j (m) are the column amounts and distance for measurement j and P_{s_i} (m.s^{-1}) is the estimated plume speed for traverse i. W_x (g.mol^{-1}) and A are the molecular weight of the target gas x and Avogadro's Constant ($6.02214199 \times 10^{23}$) respectively, used to convert molecules to grams. The molecular weight for NO_2 is 46.01 g.mol^{-1} and 64.07 g.mol^{-1} for SO_2. The summation here represents the trapezoidal rule. The calculations of the variables needed for flux estimations are detailed below. Note that the flux calculations have only been carried out for the South Africa field campaign as for the Campaign, since for the Canadian fires the plume extended over too wide an area and sampling was not able to be performed over the full duration of the fire. For the Canadian campaign therefore, only total column amounts are derived.

5.5.1   Column Amounts

The column amounts of SO_2 and NO_2 in ppmm calculated as in Section 5.4 were converted to molec.cm^{-2} using Horrocks (2001):

$$CA = \frac{k \times (7.243 \times 10^{14} \times P_p)}{P_t} \tag{5.11}$$

where P_t is gas temperature (K) , CA is the column amount in molec.cm^{-2}, k is the column amount in ppm m and P_p is pressure (HPa). The atmospheric temperature and pressure and were obtained from the weather station measurements.

5.5.2 Distance between Measurements

During the traverses, a GPS was placed in the vehicle continuously logging location waypoints (latitude and longitude) every 5 seconds. The distance between these measurements, D_i (m), was calculated using the spherical law of cosines formula (Gellert *et al.*, 1977):

$$D(j) = 1000 \times \arccos\left[\sin(\frac{lat_j\pi}{180}) \times \sin(\frac{lat_{j+1}\pi}{180}) + \sin(\frac{lat_j\pi}{180}) \times \cos(\frac{lat_{j+1}\pi}{180})\right. \tag{5.12}$$

$$\left. \times \cos\left((\frac{long_{j+1}\pi}{180}) - (\frac{long_j\pi}{180})\right)\right] \times 6371. \tag{5.13}$$

lat_j and lat_{j+1} are consecutive latitude measurements and similarly $long_i$ and $long_{i+1}$ are consecutive latitude measurements. 6371 (km) is the average radius of the Earth. The returned distances were interpolated to the time of the DOAS measurements. Note Equation 5.13 has been checked with distances on Google Earth.

5.5.3 Plume Velocity

Previous work on calculating flux rates, in particular from volcanic plumes, have reported that the biggest source of errors are from the unknown plume velocity (e.g. Mori *et al.*, 2006). Many studies have estimated plume speed from the wind speed at ground level. A key limitation here is that the plume could be tens to hundreds of meters higher in elevation compared to the weather station, potentially making the latter data unrepresentative. Rodriguez *et al.* (2008) obtained wind speed estimates from both a weather station at ground level and from a helicopter at plume height (1-3 km) for the retrieval of SO$_2$ flux rates from an active volcano (Soufrire Hills volcano, Montserrat). The wind speed at ground level was found to be $\approx$ 60 % to that at plume height. Recent studies have used the analysis of time series images to track the plume against known length scales (Weibring *et al.*, 1998; Mori *et al.*, 2006), or used data from local and national weather centers (McGonigle *et al.*, 2003;

Grutter *et al.*, 2008) or estimated plume speed from balloons or radiosondes (Rivera *et al.*, 2009). Implementing two mini DOAS instruments in DUAL mode allows for the estimation of plume speed. This method involves positioning two instruments underneath the plume with their viewing axis parallel. A correlation algorithm is applied to the retrieved column amounts from both spectrometers to determine how long it takes for plume features to get from one FOV to the next. This time lag is combined with the distance between the two instruments in order to work out plume velocity (Williams-Jones *et al.*, 2006; Boicu *et al.*, 2010). The more spectrometers used, the more accurate the plume velocity estimates (Williams-Jones *et al.*, 2006). McGonigle *et al.* (2005) used three spectrometers. The use of the mini scanning DUAL DOAS system to work out plume speed is not efficient when the plumes are of low elevation however, unless a wide lens is used to increase the FOV, for example a fish eye lens (Nadeau and Williams-Jones, 2008). Recently, UV imaging has been applied to retrieve SO_2 column amounts from volcanic plumes (Mori and Burton *et al.*, 2006; Bluth *et al.*, 2007) and in that situation wind speed can be calculated via the cross correlation of column amounts retrieved from two different pixels against time. Wind direction estimates have been made with the use of two mini DOAS systems. The direction is calculated by locating the maximum of column amount measurements (McGonigle *et al.*, 2003; Rivera *et al.*, 2010). Weibring *et al.* (1998) used LiDAR scanning of volcanic plumes to calculate plume direction.

Throughout the field experiments conducted here, wind speed and direction at ground level was continuously logged using a weather station positioned neighboring each fire plot. In order to estimate wind speed plume height, the log law wind profile (a theoretical relationship between wind speed and elevation (Oke, 1987), was used. The log law wind profile is given as follows (Oke, 1987):

$$P_s = P_{s_0}.(1 + \frac{LN(\frac{h-d}{h_0})}{LN(\frac{h_0}{z_0})}). \tag{5.14}$$

P_s is the estimated wind speed (m.s^{-1}) at elevation h (m), P_{s_0} (m.s^{-1}) is the speed at the weather station at height h_0 (m), d is the zero plane displacement, and z_0 is the surface

roughness parameter (Hicks, 1975; Garret, 1992):

$$d = 0.75h_t \tag{5.15}$$

,

$$z_0 = 0.08h_t, \tag{5.16}$$

where h_t (m) is the mean estimated tree height. d (m) is used to take into account obstacles and their effect on wind speed at ground level, whist z_0 is used to take into account the roughness of the surface (Oke, 1987). The log law is commonly used as a basis to calculate vertical wind profiles for different types of terrain (e.g. Verhoef *et al.*, 1997; Yue *et al.*, 2007)

As applied here, the log law uses tree height (measured in the field) to calculate the zero plane displacement and surface roughness parameters, which are taken as proportions of the tree height. Figure 5.18 presents the relationship between vertical height and wind speed calculated using the log law, from a fire carried out during the Australian field campaign, denoted AF3 (see Chapter 7 for more details of this fire). Plume height was estimated using the video footage captured from the helicopter hovering above the fire. Although this only provides a coarse estimate of the plume height, from Figure 5.18 it can be inferred that above a given height the change in wind speed varies at a diminishing rate with further height increases. Hence, although the plume height is not exactly known, a rough estimate is more likely to give a wind speed closer to the actual value than the ground measurements available from the weather station.
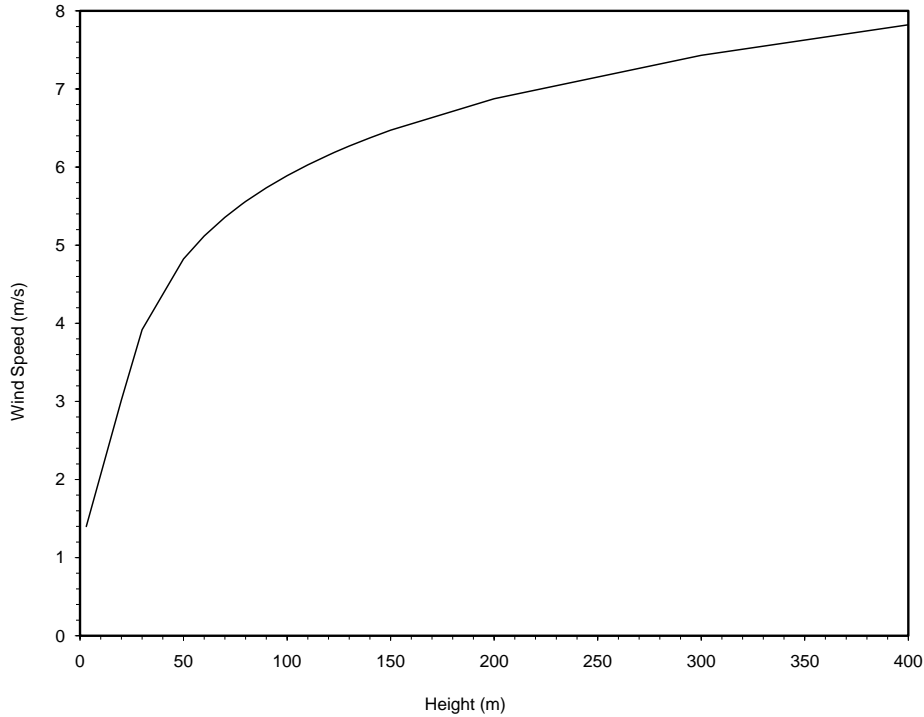
Figure 5.18: *Log law wind profile giving a relationship between elevation (m) and wind speed (m.s^{-1}). The wind speed and the local surface roughness characteristics the at target height is estimated using Equation 5.14 based on the wind speed at ground level. The relationship shows that as height increases, the wind speed increases at a diminishing rate. Data taken from a fire from the Australian field campaign, fire AF3.*

As already stated, the height of the plume was estimated using stills captured from video footage recorded via a helicopter hovering above the fires. The method is approximate, but never-the-less provides a rough estimate of plume height needed for the log law. Firstly, the width of the main road surrounding the plot in question was estimated (e.g. using Google Earth and/or local measurements). The road is then located on the video image and manual interpretation is used to determine the number of pixels spanning the road width. Using this and the estimated road width, the image pixel size is calculated and used to roughly determine plume height. This is done by depicting the shape of the plume as a triangle and using Pythagoras theorem to work out the number of pixels that span the length of plume height. The number of pixels is then converted to plume height using the estimate of the pixel size. Figure 5.19 shows an example of the methods implementation.
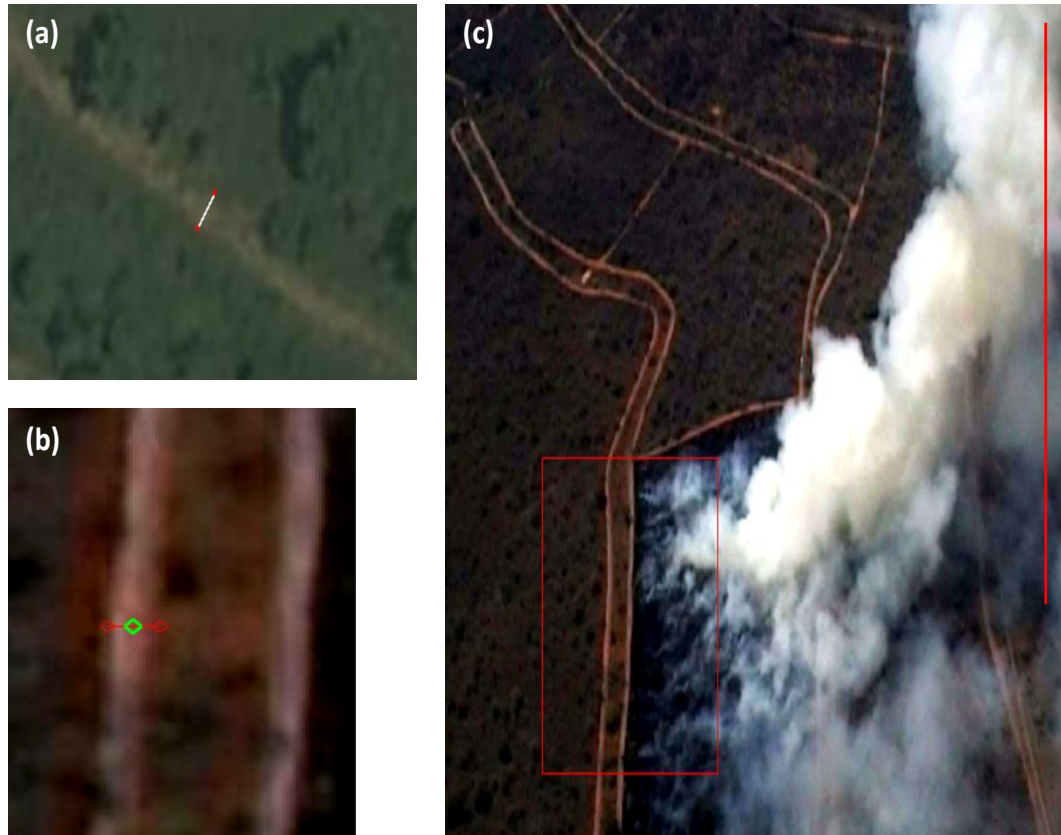
Figure 5.19: *Example of how plume height was estimated for fire SF3 of the South African field campaign. (a) depicts the road used for the traverse measurements as seen in Google Earth. This was used to estimate road width (m). (b) shows the same road identified in a still image taken from the aerial video record of this fire. Using the distance measurement tool in an image analysis system [the ENVI software of ITT] the width of the road (in pixels) is calculated. Combined with results from (a), this returns an estimate of pixel size, in meters. In (c) the number of pixels spanning the plume is determined and hence the approximate plume height. This is carried out using basic trigonometry by considering the shape of the plume as that of a triangle and applying Pythagoras theorem to return the number of pixels of the height of the plume.*

Using the helicopter recorded video footage, an attempt was also made to use the shadow of the smoke plume to estimate plume height. However it proved to be too difficult to track the plume shadow from the still images of the video at the clarity that was needed to carry out any feasible calculations.

Plume Direction

An anemometer was used to record wind direction. For fires SF3 and SF4 where there is video footage of the fire taken from the helicopter, the plume direction seen in the images agrees with this ground-level wind direction. Figure 5.12 shows the wind direction recorded for each fire plot. The wind direction was approximately perpendicular to the DOAS traverse direction in each case, and hence corrections for a non perpendicular traverse direction do not need to be made to the flux rate calculations.

The end points of each of the traverses, where the vehicle traveled outside of the plume, are not included in the flux calculations. Measurements the GPS location way points and notes taken during each fire were used to determine the endpoints of each traverse. In some cases, the beginning and end traverses have been omitted from the flux calculation due to low column amounts of the target gases of these fires. Table5.4 presents the values given to each of the variables needed for the calculation of the trace gas fluxes.

Table 5.4: *The parameters used to calculate the flux rates of SO_2 and NO_2 for all fires SF1-SF4 in the South African field campaign. Temperature and pressure taken directly from measurements at ground level. Plume height estimated from video footage recorded in a helicopter of the fires. The plume speed averaged over all the traverses was derived from plume height estimates and wind speed measurements at ground level. The average tree heights were calculated from field measurements. The surface roughness parameter, z_0 and the zero plane displacement d were estimated average tree heights (Hicks, 1975; Garret, 1992)*

Fire	Temp (k)	Pressure (hPa)	Plume Height (m)	Avg Plume Speed A (m.s^{-1})	Tree Height (m)	Z_0	d
SF1	305	939	100	12	4	0.32	4
SF2	304	958	100	4	4	0.32	4
SF3	302	939	300	10	5	0.4	3.75
SF4	307	944	300	14	6	0.48	4.5

5.5.4 Flux Errors

The flux rate error formula was derived by applying the error propagation formulas listed in Section 5.4.1 to the structure of Equation 5.10. The flux error, ΔF_i for traverse i is given

as follows:

$$\Delta F_i = \sqrt{\left[\left(\left(\frac{\Delta P_{s0_i}}{P_{s0_i}}\right)^2 + \left(\frac{\Delta z_0}{\ln(h_0/z_0)z_0}\right)^2 + \left(\frac{h_0 \Delta h_p}{[1 + \ln\frac{h_p-d}{h_0}](h_p - d)h_0}\right)^2\right) + l\right] \times F_i^2} \quad (5.17)$$

where

$$l = \left(\frac{\sum_j [(\frac{e}{CA_j})^2 + (\frac{\Delta d}{d})^2 + (\frac{\Delta P_t}{P_t})^2 + (\frac{\Delta P_p}{P_p})^2] CA_j.d}{\sum_j CA_j.D_j}\right)^2 \quad (5.18)$$

ΔP_{s0_i} is the error in the windspeed measured by the weather station, taken as 0.3 m.s^{-1} (given by the manufacturer). The error in plume temperature, P_t, is taken as $\frac{0.65h_p}{100}$, the normal lapse rate, i.e. the average decrease in temperature for an increase in 100 m of altitude. The error in plume pressure, P_p, is estimated using the barometric formula, which gives a relationship between pressure and altitude.

$$P = P_b.\exp\left[M.g_0 \frac{H - H_b}{r.T_b}\right], \quad (5.19)$$

where P is the pressure (HPa) at height H (m) above sea level, P_b and T_b are pressure (HPa) and temperature (K) at reference height H_b (m). M is the molar mass of the atmosphere (0.0289644 kg.mol^{-1}), g_0 is the gravitational acceleration (9.80665 m.s^{-2}) and r is the universal gas constant for air (8.31432 N.m.(mol.K)$^{-1}$). The error in plume pressure is taken as the difference between pressure at ground level (measured by the weather station) and at the plume height, derived using Equation 5.19. Δd is the error of the GPS estimated distance measurements (m). This is derived as the estimation of the average deviation of the DOAS vehicle traverse waypoints from the true points road, measured using Google Earth (see Figure 5.20).
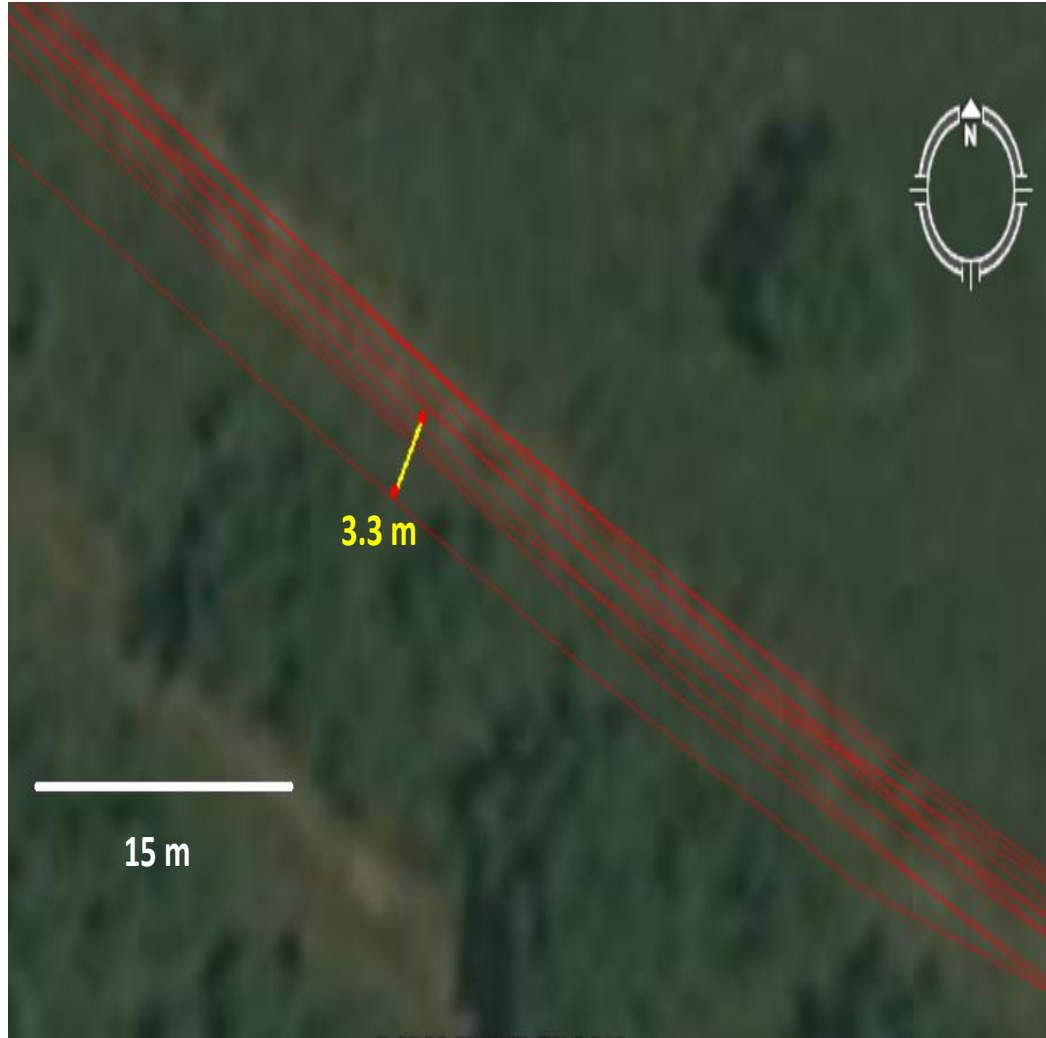
Figure 5.20: *The GPS error, Δd is estimate by taking the average of the deviation of the GPS traverse waypoints (red) from the road as seen on Google Earth. A GPS was located in the vehicle throughout the duration of the DOAS traverses for each of the fires, constantly logging the location of the vehicle every 5 seconds.*

The error of the zero plane displacement, Δz_0, is given as 0.02, taken as the the variation of z_0 (0.08) from the possible range (0.06 to 0.1) taken from Arya (2001) for forests and grasslands. Δh_p is the error given to the estimated plume speed. This is calculated by taking the standard deviation of the plume speed calculated at the estimated minimum, mean and maximum plume heights using the log law. The difference between the min/max and the mean (used for the plume speed estimations) plume hieght is up to 100 m in some of the fires. This big interval is used to take into account the error in the estimate of plume

height. Note that the error for the zero plane displacement (d) is not included as it is negligible compared to the error of the plume height.

5.6   Field Campaign Results

5.6.1   Vertical Column Amounts of SO$_2$ and NO$_2$

South Africa

Figure 5.21 shows the SO$_2$ gas cell calibration cell absorbance spectra for all 4 South African. It can be seen that for fire SF2, for each individual gas cell, the absorption features are weaker compared to the same gas cells measured at other fires. This is not the case for NO$_2$. Also note the slight wavelength shift in peaks between the first two and last two fires, identified as being due to the different instruments used. The weaker absorbance features of fire SF2 are explained by the noise level of the calibration spectra.
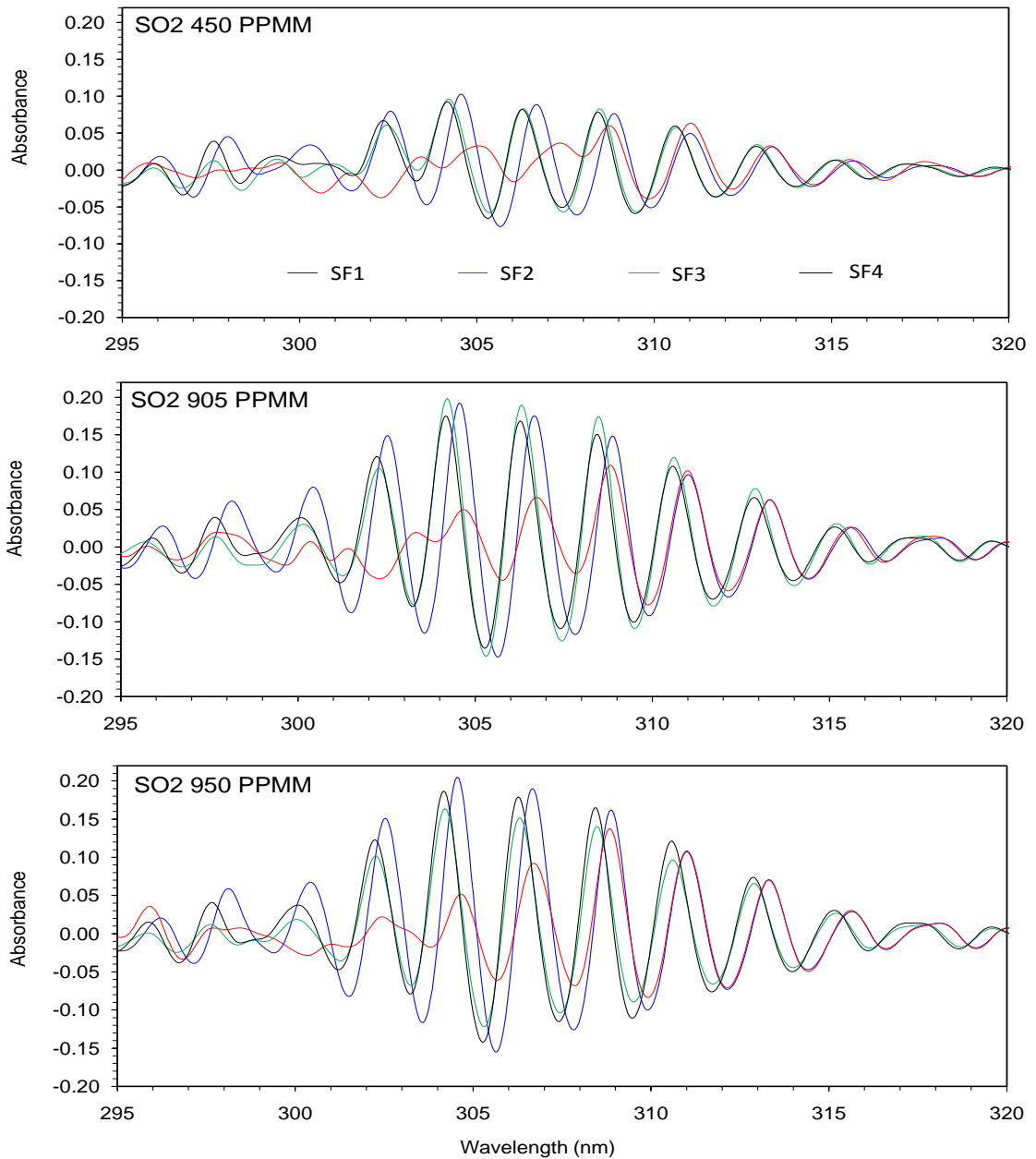
Figure 5.21: *The SO$_2$ calibration cell absorbance spectra calculated using Equation 5.1 for all fires from the South African field campaign for amounts 450 ppmm (top), 905 ppmm (middle) and 950 (bottom). It can be seen that for fire SF2 (Red), the absorbance features, present as peak and troughs, appear not as strong as for the other fires. This can be attributed to the high noise level of the calibration cell spectra, shown in Figure 5.22. Note also the wavelength shift that is attributed to the use of different instruments.*

Figure 5.22 shows an example of a 905 ppmm gas cell calibration spectrum from fires SF1

and SF2. Two raw spectra are shown in Figure 5.22 (a) and it can be seen that the spectrum from fire SF2 exhibits a much greater level of noise than does that of fire SF1. This noise is reduced in Figure 5.22 (b) when the relevant dark spectrum is subtracted from both spectra. However, when the spectra are subsequently divided by the corresponding sky spectra, as shown in Figure 5.22 (c), fire SF2 still exhibits high noise. In particular, the absorption features around wavelengths 300-305 nm are unclear because of the high noise levels at this region of lower intensity signal. PT combinations from these wavelengths were not therefore used in the SO_2 retrieval performed for fire SF2. All spectra exhibited the same high noise level throughout the fire SF2 measurements. Fluctuations in temperature of the instrument or issues with the internal optics of the spectrometer could be the case. Another possible reason could be atmospheric scattering. Such scattering can cause errors, e.g. due fog, rain and clouds (Moffat and Millan, 1971; Millan 1980). The optimal conditions would be clear blue skies, or clouds above the plume and little/no condensation in the plume. It is possible that conditions were poor for this fire, e.g low clouds, causing insufficient collection of light. The measurements of the NO_2 calibration cells were not so affected probably due to the higher light intensity at the wavelengths of the NO_2 absorption features. An additional feature to note is that the integration time of fire SF2 (1000-2000 mileseconds) is lot greater than that of the rest of the South African fires (100-250 milliseconds). Perhaps this shorter integration time caused some underlying noise during the collecting of the spectra for fire SF2 as the instrument may not be able to cope so well with collecting spectra at such a short frequency.
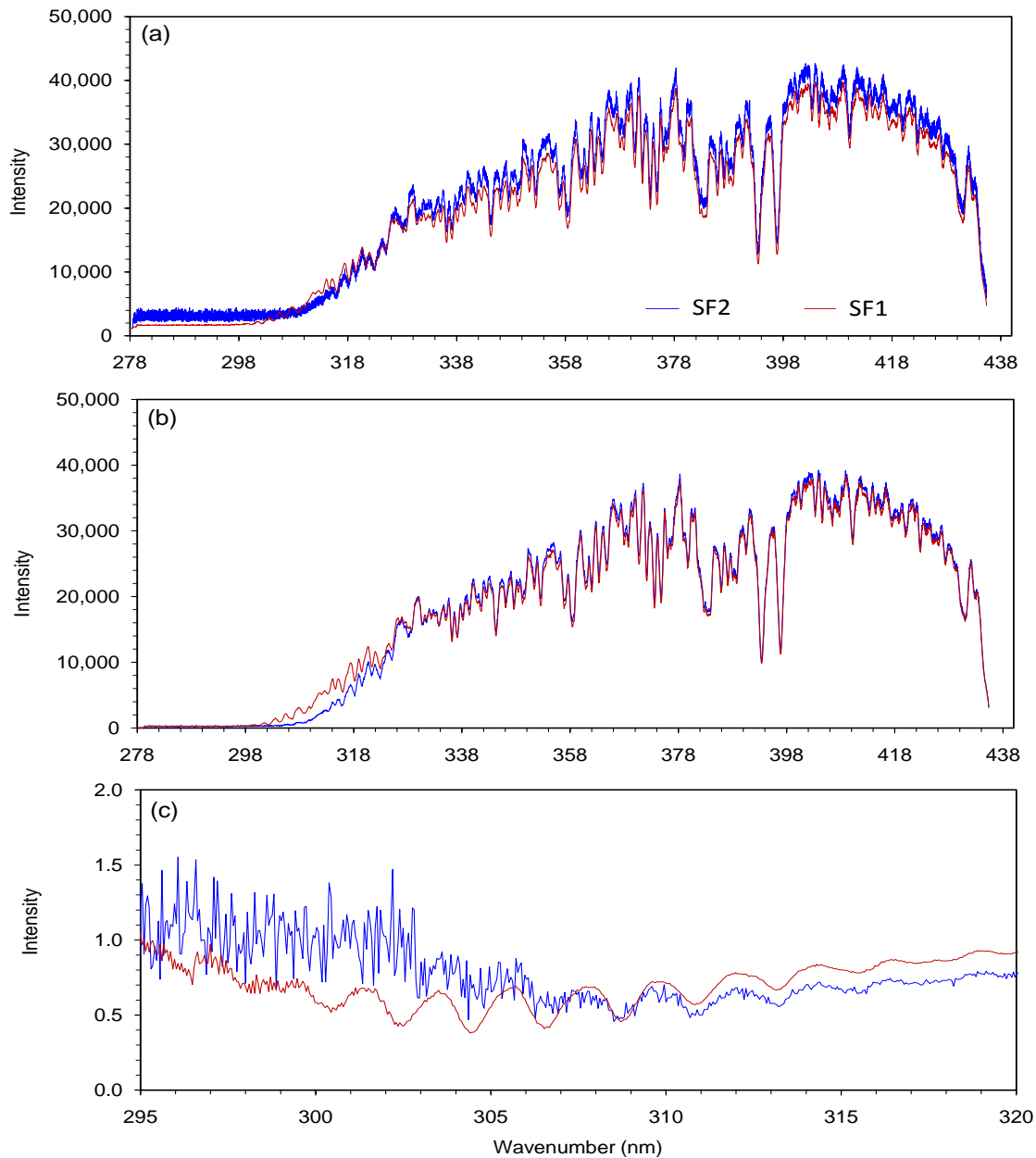
Figure 5.22: *Examples of spectral processing for fire SF1 and fire SF2. (a): SO₂ gas cell calibration spectrum of amount 905 ppmm for fires SF1 and SF2. Note the high noise level for the SF2 spectrum. (b): The same spectra with the dark signal subtracted. (c): The spectra normalized using the matching clear sky spectra (which has the dark signal subtracted). The absorption features of SF2 cannot easily be distinguished due to the underlying noise, but those of fire SF1 are quite clear.*

Figures 5.23 and 5.24 show the retrieved column amounts of NO₂ and SO₂ for all the South

African fires fires SF1 to SF4. Also shown are the estimated retrieval errors for each fire, calculated from Equation 5.8. Tables 5.2 and 5.3 detail the PT wavelength combinations used for each of the SO_2 and NO_2 retrievals. Figure 5.25 shows both target gases on the same graph for the main part of each fire.
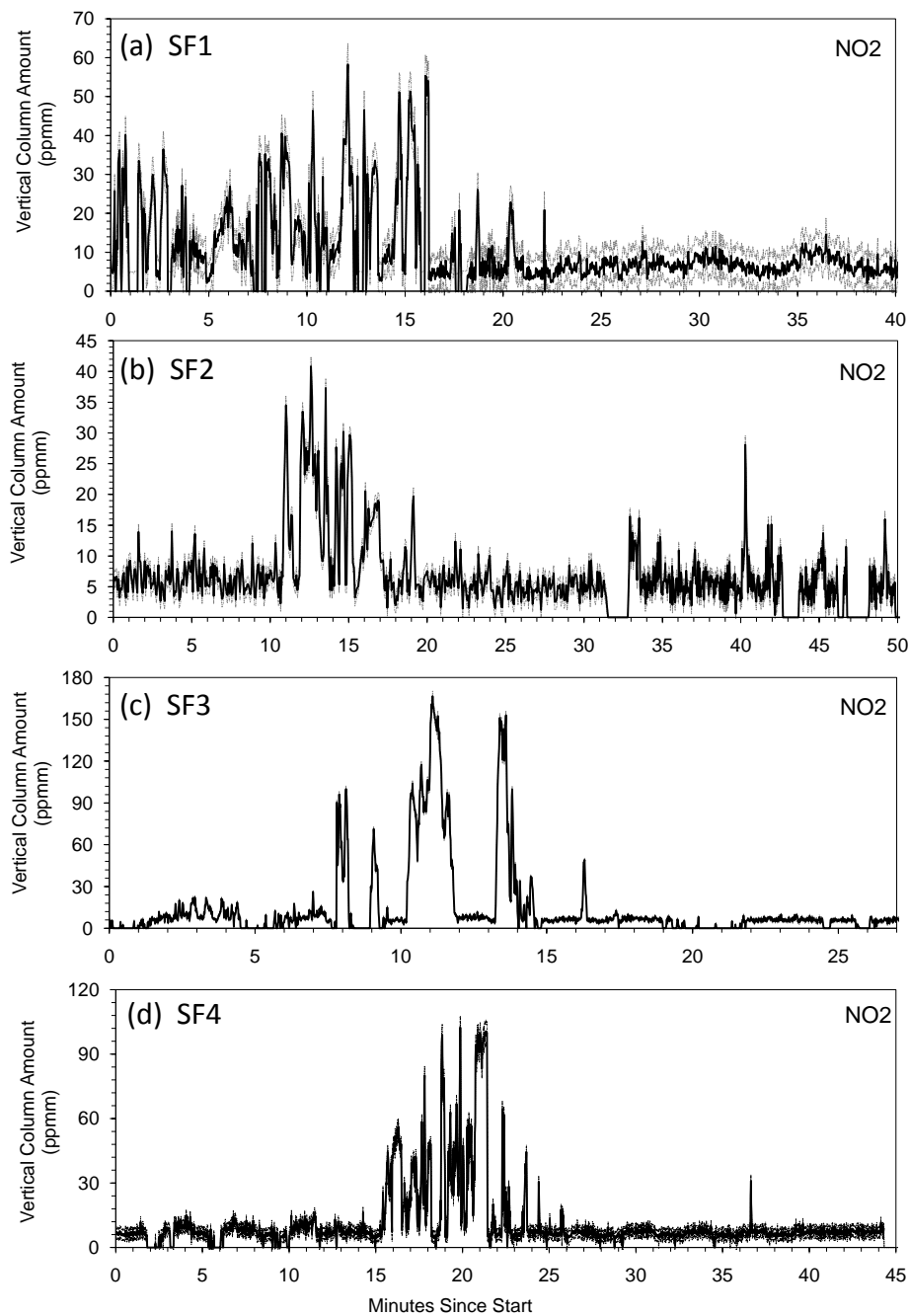
Figure 5.23: *The NO₂ vertical column amounts retrieved from the UV-DOAS smoke measurements made during the South African field campaign for fires SF1-SF4. Also shown is the estimated retrieval uncertainty calculated using Equation 5.8.*
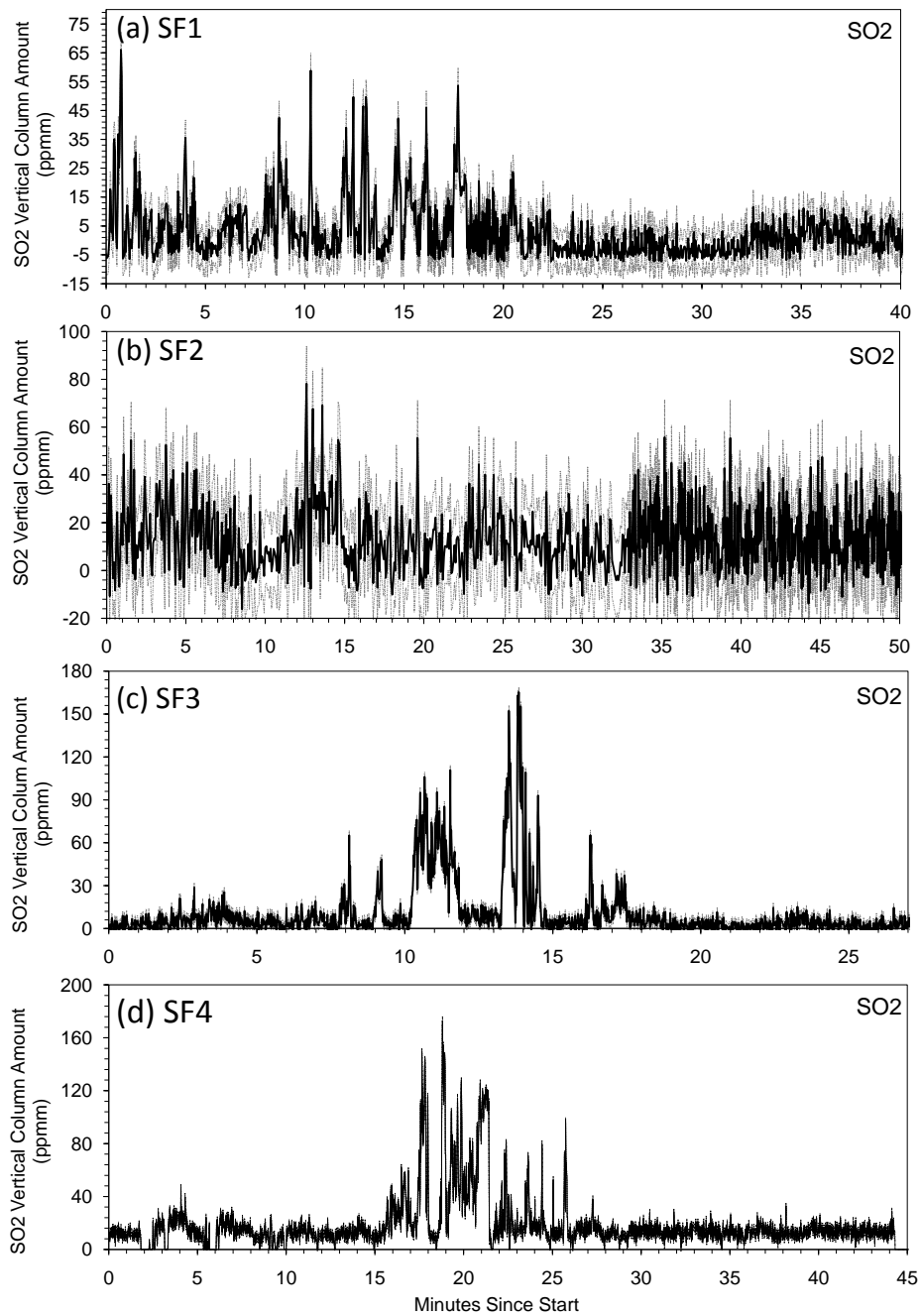
Figure 5.24: *The SO_2 vertical column amounts retrieved from the UV-DOAS smoke measurements made during the South African field campaign for fires SF1-SF4. Also shown is the estimated retrieval uncertainty calculated using Equation 5.8.*
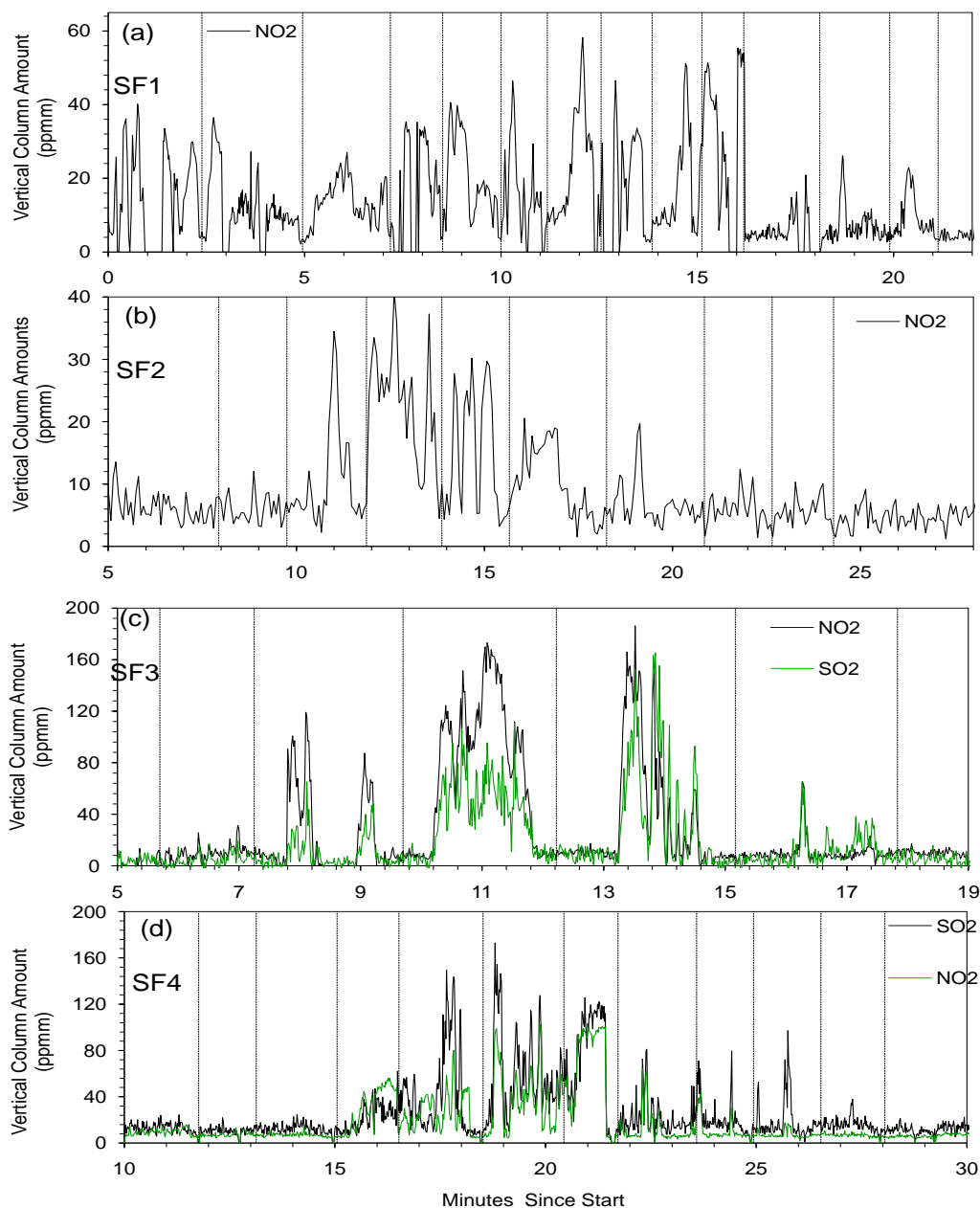
Figure 5.25: *Retrieved in plume vertical column amounts of SO$_2$ (green) and NO$_2$ (black) for all South African field campaign fires SF1-SF4 (a-d) as in Figures 5.24 and 5.23 but with a shorter duration around the main peaks, in order to better see the detail of the column amount measurements. SO$_2$ results are unavailable for fires SF1 and SF2 due to poorly retrieved column amounts too low to be considered usable. NO$_2$ also exhibits relatively low column amounts for fires SF1 and SF2. Higher amounts for both gases were retrieved in fires SF3 and SF4. There is a good agreement between the temporal variations in the amount of each gas (i.e. SO$_2$ and NO$_2$ variations appear to track another quite well). The vertical bars represent the start and end of each traverse, which also covers a single transect under the plume.*

Generally, the pattern of the NO_2 and SO_2 retrieved column amounts for fires SF1 and SF2 do not follow the expected pattern of a main emissions peak during which smoke is most prominent, and smaller peaks outside of this area where the fire is beginning or ending and thus smoke is present at lower amounts. The SO_2 results in particular are variable, with difficulty distinguishing between the peaks caused by the fire and those which are probably just noise. The proportionally high noise of the SO_2 results for fires SF1 and SF2 can probably be attributed to low SO_2 column amounts coupled with lower light intensity at the spectral region used to retrieve the SO_2 compared to that of the NO_2. Low column amounts are due to the low levels of smoke compared to the last two fires. When there exists low amounts of the target gas, low levels of light intensity of the measurement spectra make it very difficult to retrieve column amounts. The signal needs to be optimized to allow a sufficient signal for optimal retrieval. However as the target gases are retrieved in different areas of the spectrum (see Figure 5.26), the SO_2 retrieval spectral region will always be a at a lower light intensity than that of NO_2. Increasing the signal for the SO_2 spectral region may well result the saturation of the NO_2 spectral region. Hence, the conclusion is that when there are low levels of SO_2 in the path the retrieval may not be as successful as when there are low levels of NO_2 in the path. It follows from this that NO_2 may be a better gas to use to try to measure flux rates of smoke from vegetation fires, as UV light intensities are higher in the spectral region used to retrieve it
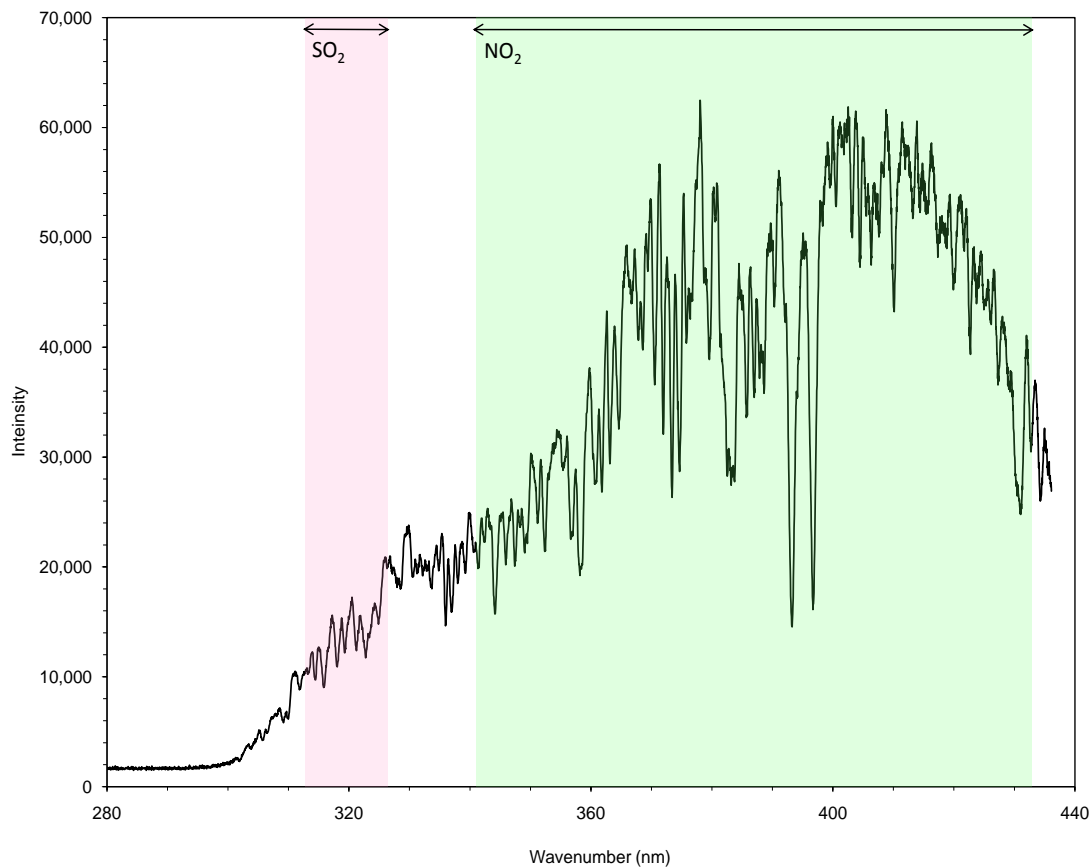
Figure 5.26: *Figure showing the fitting spectral regions used for SO_2 and NO_2. The NO_2 region always has a higher signal, a rise in the SO_2 region signal can lead to saturation in the NO_2 region.*

The NO_2 retrieved column amounts from fires SF1 and SF2 are not as noisy but are of low column amounts, again due to the low levels of smoke produced by the fire. NO_2 column amounts reach maximums of 60 and 40 ppmm for fires SF1 and SF2 respectively. Fire SF1 does not have one main peak but a series of peaks at the start of the fire, representing the fact that once the fire started the smoke plume fluctuated until the end when levels fell. Fire SF2 has more of a main peak, although maximum column amounts reached are low. Fires SF3 and SF4 exhibit more of the pattern that is expected, for both gases. Fire SF3 maxima reach close to 170 ppmm for SO_2 and 190 ppmm for NO_2, while for fire SF4 NO_2 reach 100 ppmm and SO_2 close to 180 ppmm. There is a switch in the dominant gas between fires SF3 and SF4, with NO_2 being more abundant in fires SF3 and the reverse for fire SF4. This is

228

probably a reflection of the N and S content of the different fuel types of the plots. Craine *et al.* (2009) compared the N content in various sites in Kruger National Park with numerous private protected areas adjacent to the park. It was found that in general, these private protected areas had higher N availability in plants and leaves. Sandy soiled ecosystems like those in the South African field campaign are relatively low in nutrients (Grant and Scholes, 2006). Species found in the South African field sites of this work were associated with depleted rates of N, for example *Hyperthelia dissoluta* and *Setaria sphacelata sericea*. Grant and Scholes (2006) found a link between termite mounds and higher N concentrations on a study in similar ecosystems in Kruger National Park. The same was also found for areas used as foraging patches by animals. In general, savanna forests are low in nitrogen (Näsholm *et al.*, (1998)). Hence the variations in the N:S ratio from the plots could be linked with these type of nutrient related factors. There is a good agreement between the temporal trend of the NO_2 and SO_2 column amounts for fires SF3 and SF4 (Figure 5.25 (c) and (d)). The target gases generally peak at the same times, providing evidence for the robustness of the retrieval method.

From the results shown in Figures 5.23 and 5.24 it can been seen that the retrieval errors are highest for the SO_2 vertical column amounts for fire SF2. This is attributed to the high standard deviation at the chosen PT combinations of the different gas cell spectra used for averaging,, recalling that for this fire the SO_2 absorption features measured during the calibration gas cells, were weak. Generally, errors of up to 10-30 % have been reported in the literature from the retrieval of DOAS column amounts (McGonigle *et al.*, 2002; McGonigle *et al.*, 2003; McGonigle *et al.*, 2005; Leigh *et al.*, 2007; Rivera *et al.*, 2010), which is in line with the errors given here for fires SF3 and SF4. Errors for these fires are on average below 10% for the peaks of the fire. Errors outside of the peak are greater due to the lower retrieved vertical pathlength amounts of the gases. The derivation of the errors quoted in the literature is not available. The percentage errors for fires SF1 and SF2 are greater (10-50 %) due to the lower retrieved column amounts, however the absolute errors do not vary by too much (1-15 ppmm).

Canada

Figure 5.27 shows the retrieved in-plume vertical column amounts of NO_2 for the Canadian fires CF1 and CF2. For both fires, spectra were collected at a frequency of between 7 per second to 1 every 5 seconds. Averaging was conducted resulting in one measurement per second. Errors were not included in Figure 5.27 as they were insignificant compared to the column amount for both gases.
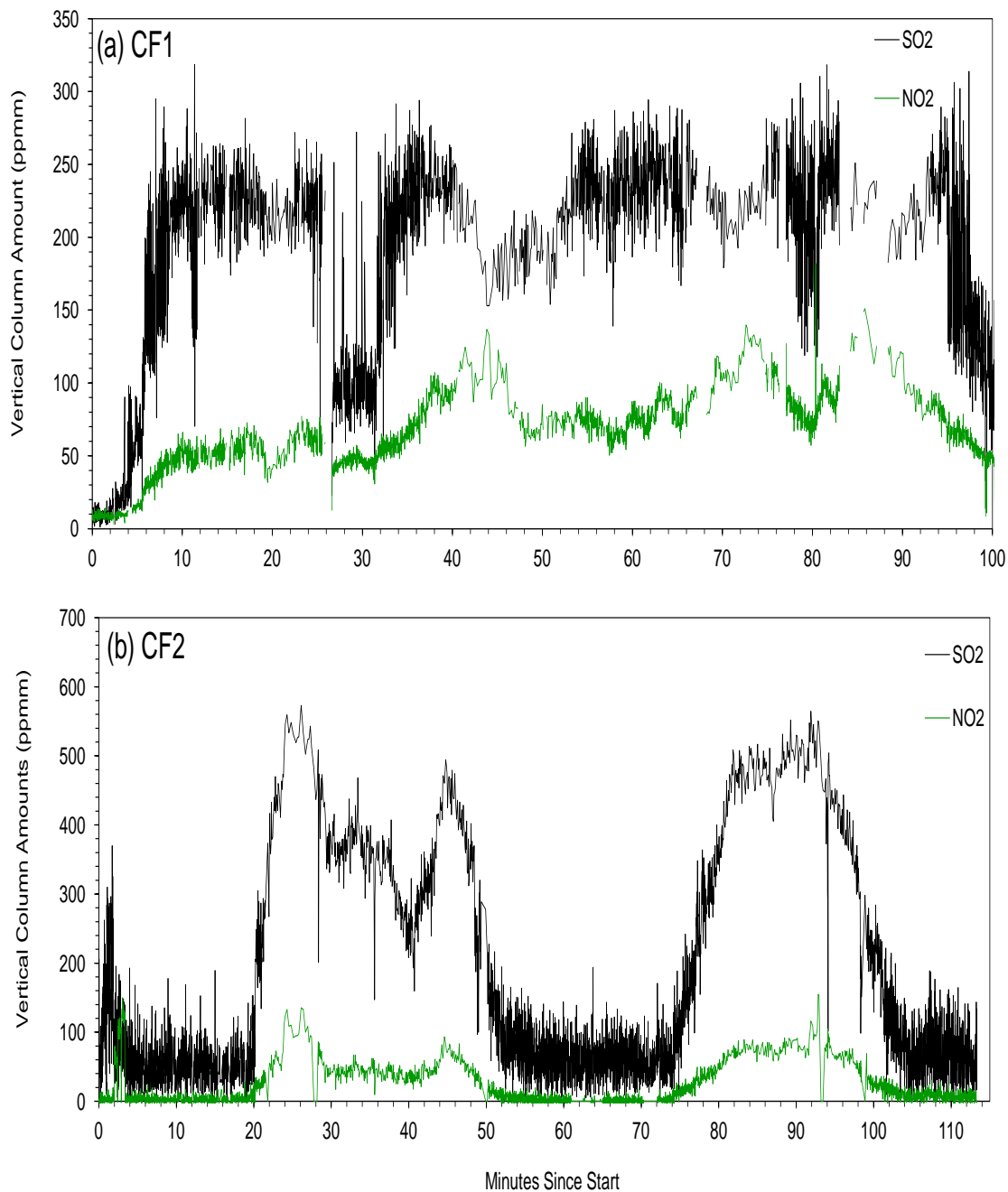
Figure 5.27: *Retrieved vertical column amounts of SO_2 and NO_2 for (a) Canadian fires CF1 and (b) CF2. The spectra collected during fire CF1 exhibited higher levels of noise and were of a lower intensity than those of fire CF2 (see Figure 5.28). This will effected the retrieval of the trace gases, in particular SO_2 due to the spectral region in which the retrieval of the vertical column amounts takes place.*

Note that there are no SO_2 gas cell calibration spectra available for SO_2 for fire CF2 due to

temporary problems with the data collection. Hence the calibration relationship derived from fire CF1 was applied to the spectra of fire CF2. Figure 5.27 (a) shows the retrieved vertical column amounts of NO_2 and SO_2 for CF1. The returned results, in particular the SO_2 results, exhibit high levels of noise. This can probably be attributed to the low intensity, noisy spectra collected during this fire. Figure 5.28 shows examples of spectra collected during fire CF1 and compared with a spectra of fire CF2. It can be seen that compared with fire CF2, the CF1 spectra are of a much lower intensity. Also note that at times during the fire, spectra like those used as the 'dark noise' spectra in the retrieval process were collected (these were removed from the results). The is probably due to the particularly thick smoke causing scattering of the light as it passes through the plume. Recall Figure 5.7 showing the extent of the plume of the Canadian fires, particularly when compared to those of the South African field campaign (Figure 5.4). The plume for CF2 was also extensive, however the integration time for this fire was was greater, resulting in a spectrum collected every 1-5 seconds, while in general spectra for fire CF1 were collected at a frequency of one or more per second. Hence the greater intensity of the CF2 spectra. The SO_2 retrieved vertical column amounts for SO_2 probably exhibit a greater level of noise as they are retrieved in the spectral region which generally is of a lower intensity compared with NO_2, as explained above (See Figure 5.26).
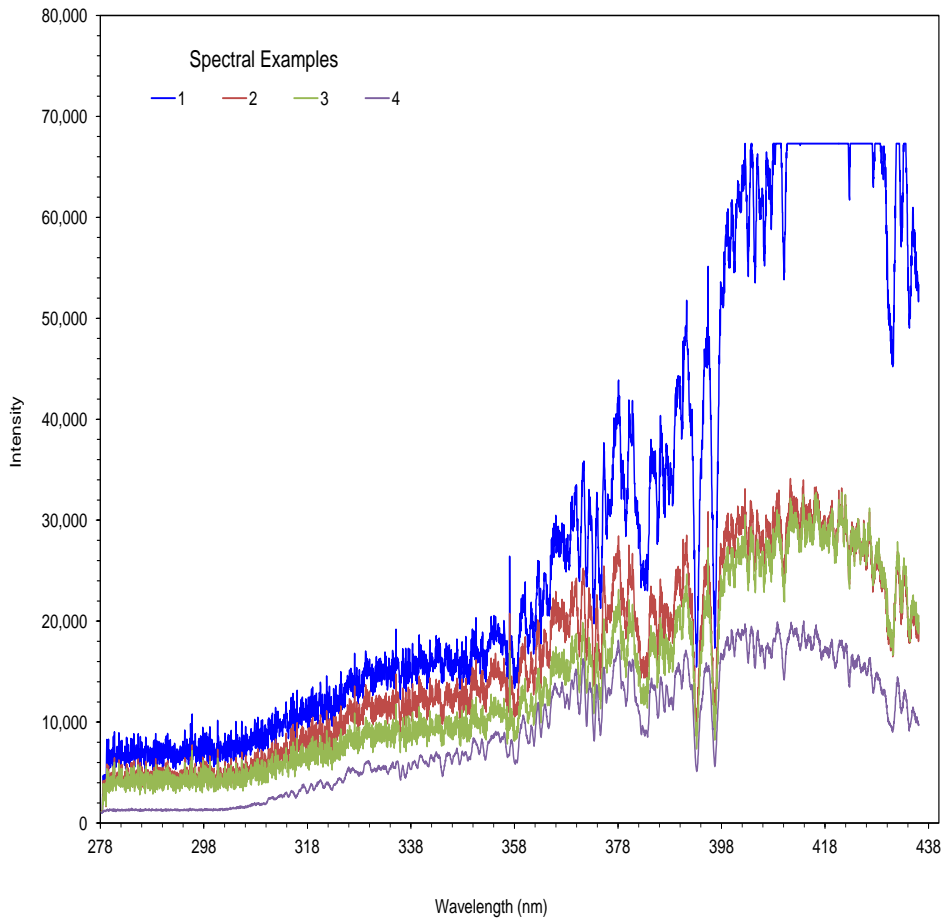
Figure 5.28: *Examples of spectra corresponding to the peaks of the target gas column amounts in Figure 5.27 (a) (1-3) with high noise levels and variations in light intensity. Spectra 4 is taken from outside the peak.*

Results for CF2 do not exhibit such noise. Although the fires are of the same fuel type, the ratio of NO_2 to NO_2 does not appear to be the same. SO_2 vertical column amounts peak less than those of fire CF2, approximately 300 and 600 ppmm. However for NO_2, both fires peak at approximately 150 ppmm. The accuracy of the retrieved results of SO_2 for fire CF1 is questionable, due to reasons given above. Nevertheless, retrieved SO_2 levels are also much higher than retrieved column amounts of NO_2. This is linked with the fuel type that was burnt. In a study in Northern Alberta, Cortini and Comeau (2008) reported that white spruce and lodgepole pine, both species found in the Canadian field site, were low in nitrogen. Yokelson *et al.* (1996), in laboratory biomass burning experiments, calculated

emission factors of pine needle fuel types (*pinus ponderosa*), with SO_2 EFs (1.12 g.kg^{-1}) just under three times that of NO_2 (0.41 g.kg^{-1}) Although this is not exactly the same fuel type, this does show that for these types of ecosystems, more SO_2 is released during fires compared with NO_2. However in a study investigating fire emissions from Canadian smoke plumes, Simpson *et al.* (2011) reported a much greater NO_2 EF of 1.03 g.kg^{-1}, using airborne sampling in the field. In contrast, Yokelson *et al.* (1996) used FTIR measurements in the laboratory.

5.6.2 Flux Rates

Figure 5.29 shows the derived fluxes of NO_2 and SO_2 for all South African fires calculated from the column amounts and estimated plume speed as described in Section 5.5. Again for fires SF1 and SF2 the SO_2 results have been omitted. Uncertainties on the derived fluxes were calculated as in Equation 5.17.
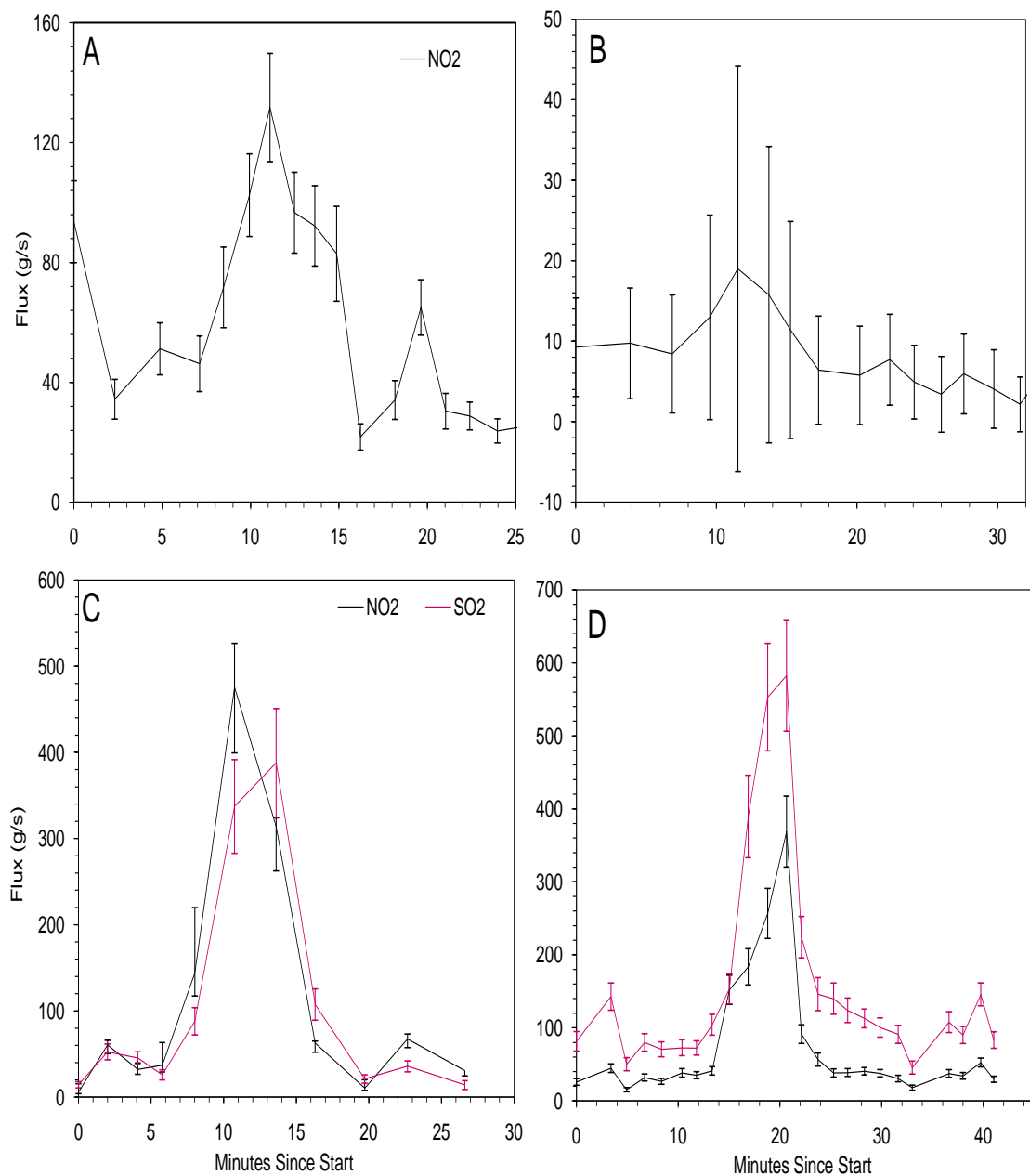
Figure 5.29: *Fluxes for the South African fires (a)-(d) SF1-SF4. Only NO_2 is shown for fires SF1 and SF2 due to low column amounts of SO_2 being retrieved. Note the high uncertainties in fire SF2 flux estimates compared to the other fires. Where both NO_2 and SO_2 fluxes are calculated (fires SF3 and SF4), there is a strong correlation between the two gases.*

It was only possible to estimate plume height from the video footage of fire SF3. Since there was no usable video data available for fires SF1 and SF2. The video footage for fire SF4

was taken directly on top of the fire such that plume height estimates were difficult to make. Hence for fire SF4, the estimated plume height from fire SF3 was used as both fires were of a similar fuel loading. The average plume height was approximated as 300 m, with maximum and minimum heights estimated as 200 and 420 m respectively. Figure 5.30 shows example images from the video footage of fire SF3, confirming the plume rose very much higher than the trees. As fires SF1 and SF2 had a smaller fuel load than fires SF3 and SF4, it was not appropriate to use the fire SF3 plume height estimate. A value of 100 m, with minimum 50 m and maximum 300 m, was selected instead. Looking at the derived NO_2 fluxes for fire SF1, Figure 5.29 (a), the 3 peaks in NO_2 flux represent groups of peaks in the retrieved column amounts in Figure 5.25 (a) and the observation that there is not solely one main emissions peak or several emission peaks as with fires SF3 and SF4. Figure 5.29 (b) shows low fluxes for fire SF2 due to the low column amounts shown in (see Figure 5.25). Figure 5.29 (c) and (d) show a good correlations between the SO_2 and NO_2 fluxes for fires SF3 and SF4. The NO_2 flux is similar to that of SO_2 for fire SF3 but greater for fires SF4.
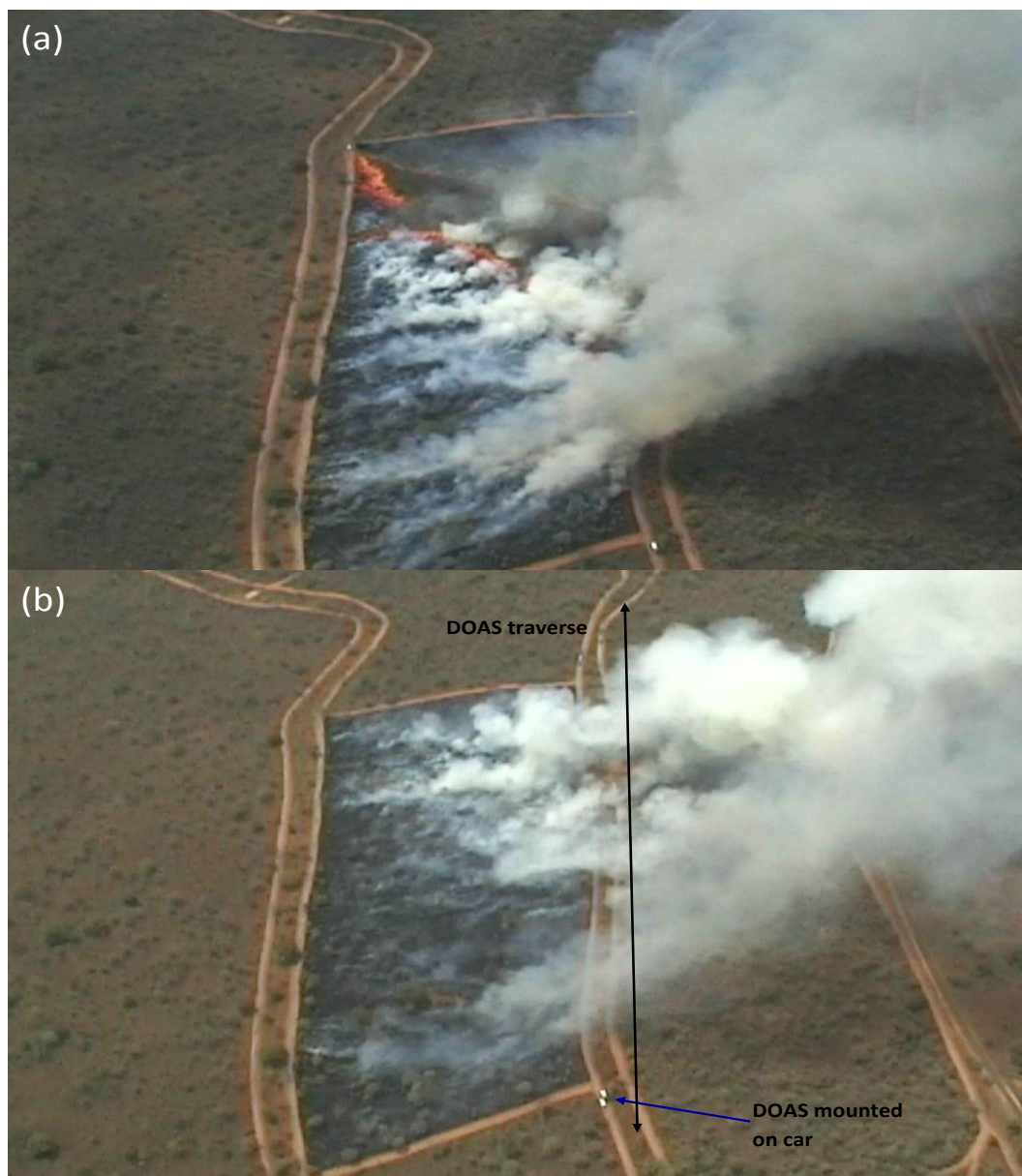
Figure 5.30: *Stills from the video footage of the South African fire SF3. The significant height of the plume can be seen, when compared to the height of the trees (5 m) and the white vans that can be seen on the bottom of each image. An arrow is presented indicating the path of the vehicle carrying the DOAS instrument back and forth underneath the plume.*

Oppenheimer *et al.* (2004) reported fluxes of up to 240 g.s^{-1} from agricultural fires in Brazil. This lies between the range of NO$_2$ fluxes derived from the South African fires (approximately 20-500 g.s^{-1}). Pathlength NO$_2$ column amounts reached up to 100 ppmm for this Brazilian fire, just under those of SF3 and SF4 (approximately 160-180 ppmm) and

distance of the DOAS traverse (over 500 m) greater than those of fires SF3 and SF4 (200-300 m). However the estimated plume speed for fires SF3 and SF4 (10 and 14 m.s^{-1}) are greater than that of the Brazilian fire (5 m.s^{-1}). SO$_2$ fluxes from volcanic plumes estimated using UV-DOAS measurements ranged between 250-160000 g.s^{-1} (Galle *et al.*, 2002; McGonigle *et al.*, 2002; Mori *et al.*, 2006; Grutter *et al.*, 2008). Peak industrial fluxes of SO$_2$ ranged from 6400 to 12474 g.s^{-1} and 614 g.s^{-1} for NO$_2$ (McGonigle *et al.*, 2004; Rivera *et al.*, 2009).

The relative uncertainties in the flux rate of NO$_2$ for fire SF2 are much greater than for the rest of the fires due to the low fluxes. Past studies have quoted flux rate uncertainties between 10 and 51 %, including processing errors, errors due to scattering, errors in wind-speed and direction, plume height signal to noise changes (McGonigle *et al.*, 2002; McGonigle *et al.*, 2003; Oppenheimer *et al.*, 2004; McGonigle *et al.*, 2005; Leigh *et al.*, 2007; Edmonds *et al.*, 2003). There is no explanation provided in the literature of how these errors are quantified, however the estimation of plume properties has the greatest uncertainty attributed towards it. Apart from fire SF2, the flux rate uncertainties here are less than 30%, with the majority less than 20%.

5.7   Conclusion

UV DOAS spectra from several managed burns were collected during vehicle transects made under smoke plumes from two field campaigns (South Africa and Canada) and were used to retrieve vertical column amounts of the target gases, SO$_2$ and NO$_2$. Measurements of gas cells of know amounts were used to derive a simple calibration relationship between trace gas column amount and absorbance features. This relationship was applied to the spectra measured during the fires to return NO$_2$ and SO$_2$ vertical column amounts. This method proved quite efficient in returning column amounts, provided there is sufficient levels of smoke and light intensity levels are sufficient. It was found that when there existed low levels of smoke, the retrieved vertical column amounts of SO$_2$ showed more noise compared to those of NO$_2$. It is thought that this is attributed to the lower light intensity of the spectral fitting region of SO$_2$. Estimated uncertainties of the derived vertical column amounts are in line with those quoted in the literature for the data sets that were measured when there was an

abundance of smoke. Uncertainties increase with lower column amounts. Generally, SO_2 column amounts were lower for the South African fires compared to the Canadian fires, due to the much larger smoke plume of the Canadian fires.

The column amounts of SO_2 and NO_2 for the South African fires were combined with GPS records and plume speed estimates to calculate corresponding SO_2 and NO_2 flux rates. Plume speed was estimated using ground wind speeds, the log law and video imagery taken from the fires to estimate plume height. Although the plume speed estimates are rather rough, they are believed to be better than using simply the wind speed at ground level. Where it has been possible to measure both target gases, the flux rates of both NO_2 and SO_2 are well correlated during the fire i.e. they generally rise and fall at the same time. Returned flux rates have errors less than the maximum quoted in the literature.

Overall, it has been proved that the lightweight, compact DOAS can be used to investigate the emissions of SO_2 and NO_2 from biomass burning plumes. Simple to use and quick to set up, column amounts can be retrieved easily from a simple algorithm. This method has the potential to provide an easy, cheap way of consistently measuring emissions of trace gases released from open vegetation of different fuel types in a consistent manner. This can possibly eliminate the variation in data of current emission estimates used to model biomass emissions. The portable nature of this instrument allows for easy transportation and implementation to different global sites to investigate biomass burning emissions. In addition, the flux rates calculated from the data collected from the UV-DOAS instrument can potentially be useful for modeling biomass burning emissions as they provide information of how the emissions of the target gases vary over time. However, the use of the UV-DOAS is restricted to gases with absorption features in the UV and fires that emit a sufficient amount of smoke.

Chapter 6

FTIR Synthesis; Methods, Analysis and Results

Contents

This chapter details the specific methods used for the collection and analysis of the FTIR measurements of the smoke plume of the prescribed burns conducted during the South African field campaign. The IR spectra were used to retrieve pathlength averaged mixing ratios of CO_2, CO and CH_4, which were subsequently used to derive the emission ratios and emission factors of these gases. The flux rates calculated from Chapter 5 were taken and combined with the emission ratios to give an estimate of the total carbon flux of the carbon emitted by each of the fires. This is then compared to the FRP series derived from the thermal camera measurements of the same fires.

Due to problems with the instrument and FTIR data exists only from fire SF1. For fire SF2, the battery used led to poor quality spectra being collected. The instrument was unavailable for measurements during fires SF3 and SF4. Hence, the FTIR measurements and analysis for the South African burn should be viewed as more of a pilot study to investigate the implementation of FTIR measurements and retrievals for this field set up, and to explore the synthesis of the FTIR-derived results with the trace gas fluxes derived from the UV-DOAS measurements, and also the synergy with the FRP time series derived from the thermal camera measurements. There were also no ground-based open path FTIR data collected for the Canada field campaign, due to the excessive plume height and a lack of smoke at ground level. Spectra were taken in solar occultation mode instead, i.e. with the sun as the source of radiation. This set up was more suitable for the Canadian fires, as the plumes reached very large altitudes, but that set up required different analysis techniques not used in this thesis. However, the FTIR data from the Australian field campaign, presented in Chapter 7 follow on from this South African pilot study, allowing for the developed technique to be tested on a series of further burns.

6.1 FTIR data collection

An IR lamp was employed as the radiation source for all the ground-based open path FTIR spectrometer observations described herein. The specifications of the FTIR are detailed in Chapter 2. The lamp used for this field campaign, mounted on a tripod, was a 1275^oC silicon carbide glower on an approximately 50 cm gold plated aluminum reflector (Wooster *el al.,*

2011). For South Africa, the position of the FTIR and lamp with respect to the burn plot and UV-DOAS traverse is shown in Figure 6.1.
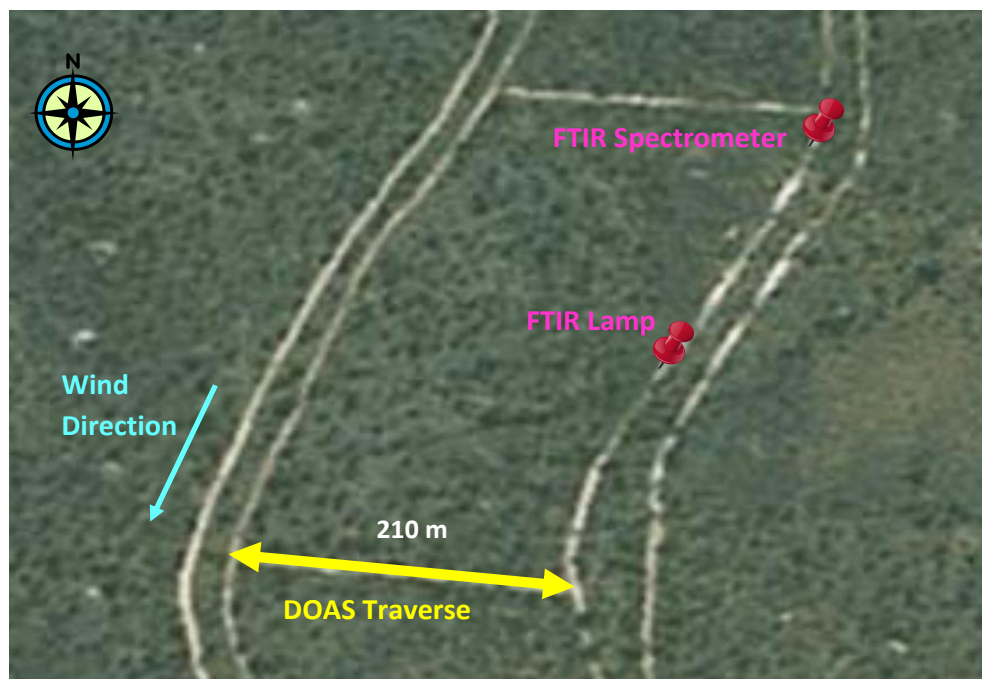
Figure 6.1: *Layout of the South African fire SF1, depicted on a Google Earth image. The position of the FTIR spectrometer and IR lamp are shown, along with the path taken during the DOAS traverses. Plot is approximately 370×180 m in size.*

The FTIR and IR source were positioned stationary, slightly distant from the plot edge, and approximately 190 m apart such that the plume was able to pass between them. Smith *et al.* (2011) and Wooster *et al.* (2011) describe similar OP-FTIR set-ups. Figure 6.2 shows two images taken during fire SF1 of the spectrometer (a) at one end of the optical path and the lamp (b) at the other end.
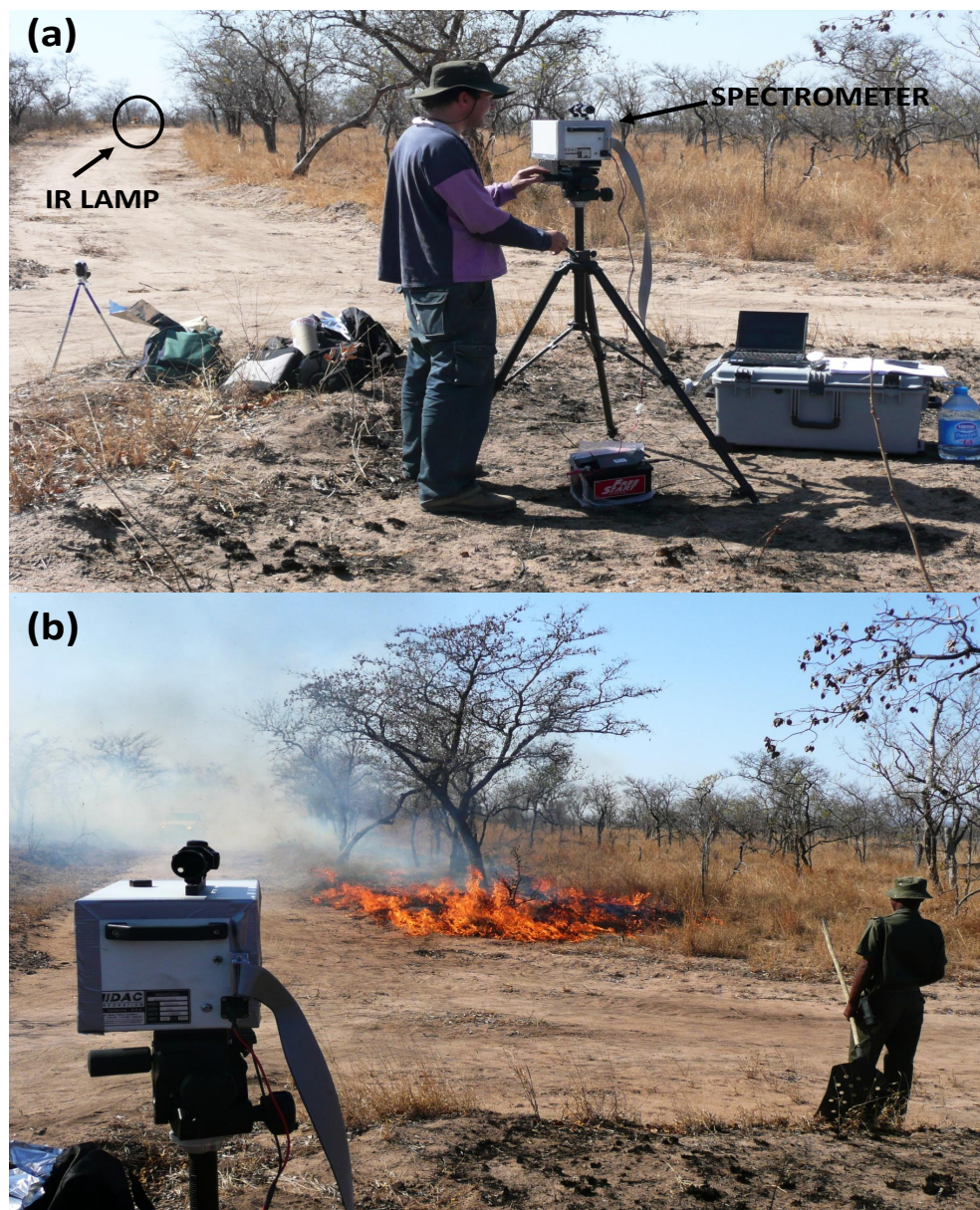
Figure 6.2: *The FTIR set up in operation (a) before and (b) after the start of the South African fire SF1.*

As already mentioned, FTIR measurements were also taken of the South African fire SF1. However, due to low voltage on the battery, the spectra were not of acceptable quality to be used (Figure 6.3).
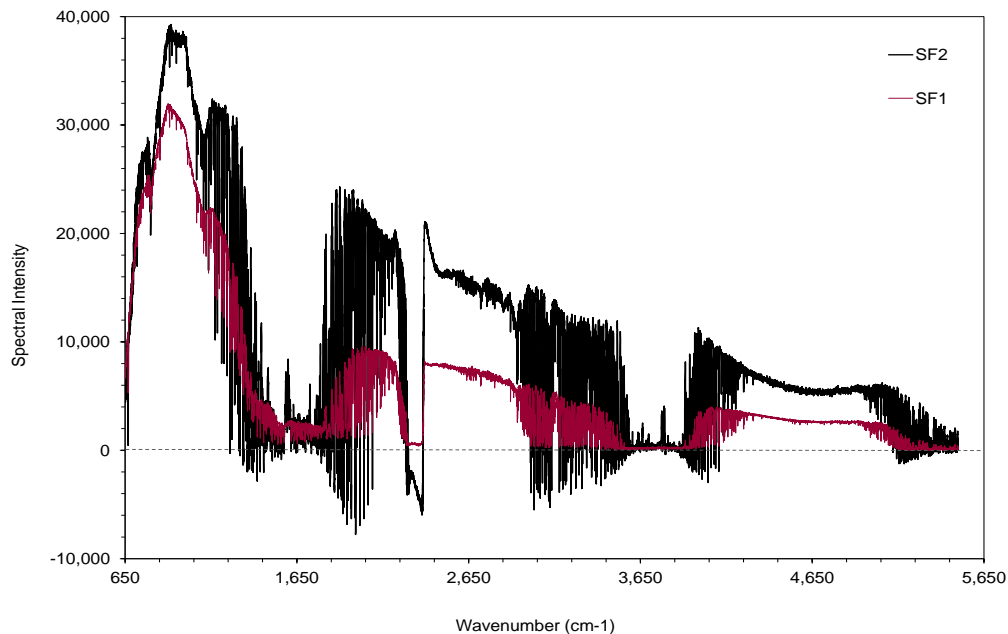
Figure 6.3: *Example of spectra collected by the FTIR spectrometer during South African fires SF1 (purple) and SF2 (black). The battery used to operate the spectrometer had a low voltage during fire SF2, leading to poor quality spectra. This can be seen as negative values of spectral intensity. In contrast, spectra collected during fire SF1 do not exhibit intensities below zero.*

The FTIR spectra were recorded on average every 5 seconds, with one spectra a result of a coadd of four mirror scans. This signal averaging is carried out to reduce measurement noise. Note that measurements from the FTIR also terminated during fire SF1, such that there is only a few minutes overlap between the FTIR and UV-DOAS measurements.

6.2 Specific Methods Used for Data Analysis

6.2.1 Pathlength averaged mixing ratios of target gases

The target gases CO_2, CO, CO_2, NO_2 and SO_2 were retrieved from the FTIR spectra using the non linear least squares fitting algorithm MALT (Griffith, 1996) detailed in Chapter 3. As detailed in Chapter 3, the input parameters of plume temperature, plume pressure, optical pathlength, and *a priori* target gas pathlength averaged mixing ratios are set in MALT, which then creates a synthetic spectrum within the defined spectral fitting region via use of

these parameters. The synthetic spectrum is iteratively matched with the measured spectrum by altering the pathlength averaged mixing ratios of the target gases until the best match is found by minimizing the residual. Once the closest match between the measured and synthetic spectra has been found, the target gas pathlength averaged mixing ratios from the corresponding synthetic spectrum are taken as the retrieved mixing ratios (ppm).

The optical pathlength is measured in the field by measuring the distance (m) between the spectrometer and IR lamp, which was 188 m for fire SF1. This was done using a 50 m tape measure, and is believed accurate to within 3 m. Since the distance acts equally for all gases, errors to the distance do not effect the derived emission ratios and emission factors, only the pathlength averaged mixing ratios. The plume temperature (kelvin) and pressure (hPa) are estimated using measurements recorded by the weather station. As previously mentioned, the weather station for SF1 was located at a height of 1.3 m close to the plot and was continuously including ambient pressure and temperature every 5 seconds. An average of these values during the fire was used to parametrize MALT. The *a priori* pathlength averaged mixing ratios of the target gases do not affect the end result of the fitting unless they are extremely different to the true pathlength averaged mixing ratios and are simply used as a first guess of the target pathlength averaged mixing ratios. The spectral fitting windows to use were determined by running MALT for spectral regions where the target gases have absorption features. Results were compared to decide which spectral fitting window was most suitable (see Chapter 7 for examples of results from different spectral fitting windows). Along with the target gas, other gases that have absorption features at the chosen spectral window were included in the fit. As detailed in Chapter 3, the apodization function for all the FTIR retrievals was the triangular function and the background polynomial fitted was of order 4. A 4th order polynomial was sufficient to fit the background without fitting the trace gas absorption features. Table 6.1 gives the details of the parameters used for the fitting of each of the target gases.

Table 6.1: *The specific parameters needed for input to the MALT to retrieval scheme (Griffith et al., 1996) used to retrieve the pathlength averaged mixing ratios of the target gases from the recorded IR spectra.*

Maximum iterations			30
Order of Polynomial			4
Spectral Resolution (cm^{-1})			0.5
Spectral Shift			0, fit
FOV (mrad)			20, fit
Phase Shift			0, fit
Plume Pressure(hPa)			959
Plume Temperature (K)			305
Optical Pathlength (m)			188
Apodization Function			Triangular
Background Polynomial Order			4
Target Gas	**Spectral Fitting Region (cm^{-1})**	**Interfering Species**	*A priori* **mixing ratios(ppm)**
CO_2	2225-2310	N_2O, H_2O	300
CO	2050-2132	CO_2, H_2O	3
CH_4	2980-3090	H_2O	3.5
NO_2	2910-2940	H_2O, CH_4	0.01
SO_2	1120-1200	H_2O, N_2O	0.01

The zero offset parameter was fitted for the CO_2 retrievals as the spectral region for the fitting included part of the absorption band that was in theory equal zero due to total absorption of the IR beam by CO_2. An average of the resultant zero offset for CO_2 was used as a fixed parameter for the rest of the target gases. Muller *et al.* (1999) and more recently, Wooster *et al.* (2011) described the process of subtracting the radiation signal recorded by the spectrometer in the absence of the IR source in order to take into account the effect of the energy emitted by the instrument itself and by ambient temperature surroundings. The magnitude of this self-emitted energy varies strongly with wavenumber and peaks around the areas 650-1300cm^{-1}, since ambient bodies emit most strongly in this region. Outside this spectral region the effect is negligible and the procedure is usually not applied (Wooster *et al.*, 2011). It was not possible to take into account this effect for the South African fires

studied here due to the absence of spectra measured without the IR source. Fortunately, all the target gases are retrieved outside of this spectral region apart from SO_2. However, as seen in the next section, the levels of SO_2 within the South African plume are very low and the measurements are not used for further analysis. In Chapter 7 this subject is discussed further. Figure 6.4 shows an example of FTIR spectra measured before and during the fire with regions of more depth clearly seen during the presence of the smoke. Figure 6.5 shows extracts from the same spectra, focusing on the spectral fitting regions of the target gases.

Note that whilst Castro *et al.* (2007) state that when burning experiments are conducted in open air, the optical pathlength of the smoke filled portion of the path cannot accurately be determined due to the changing location of the target gases in the smoke. They overcome this by using the "path-integrated" concentration i.e. concentration times pathlength, in ppmm. However pathlength is not important when calculating emission ratios, which is the focus of the current work as discussed below.
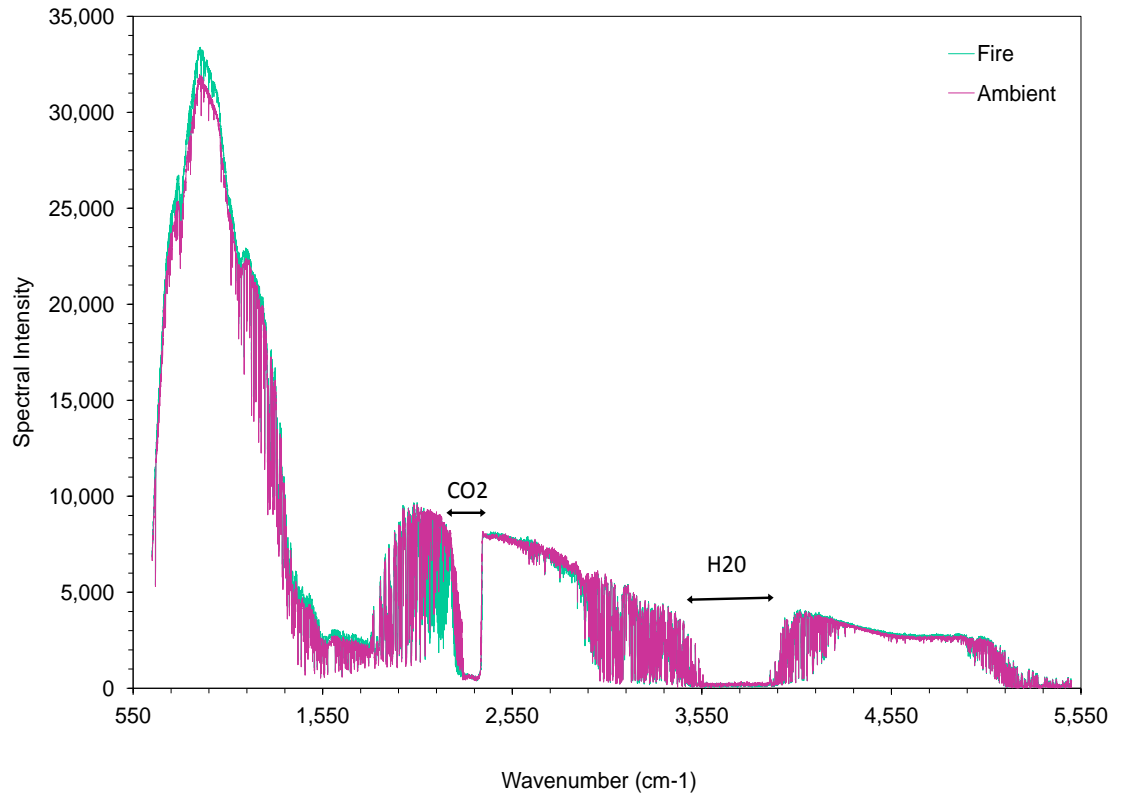
Figure 6.4: *Example FTIR spectra collected before ("ambient") and during ("fire") the SF1 fire in South Africa, with spectral regions identified in which spectral intensity has fallen to zero due to complete absorption by atmospheric CO_2 and H_2O.*
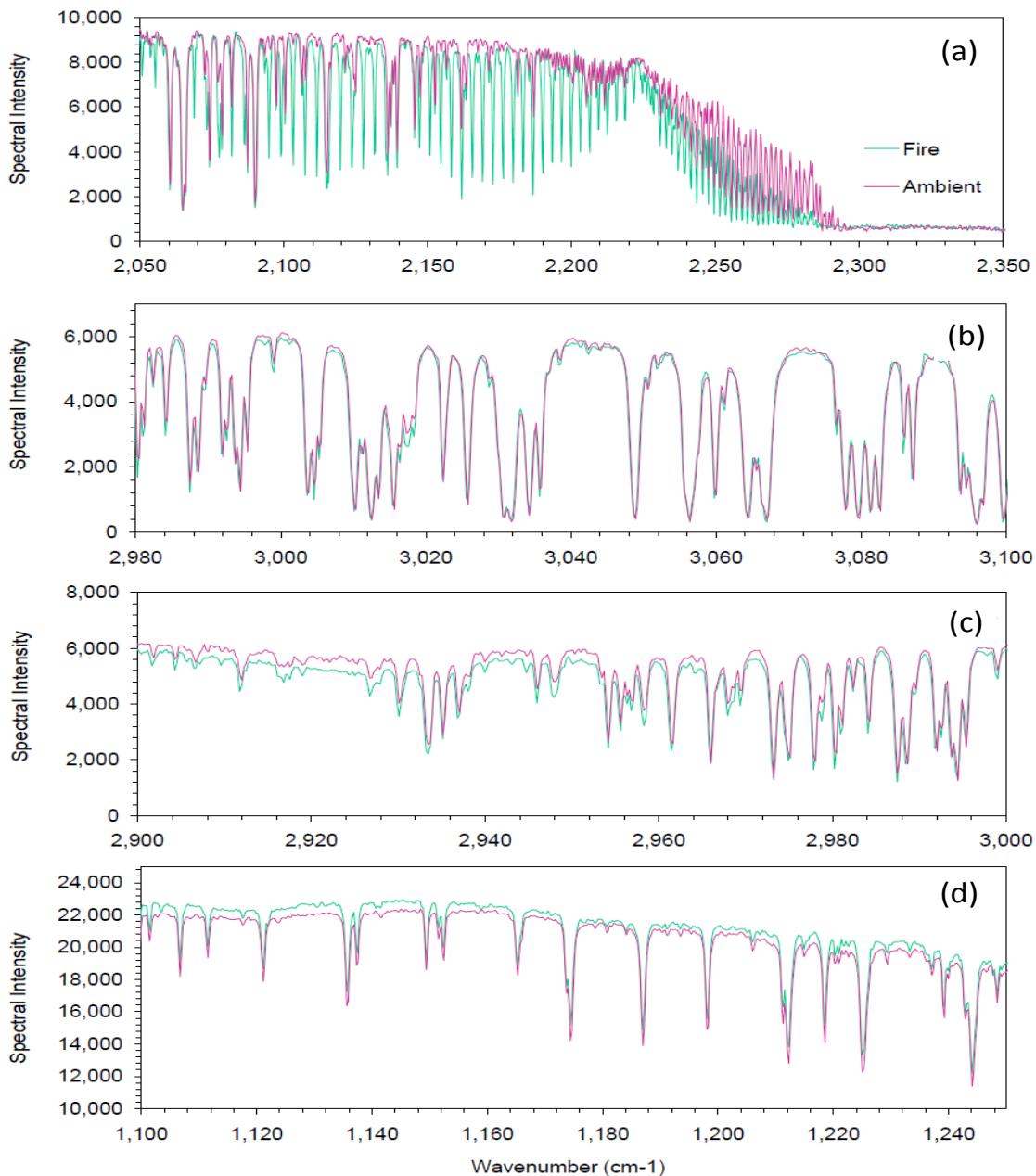
Figure 6.5: *Same spectra as shown in Figure 6.4, but now focusing in on the spectral windows used to retrieve the target gases: (a) CO_2, (a) CO, (b) CH_4(B), (c) NO_2 and (d) SO_2. The red spectrum measured before the fire ("ambient") and the green spectrum ("fire") during. Note increasing line presence and depth during the fire spectra, especially in (a) due to high amounts of CO_2 and CO.*

Figure 6.7 gives an example of the MALT fit for one of the "during fire" spectra for each of the spectral regions seen in Figure 6.5. The spectral region for CO_2 of 2150-2310 cm^{-1}

was used for the MALT fit, however the returned modeled spectra did not fit the measured spectra very well, as shown in Figure 6.7. The window was replaced by an alternative region of 2250-2310 cm^{-1}.
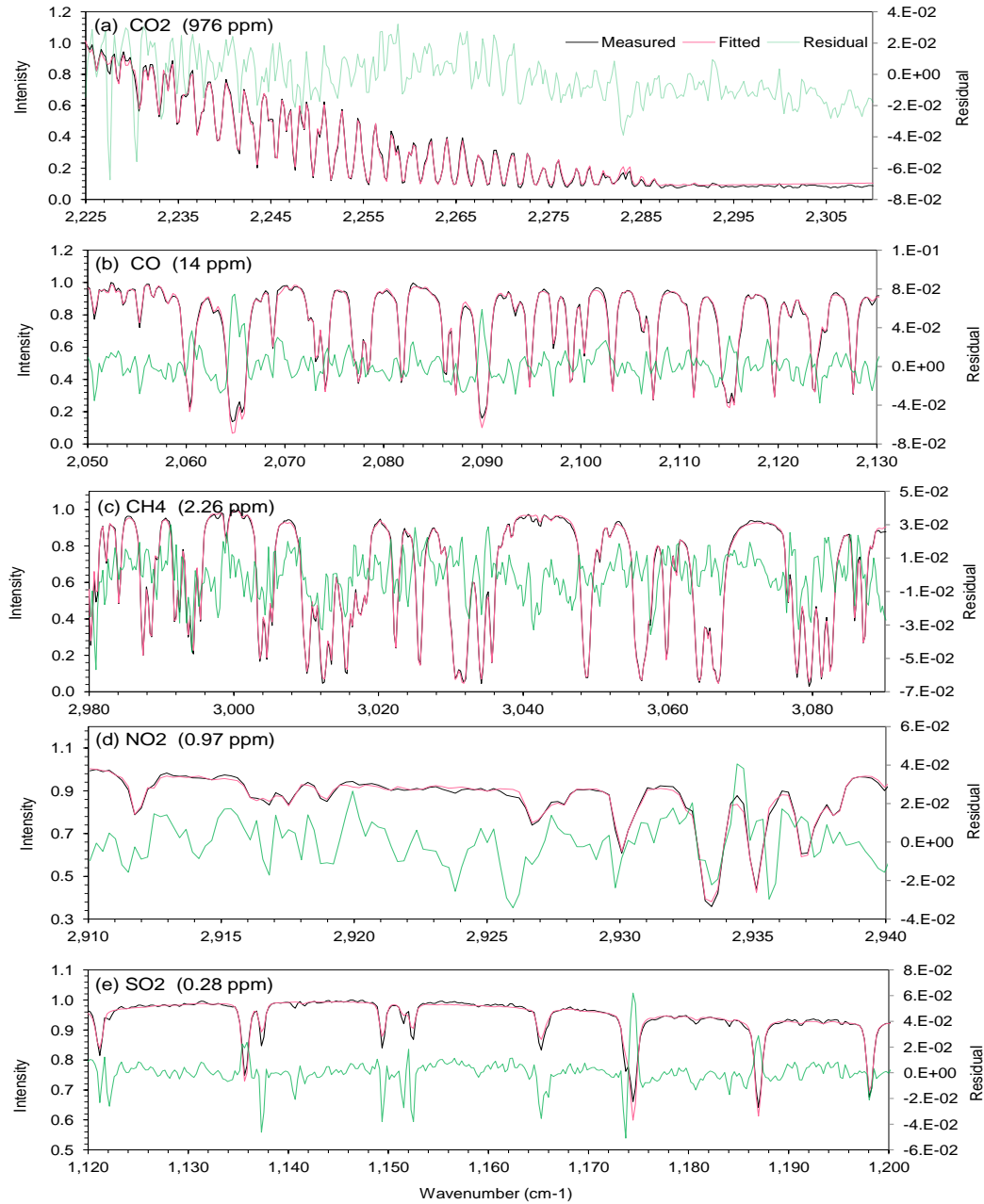
Figure 6.6: *An example of the fitted (black) and measured (red) fire spectra for all the target gases (a) CO_2, (b) CO, (c) CH_4, (d) NO_2 and (e) SO_2. Also shown is the residual between the two spectra (grey) and the pathlength averaged mixing ratio retrieved for each species (brackets). MALT (1996) was used to perform the fitting, it can be seen that there is a good fit between spectra for all wavenumber regions.*
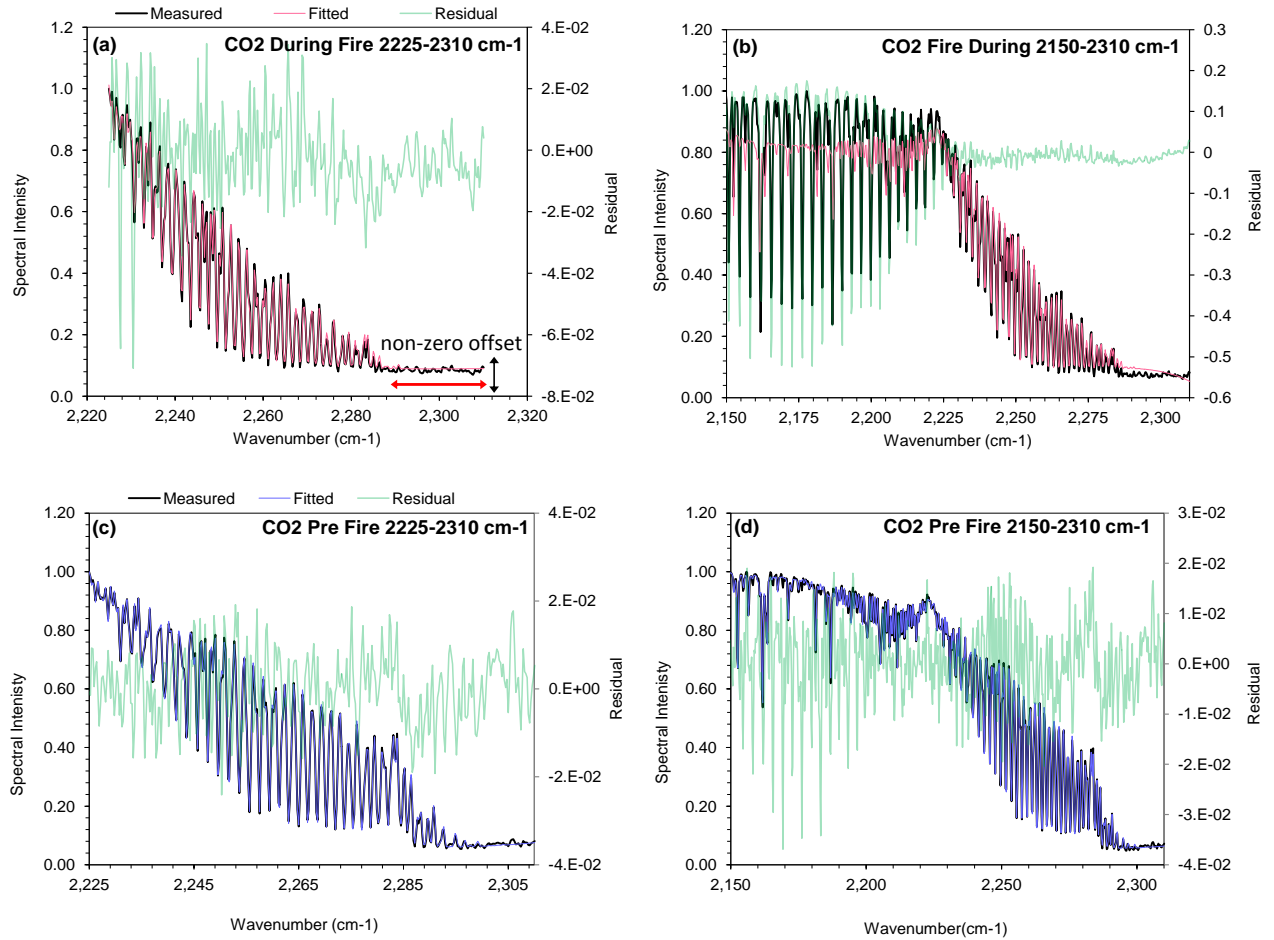
Figure 6.7: *Comparison of the spectral fitting windows [2225-2310] cm^{-1} and [2150-2310] cm^{-1} used for retrieve pathlength averaged mixing ratios of CO_2. Shown is the measured (black), fitted (pink) and residual (grey) spectrum for fits run on an ambient and fire spectrum. It can be seen that for the [2150-2310] cm^{-1} window the fit breaks down for the fire spectra (b) and the absorption features between 2150-2225 cm^{-1} are not evident in the fitted spectrum and thus are present in the residuals. Hence this window was not used in the retrievals of CO_2. Also note in (a) and (c) for the [2150-2310] cm^{-1} window, from 2288 cm^{-1} onwards the non zero offset can be seen. In this region the spectral intensity should fall to zero due to total absorption by CO_2. However this is not the case, due to for example, detector saturation and/or phase errors close to the absorption bands (Griffith et al., 2003).*

The fit across the spectral region of 2150-2310 cm^{-1} breaks down when there is strong absorption of CO_2 in the plume around 2150-2220 cm^{-1} (Figure 6.7 (b)), but appears adequate for ambient levels of CO_2 (Figure 6.7 (d)). It can be seen that the absorption features of CO_2 are present in residual, not the modeled spectrum in the former case. It is important

to look at the residual, for example if any asymmetrical features are found, this could be an indication of inaccurate FOV estimations or line strength positions. Inaccurate FOV values could be a result of the incorrect use of a symmetrical ILS when in reality instrument misalignments lead to an asymmetrical ILS. The features found in the residual in Figure 6.7 (b) can most probably be identified as the absorption features of the CO_2 in the plume. This breakdown of the fit for this spectral region could be due to the fitting of the zero offset. The zero offset is calculated in the region greater than 2300 cm^{-1} (see Figure 6.7), and the effect of any uncertainties in the calculation will be magnified in wavelengths further away from this area (Smith *et al.*, 2011). Also in the region of 2100-2200 cm^{-1}, there exists strong H_2O absorption features, which could have led to an inaccurate fit of the "fire" smoke plume spectrum in wavenumber region 2150-2310 cm^{-1}, due to the presence of the increased water vapour (H_2O) emitted by the fire.

6.2.2   Emission Ratios

The emission ratios were calculated using the retrieved pathlength averaged mixing ratios amounts as calculated above for the main parts of the fire. As detailed in Chapter 4 the emission ratio of a particular species x is usually calculated with CO_2 or CO as the reference species y, depending on whether species x is predominantly emitted in the flaming or smoldering phase of the fire. CO_2 is used for 'flaming' gases and CO for the 'smoldering' gases. Here emission ratios with respect to both gases have been calculated for comparison and later used in calculating emission factors. A linear regression method was used to derive the gradient between target gas x and reference gas y by fitting the data to the linear equation $y = a + bx$ by minimizing the chi-square error:

$$\chi^2 = \sum_i \frac{(y_i - y^*_i)^2}{y^*_i},$$
(6.1)

where y is the measured reference species (ppm) and y^* (ppm) is the is reference species derived by the model equation $y = a + bx$. Therefore the emission ratio $\mathrm{ER}_{\frac{x}{y}}$ for the species x with respect to reference species y is then taken as the derived gradient b. The Pearson correlation coefficient (r^2) is also calculated to evaluate the strength of the correlation between amounts of gases x and y. The errors computed for the emission ratios are described

in the next section.

It has been a standard procedure to use the excess amounts above background (for both target and reference gas) when deriving the emission ratios, i.e. by subtracting an ambient pathlength averaged mixing ratios outside of the fire plume (e.g. Yokelson *et al.*, 2007; Zhang *et al.*, 2008). However, others (e.g. Guyon *et al.*, 2005; Wooster *et al.*, 2011) have argued that subtraction is unnecessary. From Wooster *et al.* (2011) it can be inferred that, providing the target gas volumetric concentration is in the plume is much greater than in the ambient atmosphere, and that the plume does not take up the whole optical path between the spectrometer and lamp, the ambient pathlength averaged mixing ratios need not be subtracted from the measurements made during the fire. Suppose the x_p and x_a are the volumetric concentrations (molecules cm^{-3}) of target species x in the plume and ambient respectively. Denote y_p and y_a similarly for reference species y.

$$x_t = \delta l.x_p + (1 - \delta l).x_a \tag{6.2}$$

$$y_t = \delta l.y_p + (1 - \delta l).y_a \tag{6.3}$$

where δl is the proportion of the pathlength l taken by the plume and x_t and y_t are the total horizontal amounts (molecule cm^{-2}) of x and y measured in the pathlength between the spectrometer and lamp. Subtracting the ambient pathlength averaged mixing ratios of the species measured within the optical path without the presence of the plume will underestimate the above background pathlength averaged mixing ratios. The fraction of the total optical pathlength that is taken up by the plume, δl, is unknown and can vary during the duration of the fire, e.g. as the plume changes position and shape with the wind. However, by a simple rearrangement of Equations 6.2 and 6.3, the dependence of δl can be removed:

$$y_t = \left(\frac{y_p - y_a}{x_p - x_a}\right)x_t - \delta l\left[\left(\frac{y_p - y_a}{x_p - x_a}\right)x_a - y_a\right]. \tag{6.4}$$

This equation can be taken as the straight line equation used to calculate the emission ratios, with the gradient, m as the ratio of the excess pathlength averaged mixing ratios of the reference species to the excess pathlength averaged mixing ratios of the target species

$\frac{y_p - y_a}{x_p - x_a}$. If it is assumed that the mixing ratio of both species are much larger in the plume than in the ambient atmosphere, then the gradient m can be taken as the ratio of the two species in the plume, $\frac{y_p}{x_p}$. Section 6.3.1 shows that the retrieved pathlength averaged mixing ratios of the target gases in the presence of plume are very much greater than those measured just in the ambient atmosphere, hence it is reasonable to assume that the plume pathlength averaged mixing ratios are more abundant than background pathlength averaged mixing ratios and the ER can be calculated without the subtraction of the background abundances (Wooster *et al.*, 2011). The equations above are in molecule cm^{-2}, but the same applies when amounts are expressed as ppmm units and hence also ppm.

6.2.3   Emission Factors

Emission factors (EFs) for each of the target gases were calculated using the derived emission ratios. The method used is the carbon mass method, described in Delmas *et al.,* (1995). It assumes that all the carbon in the fuel combusted in the fire is released in the smoke as CO_2, CO, CH_4, non-methane hydrocarbons (NMHC) and particulate carbon (PC) (Sinha *et al.*, 2003). For this work, PM and NMHC shall not be included in the calculations of EF, but since the three species measured (CO_2, CO and CH_4) constitute more than 95% of the total carbon released by a fire (Delmas *et al.*, 1995), not including these other products will only underestimate the derived EF by 1-2 %(Yokelson *et al.*, 1999). The EF (gk.g^{-1}) for species x are hence calculated as follows (Ward and Radke, 1993):

$$EF_x = 1000 \times F_c \times \frac{mm_x}{mm_C} \times \frac{ER_{\frac{x}{CO_2}}}{1 + ER_{\frac{CO}{CO_2}} + ER_{\frac{CH_4}{CO_2}}} \qquad (6.5)$$

where F_c is the carbon content of the fuel (taken as 50% here (Susot *et al.,* 1997)), 1000 is used to convert units, mm_x is the molecular mass (g.mol^{-1}) of species x (see Table 6.2), mm_C is the molecular mass of carbon (12 g) and $ER_{\frac{x}{y}}$ is the emission ratio of species x to species y.

Table 6.2: *Molecular mass of the compounds used in the emission factor derivations according to Equation 6.5.*

Species	Molecular Mass $(g.mol^{-1})$
C	12
CO_2	44.01
CO	28.01
CH_4	16.04
NO_2	46.05
SO_2	64.07

6.2.4 FRP

The AGEMA-550 thermal camera, with a 3 - 5 μm spectral range, was used to collect airborne thermal images across a 320 x 240 pixel detection array during several fires. Note that a filter centered at 3.9 μm (as per the MODIS band 21 channel, used to generate the MODIS 'MOD14' fire products) was fitted to prevent saturation over high intensity fire pixels. The thermal camera made measurements during the fires on board a GPS-equipped helicopter hovering a few hundred meters above the plots. The camera is sensitive to brightness temperatures greater than 475 K (for brightness temperatures below this, no signal is observed with the filter however unsaturated data of fire pixels exceeding 1000 K can be obtained). This 475 K threshold was used to select active fire pixels within each image. Depending on the altitude of the helicopter, the pixel size was a few meters. The pixel size was determined using the viewing distance and the angle from helicopter to the plot (from GPS records). In addition to this, 'corner bonfires,' lit as ground-control points where possible if geocorrection of the imagery was required.

The brightness temperatures recorded by the AGMEA at each fire pixel were converted into spectral radiances using the Planck function, and the MIR radiance FRP retrieval method (Equation 4.9 in Chapter 4) was applied to calculate FRP (in Watts) of each pixel. The

results from all pixels with an image were summed to obtain a per fire FRP measure for that observation time. An FRP time-series was then generated using each image in turn ($\approx$ 5-second intervals) for the entire fire duration - or at least as long as the helicopter maintained position. Full details of this processing approach are given in Wooster *et al.* (2005) and Freeborn *et al.* (2008), and the methods used with the airborne deployment of the MIR camera are detailed in Wooster *et al.* (2011).
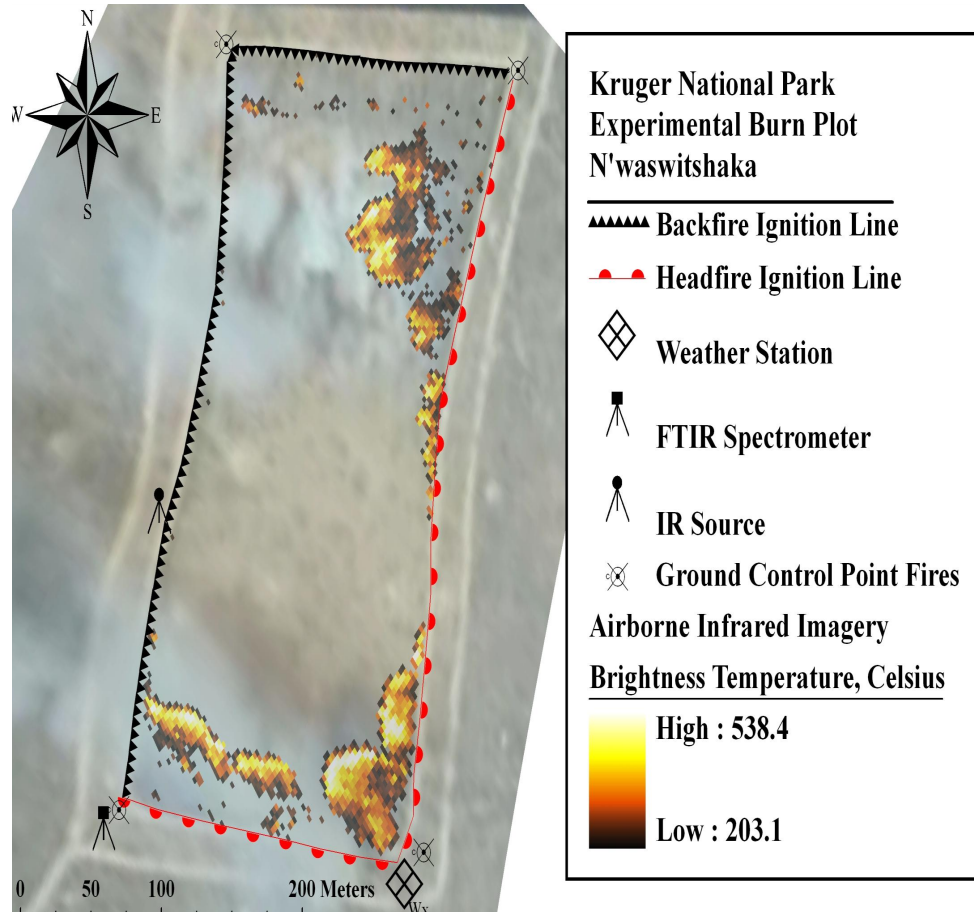
Figure 6.8: *Image from the from AGEMA-550 thermal camera of a fire in 2007 of the same area in Kruger National Park as that of this work. It is possible to see the spreading flame front highlighted by the AGEMA pixels identified as being above 475 K (Wooster et al., 2011)*

A digital video camera was mounted alongside the thermal camera, which was later useful for reviewing the location of the smoke plume with respect to the UV-DOAS traverses, and in helping to estimate the smoke plume height above ground. It is the case, that

where fire pixels were only weakly burning they may have pixel brightness temperatures below the 475 K threshold, and thus been missed by the detection algorithm and not had their FRP assessed. However, calculations indicate that only if we assume the flaming area has a temperature of 900 K (Wooster et al., 2003), for a background temperature of 300 K only 2% of the AGMEA pixel actually needs to be covered by flames for the pixel brightness temperature to rise above the 475 K detection threshold. For this reason, fire is very detectable in the AGEMA imagery, and the small pixel area obtained from the low altitude airborne imagery appears to ensure that the spreading fire front is reliably captured (see Figure 6.8) and inspection of the raw time-series clearly shows the fire front moving across the plot in the expected manner.

6.2.5 Trace Gas Fluxes

The FTIR derived emission ratios for fire SF1 can be combined with the DOAS derived flux rates of NO_2 in order to estimate the total carbon flux. This can then be compared to the FRP as calculated above, since FRP should in theory also vary with the rate of fuel consumption (i.e. rate of C flux). For this pilot study in South Africa, note that the NO_2 fluxes will be used, not the SO_2 due to generally higher pathlength averaged mixing ratios and less noisy retrieval of the former gas. For traverse i, the estimated total carbon flux $(g.s^{-1})$ released, F_{iC} is given as (Hager *et al.,* 2008)

$$F_{iC} = \left(\frac{F_{iNO2}}{ER_{\frac{NO2}{CO2}}} \times \frac{mm_{CO2}}{mm_{NO2}} \right) + \left(\frac{F_{iNO2}}{ER_{\frac{NO2}{CO}}} \times \frac{mm_{CO}}{mm_{NO2}} \right) + \left(\frac{F_{iNO2}}{ER_{\frac{NO2}{CO}}/ER_{\frac{CO}{CH4}}} \times \frac{mm_{CH4}}{mm_{NO2}} \right), \quad (6.6)$$

where the products in the brackets represent the flux rates of the individual gas rates CO_2, CO and CH_4. F_{iNO2} $(g.s^{-1})$ is the flux rate of NO_2 at traverse i. The rest of the terms are as above.

6.2.6 Error Budget

Retrieved Pathlength Averaged Mixing Ratios

The error is calculated using the covariance matrix S of the fitted parameters (Rogers, 2000):

$$S_{ij} = E[(x_i - \bar{x}_i)(x_j - \bar{x}_j)]. \tag{6.7}$$

The operator $E(.)$ is the expected value and $\bar{a} = E(a)$. Each element S_{ij} represents the relationship between fitting parameters x_i and x_j, with $S_{ij} = 0$ for independent x_i and x_j. Diagonal elements of S are equal to 1, with the off-diagonal elements ideally having values close to or equal to 0. Off diagonal values close equal to or equal to 1 should be avoided unless a change in the value of one parameter does in fact affect the value of another parameter. The errors associated with the pathlength averaged mixing ratios amounts of the target gases are calculated in MALT as their standard errors (Griffith *et al.*, 2003). For a given parameter i, its standard error is the sqaure root of the ith diagonal element in the covariance matrix $\sqrt{S_{i,i}}$.

Although the retrieval errors output by MALT are useful when investigating the quality of the retrieved target gas amounts, they should not be regarded as a true representation of how accurate the retrieved amounts actually are. In particular, Smith *et al.* (2011) found that when using MALT for OP-FTIR spectra collected from IR transparent cells containing known gas pathlength averaged mixing ratios, the reported retrieval errors were usually lower than the actual errors and did not show a strong correlation with them. Hence here retrieval errors have not been included in the error budgeting. When deciding which spectral fitting regions to use for each target gas, the strength of the match between the measured and modeled spectra played a greater role in the decision than the reported retrieval errors.

Emission Ratios

Uncertainties in the emission ratios were calculated from both the derived slope and intercept of the linear best fit $y = mx + c$. It is assumed that the a linear fit is the best model to fit

to the trace gas data of the two species. The error in the slope, δm is calculated as:

$$\delta m = \sqrt{\left(\frac{\sum_{i=0}^{N-1} x_i{}^2}{\sum_{i=0}^{N-1} x_i{}^2 - (\sum_{i=0}^{N-1} x_i)^2}\right) \cdot \left(\frac{\sum_{i=0}^{N-1} (y_i - a - bx_i)^2}{N - M}\right)} \quad (6.8)$$

and the uncertainty in the intercept δc similarly as:

$$\delta c = \sqrt{\frac{\sum_{i=0}^{N-1} (y_i - a - bx_i)^2}{(N - M) \cdot (\sum_{i=0}^{N-1} x_i{}^2 - (\sum_{i=0}^{N-1} x_i)^2)}} \quad (6.9)$$

The uncertainties of the slope were used in the in the calculation of the EF uncertainties, as detailed below.

Emission Factors

The emission factor error formula for each target gas is computed using the error relationships in Chapter 5. The formula is given as:

$$\delta ER_x = ER_x \sqrt{\left(\frac{\Delta FC}{FC}\right)^2 + \left(\frac{\Delta ER_x}{ER_x}\right)^2 + \frac{1}{(1 + ER_{CO} + ER_{CH4})^2}\left(\frac{\Delta ER_{CO}}{ER_{CO}} + \frac{\Delta ER_{CH4}}{ER_{CH4}}\right)^2},$$
$$(6.10)$$

where ΔER_x is the error of emission ratio ER_x of species x (whether its with reference species CO_2 or CO) as calculated above. ΔFC is the error for the fuel consumption FC, taken as 0.05 (taken from Sinha *et al.*, 2003). This formula is taken from Wooster *et al.* (2011).

Flux Rates

The flux rate uncertainties EF_x (g.s^{-1}) for species x ($x=CO_2$, CO and CH_4) are computed using the following formula:

$$\delta EF_x = EF_x \sqrt{\left(\frac{\Delta F_{NO2}}{F_{NO2}}\right)^2 + \left(\frac{\Delta ER_{\frac{NO2}{x}}}{ER_{\frac{NO2}{x}}}\right)^2}. \quad (6.11)$$

Note that for CH_4 the emission ratio $ER_{\frac{NO2}{CH4}}$ is calculated as the fraction $\frac{ER_{\frac{NO2}{CO}}}{ER_{\frac{CO}{CH4}}}$. The error for emission ratio, $\Delta ER_{\frac{NO2}{CH4}}$ is calculated in a similar manner.

6.3 Results from the South African Pilot Study

6.3.1 Pathlength Amounts

Figure 6.9 shows the retrieved horizontal pathlength amounts (ppm) for fire SF1 for the gases CO_2, CO, CH_4, NO_2 and SO_2. The NO_2 and SO_2 pathlength amounts were subject to a moving average (of 4) due to noisy results particularly out of the plume. No averaging was carried out with the rest of the target species as results appeared far less noisy in comparison to SO_2 and NO_2.
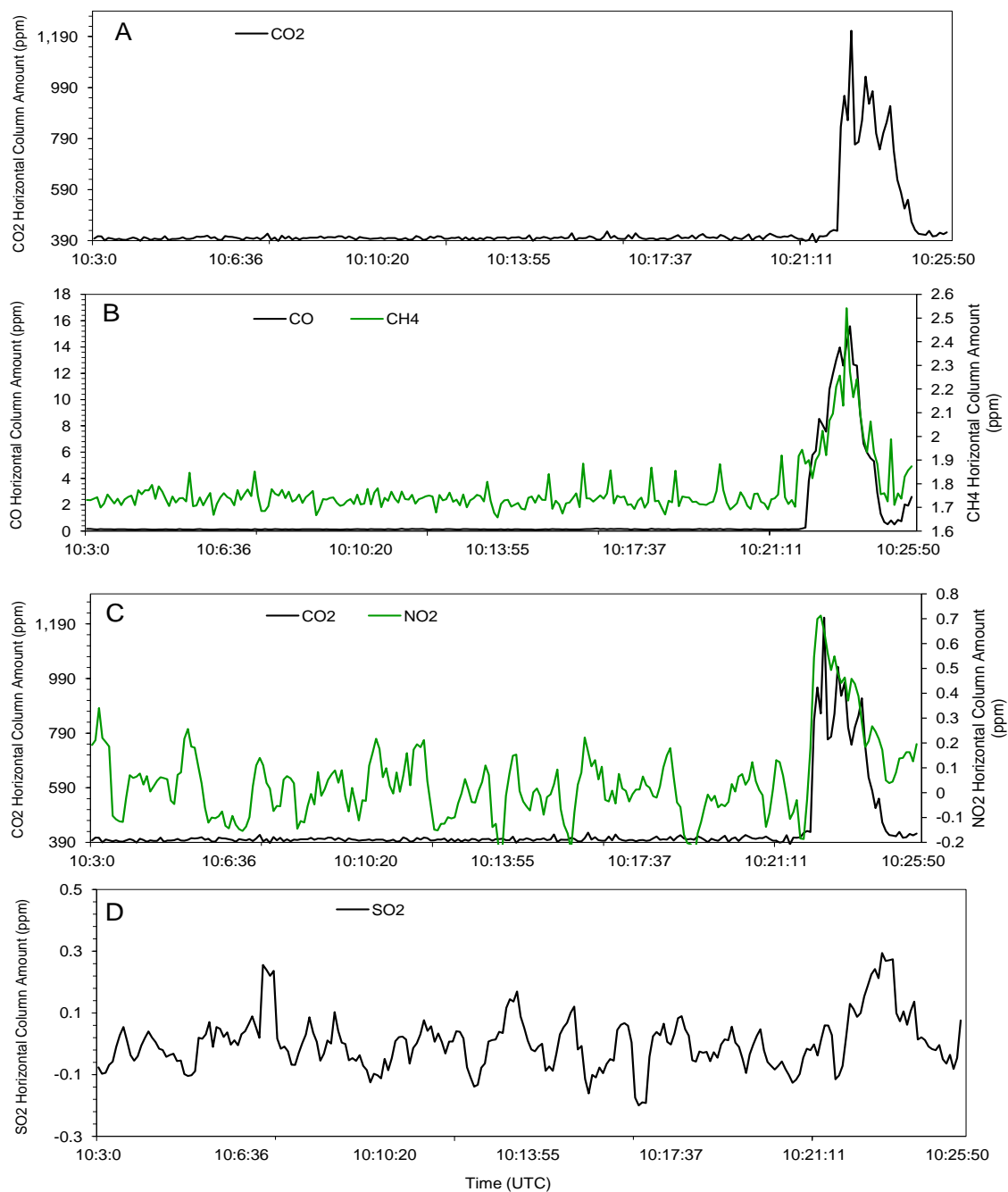
Figure 6.9: *The pathlength averaged mixing ratios amounts of CO_2 (a), CO (a), CH_4 (a), NO_2 (a) and SO_2 (d) retrieved by applying MALT to the FTIR spectra collected during South African fire SF1. Details of the retrieval variables are given in Table 6.1. A running average of factor 4 was applied to the SO_2 and NO_2 data for smoothing purposes. All gases show elevated amounts during the fire, apart from SO_2. This suggests that there was not sufficient SO_2 in the smoke to be able to be detected in the given spectral fitting window.*

For all target species apart from SO_2, there is a clear peak beginning at around 10:23. This is due to the presence of the smoke plume, resulting in pathlength averaged mixing ratios well above background level. For the case of retrieved pathlength averaged mixing ratios of SO_2, (Figure 6.9 D), there is no peak and hence no evidence of the plume. The suggests that the levels of SO_2 in the plume were too low to be detected by the FTIR in the spectral fitting region selected. NO_2 also has weaker absorption features in the IR compared to the carbon molecules, however retrieved levels were above background in the presence of the plume. This agrees with the results from the DOAS retrievals, that also indicate higher pathlength amounts of NO_2 existed compared to SO_2. However it is not possible to directly compare the FTIR and DOAS pathlength amounts, as the FTIR measurements unfortunately stop prior to the main part of the fire measured by the DOAS. The FTIR measured only towards the beginning of the fire, with smoke that had probably not yet reached the downwind DOAS instrument. Nevertheless, the emission ratios derived using the IR spectra for this part of the fire are expected to be valid for the whole fire event, and can be combined with the DOAS derived fluxes to calculate the total carbon flux.

The peaks of CO_2 and NO_2 have their maximum at a slightly earlier time compared with CO and CH_4. Figure 6.10 shows the retrieved pathlength averaged mixing ratios of CO_2 and CO, with the CO_2 pathlength averaged mixing ratios clearly peaking before CO. This is most likely because CO_2 and NO_2 are released mainly during flaming activity, while CO and CH_4 were emitted mainly during smoldering activity. When the fire starts, the majority of the the activity is flaming, whereas an area of smoldering fuel develops behind the flame front as the fire continues to advance across the plot. For NO_2, the plume elevated the pathlength averaged mixing ratios to approximately 7 times above background. For CO_2 and CH_4, during plume levels were approximately treble and double ambient levels. CO pathlength amounts were raised by 100 times more in the presence of the plume compared to the ambient background. These strong elevated amounts in the presence of the plume confirm that the subtraction of the background is not required to calculate the emission ratios, as detailed in Section 6.2.2.
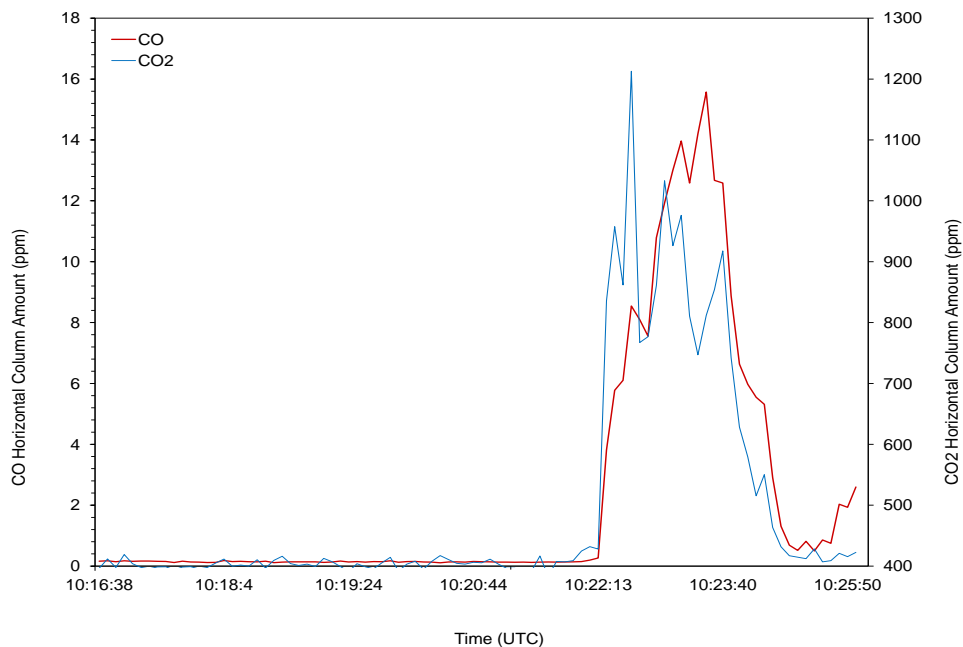
Figure 6.10: *The pathlength averaged mixing ratios of CO_2 and CO retrieved by applying MALT to the IR spectra collected during South African fire SF1. The CO_2 pathlength averaged mixing ratios peak early than those of CO, most likely as CO_2 is emitted predominately due to flaming activity, while CO is released mainly during smoldering activity, which only develops somewhat after the flaming front has moved across the plot.*

An attempt was made to separate the retrieved amounts of all target species according to the flaming and smoldering phases of the fire. However since only a relatively limited number of spectra were measured due to the FTIR operation ceasing midway through the burn, there was little variation in MCE and hence all pathlength amounts were kept together as the sampled smoke was most likely from a single fire phase. Figure 6.11 shows the MCE for the FTIR measurements calculated using Equation 7.1 in Chapter 1:

$$MCE = \frac{\Delta CO_2}{\Delta CO_2 + \Delta CO},$$ (6.12)

where ΔCO_2 and ΔCO are the elevated mixing ratios (plume mixing ratios minus the background mixing ratios) of CO_2 and CO respectively. According to Sinha *et al.* (2003), an MCE less than 0.90 represents smoldering activity within a fire. From Figure 6.11 it can be seen that the MCE for fire SF1 does not drop below 0.95, implying that the sample period was dominated mainly by flaming activity.
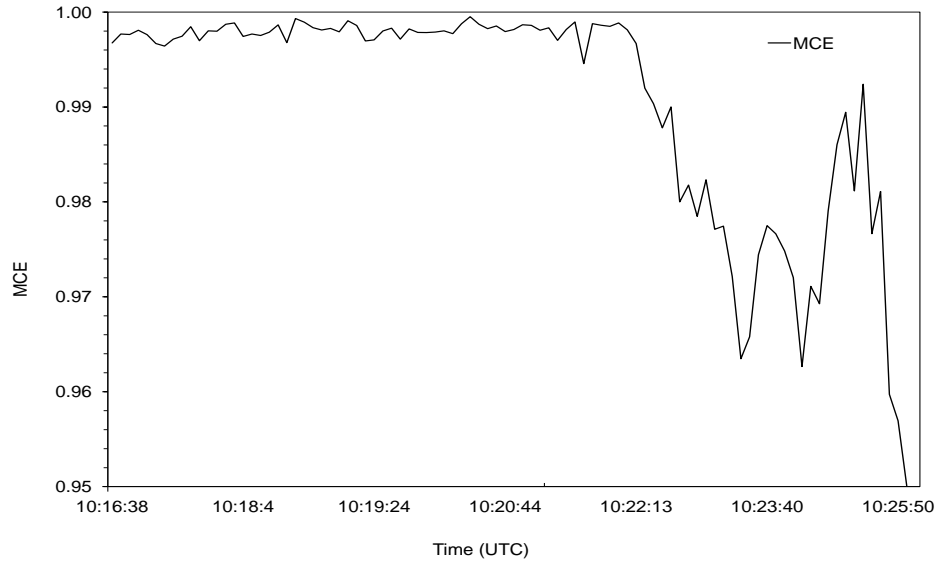
Figure 6.11: *The MCE calculated for fire SF1 according to Equation 6.12, using the mixing ratios of CO_2 and CO derived from the IR spectra. Notice that that MCE does not fall below 0.95, which suggests predominantly flaming combustion during the measurement period (Sinha et al., 2003)*

6.3.2   Emission Ratios and Emission Factors

The derived emission ratios from fire SF1, calculated from the retrieved mixing ratios of each of the target gases during the fire, are shown in Figure 6.12. The ratios were calculated with respect to both CO_2 (Figure 6.12 (a)-(d)) and CO (Figure 6.12 (e)-(g)).
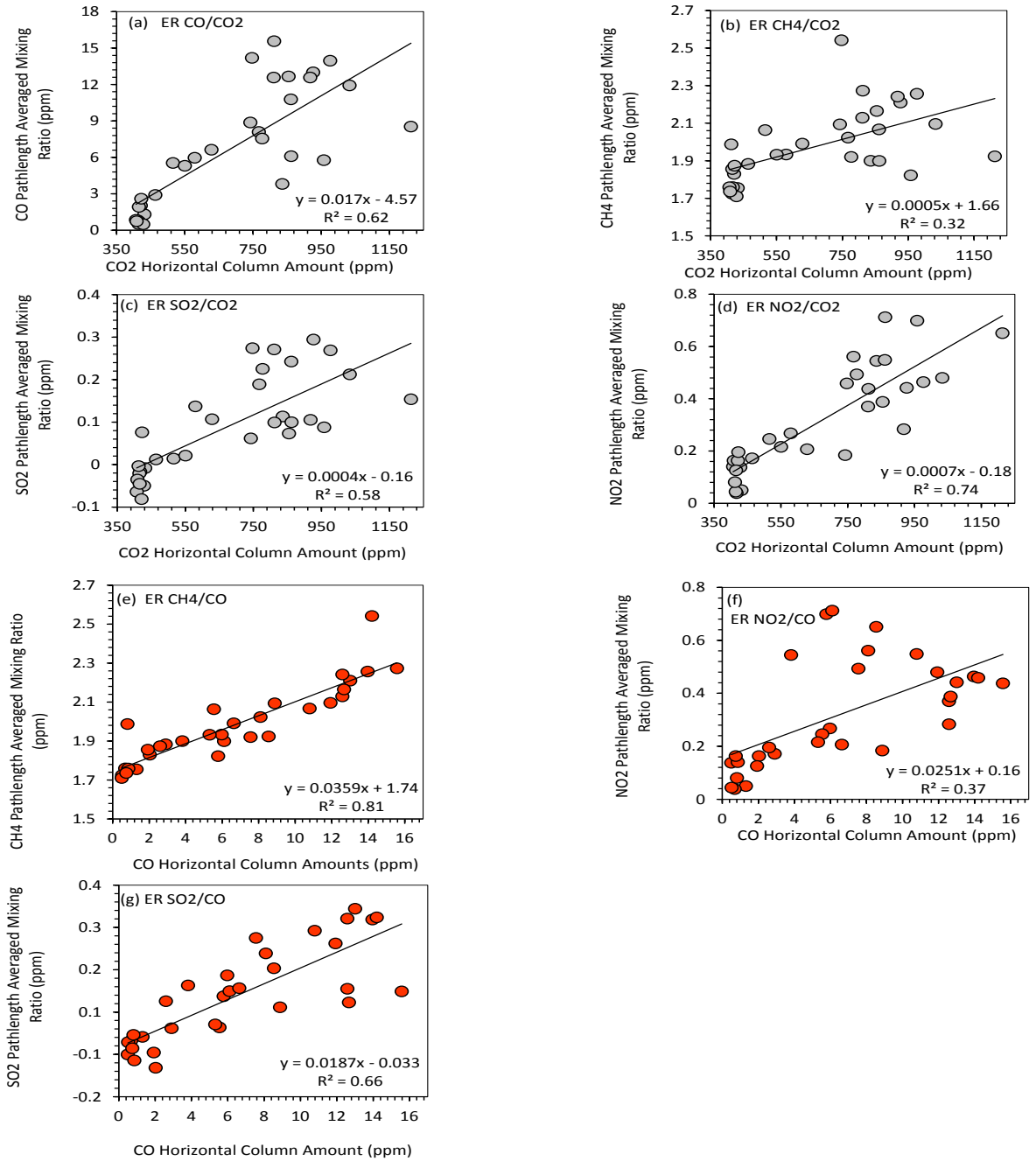
Figure 6.12: *Derivation of the Emission Ratios (ERs) of the target gases using CO_2 ((a)-(d)) and CO ((e)-(g)) as the comparison species. Values of the emission ratios are given in Table 6.3.*

Table 6.3 details the derived emission ratios for fire SF1 and their associated uncertainties.

Table 6.3: *Emission Ratios (and their uncertainties) calculated for all target gases with respect to CO_2 and CO for fire SF1 as shown in Figure 6.12. The r^2 value represents the strength of the linear fit to the data (used to derive the ER value), as shown in Figure 6.12.*

Species	Emission Ratio	Uncertainty	r^2
$\frac{CO}{CO_2}$	0.0165	0.0049	0.62
$\frac{CH_4}{CO_2}$	0.0005	0.0003	0.32
$\frac{NO_2}{CO_2}$	0.0007	0.0002	0.74
$\frac{SO_2}{CO_2}$	0.0359	0.0066	0.81
$\frac{CH_4}{CO}$	0.0251	0.0124	0.37
$\frac{NO_2}{CO}$	0.0002	0.0002	0.25
$\frac{SO_2}{CO}$	0.014	0.0082	0.38

It is clear to see from both Figure 6.12 and Table 6.3 that NO_2 shows a greater correlation with CO_2 (r^2=0.74) than with CO (r^2=0.37), suggesting that NO_2 follows CO_2 with emissions released predominantly in the flaming phase of the fire. This agrees with Figure 6.9 C where NO_2 and CO_2 have an emission peak at the same time. The remaining gases, CH_4 and SO_2, are better correlated with CO and hence appear to be emitted more preferentially during smoldering activity.

According to derived ratios in Table 6.3, out of all the target gases, CO is emitted in the greatest proportion with respect to CO_2, followed by NO_2 then CH_4. The emission ratio of CH_4 to CO_2 is comparably low, probably due to the part of the fire that was sampled. In comparison, the ratio for all target species to CO is much greater.

There exists a 'clump' of values from the CO_2 emission ratios, as sees in Figure 6.12 (a)-(d). This can be attributed to the end of the FTIR sampling period when CO_2 pathlength amounts fall to near ambient levels but the rest of the target species start to increase again, as seen around 10:25:00 in Figure 6.9. This could be due to smoldering activity where CO_2 ceases to be released in great quantities. From Figure 6.12 it can be seen that there are

points in the sampling period in which NO_2 emissions are high but CO are not, this corresponds to the flaming activity as these points are more correlated with the CO_2 emissions.

The derived emission ratios can be compared with those from previous studies. Although care should be taken when comparing from other studies due to different fuel types, measurement methods, smoke age and and sampling location (ground based or airborne), as for example, the composition of the smoke changes with time and possibly also with plume height. Table 6.4 lists emission ratios from previous studies with similar biomass types to this experiment, some have been averaged as there were multiple fire results from the same study. Note that emissions from a wider range of biomass types shall be investigated in Chapter 7. The ratio of CO to CO_2 from this experiment is lower compared to the equivalent literature values, particularly when comparing to Wooster *et al.* (2011) where measurements of smoke plume were made from the same ecosystems using the same instrumentation. This suggests that lower levels of CO were emitted with respect to CO_2 in the currently analyzed fire. This is probably due to the current data only being from a part of the fire, i.e. right at the beginning. If measurements were to be taken for a greater duration then it is probable that the proportion of CO to CO_2 would increase as more CO will be released in the smoldering zone that burns behind the flaming front. The same applied to the ratio of CH_4 to CO_2, because of the low levels of CH_4 emitted during the measurement period. Prasad *et al* (2000) estimated the ER $\frac{CO}{CO_2}$ for both smoldering and flaming stages of tropical forest fires in India. Values of this ratio ranged between 0.029-0.032 for flaming combustion and increased to 0.27 for smoldering combustion. Thus the $\frac{CO}{CO_2}$ ER for flaming combustion was much lower, implying the larger this ratio, the less efficient the combustion is. This backs up the suggestion that the $\frac{CO}{CO_2}$ ER derived in this pilot study represents mainly flaming combustion. Cofer *et al.* (1990) also found a fall in the $\frac{CO}{CO_2}$ ER when comparing smoldering and flaming combustion of African Savannas (0.048 and 0.046 respectively).

The value for ER $\frac{CH_4}{CO}$ is also lower compared to literature values, however by a lesser extent than foe CO. There is a lack of ER data for SO_2 and NO_2 in the literature, probably a result of the difficulties in measuring these gases in the smoke plume due to low pathlength

Table 6.4: *Emission Ratios of the target species CO_2, CH_4, CO, NO_2 and SO_2 derived from this work and selection of those available in the literature for several fuel types and sampling/analysis methods. Note that (AB) OP FTIR denotes (airborne) open-path Fourier Transform Infra-red measurements and (AB) GC (airborne) gas chromotography.*

Study	$ER_{\frac{CO}{CO_2}}$	$ER_{\frac{CH_4}{CO_2}}$	$ER_{\frac{CH_4}{CO}}$	$ER_{\frac{NO_2}{CO_2}}$	$ER_{\frac{NO_2}{CO}}$	$ER_{\frac{SO_2}{CO_2}}$	$ER_{\frac{SO_2}{CO}}$	Fuel Type	Sampling
This study	0.0165	0.0005	0.0251	0.0007	0.0002	0.0359	0.014	African Savanna	OP FTIR
Ferek et al. (1998)	0.0685	0.0069	0.124	-	-	-	-	Amazon /Cerrado	AB GC
Yokelson et al. (1999)	0.082		0.076	-	-	-	-	Pine	AB FTIR
Hobbs et al. (2003)	-	-	0.0398	-	-	-	0.01068	African Savanna	AB GC
Hobbs et al. (2003)	-	-	0.058455	-	0.0254	-	-	African Savanna	AB FTIR
Pak et al. (2003)	0.0214	0.0098	0.55	-	-	-	-	-	AB GC
Sinha et al. (2003)	0.072	-	0.039	-	-	0.00085	-	African Savanna	AB GC
Sinha et al. (2003)	0.064	-	0.053	0.0020	-	-	-	African Savanna	AB FTIR
Shirai et al. (2003)	0.089	-	0.043	-	-	-	-	Aus Savanna	AB insitu
Wooster et al. (2011)	0.096	0.0043	0.046	-	-	-	-	African Savanna	OP FTIR

averaged mixing ratios and weak absorption features in the IR. Apart from Wooster *et al.* (2011), the emission ratios in the literature have been calculated using airborne sampling methods. The chemical processes in the smoke evolve as it travels to greater altitudes hence gas pathlength averaged mixing ratios will be different when comparing airborne and ground based sampling (Shirai *et al.*, 2003). There needs to be more ground based measurements to give a wider degree of comparison and greater understanding of the activity of the smoke at ground level. For example CO gets removed from the plume as it travels long distances, hence the ER with respect to CO should increase with time (Pak *et al.*, 2003). Even if a species is not effected by chemical reactions in the plume, its mixing ratio will fall as the plume mixes with the air, however this effect should be removed when looking at in-plume ratios (Hobbs *et al.*, 2003). Shirai *et al.* (2003) compared airborne and ground samples from biomass plumes of Australian savannas. They found that the level and variation of ER was greater for the ground based samples compared to airborne. The high variability in ground based samples was accounted for by the short sampling period from just one fire in contrast to the airborne samples that were from many fires at different pyrogenic stages.

When looking at the individual fires sampled by Sinha *et al.* (2003) using the AFTIR, estimated ER are closer to the values returned for this study. In particular for one of the fires, the ER of CO with respect to CO_2 is given as 0.026, close to the value given here as 0.017. For the same fire, the ratio CH_4 to CO is reported at 0.038, with another fire as 0.036, compared to the value of this study of 0.025.

Hobbs *et al.* (2003) and Sinha *et al.* (2003) both used gas chromatography and FTIR measurements to estimate the emission ratios. Both studies show variations in the ER derived using the two methods. Although the samples for both methods were probably not made using exactly the same smoke, this shows how variable derived emission data an be and re-enforces the need for accurate estimates of such emissions.

Table 6.5 gives the emission factors calculated from the emission ratios given above. The first thing to note are the large relative errors. This can be attributed to the low emission

ratio of CH_4 to CO_2 and its high relative error. This reflects the low level of CH_4 that was emitted during this sample period. The low CH_4 to CO_2 ratio has subsequently lead to a low emission factor for CH_4. In contrast, the emission factor of NO_2 is relatively high, due its higher emission ratio with respect to CO_2. To get a more accurate measure of the emission factors, more samples need to be undertaken. However this sample is sufficient enough to be used to get an idea of the emission behaviors of the fire.

Table 6.5: *Emission Factors (and their uncertainties calculated) for fire SF1.*

Gas Species	Emission Factor $(g.kg^{-1})$	Error $(g.kg^{-1})$
CO_2	1803.10	1200.56
CO	18.93	13.80
CH_4	0.33	0.29
NO_2	1.32	0.96
SO_2	0.52	0.63

As with the emission ratios, the emission factors calculated here are compared with EF from the literature of studies in which fires of similar vegetation type have been analyzed, shown in Table 6.6.

Table 6.6: *Emission Factors (g.kg^{-1}) of the target species CO_2, CH_4, CO, NO_2 and SO_2 derived from this work and a selection of those available in the literature for several fuel types and sampling/analysis methods. Note that (AB) OP FTIR denotes (airborne) open-path Fourier Transform Infra-red measurements and (AB) GC (airborne) gas chromotography.*

Study	EF CO$_2$	EF CO	EF C4$_4$	EF SO$_2$	Fuel Type	Sampling
This Study	1803.10	18.93	0.33	0.52	African Savanna	OP FTIR
Sinha *et al.* (2003)	1700	68	1.7	0.43	African Savanna	AB GC
Sinha *et al.* (2003)	1706	69	2.2	-	African Savanna	AB FTIR
Shirai *et al.* (2003)	1613	88	2.22	-	Aus Savanna	AB GC
Wooster *et al.* (2011)	1665	101	2.5	-	African Savanna	OP FTIR

The EF for CO_2 derived in this work is generally greater than those from the literature (Table 6.6). This is due to the high levels of CO_2 emitted relative to the other carbon species measured, as shown by the ERs listed in Table 6.4. In contrast, the EF for CH_4 and CO are lower, are a result of low emission ratios of these gases to CO_2. However, when looking at the EF from the individual fires from Sinha *et al.* (2003) that were derived using gas chromatography methods, some results are a close match to the EF results of this pilot study. For example, for two individual fires from Sinha *et al.* (2003), the derived EFs of CO are 24 and 23 respectively and for the same fires the CH_4 EFs are given as 0.6 and 0.8. The relatively high CO_2 EF compared to that of CO and CH_4 suggests that the part of the fire that was sampled in this pilot study was dominated by flaming activity. Ward *et al.* (2004) derived flaming and smoldering EFs from tropical forests and pasture fires in the Brazilian Amazon. The smoldering EFs for CO_2 were almost 10% lower than the flaming for both tropical forests (1528 gKg^{-1} and 1665 gKg^{-1} respectively) and the tropical pastures (1529 gKg^{-1} and 1698 gKg^{-1} respectively). The converse is true for CO and CH_4, where smoldering EFs for CO reach up to double those of the flaming EFs and smoldering

CH$_4$ three times greater than the equivalent CH$_4$ EF. Yokelson *et al.* (2007) suggests that a high MCE value for one of the sampled smoke plumes was due to sampling not carried out for the whole fire, hence only the beginning of the fire was sampled where smoldering combustion contributes less. Again there is a lack of EF for savanna ecosystems for SO$_2$ and NO$_2$, Though the EF for SO$_2$ given by Sinha *et al.*, (2003) is close to that found here. Sinha *et al.* (2003) reports high errors for this EF due to the high variability of the sulphur content in the fuels that were sampled. In Chapter 7 the EF results determined using the FTIR approach shall be compared with those from different ecosystems from the literature.

6.3.3 Fluxes and FRP

The emission ratios calculated during this pilot study in South Africa were combined with the NO$_2$ fluxes derived via the UV-DOAS spectrometer transects in order to estimate the fluxes for each of the carbon species. The NO$_2$ flux was chosen as it was generally more abundant for both the DOAS and FTIR measurements. The method used to combine this data was detailed in Section 6.2.5, results are shown in Figure 6.13.
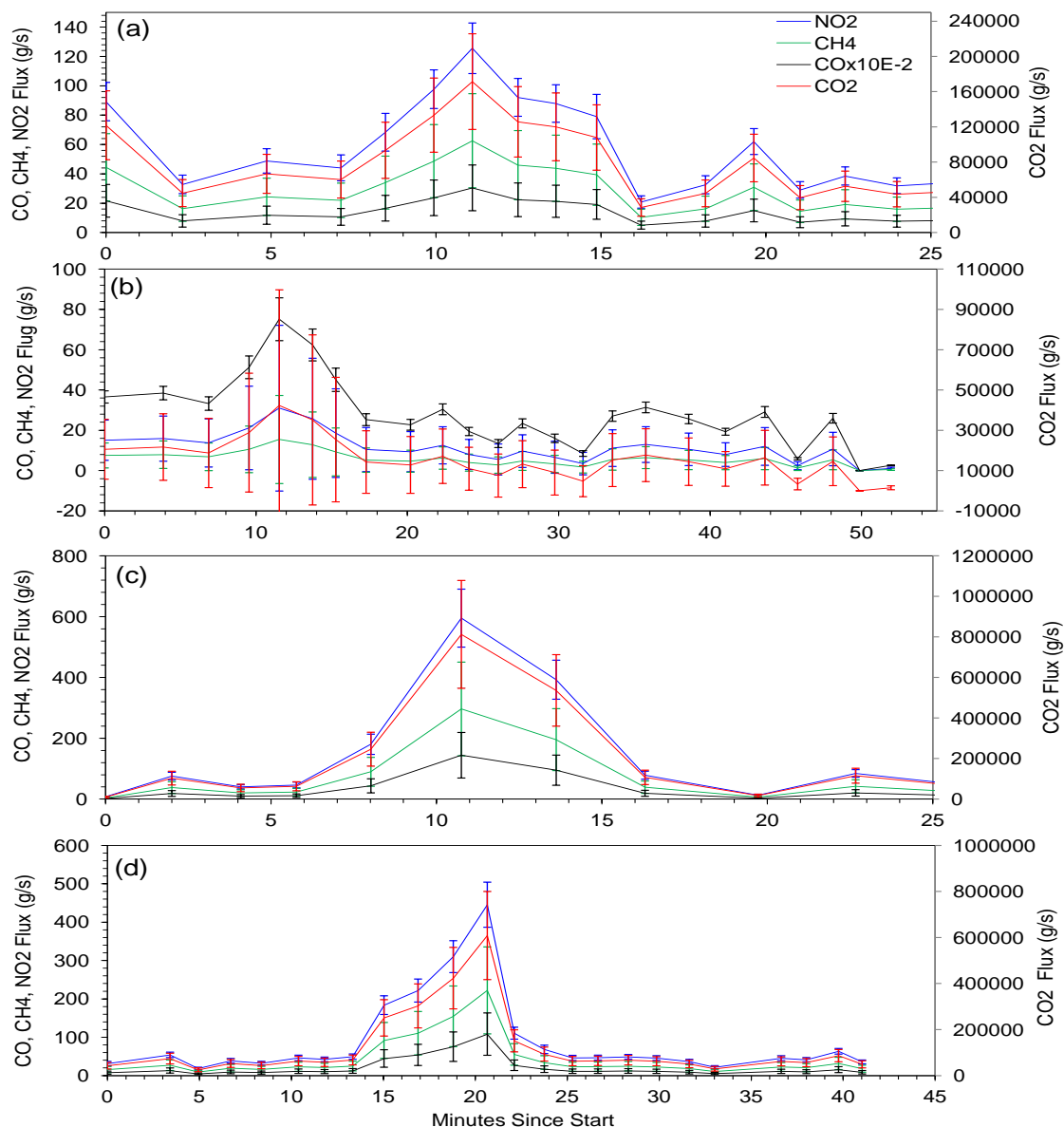
Figure 6.13: *The fluxes of NO_2, CO_2, CO and CH_4 for fires SF1-SF4 (a-d) from the South African pilot study. The NO_2 flux for each fire was calculated using the pathlength averaged column amounts of NO_2 derived from the UV-DOAS spectra, as detailed in Chapter 5 and shown in Figure 5.29. The emission ratios in Table 6.3 were applied to the NO_2 flux rate for each fire to calculate the flux rates of CO_2, CO and CH_4, as in Equation 6.6.*

Figure 6.13 presents the flux rates from the four different South Africa fires SF1-SF4 (a-d), using the different flux rates of NO_2 derived from the UV-DOAS spectra, detailed in Chapter 5 using the emission ratios of SF1, from Table 6.3. Although the fuel type of fires

SF2-SF4 are not exactly the same as that of SF1 they are similar and for this pilot study it is assumed sufficient to use the emission ratios of SF1 for the rest of the fires. If can be seen that because of the low emission ratio of CH_4 to CO_2 compared with NO_2, the CH_4 fluxes for all fires are relatively lower than those of NO_2, with a ratio of approximately 0.5. CO_2 fluxes reach high values, ranging from 40 $kg.s^{-1}$ for fire SF2 to 800 $kg.s^{-1}$ for fire SF3. These high values can possibly be attributed to the low ratio of NO_2 to CO_2, (0.0007). From Table 6.4, it can be seen that Sinha *et al.* (2003) presents an equivalent emission ratio at 0.002, almost three times higher than the value derived here. Due to the short sampling time of the FTIR measurements for this pilot study, it could be that the NO_2 to CO_2 derived emission ratio for SF1 is unrealistically low, leading to the high CO_2 flux rates. However there is not enough ER data in the literature to make strong comparisons. The high errors from fire SF2 (Fig 6.13 (b)) are due to the high errors from the NO_2 DOAS flux, determined in Chapter 5. Note that the UV-DOAS and FTIR in general do not sample the same smoke from the fires. The UV-DOAS, with its telescope pointing zenith, tends to sample smoke that rises to higher altitudes compared to that sampled by the FTIR, which makes measurements from ground level smoke, emitted from more smoldering combustion than the smoke that is injected to higher altitudes. Hence although each of the instruments may favor either flaming (UV-DOAS) or smoldering (FTIR) combustion at times, the carbon species derived flux rates are an integration of both.

The fluxes of CO_2, CO and CH_4 were used to calculate a total carbon flux, via Equation 6.6, which was then compared to the corresponding FRP time series. This is shown in Figure 6.14, results for fire SF1 are absent as there is no FRP data for that fire.
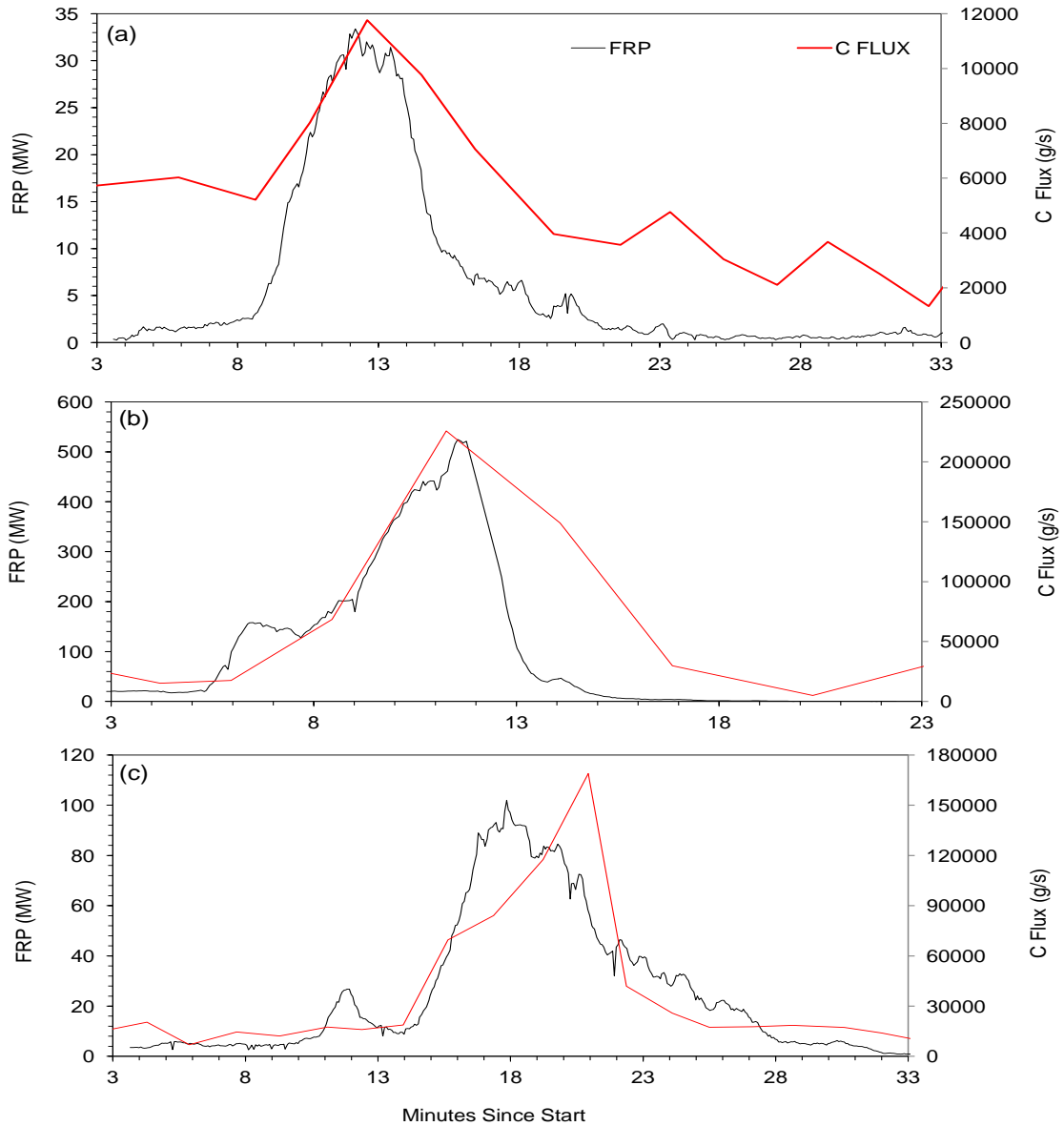
Figure 6.14: *The total carbon flux rates (g.s^{-1} of the South African fires SF2-SF4 (a-c) shown in red and calculated by applying Equation 6.6 to the flux rates of CO_2, CO and CH_4 in Figure 6.13. These are compared with the FRP time series (mw) of the same fires derived from the MIR thermal camera observations made in a helicopter above the fires, shown in black.*

It can be seen that in general the fluxes and the FRP follow a similar temporal pattern, peaking at similar times. There is a discrepancy with respect to time for the 2 sets measurements, due to the infrared imager instantaneously measuring changes in the fire radiation

energy signature (corresponding to changes in the fuel consumption rate), whereas the flux rates change only after the plume has reached the downwind DOAS measurement location. The FRP time series has a measurement for each point in time whereas the fluxes have a measurement over a period of time, i.e one measurement for of each traverse of the UV-DOAS spectrometer. Hence the datasets are not directly comparable in time, and are not expected to peak at exactly the same time. However the strong correlation between the two measurements gives confidence to the efficiency of the methods used. Note that the FRP time series has an error of approximately $\pm 20\%$, coming from pixel level uncertainty and cooler parts of the fire remaining undetected due to a detection limit of 200^oC of the camera. A consequence of this detection limit is that some of the fire pixels remain undetected by the thermal camera, causing the FRP of the fires to be underestimated.

6.4   Conclusion

A pilot study was conducted to explore the use of field spectroscopy methods to determine trace gas mixing ratios from prescribed open vegetation fires and subsequently the estimation of carbon fluxes from these fires using the synthesis of two ground based remote sensing instruments. For this pilot study, FTIR measurements were only available for a short period at the beginning of one fire (SF1). This has allowed for the investigation of the OP-FTIR measurements in this experimental set up and the synthesis of these measurements with UV-DOAS derived trace gas fluxes and MIR thermal camera derived FRP rates. FTIR measurements were not used from the remaining fires due to instrumentation problems and unavailability. Despite the sampling not being totally representative of the actual fire of SF1 as not all the characteristics of the whole fire were sampled, it has allowed from some useful insight into the behavior of emissions from the fire.

Pathlength averaged mixing ratios of the main carbon species, CO_2, CO and CH_4, in the smoke plume emitted by SF1 were quantified using measurements from the OP-FTIR during. Pathlength averaged mixing ratios of SO_2 and NO_2 were also derived. Pathlength averaged mixing ratios of all the target gases, apart from SO_2, exhibited above background levels when the fire started. This allowed for the calculation of emission ratios and emission

factors of the target gases. The inability to detect an increase in SO_2 pathlength averaged mixing ratios can be attributed to the low pathlength averaged mixing ratios of this gas in the smoke along with the weak absorption features within the FTIR spectral range.

Due to the timing of the FTIR measurement period at the start of the fire, the smoke that was sampled was probably emitted from predominately flaming combustion. This can be inferred by the corresponding MCE measurements not falling below 0.95, suggesting predominately flaming combustion (Sinha *et al.*, 2003). This can be used to explain the relatively low ERs of the target species with respect to CO_2 in comparison with those in the literature. When comparing the calculated EFs from this pilot study with those found in the literature, the CO_2 value given here was found to be relatively high while the remaining gases low. This again can possibly be attributed to the high level of flaming combustion that was sampled by the FTIR. There was a notably lack of ER and EF data for both NO_2 and SO_2 in the literature. Also the majority of studies have used airborne measurements, this gives a bias on the emissions from airborne measurements. This work can help fill these gaps.

Emission ratios were combined with the NO_2 flux rates for each of the South African fires to get an estimate of the total carbon flux. Although fuel types varied for each fire, they are are all still within the savanna ecosystem group. Another point to note is that the FTIR and DOAS are not sampling exactly the same smoke, hence the CO_2, CO and CH_4 flux rates derived using the UV-DOAS NO_2 fluxes and FTIR ERs represent an integration of the smoke measured by UV-DOAS and FTIR. The estimated CO_2 fluxes reached high values, up to 800,000 g.s^{-1}. This can possibly be attributed to the low derived ER of NO_2 to CO_2.

The total carbon flux for fires SF2-4 was compared with the FRP time series from the same fire. The was a good correlation between the two measurements, giving confidence to the two methods, as both showed the same pattern of increasing and decreasing with the time of the fires. Both the carbon flux and the FRP are assumed to vary with fuel consumption, the former relating to the carbon content of the fuel and the latter to the intensity of the fire. The fact that both variables follow the same trends with respect to time gives

279

confidence, particularly as they were derived from completely different methods, one based on the smoke released by a fire and the other by the energy emitted.

In conclusion, the FTIR is a potentially useful tool in terms of obtaining consistent estimations on ERs and EFs, which are used to model biomass burning emissions, particularly EFs in Equation 1.7. Currently EFs used in biomass burning emission estimation models are derived from a variety of methods and instruments. Hence the derivation of EFs from the FTIR of open vegetation fires from different biomass types will allow for a strong, consistent database to be used in emission models. In addition, the link between the UV-DOAS and FTIR allows for the estimation of carbon fluxes, providing information of the variation of carbon emissions of the fire over time, another useful input in emission models. However, the collection of strong data relies on enough smoke to be present during the fire. Yet it can be argued that smaller fires that do not emit substantial amounts of smoke have less of an impact on the environment. The strong correlation shown here between the carbon fluxes and FRP rate give confidence to those using FRP to estimate biomass burning emissions; currently there is no other type of validation for using the FRP in this way. However the data presented in this Chapter is pilot study, addition investigation needs to be carried out on these issues.

Chapter 7

UV and IR Spectroscopy Data Synthesis

Contents

7.1 Introduction

Subsequent to the pilot studies detailed in Chapters 5 and 6, this Chapter focuses on the analysis of spectroscopic measurements made by the DOAS and FTIR on several managed

fires in Arnhem land, Northern Australia. Here, data collection proceeded more smoothly and was more complete. Two sets of fires took place in Australian tropical savanna ecosystems, during both the early (June/July) and late (September/October) burning season of 2009. As in Chapter 5, the UV-DOAS spectral measurements were used to retrieve vertical column amounts of NO_2 and SO_2, which were then used to estimate corresponding trace gas fluxes via integration over transects made under the plume combined with the estimated wind speed at plume height. Similarly, as in Chapter 6, pathlength averaged mixing ratios of CO_2, CO, CH_4, SO_2 and NO_2 were returned via analysis of IR spectra measured by the OP-FTIR, and subsequently used for the calculation of ER and EF of these species. The DOAS flux rates and IR-derived emission ratios are combined, as in Chapter 6 to derive an estimate of the total carbon flux from each fire. Where possible, these carbon fluxes are then compared with the matching FRP time series for the same fire, as derived from MIR thermal camera measurements made from a helicopter.

The research presented in this Chapter contributes to the WALFA (West Arnhem Land Fire Abatement Project) 2009 project. This project investigated the variability of trace gas emission factors for CH_4 and N_2O from biomass fires occurring in the study area in early and late dry season of 2009. Variations in CH_4 EF from different fuel types were previously reported by (Korontzi *et al.,* 2003), mainly due to variations in fuel types, fuel load, fuel moisture, fire intensity and combustion efficiency. WALFA originated in 1997 as an initiative based on investigating the impacts of severe wildfires and fire management issues in the indigenous owned savanna ecosystems of western Arnhem Land, and subsequently included the potential incorporation GHG emission reductions into fire management practices. (Whitehead *et al.*, 2008). Two field campaigns were undertaken during WALFA 2009 in July and October, representing the early and late dry season fires respectively. Meyer *et al.* (2012) discusses the seasonal variability of biomass burning emissions from the same fires of this work. It was found that there was no major differences between GHG emissions between the early and late dry season fires due to fuel moisture etc.., however there were some differences linked with fuel composition.

The results presented here from Australia will be compared to those from the other field campaigns as well as data from the literature. This will allow for a discussion regarding the differences and similarities in emissions in different types of ecosystems.

7.2   Field Site

Vegetation

The WALFA 2009 field campaign was conducted around the area of Kabulwarnamyo, close to the Liverpool river (see Figure 7.1), in western Arnhem Land, Australia.
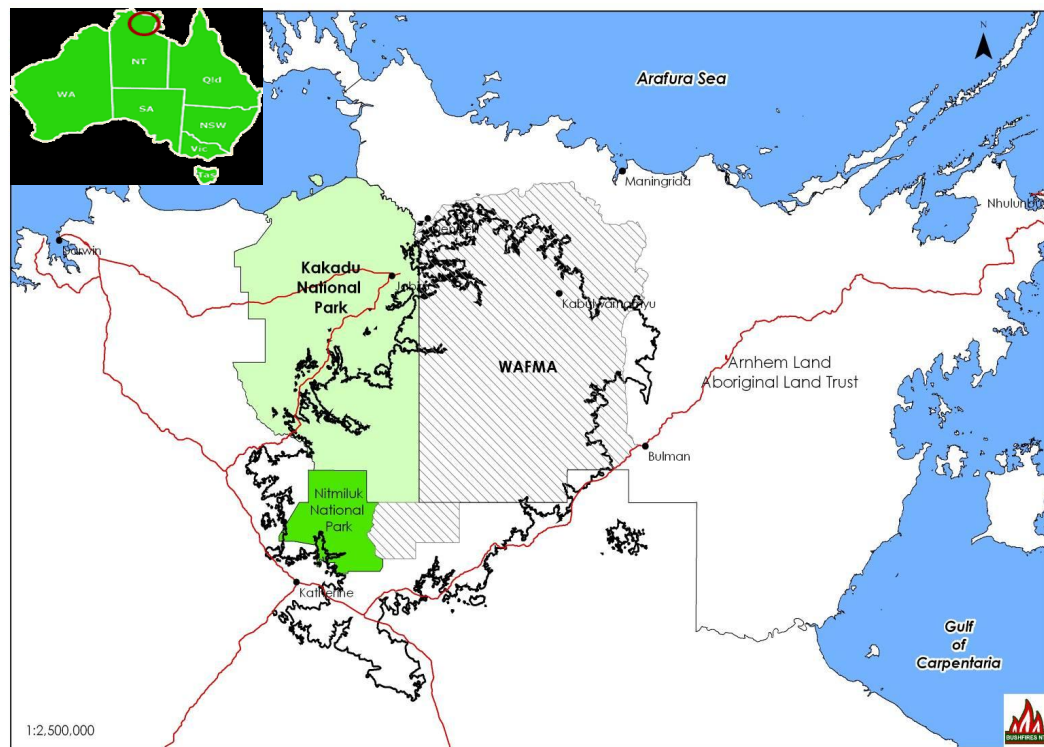
Figure 7.1: *Map of the Western Arnhem project area (WAFMA), showing the location of the Kabulwarnamyo field site. Location of Arnhem Plateau given as black line contour. From Bush Fires Northern Territory (2009). Top left shows the project area in relation to the rest of Australia.*

The WALFA study area consists of the Arnhem Land plateau, which is generally less than 400 m elevation (Russel-Smith *et al*, 1997) and the neighboring lowlands. Vegetation includes monsoon forest areas, grasslands and open forests compromising of *Melaleuca* and *Eucalypt*

savannas (Russel-Smith *et al.*, 1997). The plateau area is a mixture of mainly low woodlands with shrub species, such as *Acacia, Asteromyrtus, Calytrix, Hibbertia, Hibiscus, Pityrodia and Tephrosia* and tree species *Eucalyptus, Gardenia and Terminalia*. A common grass type is the spinifex *Symplectrodia, Triodia*, which is highly flammable. Other common grass species include *Aristida, Eriachne, Schizachyrium and Sorgum* (Russel-Smith *et al.*, 1998). The identification of different vegetation types may be important as they may in part determine the fire characteristics and the makeup of the gaseous species emitted. Figure 7.2 shows examples of the type of vegetation in the areas that were burnt.

Figure 7.2: *Example images taken from the burn plots of the Australian field campaign. Top: A pre-fire image taken in the middle of a burn plot, showing the typical savanna type vegetation found in the plots. Bottom: The road traversed by the DOAS vehicle beside a burn plot. Taken by author*

Typical fire management techniques include aerial burning, which is used to create fire breaks around and within the project site so as to prevent fires entering from other parts of the study area. This is accompanied by the implementation of fire breaks by vehicles and foot, for fires that occur within the study area. Such a two tier system aims to reduce the dangers associated with burning in an environment that is so prone to fires (Whitehead *et al.*, 2008).

7.3 Measurement Techniques

The measurement principles for the DOAS and FTIR instruments used in Australia followed those already explained in Chapters 5 and 6 respectively. To avoid repetition, below are details specific to this field campaign only. Table 7.1 presents details of the five fires analyzed during this campaign

Table 7.1: *Details of all fires carried out in both the early and late dry seasons.*

Fire Name	Season	Date	Remote Sensing Instruments Deployed
AF1	Early	02/07/2009	DOAS, FTIR
AF2	Early	03/07/2009	DOAS, FTIR
AF3	Early	04/07/2009	DOAS, FTIR, Thermal Camera
AF4	Late	30/09/2009	DOAS, FTIR
AF5	Late	01/10/2009	DOAS, FTIR, Thermal Camera

There are five fires in total, three and two for the early and late burning seasons respectively. Figure 7.3 shows some example photographs from the field campaign.

Figure 7.3: *Images of the burn plots of the Australian field campaign taken during the fires. Taken by author.*

There exists FTIR and DOAS measurements from all five fires and two fires for which comparisons can be made with FRP data derived from the thermal camera measurements. Unlike for the South African pilot study, detailed in Chapter 6, for this field campaign sufficient FTIR measurements were collected to gain strong estimates of ERs and EFs. As with the South African field campaign, a weather station positioned close to the fire plots ($\approx$ 3m height) was used to record ambient meteorology during all fires. Figure 7.4 shows the location of the fire plots with respect to one another. Fires AF1 and AF2 from the early season burns, and fires AF4 and AF5 from the late season burns were all carried out within the same area. Fire AF3, approximately 10 km from the area of the other burn plots, was chosen for its greater fuel loading compared to AF1 and AF2 during the early burning season field campaign.
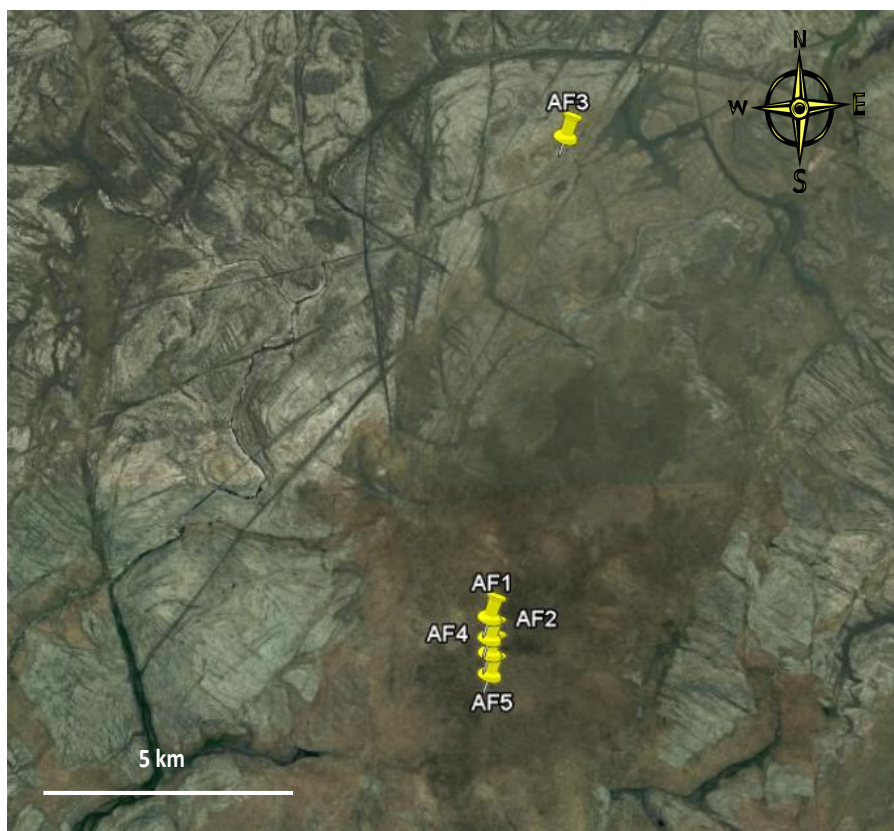
Figure 7.4: *The location of each of the burn plots of fires AF1-AF3 (early burning season fires) and AF4-AF5 (late burning season fires) from the Australian field campaign, calculated using GPS location measurements taken during the field campaign, displayed using Google Earth. Note that fire plots AF1, AF2, AF4 and AF5 lie close together however the burn plot of AF3 is located approximately 10 km away, due to its higher fuel loading in the early burning season field campaign.*

Figures 7.5 and 7.6 plot the locations in more detail. In Figure 7.5, the outline of each of the plots, measured using GPS, (in yellow). Note that the plot outline for fire AF5 is incomplete due to GPS failure. Where available, the exact locations of the FTIR spectrometer and weather station are given. The red arrow indicates the direction of the DOAS traverses. The location of the static 'corner fires' (used to georeference the aerial thermal imagery) for fire AF3 are shown in Figure 7.6 as well as the DOAS traverse path (red).
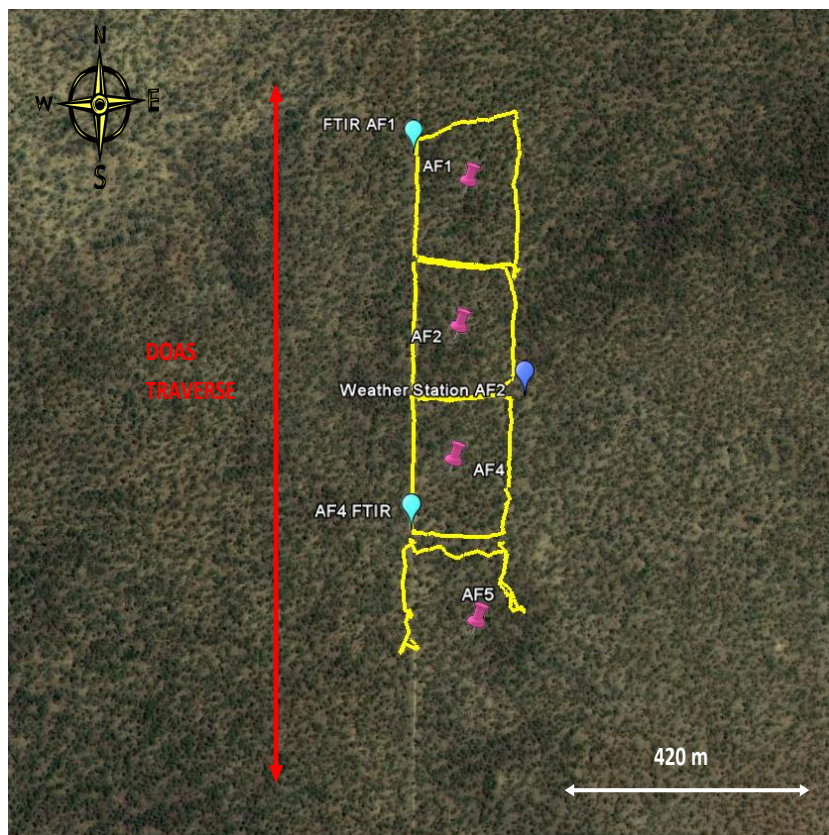
Figure 7.5: *Outline of the burn plots of fires AF1, AF2 (early burning season) and AF4, AF5 (late burning season) given in yellow. This corresponds to GPS location measurements. Note that the plot outline for the plot of fire AF5 is incomplete due to GPS failure. The red arrow indicates the direction of the traverse of the vehicle carrying the UV-DOAS spectrometer during the fires. The vehicle traveled up and down this traverse path throughout the fire duration. Also shown is the location of the FTIR spectrometer for fires AF1 and AF2, and the position of the weather station for fire AF2. Such data is not included for the other fires due to lack of GPS data. Displayed using Google Earth.*
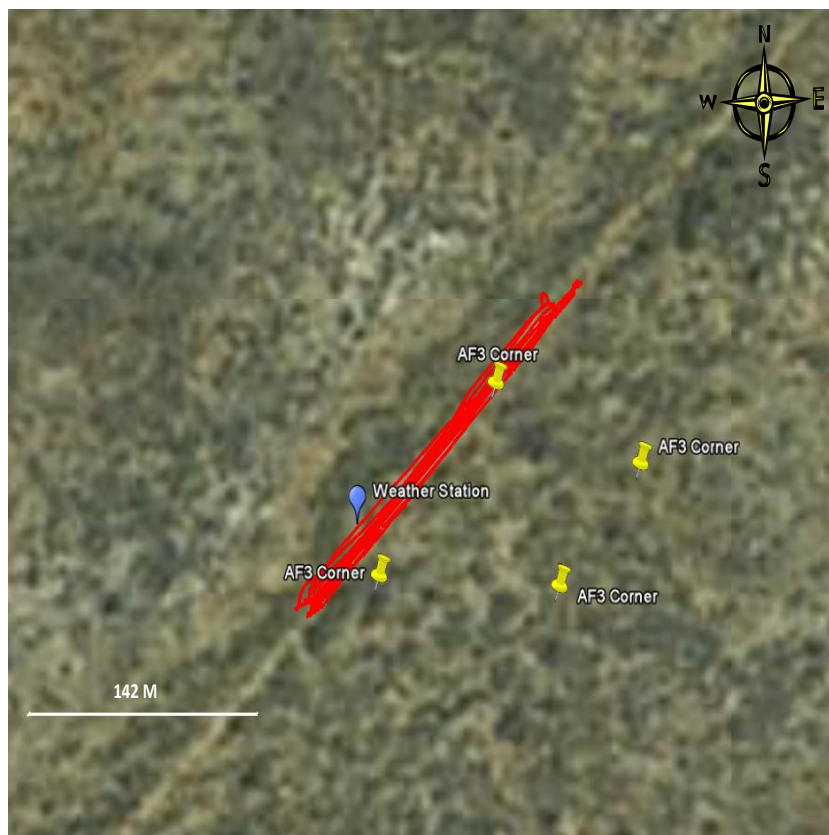
Figure 7.6: *The GPS waypoints measured in the vehicle during the DOAS traverse for fire AF3 (red), along with the location of the weather station and corner fires (used to georeference the airborne imagery). Displayed using Google Earth.*

As with the South African and Canadian field campaigns described in Chapter 5, the UV-DOAS spectrometer was deployed in a vehicle, the telescope pointing to zenith, which traversed back and fourth underneath and perpendicular to the plume during each fire. Figure 7.7 (a) shows the telescope positioned on the vehicle and 7.7 (b) an example of the path taken by the DOAS for one of the fires.

Figure 7.7: *The telescope of the UV-DOAS spectrometer attached to the vehicle pointing zenith for one of the fires of the Australian field campaign a). The vehicle then traversed back and forth during the fire, perpendicular to the direction of travel of the smoke plume, as shown in b). Images taken by author.*

The OP-FTIR was set up in an analogous manner to that used in the South African field campaign. The spectrometer has the same specifications though the IR lamp used in Australia emitted a lower intensity of IR radiation. Hence, a shorter horizontal pathlength was used for these measurements than was attempted in South Africa. Figure 7.8 shows the FTIR instrument in the field. A car battery was used to power the spectrometer for some fires (Figure 7.8 d)), otherwise a smaller motorcycle battery was used.

Figure 7.8: *The FTIR spectrometer set up beside the burn plots ((a), (c) and (d)) of the Australian field campaign. The IR lamp was positioned approximately 40 m away such that during the fires the smoke plume was able to pass between the two instruments (b). A car battery was used to power the spectrometer for some fires (d), otherwise a motorcycle battery was used. Images taken by author.*

7.4 Data Retrieval and Synthesis

7.4.1 Pathlength Amounts and Mixing Ratios

From the UV-DOAS spectral measurements recorded during each fire, the in plume vertical column amounts of SO_2 and NO_2 were retrieved as in Chapter 5. Tables 7.2 and 7.3 show the peak-trough (PT) wavelength combinations used for the retrieval in each field site. The choice of different PT combinations for each fire is discussed in Section 7.5.1.

Table 7.2: *The wavelength locations of the absorbance peak and troughs used for the SO_2 retrievals for all fires of the field campaigns in South Africa (fires SF1-SF4), Canada (fires CF1, CF2) and Australia (fires AF1-AF5). See Figure 5.14 for the identification of peak and trough features. Also labeled are the PT combinations used for the fire retrievals for each fire. These were selected on the basis of the results of the gas cell calibration retrievals.*

Trough	Channel	Wavelength (nm)	Peak	Channel	Wavelength (nm)
2 SF1	355	296.72	2	373	297.64
3 AF2, SF1	445	301.31	3	468	302.48
4 AF5, AF3, AF2, AF1, SF4	485	304.25	4	504	304.30
5 AF5, AF4, AF3, AF2, AF1, SF3, SF4, CF1	526	305.41	5	546	306.41
6 AF3, AF2, CF1, CF2	569	307.57	6	590	308.62
7 AF5, AF4, AF3, AF2, AF1 SF2, SF3, CF1, CF2	610	309.62	7	632	310.71
8 AF5, AF4, AF3, AF2, AF1 SF2	655	311.86	8	678	313.00
9 SF1	701	314.13	9	725	315.32
10 SF1	745	316.30	10	770	317.53

Table 7.3: *The wavelength locations of the absorbance peak and troughs used for the NO_2 retrievals for all fires of the field campaigns in South Africa (fires SF1-SF4), Canada (fires CF1, CF2) and Australia (fires AF1-AF5). See Figure 5.14 for the identification of peak and trough features. Also labeled are the PT combinations used for the fire retrievals for each fire. These were selected on the basis of the results of the gas cell calibration retrievals.*

Trough	Channel	Wavelength (nm)	Peak	Channel	Wavelength (nm)
3 AF3	1403	347.48	3	1424	348.44
4 AF4, AF2, SF3	1454	349.80	4	1480	350.98
5 AF3	1526	353.05	5	1557	354.44
10 AF5, SF1, SF2, SF3	1928	370.68	10	1963	372.18
15 SF3	2416	390.90	15	2436	391.70
16 AF2, SF1, SF4, CF2	2568	396.93	16	2534	395.60
17 AF2	2623	399.09	17	2601	398.23
18 AF2, AF1, SF1, SF2, SF4, CF1, CF2	2721	402.88	18	2648	400.06
19 AF1, SF1	2831	407.07	19	2781	405.17
20 AF2, SF1	2900	409.67	20	2868	408.47
21 AF5, AF4, AF2, SF4, CF1	2958	411.83	21	2920	410.42
22 AF1	3025	414.31	22	3001	413.43
24 AF5	3222	421.45	24	3240	422.09
25 AF5, AF2, SF1, SF2, SF4, CF1	3267	423.05	25	3311	424.60
26 AF2, AF1, SF2	3367	426.56	26	3409	428.02

For the FTIR analysis, Chapter 6 has already detailed the retrieval methods for CO_2, CO, CH_4, NO_2 and SO_2 pathlength averaged mixing ratios. The same spectral windows described were used to retrieve each target gas for the Australian field campaign. Temperature and pressure measurements were obtained from the weather stations positioned beside the burn plots. Table 7.4 gives the horizontal pathlength used for each fire, which varies due to different fire geometry of each plot and wind direction of the time of burning.

Table 7.4: *Horizontal pathlength between the FTIR spectrometer and IR lamp for fires AF1-AF5 of the Australian field campaign. Pathlength averaged mixing ratios of CO_2, CO, CH_4 and where possible SO_2 and NO_2, were calculated across these pathlengths using the retrieval algorithm MALT described in Chapters 3 and 6.*

Fire	Pathlength (m)
AF1	46.4
AF2	42.1
AF3	38.5
AF4	40
AF5	48.5

Chapter 6 discusses the requirement for the subtraction of "ambient" IR spectra measured by the FTIR with no radiation source. This process, detailed in Muller *et al.* (1996) and Wooster *et al.* (2011), aims to take into account any effects of the energy emitted solely by the spectrometer as this does not contain any information on the absorption by the target gases. In Chapter 6 no action was taken for the data analysis of the FTIR spectra for the South Africa fire SF1 as this self-emitted energy is negligible outside the spectral region of 650-1300 cm^{-1}. SO_2 is the only target gas that is retrieved within this region (1120-1200 cm^{-1}) and corresponding pathlength averaged mixing ratios of this gas were too low for analysis of the South African field trip. However this is not the case for the Australian field campaign, hence this non-linearity of the self emitted energy needs to be accounted for. This was implemented by subtracting a spectrum that was recorded in the absence of the IR source. Figure 7.9 (a) shows and example of a *Fire* spectrum, i.e. an uncorrected spectrum recorded during the fire and an *Ambient* spectrum collected with no IR source. The blue spectrum in the figure is the resultant spectrum after the *Ambient* spectrum is subtracted from the *Fire* spectrum. However, evidence of non-linear detector MCT effects can still be seen even after the subtraction, as discussed by Muller *et al.* (1996). Figure 7.9 b) focuses in on the spectral region of 660-675 cm^{-1}. This includes the CO_2 absorption band at 668-670 cm^{-1} which in theory should show a zero signal due to the complete CO_2 absorbance at this wavelength (Wooster *et al.*, 2011). However, neither the *Fire*, *Ambient* or *Subtracted* spectrum are zero. Hence a scaling factor is applied, derived by equating the intensity of

the *Fire* spectrum at 668 cm^{-1} to zero then applying this to the rest of the spectrum. The *Ambient* spectrum is subsequently subtracted, shown in Figure 7.9 as the green *Corrected* spectrum, which is scaled and then subtracted (Muller *et al.*, 1996; Wooster *et al.*, 2011).
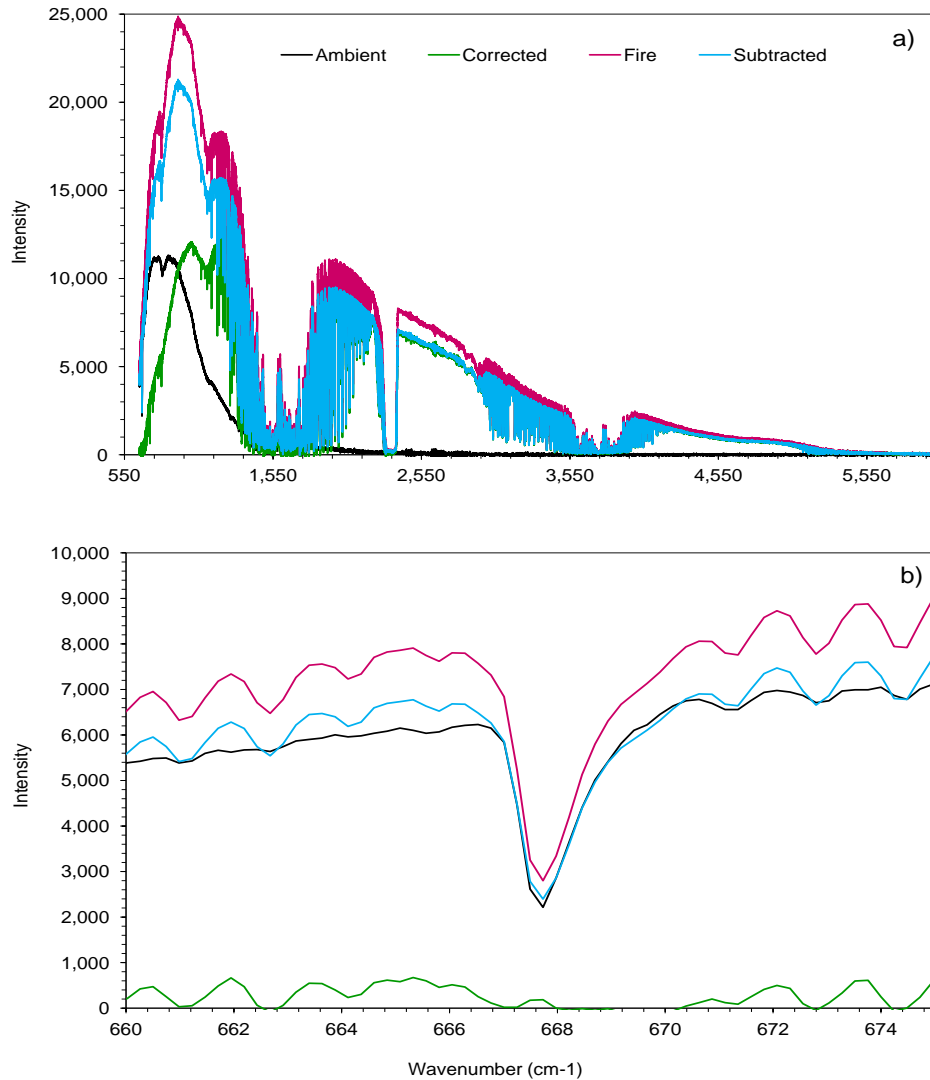
Figure 7.9: *a) An example of a Fire FTIR spectrum measured during the fire (pink) of AF3 and Ambient spectrum collected in the absence of the IR source (black). The energy emitted solely by the spectrometer can be noted in the spectral window of 650-1300 cm^{-1}, which contains the retrieval window of SO_2 (1120-1200 cm^{-1}). The blue spectrum is the result of the Fire spectrum minus the Ambient spectrum and the green of the corrected spectrum. b) zooms in on the spectral region of 660-675 cm^{-1}, containing the CO_2 absorption band at 668-670 cm^{-1}, which should in theory fall to zero in the measured spectra but does not due to the self emission of the spectrometer. It can be seen that subtracting the Ambient spectrum from the Fire does not corrected for this as the intensity does not fall to zero. Therefore a scaling factor is applied to the Fire spectrum such that the intensity at 668 cm^{-1} is zero. The Ambient spectrum is then subtracted from this scaled Fire spectrum to derive the corrected spectrum (green).*

It can be seen from Figure 7.9 a) that the *Ambient* spectrum has a maximum around 1000 cm^{-1} and for wavelengths less than 1500 cm^{-1} the signal is close to or equal to zero. Figure 7.10 shows some example retrieved pathlength averaged mixing ratios (ppm) for CO_2, CH_4, CO and SO_2 from one of the fires, using both the original *Fire* and *Corrected* spectra. For CO_2 and CH_4 the results do not have any variation between the use of the *Fire* and *Corrected* spectra. CO results show a slight variation but this is a small proportion of the retrieved mixing ratios (average variation of 5%), with the mixing ratios of the corrected spectra being slightly higher. The greatest variation in results can be seen for SO_2 (Figure 7.10 d)), where the mean difference between the retrievals from the "fire" and "ambient" spectra is 29%, confirming that the self emission of the instrument needs to be taken into account for the retrievals of this gas.
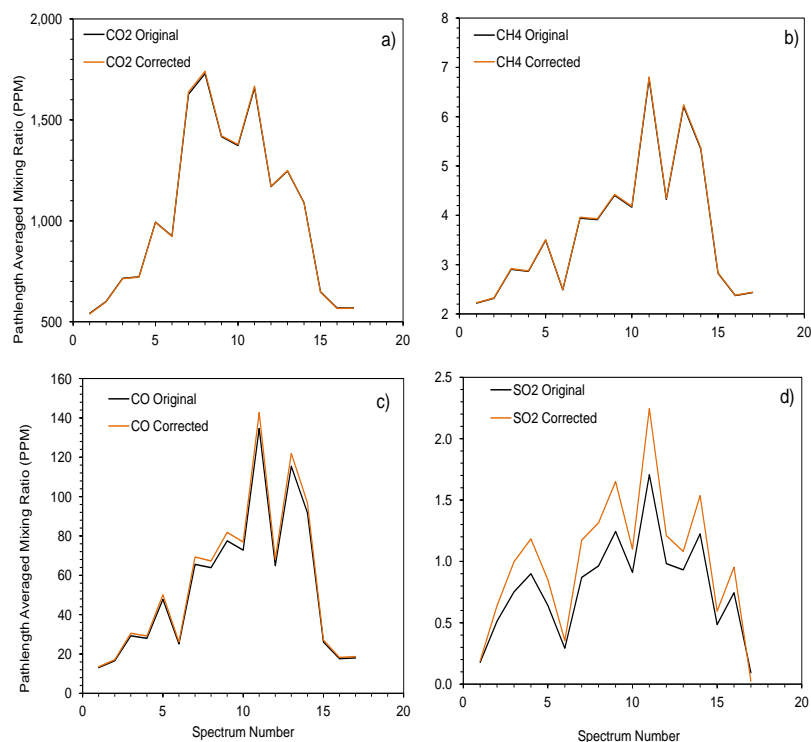
Figure 7.10: *Retrieved pathlength averaged mixing ratios of CO_2, CO, CH_4 and SO_2 using MALT on the original (black) and corrected (orange) spectra. The difference between the mixing ratios from the two types of spectra for the gases CO_2 and CH_4 is trivial. For CO, there exists a slight variation (average 5%), however the greatest difference between the retrieved mixing ratios of the original and corrected spectra lies with SO_2 (average variation of 29%). This suggests that, for SO_2, the effect caused by the self emission of the spectrometer is significant for providing an accurate retrieval.*

7.4.2   ER, EF and Fluxes

Chapter 6 details the calculation process for the ER, EF and the trace gas fluxes. Note that there was no need to calculate the plume direction for the flux calculations as the plume traveled approximately perpendicular to the UV-DOAS traverse. This can be seen from the videos recording in the helicopter above the fires, an example from fire AF1 is shown in Figure 7.11 a. There was no video for fire AF2. The direction of the plume was obtained from a camera positioned on top of the FTIR spectrometer (see Figure 7.11 b). The plume speed was taken as the speed derived from the helicopter video of the previous fire, AF1. Both fires were of a similar size.
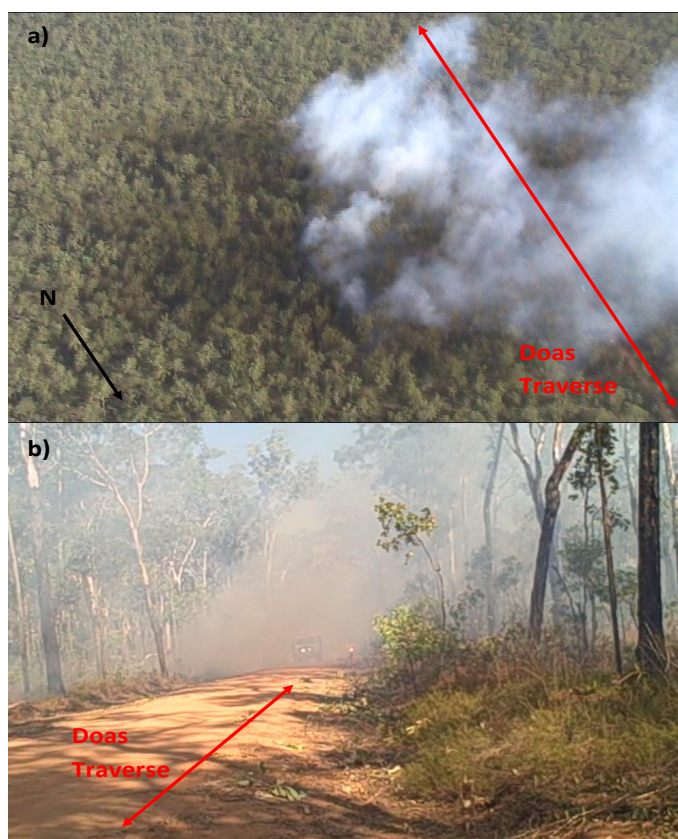
Figure 7.11: *Example aerial image recorded during fire AF1 from helicopter hovering above the fire a) and image recorded at ground level positioned on the FTIR spectrometer b). Such images show that the path of the plume was generally perpendicular to the direction of traverse of the DOAS vehicle, such that no correction for plume direction was needed to calculate the flux rates of SO_2 and NO_2 derived from the UV-DOAS spectra.*

Table 7.5 details the values of the parameters needed in the estimation of the trace gas fluxes

Table 7.5: *The parameters used to calculate the flux rates of SO_2 and NO_2 for fires AF1-AF5. Temperature and pressure taken directly from measurements at ground level. Plume height estimated from video footage recorded in a helicopter of the fires. The plume speed averaged over all the traverses was derived from plume height estimates and wind speed measurements at ground level using the log law (see Chapter 5). The average tree heights were calculated from field measurements. The surface roughness parameter, z_0 and the zero plane displacement d were estimated from these average tree heights (Hicks, 1975; Garret, 1992)*

Fire	Temp (k)	Pressure (hPa)	Plume Height (m)	Avg Plume Speed $(m.s^{-1})$	Tree Height (m)	Z_0	d
AF1	303	978	100	4	8	0.9	7
AF2	273	978	120	8	1 8	1	14
AF3	302	991	80	5	13	1.04	10
AF4	308	993	110	17	13	1.04	10
AF5	306	975	90	4	9	0.72	7

7.5 Results

7.5.1 In-Plume Pathlength Amounts

Figures 7.12 and 7.13 present the retrieved vertical column amounts of SO_2 and NO_2 for each of the Australian fires derived from the UV-DOAS spectra. Also included are the corresponding uncertainty estimates, calculated as in Chapter 5. The results for both gases for the most significant part of each fire are shown in Figure 7.14. The high uncertainties shown in fire AF4 for NO_2 are most likely due to the high variation in the PT combination values at PT4 (see Table 7.3), used in the derivation of the calibration equation for this fire. This variation can be attributed to several of the NO_2 gas cell spectra having weak absorption features. This caused high uncertainty for the NO_2 calibration equation for this fire and therefore high overall uncertainties.

For all Australian fires, NO_2 levels were significantly lower than those of SO_2. In particular, for Fire AF2, NO_2 was in fact unable to be detected in any significant quantity (as smoke amounts seem to be too low). This is consistent with the inability of the FTIR to detect NO_2 due to low in-plume pathlength averaged mixing ratios. These low NO_2 plume

column amounts suggest a relatively low level of nitrogen in these ecosystems. Cook (2001) suggested that burning decreases levels of nitrogen in the soil, which in turn affects the nitrogen content in vegetation and hence in the fire plumes. Schmidt and Stewert (2003) found that N levels in tropical savanna species were lower for annually burnt savannas compared to those that were burnt at a lower frequency. For such savanna ecosystems, the release of NO_x from biogenic processes may have a small effect on the total NO_x budget of that area (Parsons *et al.,* 1996; Takegawa *et al.,* 2003). Schmidt and Stewert (2003) found that the average foliar N in northern Australian savanna samples such as those in this study were lower than those of equivalent African species. It is suggested that the overall lower level of N in leaves supports the theory that Australian savanna and woodland species are more N deficient, which may be linked to low levels of N in these ecosystems (Schmidt and Stewert, 2003).

Outside of the plume/at times where there is not much smoke present (i.e. outside the main peaks showing high column amounts in Figure 7.14) the retrieved column amounts do not fall exactly to zero. This is also seen in the SO_2 and NO_2 retrieved pathlength amounts from the gas cell measurements. In these calibration spectra "clear sky" amounts fluctuate around approximately 5-30 ppmm, while gas cell amounts are apparently retrieved correctly. Figure 7.15 (a) shows an example of ambient retrieved pathlength amounts of NO_2 and SO_2 before the fire started during the collection of the gas cell spectra, from fires AF1 and AF2 respectively. Figure 7.15 (b) and (c) shows the retrieved gas cell amounts of NO_2 and SO_2 for the same fires using the PT combinations detailed in Tables 7.3 and 7.2. It can be seen that ambient "clear sky" NO_2 amounts fluctuate between 5-15 ppmm while SO_2 amounts vary from 10 ppmm to 30 ppmm. However the gas cell retrieved amounts are close to the actual quoted amounts; with an average variation of 8% for NO_2 and 2% for SO_2 from the qouted gas cell amounts. The same effect can be seen in the South African retrieved vertical column amounts (Chapter 5). This suggests that the retrieval method is not able to accurately return the trace gas amounts when amounts are close to zero, yet the method works well when levels are above background (as shown by the correct gas cell ppmm retrievals). This effect could result in the incorrect elevation of the subsequently calculated

trace gas flux rates, since the lower pathlength amounts are artificially elevated above the zero level. However, the end points of the traverses, where the DOAS vehicle is outside of the plume, are not included in the flux calculations. The 'true' detection limit for the DOAS measurement and retrieval method needs to be investigated, to determine the lowest column amount that can be accurately retrieved. The higher retrieved column amounts of ambient SO_2 compared to ambient NO_2 seen in Figure 7.15 can possibly be attributed to the spectral region in which retrieval of the SO_2 is carried out. As seen in Figure 5.26, this region exhibits a lower light intensity compared to the retrieval region used for NO_2, hence the signal to noise ratio appears worse.

Only fires AF2 and AF3 (Figure 7.14) exhibit the expected trend in the retrieved column amounts of a main peak in the middle of the fire, where smoke levels are expected to have been most elevated and smaller peaks on either side. The remaining fires can be seen to have a more variable pattern with no clear trend and with several column amount peaks throughout the fires, in particular for fires AF4 and AF5. Comparing this pattern with the optical video imagery taken from the helicopter it can be seen that for these later fires there was a strong plume present for a substantial amount of time (approximately 20 minutes) during each fire, which probably contributes to the occurrence of multiple peaks in the pathlength amounts as the vehicle traversed back and forth under the plume. By contrast, for fire AF3 the video shows an apparently more substantial plume that was of a shorter duration (approximately 10 minutes) resulting in the mean column amount peaks towards the middle of the fires as seen in Figure 7.14.
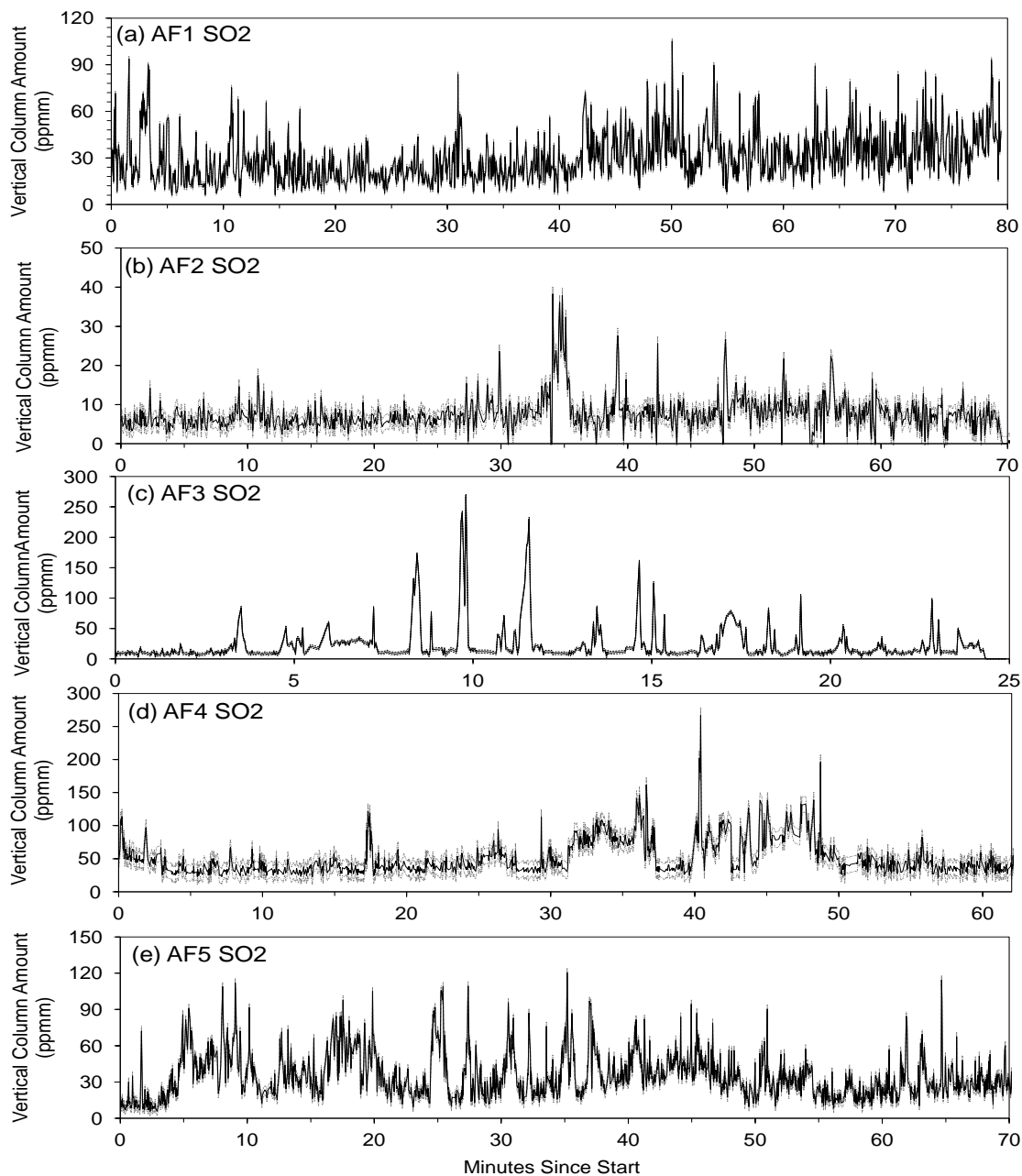
Figure 7.12: *SO$_2$ vertical column amounts retrieved from the UV-DOAS smoke smoke measurements made during the Australian field campaign for fires AF1-AF5. Also shown is the estimated retrieval uncertainty calculated using Equation 5.8. Notice only fires AF2 and AF3 exhibit a main maximum/group of maxima in the time series representing the peak emissions of the smoke. The remaining fires show a more variable time series, representing the longer persistence of a smoke plume during these fires. Fire AF2 produced the lowest column amounts due to low levels of smoke resulting from a low fuel load in the fire plot.*
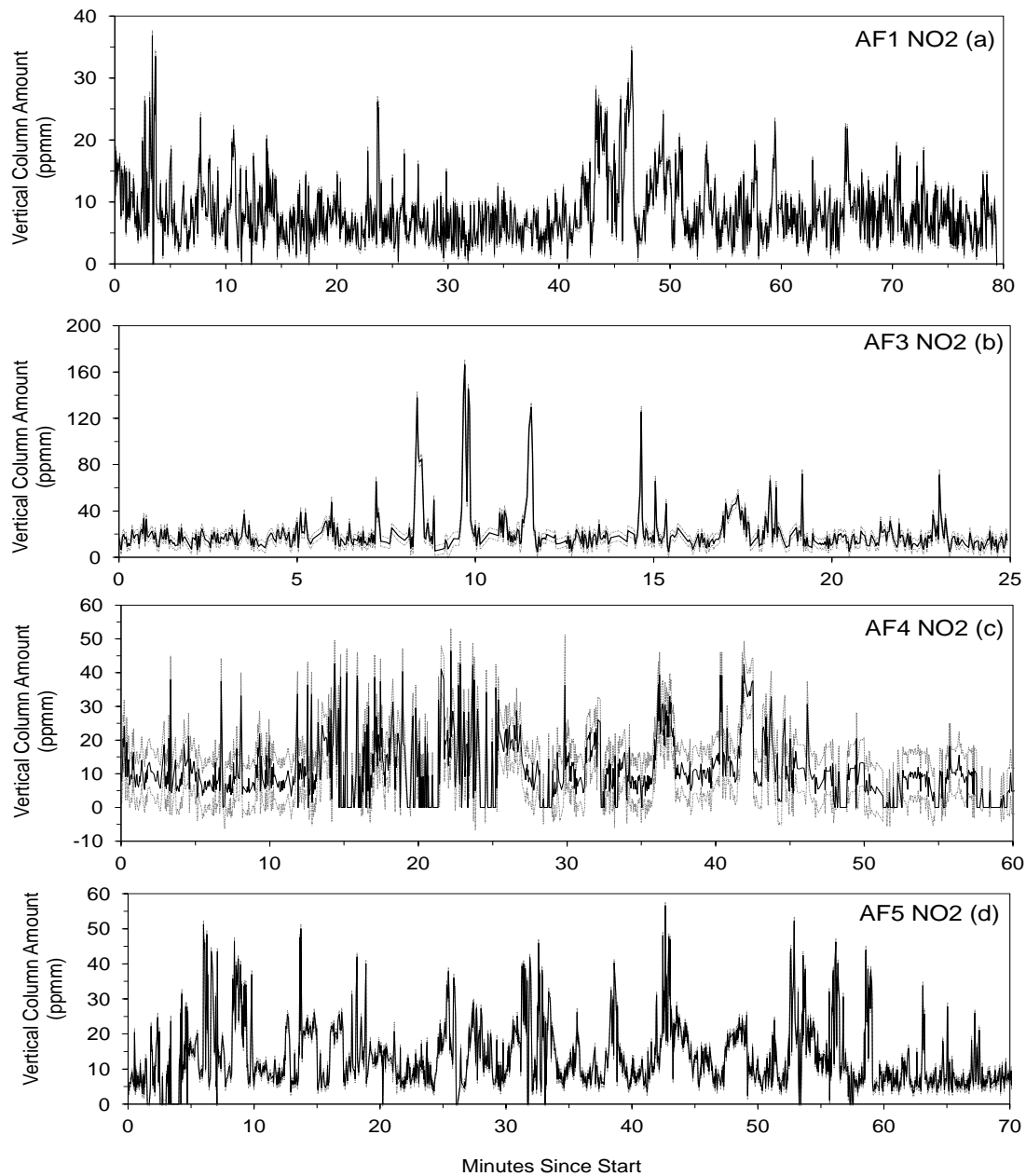
Figure 7.13: *NO$_2$ vertical column amounts retrieved from the UV-DOAS smoke smoke measurements made during the Australian field campaign for fires AF1-AF5. Also shown is the estimated retrieval uncertainty calculated using Equation 5.8. The NO$_2$ vertical column amounts for all fires are lower than those of SO$_2$ shown in Figure 7.12. This suggests that the relative amount of nitrogen in the fuel of these Australian tropical savanna ecosystems is lower than that of sulphur. Note that for fire AF2, levels of NO$_2$ were too low to be detected. This corresponds to the retrieved column amounts of SO$_2$ for this fire (Figure 7.12 b), which exhibited the lowest levels from all fires.*
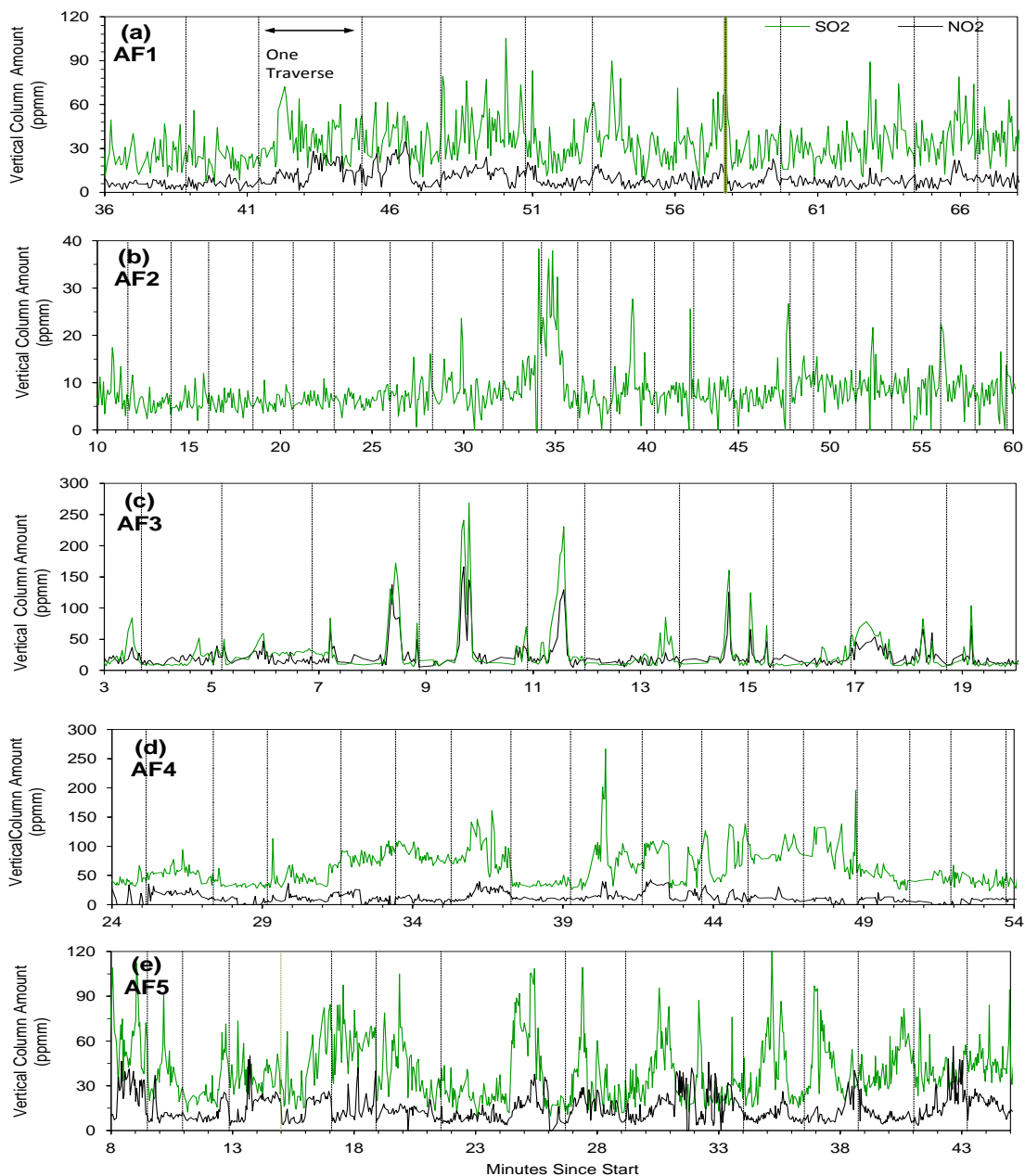
Figure 7.14: *Retrieved in plume vertical column amounts of SO_2 (green) and NO_2 (black) for Australian field campaigns AF1-AF5. NO_2 results are unavailable for fire AF2 due to poorly retrieved column amounts too low to be considered usable. SO_2 exhibits relatively low column amounts for fires AF1 and AF2. SO_2 exhibits greater column amounts compared to NO_2 for all fires. Higher amounts for both gases were retrieved in fires AF3-AF5. There is a good agreement between the temporal variations in the amount of each gas (i.e. SO_2 and NO_2 variations appear to track another quite well). The dotted lines indicate the start and end of each traverses*
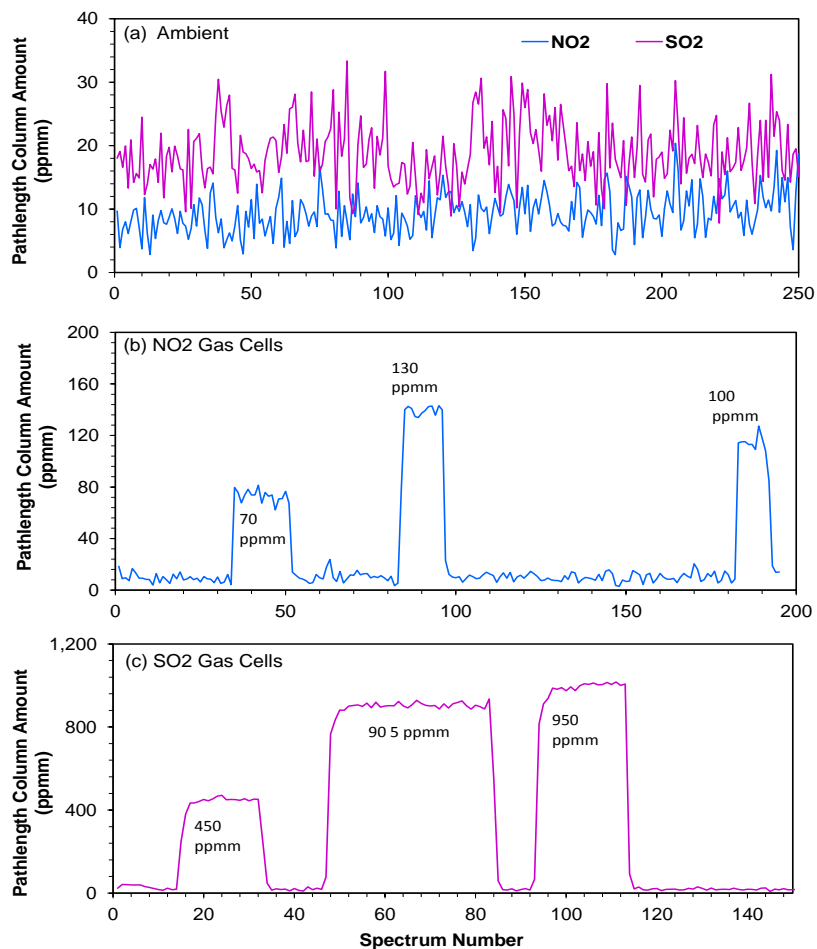
Figure 7.15: *(a) Example ambient retrieved pathlength column amounts of NO_2 and SO_2 before fires AF1 and AF2 respectively. Ambient column amounts fluctuate between 5-15 ppmm for NO_2 and 10-30 ppmm for SO_2. (b) The retrieved NO_2 gas cell amounts from fire AF1 and (b) the retrieved gas cell amounts from fire AF2. The quoted gas cells for NO_2 are of amounts 70, 100 and 130 ppmm and those of SO_2 are 450, 905 and 950 ppmm. The PT combinations used for the retrieval of the column amounts are detailed in Tables 7.3 and 7.2. The retrieved column amounts for both gases are close to the quoted values (with mean variation of 8% for NO_2 and 2% for SO_2.*

For all fires, and indeed for all field campaigns, there was some variation in the DOAS returned vertical column amounts calculated using the different peak-trough (PT) combinations for both target gases during the fires themselves. This variation was not present for the retrieval of the calibration gas cell pathlength amounts, however, suggesting that some characteristic of the smoke plume might be a possible cause. The coefficient of variation between the retrieved column amounts from the chosen PT combinations of each of the fires

ranges from approximately 30-60% for the whole fire, with lower variation when just the peak column amounts are included in the middle of the fire (i.e. without the lower ambient column amounts included). For the retrieved column amounts of the gas cell spectra, the equivalent range for the coefficient of variation is much smaller, approximately 3-12%. There is no distinct pattern between gas species or particular PT combinations, i.e. on average the variation is the same for both gases for all peak and trough combinations. Figure 7.16 shows the retrieved vertical column amounts for SO_2 for Australian fire AF3, South African fire SF3 and Canadian fire CF2 for each of the respective PT combinations that were selected on the basis of the calibration gas cells retrievals. Figure 7.17 shows the same results for NO_2. For these example fires, it can be seen that, particularly for SO_2, the retrieved column amounts between the individual PT combinations are somewhat inconsistent.
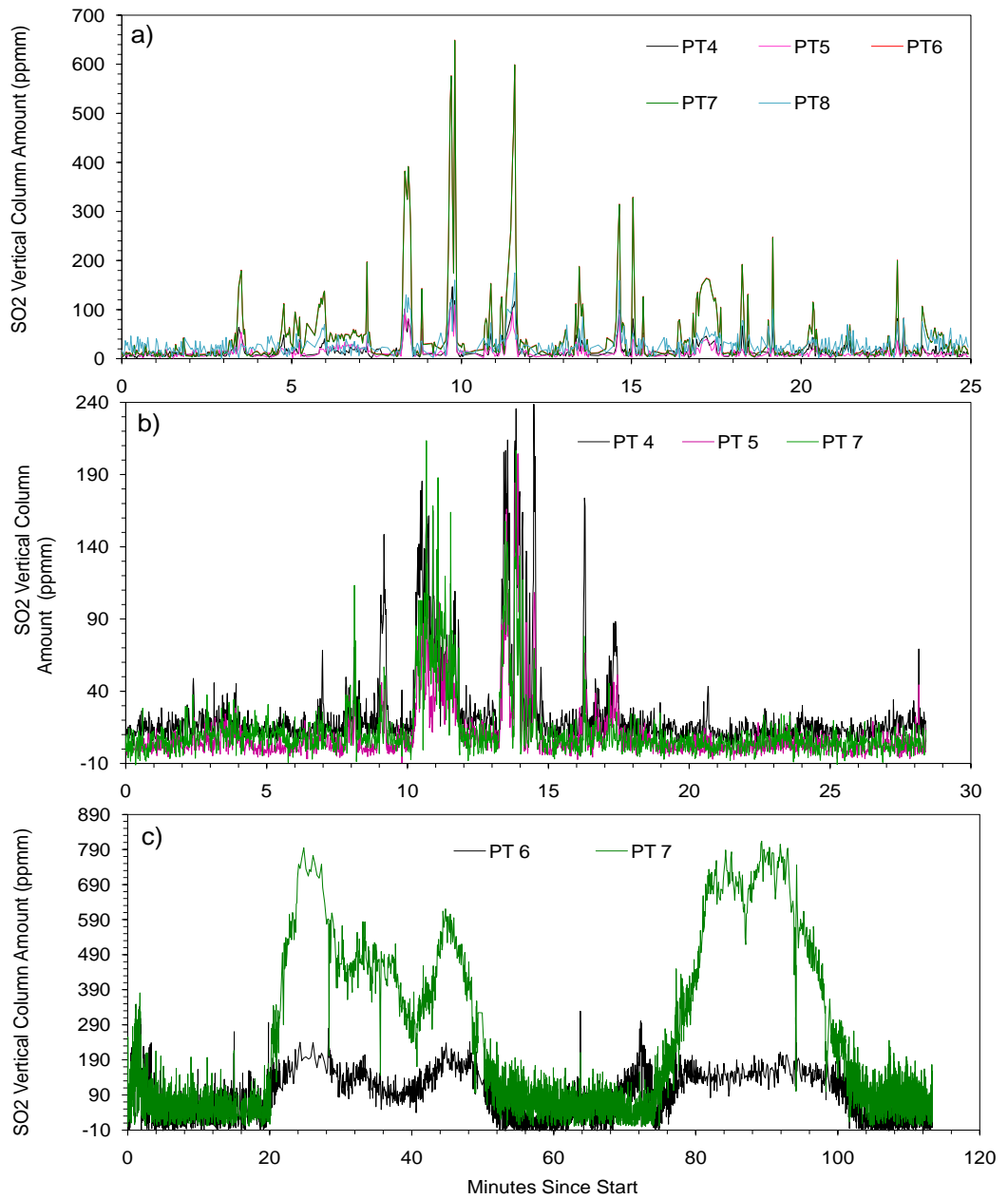
Figure 7.16: *Retrieved vertical column amounts of SO₂ for fires (a) AF3, (b) SF3 and (c) CF2 for each of the individual PT combinations that were selected on the basis of the calibration gas cell retrievals. Notice the difference in column amounts between the respective PT combinations used, in particularly those of fire CF2.*
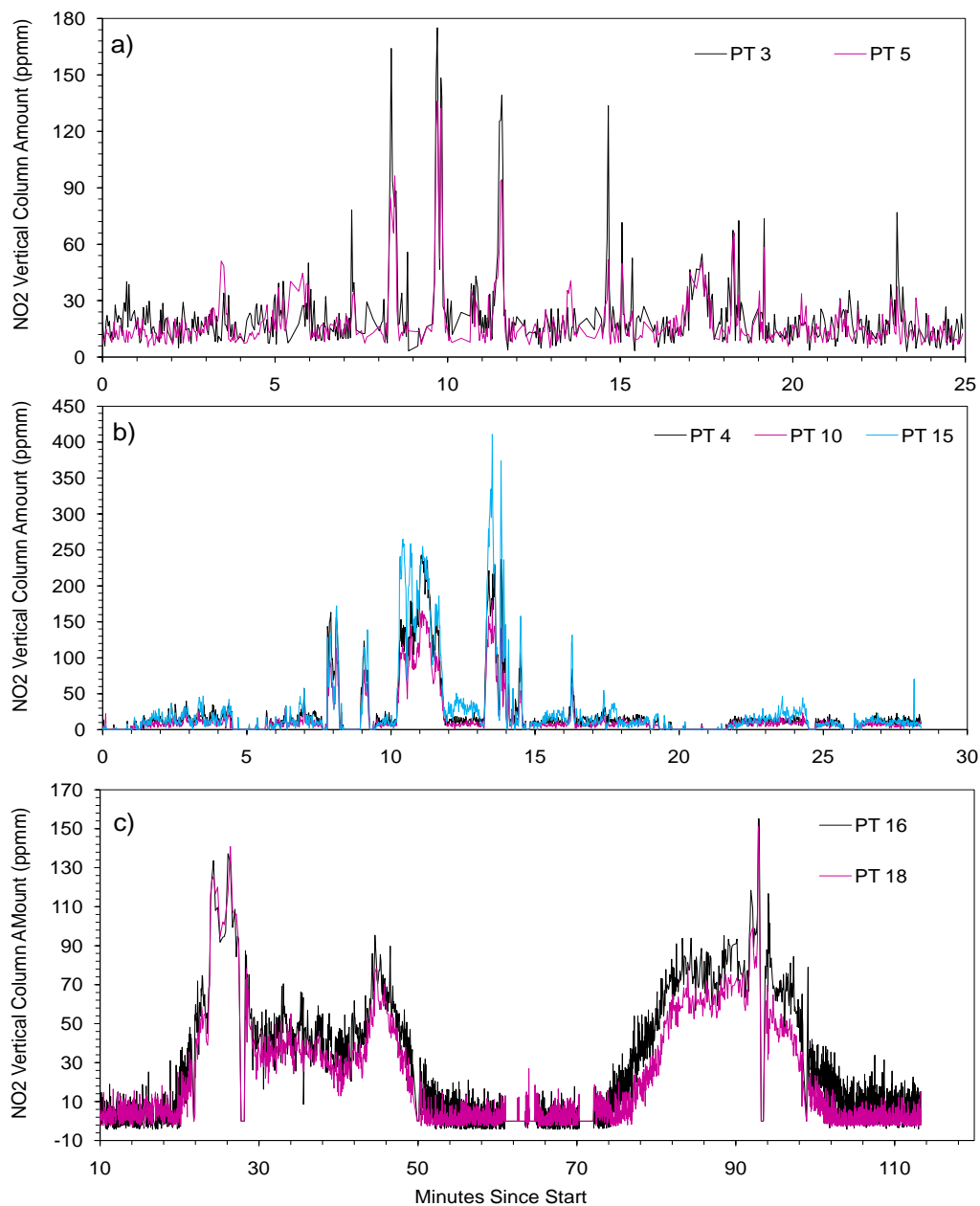
Figure 7.17: *Retrieved vertical column amounts of NO_2 for fires (a) AF3, (b) SF3 and (c) CF2 for each of the individual PT combinations that were selected on the basis of the calibration gas cell retrievals. There is less of a variation between column amounts retrieved by individual PT for each fire compared to those of SO_2, particularly for fire CF2.*

As already stated, this inter-PT retrieval variability is not seen in the the retrieved column amounts from the gas cell calibration measurements when made with the same PT combinations. Figure 7.18 shows pathlength column amounts of the SO_2 gas cells of the individual

PT combinations chosen for the retrievals of fires AF3 a), SF3 b) and CF2 c). Figure 7.19 shows the same for the NO_2 calibration gas cells. It can be seen that for the retrieved column amounts from the gas cell spectra, there does not exist as much variation between the individual peak and trough combinations used in analysis compared to the column amounts retrieved from the fire spectra. Note also that it is not that case that the same PT combinations were chosen for each fire for SO_2 and NO_2. This could be due to conditions on the day of the measurements, for example cloud cover and light intensity. It could also be attributed to the presence of the plume, as the choice of the PT combinations were generally consistent for the gas cell retrievals. Mori *et al.* (2006) investigated the UV scattering effect on SO_2 emissions of volcanic plumes derived from spectra collected using the UV DOAS. Measurements were made at 3 distances from the volcanic plumes; 640, 1660 and 1660 m. In particular, absorbance spectra collected at each distance were compared to a standard SO_2 absorbance spectrum of 900 ppmm within the spectral region of 300-320 nm. It was found that the absorbance at shorter wavelengths decreased with distance, with measurements from the closet point to the plume (640 m) agreeing with the standard spectrum at the target wavelength region. This appears to correspond to the findings here; where there is more of a variation between the SO_2 retrievals for different PT combinations, which are located at shorter wavelengths compared to the NO_2 PT combinations. The estimated plume heights from the open vegetation fires in this work are much less than the smallest distance of measurements in Mori *et al.* (2006). As Mori *et al.* (2006) found a correlation between decreases in absorbance caused by scattering and the distance between the measuring DOAS instrument, this may imply that there is a reduced scattering effect from the smoke plume of the fires due to the smaller measurement distance from the instrument.

Scattering depends also on the number, size and type of aerosols that are scattering the incoming radiation as well as atmospheric conditions during measurements. It is possible that the variation in PT combinations is in fact caused by absorption of aerosol particles in the plume. The light absorbing properties of aerosols in the atmosphere, in particular those emitted from biomass burning, are under quite a substantial amount of investigation. This is partly due to the differences in aerosols emitted from flaming and combustion (Moosmüller

et al., 2009). Aerosol scattering depends mainly on particle size whereas aerosol absorption is strongly correlated with chemical composition. Aerosols that do not have any absorption features in the UV, such as sulfate, tend to scatter incoming radiation (Marley *et al.,* 2009). Light absorption by aerosols is dominated by black carbon (BC), released during man made and natural fires (Graf *et al.,* 2007; Marley *et al.,* 2009; Moosmüller *et al.,* 2009). Also emitted during combustion processes is OC, which may include the light absorbing species of BrC (brown carbon). The amount of BrC emitted is uncertain, as is its ability to absorb shortwave radiation (Moosmüller *et al.,* 2009). The absorption of BC is stronger at shorter wavelengths due to a rise in aerosol optical thickness, however the single scattering albedo increases with wavelength (Hobbs *et al.,* 2003; Graf *et al.,* 2007). Smoke emitted from boreal forest fires tends to scatter light as there is a high amount of particles emitted from the smoldering combustion of woody fuels. For these types of fires, less BC tends to be produced, which have more absorbing properties rather than scattering (Krotkov *et al.,* 2005). More work needs to be carried out to investigate and subsequently quantify the effects of scattering on the absoprtion of the target gases by the aerosols in the biomass burning plumes
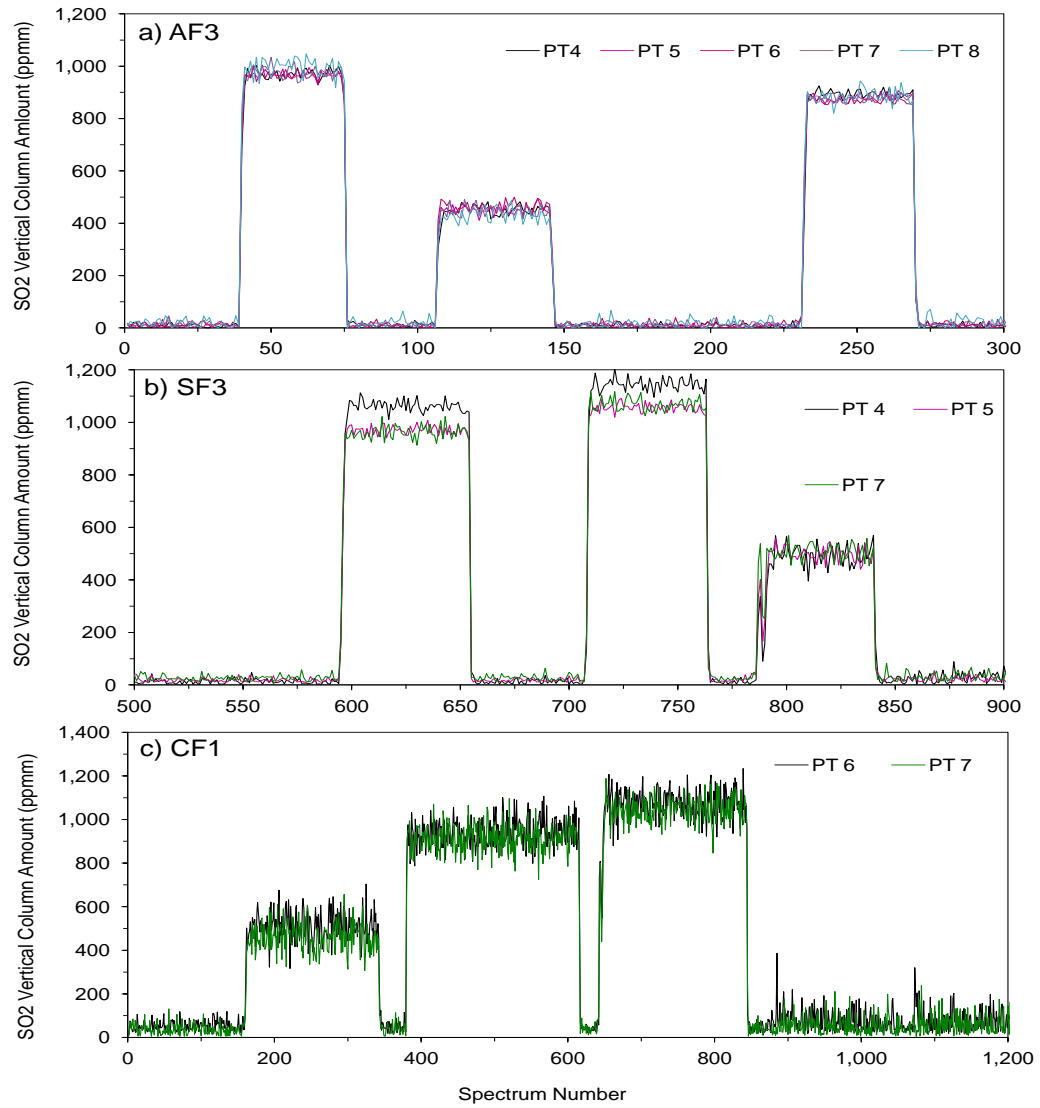
Figure 7.18: *The pathlength column amounts of the SO₂ gas cells of the individual PT combinations chosen for the retrievals of fires AF3 a), SF3 b) and CF2 c). Gas cell quoted amounts are 405, 905 and 950 ppmm.*
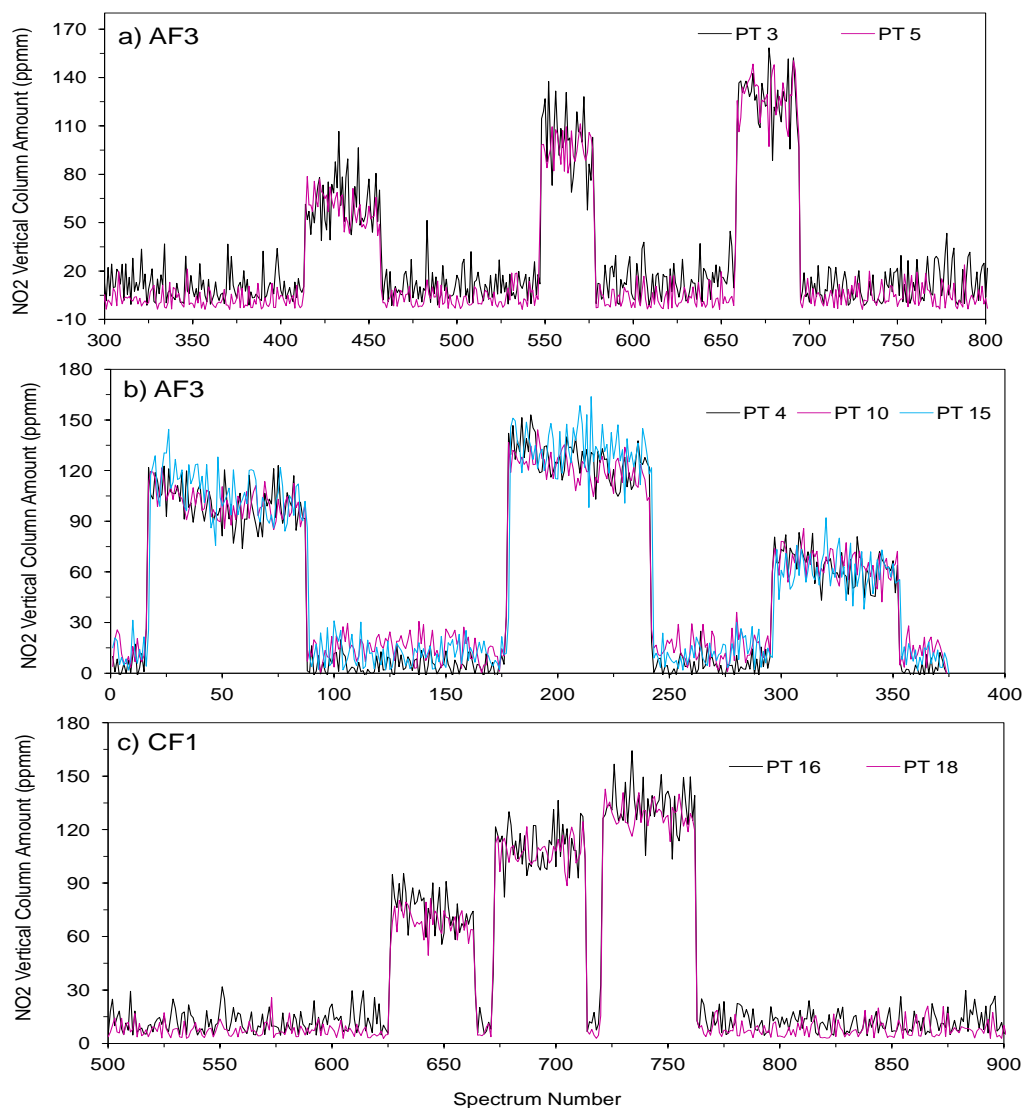
Figure 7.19: *The pathlength column amounts of the NO_2 gas cells of the individual PT combinations chosen for the retrievals of fires AF3 a), SF3 b) and CF2 c). Gas cell quoted amounts are 70, 100 and 130 ppmm.*

An attempt was made to investigate the the SO_2 and NO_2 ratio during these fires but the relationship was poor due to the noisy trend found in the NO_2 retrieved column amounts. Only from fires AF1 and AF3 was a reasonably strong positive upward trend (as expected) was found, as shown in Figure 7.20, with r^2 values of 0.65 and 0.80 respectively. These appear quite consistent between fires, with ratios of 1.4 and 1.5 for fires AF1 and AF3 respectively. The average of the retrieved vertical column amounts of NO_2 and SO_2 for each

traverse were taken to represent each point on the scatter plot. Note that although from the time series the NO_2 and SO_2 retrieved peak column amounts reach almost up to 200 and 300 ppmm respectively, in Figure 7.20 the averaged traverse column amounts are lower due to the inclusion of column amounts not included in the peaks of the fire. Any further analysis using the DOAS retrieved column amounts will focus mainly on the SO_2 time series due to the low NO_2 derived amounts. This contrasts with Oppenheimer *et al.*, (2004) where column amounts of NO_2 from agricultural fires in Brazil reached values up to 100 ppmm. For the results here, only AF3 reaches those levels, with column amounts exceeding 150 ppmm.
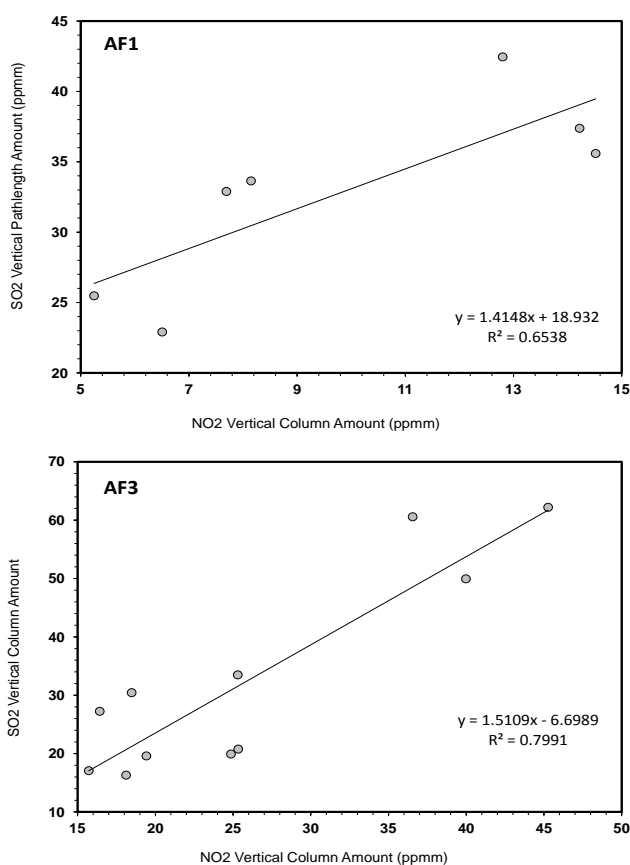
Figure 7.20: *Emission ratios of SO_2 and NO_2 derived from the relevant column amount for AF1 and AF3. The relationship between the two cases was found to be poor. The ratios between the two fires appear to be quite consistent, at 1.4 and 1.5 for fires AF1 and AF3 respectively. Note that an average of the retrieved vertical column amounts of NO_2 and SO_2 for each traverse were taken to represent each point on the scatter plot. There is a reasonably strong correlation between the two gases, with an r^2 value of 0.65 (AF1) and 0.80 (AF3).*

Field Campaign Inter-Comparison of Retrieved Column Amounts

From the vertical pathlength amounts derived from the UV-DOAS spectra of the Australian field campaign, SO_2 was present in more abundance compared to NO_2. This contrasts with the vertical pathlength amounts derived from the South African field campaign, where in general NO_2 was more dominant (see Figure 5.25 in Chapter 5). In particular, for fires SF1 and SF2, SO_2 retrieved column amounts exhibited high variability, in comparison to the equivalent NO_2 results. However for SF4, SO_2 pathlength amounts reached higher levels. Looking at the SO_2 and NO_2 amounts from the Canada field campaign, SO_2 was emitted at much greater levels compared to NO_2, as discussed in Chapter 5 (see Figure 5.27), in particular for CF2 SO_2 peak amounts were almost 5 times greater than equivalent NO_2 peaks. These differences can probably be attributed to the varying levels of nitrogen and sulphur in the different fuel types. The plume was a lot larger and thicker in Canada than South Africa and Australia, due to a much larger burnt area and higher fuel consumption, by at least one order of magnitude. The areas burnt in South Africa and Australia were a mixture of trees, bushes and grass, none very dense. However those in Canada were dense pine forests. This is reflected in the retrieved column amounts of SO_2, which is much higher in Canada than South Africa and Australia. However, this is not the case for NO_2, suggesting that the ratio of N to S in the Canada ecosystem is a lot lower than in South Africa and Australia. Sinha *et al.* (2003) reported EF of SO_2 from savanna fires in southern Africa (South Africa, Zambia, Mozambique and Botswana) of 0.43 g.kg^{-1}, approximately one third of the SO_2 EF given by Yokelson *et al.* (1996) derived from pine needle laboratory fires. For savanna ecosystems, current NO_2 literature values are reported as NO_x, hence it is difficult to investigate NO_2 EF. However Sinha *et al.* (2003) calculated a $\frac{NO_2}{SO_2}$ ER of 2.35 (note that the individual $\frac{NO_2}{CO_2}$ and $\frac{SO_2}{CO_2}$ were analyzed with different methods, by pulsed fluorescence detection and AFTIR respectively). This is much higher than the ratio of the NO_2 to SO_2 EFs calculated by Yokelson *et al.* (1996), at 0.36, detailed in Chapter 5.

The relationship between the SO_2 and NO_2 ratio was investigated for fires where both gases were well retrieved (SF3, SF4, CF1 and CF2). Fires SF1 and SF2 were omitted because of the low SO_2 column amounts. Figure 7.21 shows scatter plots of NO_2 versus SO_2 column

amounts for each of the these fires. For fires SF3 and SF4, the average of the retrieved vertical column amounts of NO_2 and SO_2 for each traverse were taken to represent each point on the scatter plot. However this averaging was not carried out for the Canadian fires as it was difficult to distinguish the start and endpoints of the traverses because of the extensiveness of the plume. Instead only the results of the peaks of the fires have been included for CF2 as there was a poor relationship between the two gases when all results from the whole measurement period were included. When comparing the relationship of both gases between field trips (Figures 7.20) and 7.21), as expected, the relationship is different for each of the fires as NO_2 dominates the column amounts for fire SF3, while the opposite is true for the rest of the savanna fires and fires CF1 and CF2 is a different biomass type. The greater column amounts of SO_2 compared to NO_2 are visible through the slopes of the derived linear relationship between the two gases; greater than 1 for fires AF1(1.41), AF3(1.51) SF4 (1.11), CF1 (2.81) and CF2 (4.77) while less than 1 for fire SF3 (0.57). However, for SF3, the ER has fewer points compared to the other fires (due to the smaller number of traverses for this fire), hence this low ER is less trustworthy. Although fires CF1 and CF2 are of the same biomass type, the slope of CF2 is much greater than that of CF1, reflecting the fact that greater amounts of SO_2 were emitted compared to NO_2 amounts for the second Canadian fire. However this discrepancy could be due to the possible inaccuracy associated with the vertical column amounts due to noisy spectra collected at low intensities. There is a reasonably strong correlation between SO_2 and NO_2 for all fires (an r^2 between 0.65 and 0.93).
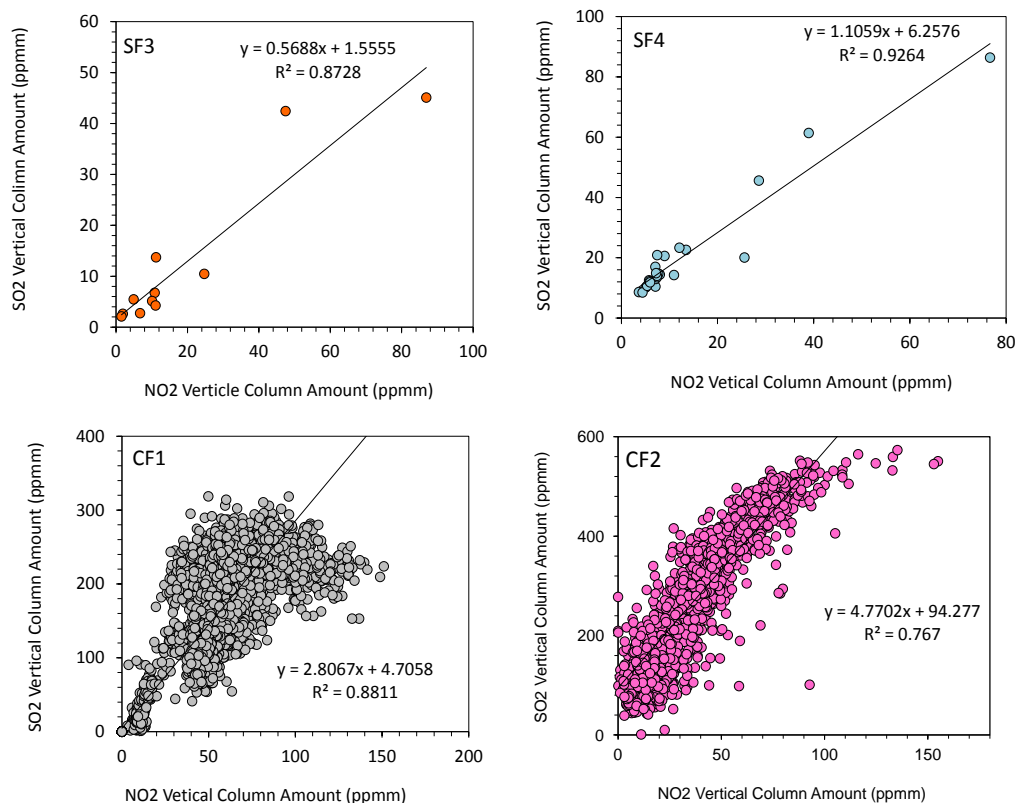
Figure 7.21: *Emission ratios of SO_2 and NO_2 derived from the relevant column amount for SF3, SF4, CF1 and CF2. There is a strong correlation between SO_2 and NO_2 for all fires (an R^2 between 0.77 and 0.93). The slope of fire SF3 reflects greater column amounts of NO_2, while for SF4 the SO_2 column amounts are slightly greater than those of NO_2. However there are fewer points for the ER of fire SF3, due to the smaller number of traverses for this fire. The relationship between the gases for CF1 and CF2 exhibits the dominance of SO_2 in the smoke plume over NO_2.*

Oppenheimer *et al.* (2004) investigated NO_2 emissions from agricultural burns in Brazil using the DOAS traverse method. This is the only previous attempt of using the method known to the author. Attempts were made in that work to also retrieve SO_2 but due to the late time of day, solar light intensity levels were too low to make accurate SO_2 retrievals. NO_2 was retrieved, and emission peaks ranged between 50-100 ppmm. This is in line with fires SF1, SF2, AF1, AF4 and AF5 seen in the current work, but lower than the column amounts returned for fires SF3, SF4, AF3, CF1 and CF2. The burn plot size of Oppenheimer *et al.* (2004) was 10 ha, a little larger than the 7 ha plots in South Africa and 4 ha plots in Australia, however column amounts cannot be directly compared as the fuel type for the fires

was Brazilian sugar cane whereas the vegetation sampled in this research were of savanna and boreal forest ecosystems. The majority of the experiments carried out using the UV-DOAS are for the purpose of investigating SO_2 emissions from volcanic plume. Measured emissions from such plumes range from 200 1000 ppmm (e.g Galle *et al.*, 2002; McGonigle *et al.*, 2003; Elias *et al.*, 2006; Mori *et al.*, 2006). In addition, studies have been conducted with the UV-DOAS to investigate SO_2 industrial emissions (e.g. McGonigle *et al.*, 2004) reaching up to 1000 ppmm. The bottom range of these literature values is comparable with the SO_2 vertical column amounts derived from the South African fires and higher values with those from the Canadian fires.

7.5.2 In-plume FTIR Mixing Ratios

The pathlength averaged mixing ratios of CO_2, CO, CH_4 and SO_2 retrieved from the FTIR spectra for all Australian fires are shown in Figures 7.22 and 7.23. SO_2 was not detected for fires AF1 and AF2 due to apparently too low a pathlength averaged mixing ratio. The pathlength averaged mixing ratios for all gases exhibit the same trends within a single fire i.e they peak and fall at the same time. All fires also show elevated above background mixing ratios for all gases. The large peaks can be attributed to mainly flaming phase of the fire and smaller peaks and fluctuations caused by the more smoldering phase. FTIR retrieved pathlength averaged mixing ratios of fire AF4 were the highest for all gases. This does not correspond with the DOAS measurements of the same fire shown in Figure 7.14 however, in which fire AF3 returned the highest column amounts for both SO_2 and NO_2. This difference could result from the fact that the instruments are not measuring the same smoke due to their different observing geometries and their difference of scattering on their observations/which are made at very widely differing regions of the electromagnetic spectrum: UV at 270-420 nm and MIR to LWIR 600-6000 cm^{-1}. The moving DOAS instrument captures spectra from the smoke plume present along the full length of the plot edge, including that at higher altitudes hence probably sampling emissions from the full range of fuel. The fixed FTIR collects measurements that correspond to smoke at near ground level and over a fixed path, not necessary in the full plot pathlength, and maybe likely to be preferentially capturing the smoke emitted from more smoldering combustion due to the ground level nature of

the smoke. For fire AF4, FTIR may have been positioned near an intensely burning patch of fuel causing the sampling of a thick plume of smoke which the DOAS did not measure, at least during the same time period as the FTIR. Also it should be noted that the DOAS results were averaged to a measurement per one second, or sometimes more, whilst the FTIR retrievals were not. Fires AF3, AF4 and AF5 were averaged to 1 measurement per 2 seconds and 3 and 4 seconds for fires AF1 and AF2 respectively. However even without the additional averaging, the DOAS column amounts of fire AF4 did not reach the levels of fires AF3. Additionally, it could that the FTIR measurements for some fires, the optical path was fully filled by smoke, whereas for others not so much due to e.g. fire activity or the pathlength such that more ambient air fills the path. This could explain why the derived pathlength averaged mixing ratios of AF3 were not as high as those of fire AF4, as the mixing ratios are given as the concentration of the target species averaged over the whole path.

Also shown in Figure 7.22 is the time series of the Modified Combustion Efficient (MCE) was used to separate the flaming and smoldering phases of the fire (Yokelson *et al.*, 2008):

$$MCE = \frac{\Delta CO_2}{\Delta CO_2 + \Delta CO},\tag{7.1}$$

where ΔCO_2 and ΔCO are the elevated pathlength averaged mixing ratios (i.e. those of the plume measurements minus those of the ambient background). A low MCE (e.g. < 0.9) indicates that the fuel has a low efficiency, i.e. a large flaming phase (Blake *et al.* 1996). An MCE greater than 0.9 suggests that over 50% of the combustion is smoldering and an MCE less than 90% suggests over 50% smoldering combustion (e.g. Sinha *et al.*, 2003). At the beginning (or end) of the measurements, when target gases are close to ambient level, the MCE is not important and values can range from close to zero to above 1. For example at 6 minutes into fire AF5, the MCE rises above 1 with both CO_2 and CO are at ambient levels still (405 and 0.15 ppm respectively). Generally, the MCE level for all fires fluctuates between 0.95 and 0.85, suggesting the fire moves from predominantly flaming to predominantly smoldering combustion. MCE values only fall out of this range a few times for each fire (excluding the start and end part corresponding to an MCE is greater than 0.90 due to gases close to ambient levels). Fire AF2 was the fire that burnt the least intensely, producing

the least amount of smoke, hence flaming combustion phase could possibly not have been that strong.

In general, the retrieved mixing ratios of the IR target species from the pilot study of South Africa were of lower levels that those from the Australia field campaign. This is due to the short sampling time of the smoke plume of the pilot study at the beginning of the fire. Hence it is not possible to carry out a detailed comparison between the results from the two field campaigns. The single exception is the mixing ratios of CO_2 for SF1 reached larger values than those from AF2 (1200 ppm compared to 800 ppm). As already mentioned, fire AF2 did not produce much smoke due to low fuel loading of the plot. Of the mixing ratios of remaining target gases that were detectable for fire AF2, CH_4 reached similar values to the mixing ratios of SF1 (3.4 ppm (AF2) and 2.6 ppm (SF2)). However estimated mixing ratios of CO from fire AF2 reach levels almost 2 times greater than those of fire SF1 (30 ppm (AF2) and 17 ppm (AF1)). Hence for SF1, although CO_2 mixing ratios reached quite high levels, CO did not, compared to AF2, suggesting that for the pilot study measurements captured smoke produced mainly by the flaming activity of the fire. This is backed up by an MCE greater than 0.95, discussed in Chapter 6.
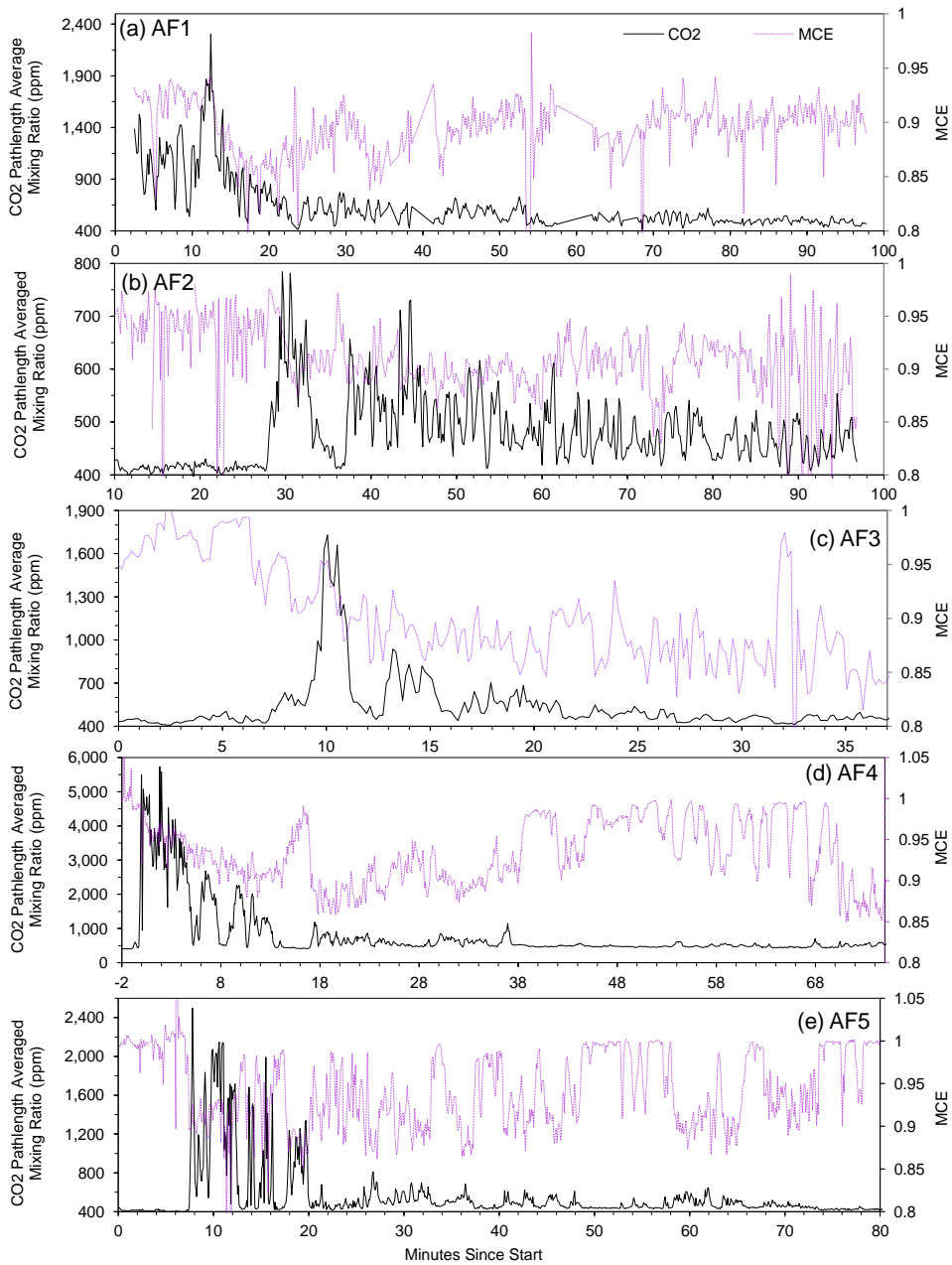
Figure 7.22: *The pathlength averaged mixing ratios of CO_2 (black) retrieved by applying MALT to the IR spectra collected during the Australian fires (a) AF1, (b) AF2, (c) AF3, (d) AF4 and (e) AF5. Also shown for each fire is the MCE (purple), calculated via Equation 7.1. An MCE greater than 0.9 suggests that over 50% of the combustion is smoldering and an MCE less than 90% suggests over 50% smoldering combustion (e.g. Sinha et al., 2003)*
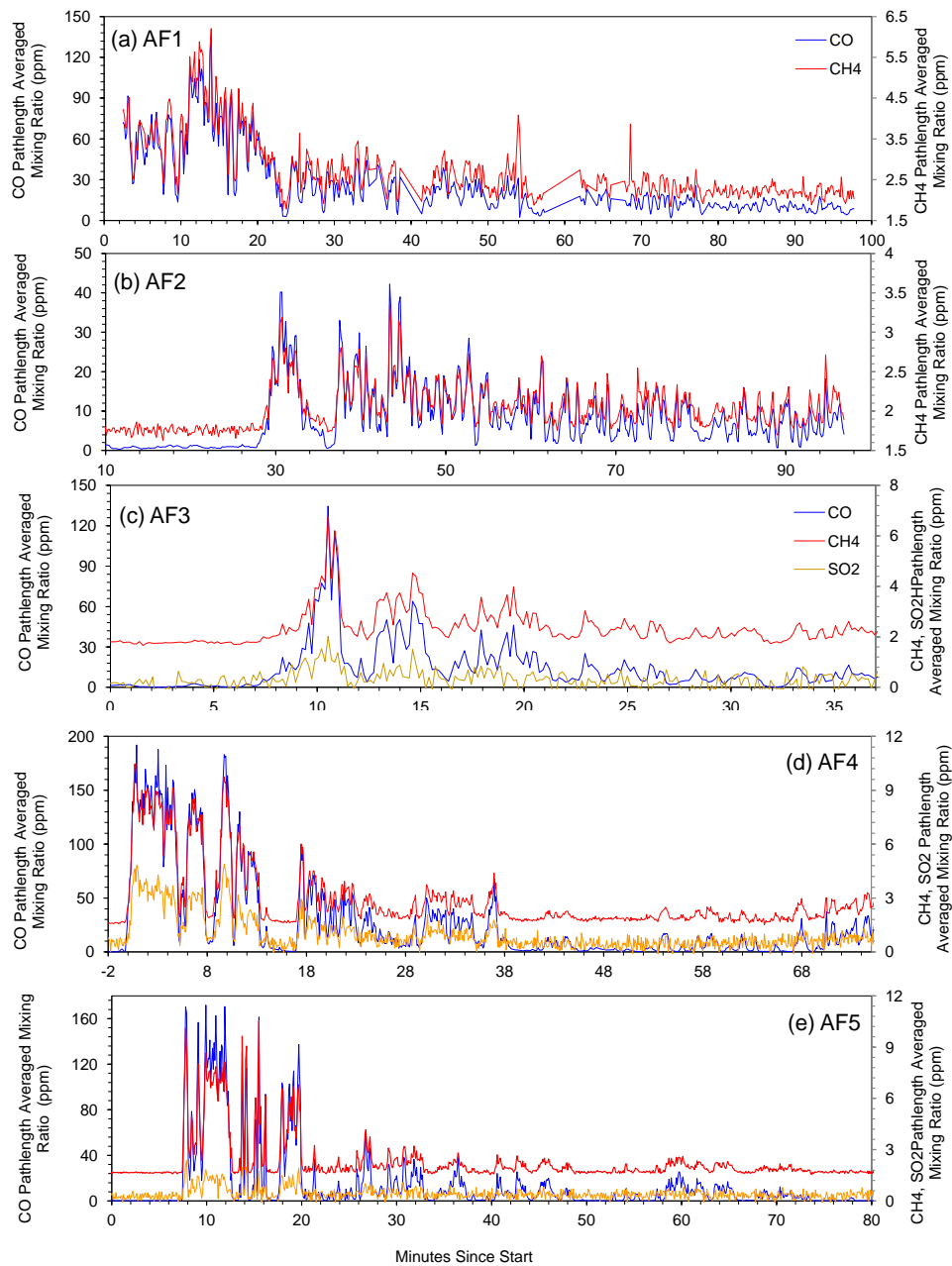
Figure 7.23: *The pathlength averaged mixing ratios of CO (blue), CH_4 (red) and SO_2 (yellow) retrieved by applying MALT to the IR spectra collected during the Australian fires (a) AF1, (b) AF2, (c) AF3, (d) AF4 and (e) AF5. It was not possible to detect NO_2 for any of these fires. Note that for fires AF1 and AF2, SO_2 was unable to be detected due to low levels of smoke emitted by these fires.*

7.5.3 Emission Ratios and Emission Factors

The emission ratios of CO, CH_4 and where possible, SO_2, where derived using the pathlength averaged mixing ratio measurements calculated from the FTIR spectra (i.e. the ppm time series shown in Figure 7.22 and 7.23). Figures 7.24, 7.25, 7.26, 7.27 7.28 and 7.29 and Table 7.6 show the calculated emission ratios. Sinha *et al.* (2003) consider biomass burning to be a significant source of a species if the correlation coefficient (r^2) between its mixing ratio with that of CO_2 or CO is greater than 0.5. Emission ratios were calculated separately for the predominately flaming and smoldering phases and also a fire integrated emission ratio was derived, according to the MCE of either less than 0.9 (smoldering) and 0.9 (flaming).

All ratios with respect to CO_2 are larger for the smoldering phase points, suggesting that greater amounts of these gases are released during the smoldering phases of the fire compared to CO_2. The smoldering $\frac{CO}{CO_2}$ ERs are consistently larger than their flaming counterparts. Conversely, the $\frac{CH_4}{CO}$ ratio is greater during the flaming phase as although both CH_4 and CO are both released more preferentially during the smoldering stage, CO is emitted at proportionally a greater rate. This ratio shows the least variability between stages for all fires, with the greatest difference being 10 % between the smoldering and flaming stages for fire AF2. The CO_2 ratios for all species have a inter stage variability, for example the flaming ratio for $\frac{CO}{CO_2}$ of fire AF4 is one third that of its smoldering equivalent. This reflects the variability of CO_2 emissions between flaming and smoldering stages. Despite the differences in whole fire, flaming and smoldering phase ratios, the whole fire ratios shall be used from this point onwards for simplicity for the remaining analysis as an averaged value of the separate flaming and smoldering ratios. The $\frac{CH_4}{CO}$ ratio is reasonably stable between the early season fires AF1, AF2 and AF3 and subsequently increases for fires AF4 and AF5, implying that more CH_4 per unit of CO released was emitted during the late season fires. Early burning season fire averaged $\frac{CH_4}{CO}$ ratios are between 0.315-0.038 while equivalent late season ratio range from 0.0441 to 0.0453. This is not the case for any of the other target species. For SO_2, there is no pattern between ratios and seasonality.
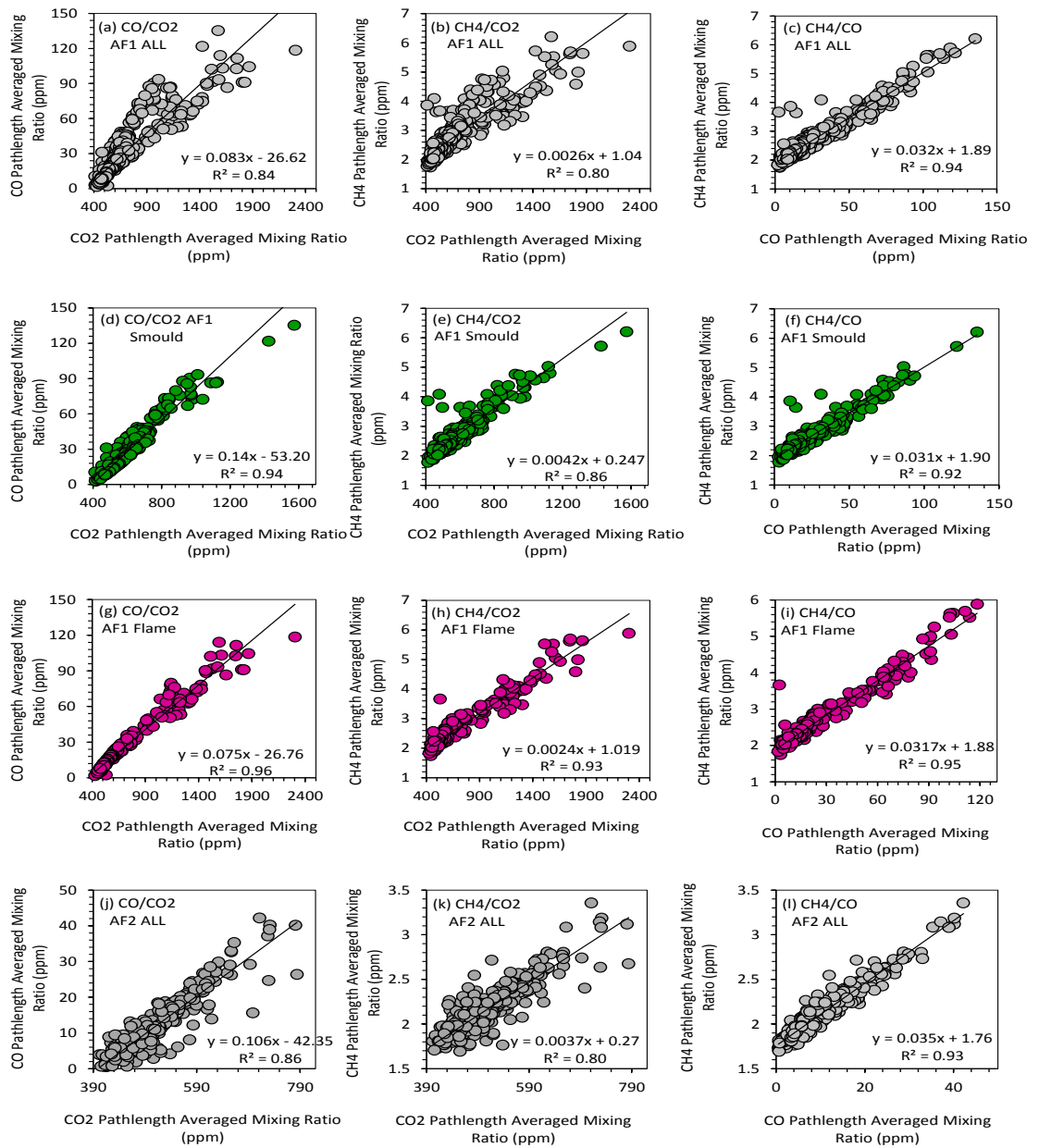
Figure 7.24: *Derivation of the Emission Ratios (ERs) for fires AF1 and AF2 of the target gases using CO_2 and CO as the comparison species. The ERs are taken as the line of best fit between the pathlength averaged mixing ratios of CO_2 (or CO) and the target gas: CO, CH_4 and SO_2. Shown is the fire averaged (grey), smoldering (green) and flaming (pink) ERs, with the flaming and smoldering split according to the MCE calculated as in Equation 7.1, with values greater than 0.9 suggesting flaming combustion and less than suggesting smoldering. Values of the emission ratios are given in Table 7.6.*
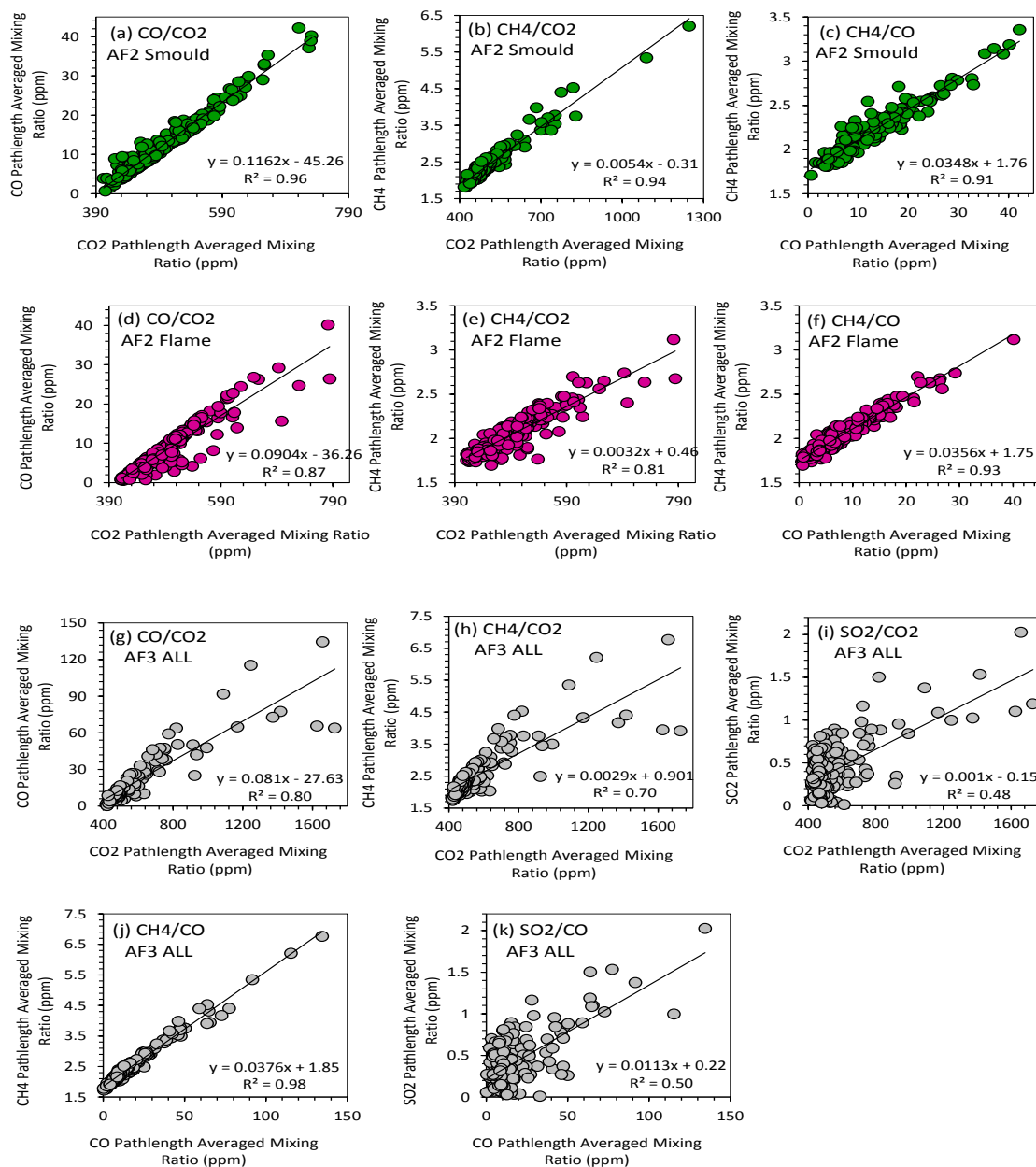
Figure 7.25: *Derivation of the Emission Ratios (ERs) for fires AF2 and AF3 of the target gases using CO_2 and CO as the comparison species. The ERs are taken as the line of best fit between the pathlength averaged mixing ratios of CO_2 (or CO) and the target gas: CO, CH_4 and SO_2. Shown is the fire averaged (grey), smoldering (green) and flaming (pink) ERs, with the flaming and smoldering split according to the MCE calculated as in Equation 7.1, with values greater than 0.9 suggesting flaming combustion and less than suggesting smoldering. Values of the emission ratios are given in Table 7.6.*
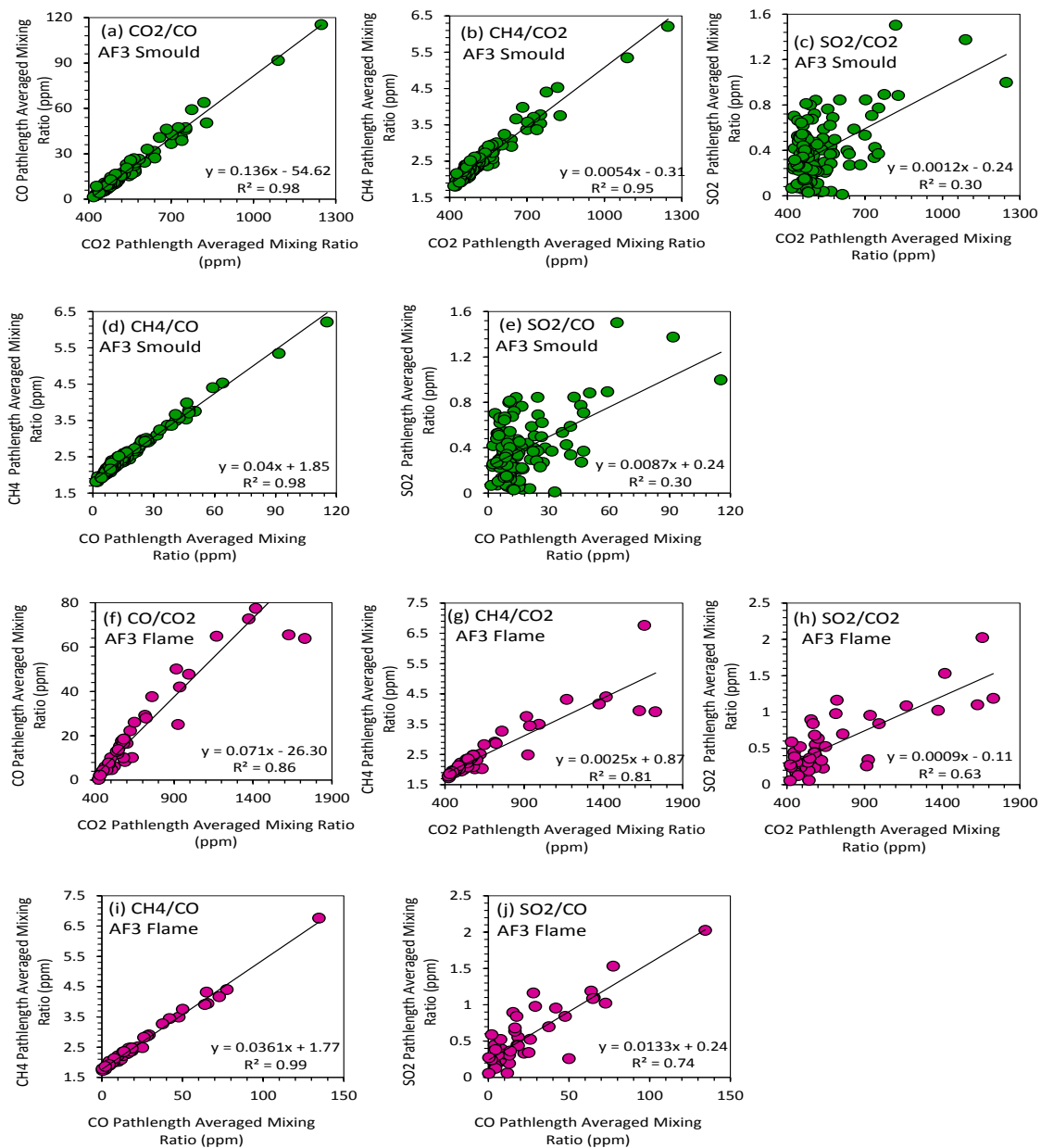
Figure 7.26: *Derivation of the Emission Ratios (ERs) for fire AF3 of the target gases using CO_2 and CO as the comparison species. The ERs are taken as the line of best fit between the pathlength averaged mixing ratios of CO_2 (or CO) and the target gas: CO, CH_4 and SO_2. Shown is the fire averaged (grey), smoldering (green) and flaming (pink) ERs, with the flaming and smoldering split according to the MCE calculated as in Equation 7.1, with values greater than 0.9 suggesting flaming combustion and less than suggesting smoldering. Values of the emission ratios are given in Table 7.6.*
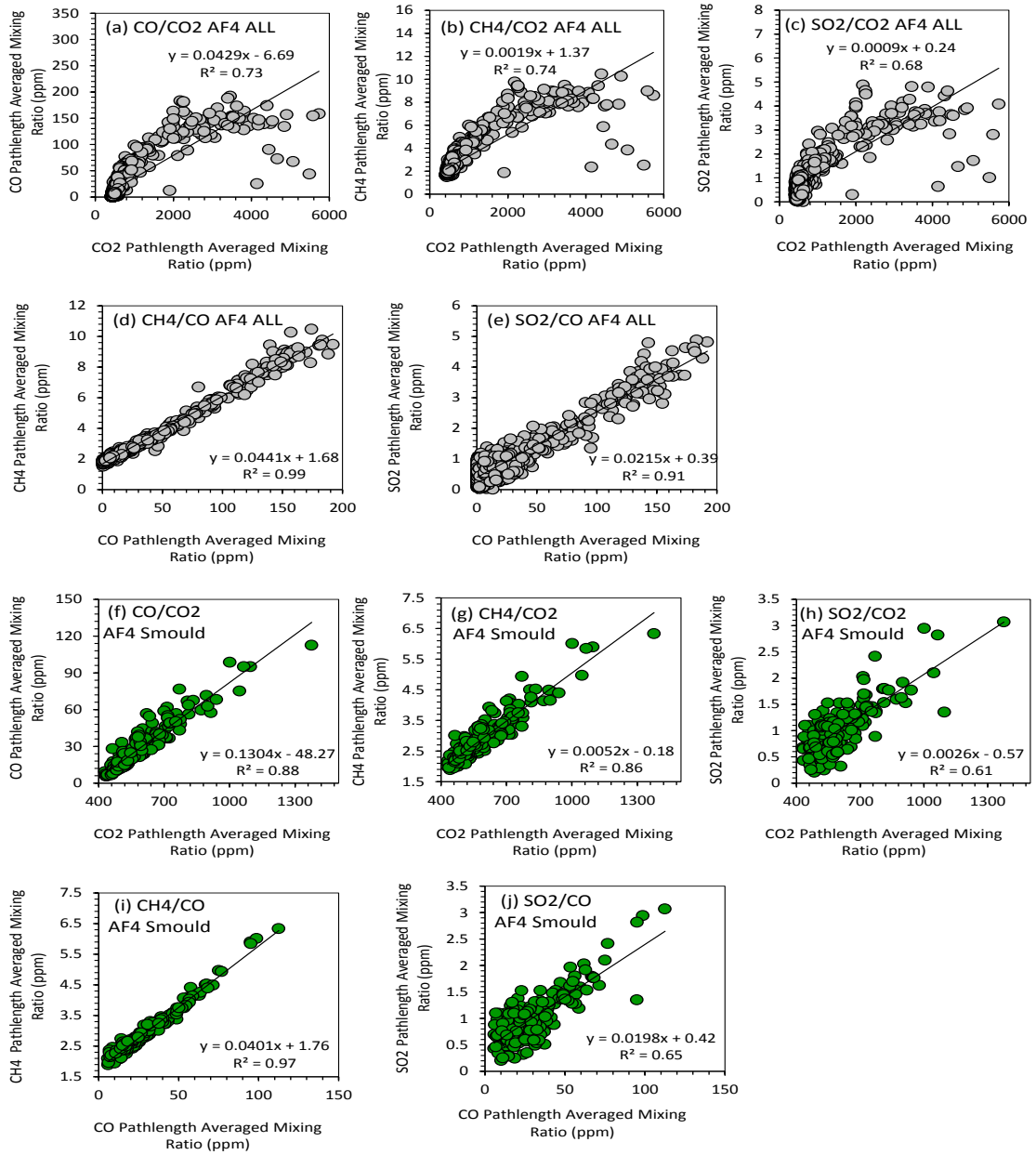
Figure 7.27: *Derivation of the Emission Ratios (ERs) for fire AF4 of the target gases using CO_2 and CO as the comparison species. The ERs are taken as the line of best fit between the pathlength averaged mixing ratios of CO_2 (or CO) and the target gas: CO, CH_4 and SO_2. Shown is the fire averaged (grey), smoldering (green) and flaming (pink) ERs, with the flaming and smoldering split according to the MCE calculated as in Equation 7.1, with values greater than 0.9 suggesting flaming combustion and less than suggesting smoldering. Values of the emission ratios are given in Table 7.6.*
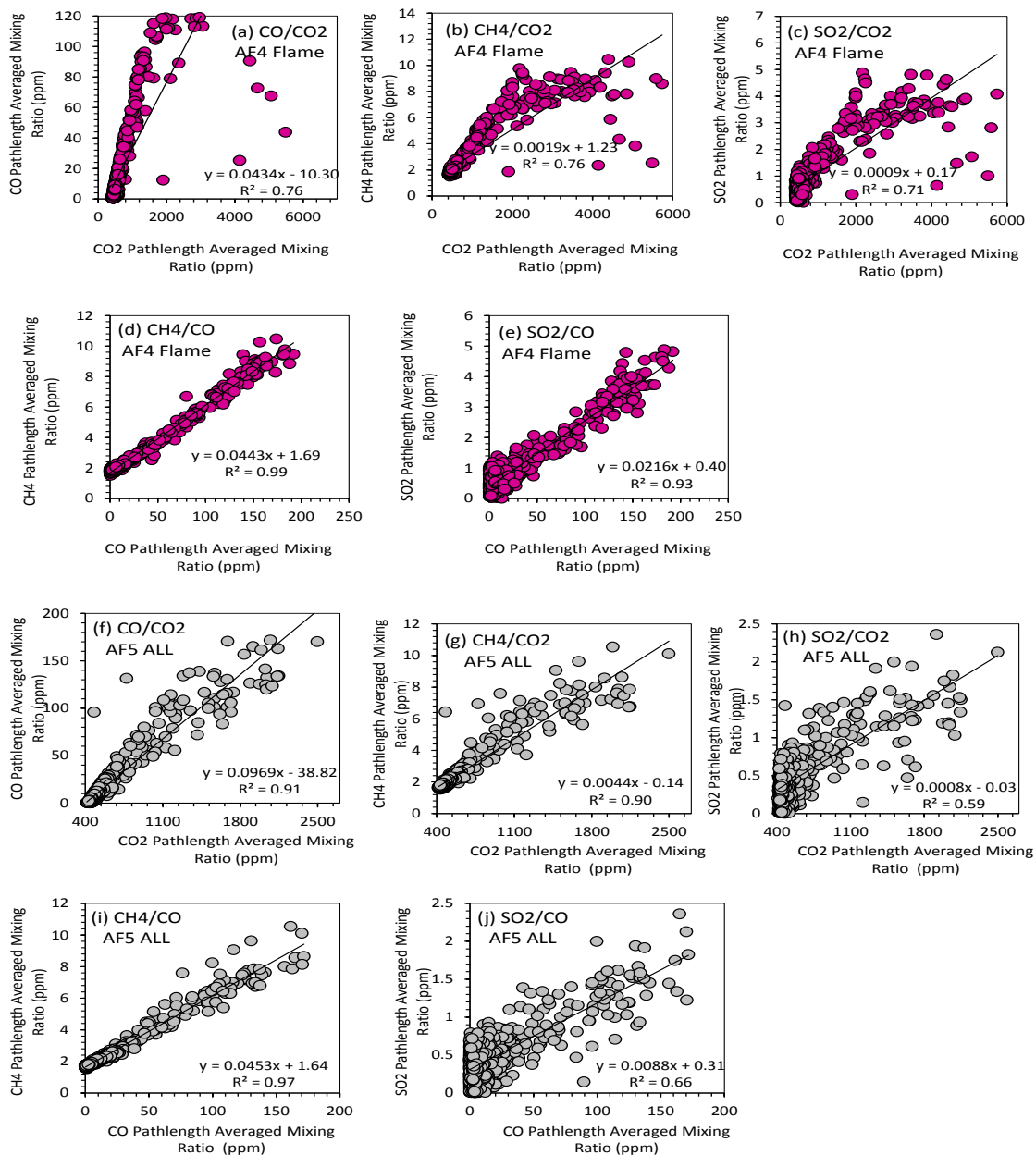
Figure 7.28: *Derivation of the Emission Ratios (ERs) for fires AF4 and AF5 of the target gases using CO_2 and CO as the comparison species. The ERs are taken as the line of best fit between the pathlength averaged mixing ratios of CO_2 (or CO) and the target gas: CO, CH_4 and SO_2. Shown is the fire averaged (grey), smoldering (green) and flaming (pink) ERs, with the flaming and smoldering split according to the MCE calculated as in Equation 7.1, with values greater than 0.9 suggesting flaming combustion and less than suggesting smoldering. Values of the emission ratios are given in Table 7.6.*
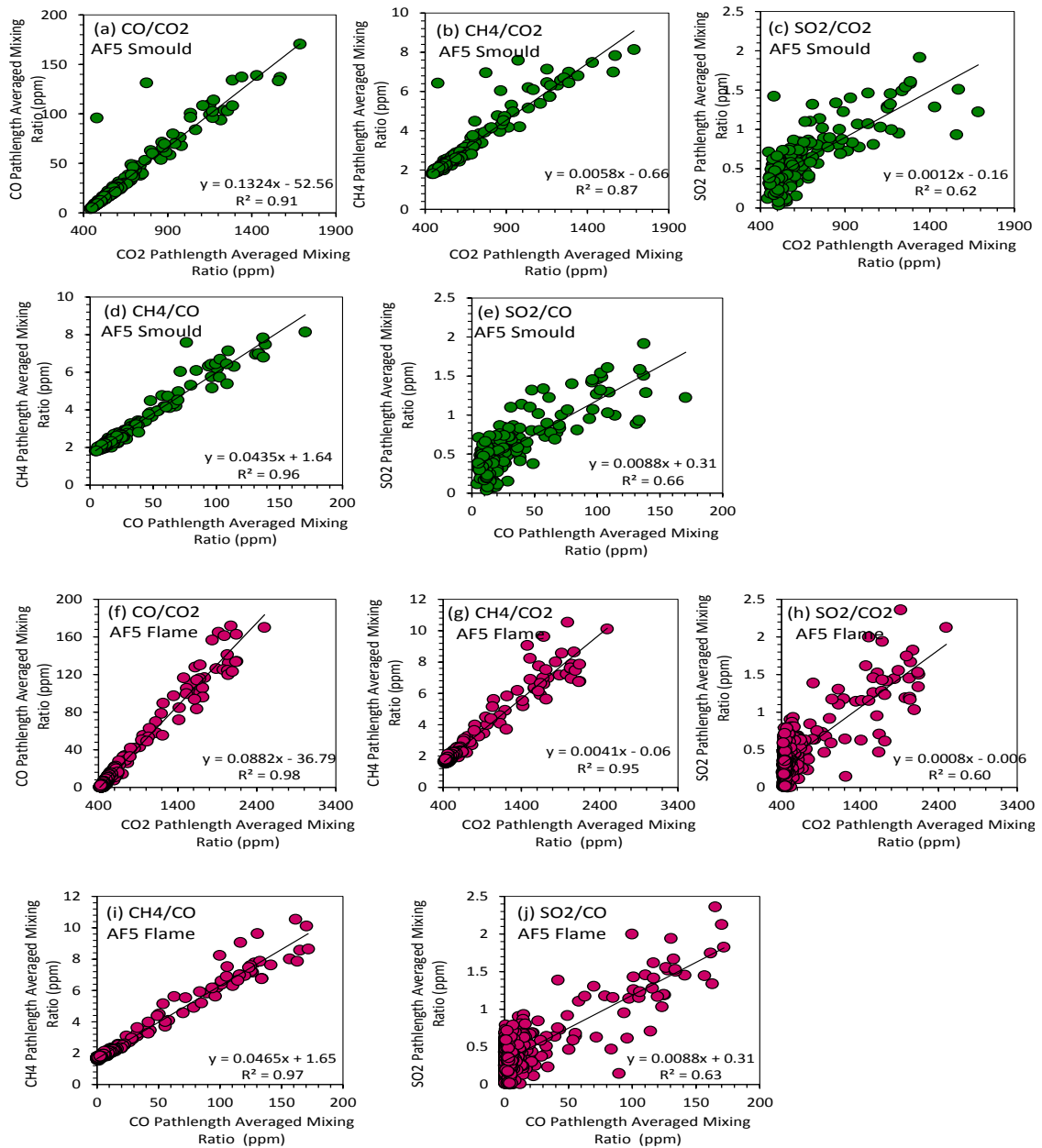
Figure 7.29: *Derivation of the Emission Ratios (ERs) for fire AF5 of the target gases using CO_2 and CO as the comparison species. The ERs are taken as the line of best fit between the pathlength averaged mixing ratios of CO_2 (or CO) and the target gas: CO, CH_4 and SO_2. Shown is the fire averaged (grey), smoldering (green) and flaming (pink) ERs, with the flaming and smoldering split according to the MCE calculated as in Equation 7.1, with values greater than 0.9 suggesting flaming combustion and less than suggesting smoldering. Values of the emission ratios are given in Table 7.6.*

In contrast, Korontzi *et al.* (2003) exploring the variation in biomass burning emissions with regards to the burning season (May-October) on African savanna fires, found that if most of the burning occurred at the start of the burning season, suggesting there would be a rise in incomplete combustion products, such as CO (by a factor of 2) and CH_4 (by a factor of 4). However, for the scenario of fires occurring predominantly at the end of the burning season, the timing and amount of burning is more significant in determining the level emissions when compared to emission factors. When burning is evenly distributed, fires from both the early and late season will contribute significantly to total emissions from species emitted during incomplete combustion. It was found that emissions from CO_2 are not as variable, such that the timing of fires does not have a significant impact on the variation of total emissions of this gas.

Table 7.6: *Emission Ratios (ERs) for fires Australian fires AF1-AF5, shown in Figures 7.24, 7.25, 7.26, 7.27, 7.28 and 7.29. Given are the fire averaged, smoldering and flaming ERs, with the flaming and smoldering split according to the MCE calculated as in Equation 7.1, with values greater than 0.9 suggesting flaming combustion and less than suggesting smoldering.*

All

Ratio	$\frac{CO}{CO_2}$	$\frac{CH_4}{CO_2}$	$\frac{SO_2}{CO_2}$	$\frac{CH_4}{CO}$	$\frac{SO_2}{CO}$
AF1	0.0825 +/- 0.0031	0.0026 +/- 0.0001	-	0.0315 +/- 0.0007	-
AF2	0.1063 +/- 0.0040	0.0037 +/- 0.0002	-	0.0351 +/- 0.0009	-
AF3	0.0810 +/- 0.0063	0.0029 +/- 0.0003	0.0010 +/- 0.0002	0.0376 +/- 0.0009	0.0113 +/- 0.0018
AF4	0.0429 +/- 0.0017	0.0019 +/- 7.6290e-5	0.0009 +/- 0.0003	0.0441 +/- 4.2447e-5	0.0215 +/- 0.0004
AF5	0.0969 +/- 0.0022	0.0044 +/- 0.0001	0.0008 +/- 5.0058e-5	0.0453 +/- 0.0006	0.0087 +/- 0.0005

Flaming

Ratio	$\frac{CO}{CO_2}$	$\frac{CH_4}{CO_2}$	$\frac{SO_2}{CO_2}$	$\frac{CH_4}{CO}$	$\frac{SO_2}{CO}$
AF1	0.0750 +/- 0.0018	0.0024 +/- 7.8986e-5	-	0.0317 +/- 0.0009	-
AF2	0.0904 +/- 0.0044	0.0032 +/- 0.0002	-	0.0356 +/- 0.0012	-
AF3	0.0710 +/- 0.0089	0.0025 +/- 0.0004	0.0009 +/- 0.0002	0.0361 +/- 0.0012	0.0133 +/- 0.0025
AF4	0.0434 +/- 0.0018	0.0019 +/- 8.2405e-5	0.0009 +/- 4.5141e-5	0.0443 +/- 0.0004	0.0216 +/- 0.0004
AF5	0.0882 +/- 0.0012	0.0041 +/- 8.0421e-5	0.0008 +/- 5.0508e-5	0.0465 +/- 0.0006	0.0087 +/- 0.0005

Smoldering

Ratio	$\frac{CO}{CO_2}$	$\frac{CH_4}{CO_2}$	$\frac{SO_2}{CO_2}$	$\frac{CH_4}{CO}$	$\frac{SO_2}{CO}$
AF1	0.1351 +/- 0.0040	0.0042 +/- 0.0002	-	0.0311 +/- 0.0011	-
AF2	0.1162 +/- 0.0032	0.0042 +/- 0.0002	-	0.0311 +/- 0.0011	-
AF3	0.1360 +/- 0.0039	0.0054 +/- 0.0002	0.0012 +/- 0.0003	0.0400 +/- 0.0009	0.0087 +/- 0.0025
AF4	0.1304 +/- 0.0066	0.0052 +/- 0.0003	0.0026 +/- 0.0003	0.0401 +/- 0.0009	0.0198 +/- 0.0020
AF5	0.1324 +/- 0.0064	0.0058 +/- 0.0003	0.0012 +/- 0.0001	0.0435 +/- 0.0015	0.0088 +/- 0.0010

Table 7.7 lists the emission factors (gkg^{-1}) of the target gases calculated using the derived emission ratios. Emission factors vary between fires for all species, as seen by the coefficient of variation (CV) given in the table. Prasad *et al.* (2000) used ground based measurements to investigate emissions from two tropical forest fires in India. When comparing the two fires, it was found that one had greater rate of spread, flame length and height and fire intensity (Prasad *et al.*, 2000; Wooster *et al.*, 2011). It is suggested that this could have caused higher burning efficiency and burning more fuel. This highlights that emissions are expected to vary even for the same fuel types, depending on the nature of the fire. CO_2 exhibits the least amount of variation (with a coefficient of variation ranging between 0.76 to 2.35). The level of inter-fire variation for the CO EFs are are greater for the fire averaged and flaming phases of the fire (CV of 27.87 and 24.17 respectively) compared to the smoldering phase (CV of 5.48), where CO is predominately emitted. The EFs of CH_4 follow the same pattern. The same was found in Ward *et al.*, (2003) for EFs derived from tropical vegetation fires and reflects the fact that CO_2 is emitted predominantly during flaming combustion while CO and CH_4 during smoldering combustion.

The inverse is true for SO_2 and CO_2, with CV seen to be smallest for the flaming phase (1.84 and 8.34 respectively), both of which are thought to be predominantly emitted during the flaming phase of the fire. However, looking at Figures 7.26, 7.27, 7.28 and 7.29, which show the derived ERs for SO_2 with respect to CO_2 and CO fire fires AF3-AF5, the SO_2 ER with respect to CO proves to have a stronger relationship for all cases, apart from the smoldering ERs for AF3, in which the correlation is weak and equal for both ratios (r^2=0.3). Note that the same is true for the SO_2 ERs derived for the South African pilot study (see Figure 6.12). As CO is emitted in greater amounts during smoldering and CO_2 during flaming combustion, these results suggest that for the fires shown here, SO_2 emissions were more prominent in the smoldering phase of the fires. Sinha *et al.* (2003) found that SO_2 emissions were negative relationship with MCE, despite SO_2 emissions associated with flaming combustion in laboratory studies. It is suggested that this could be caused by fuels with high S content producing low values of MCE. Ferek *et al.* (1998) found that SO_2 and NO_x emissions were correlated more with flaming conditions in tropical vegetation fires in Brazil.

However this relationship was not as strong as that of measured emissions of hydrocarbons and smoldering combustions and it is suggested that the derived dependency of NO_x and SO_2 on combustion efficiency could have been due to higher burning temperatures and more complete burning of the fuel.

From Table 7.7, it can be seen that the CO and CH_4 fire averaged EFs for fire AF4 are the lowest for all fires (48 gkg^{-1} and 1.215 gkg^{-1}) respectively, while the corresponding CO_2 EF is the highest (1755 gkg^{-1}). The same is true for the flaming EFs, however not for the smoldering. Again, due to the relationship CO_2 and CO have with the flaming and smoldering phases of a fire, this suggests that fire AF4 was dominated by flaming combustion over smoldering. Looking at the MCE values in Figure 7.22 for fire AF4, values to not fall below 0.9 during the emission peaks as much as the remaining fires do. The low fire averaged and flaming CH_4 EFs for fire AF4 contrast with the higher CH_4 to CO ERs for the late season burns compared to the early season fires. This is due to the ER of CH_4 to CO_2 for the corresponding fire phases, again suggesting that higher levels of CO_2 in relation to CH_4 were emitted compared to the other fires. The EFs of SO_2 are relatively high compared to the CH_4 EFs, in particular for fire AF4 it is double that of CH_4 (3.1 and 6.1 gkg^{-1} respectively). This seems unrealistically high and causes some doubts on the accuracy of the FTIR derived mixing ratios of SO_2.

Inter-comparison of Emission Ratios and Emission Factors with the Literature

Below the ERs and EFs derived in this work shall be compared with current estimations found in the literature. Chapter 6 already discusses such a comparison (see Tables 6.4 and 6.5), however in this section a wider range of references from a variety of fuel types is provided. Tables 7.8 and 7.9 detail ERs and EFs of the target gases from numerous studies, as well as the values derived from this study. Note that for the Australian results, the mean of the fire averaged ERs and EFs are presented.

From Table 7.8 it can be seen that the $\frac{CO}{CO_2}$ ER from the pilot study in South Africa is the lowest of all studies. This is partly due to the sampling of the fire plume only taking occurring for a short time at the beginning of the fire and also that the smoke that was

Table 7.7: *Emission Factors (and their uncertainties calculated) for all target gases for Australian fires AF1-AF5, according to Equation 6.5. The MCE has been used to separate the fire averaged EFs into flaming and smoldering components, using Equation 7.1, with values greater than 0.9 suggesting flaming combustion and less than suggesting smoldering. Also shown in the mean, standard deviation and coefficient of variation (CV) between EFs for each species across the different fires.*

	All			
Fire	EF CO_2	EF CO	EF CH_4	EF SO_2
AF1	1689.94 ±188.60	88.73 ± 10.45	1.60±0.19	-
AF2	1652.03 ± 192.10	111.77 ± 13.66	2.23 ± 0.29	-
AF3	1691.81 ± 263.50	87.22± 15.18	1.79 ± 0.33	2.46 ± 0.62
AF4	1755.12 ± 199.46	47.92 ± 5.768	1.215 ± 0.15	2.30 ± 0.28
AF5	1665.08 ± 173.45	102.69 ± 10.95	2.67 ± 0.28	1.94 ± 0.24
Mean	1690.80	87.67	1.90	2.23
STDEV	39.80	24.43	0.56	0.27
CV	2.35	27.87	29.68	11.92

	Flaming			
Fire	EF CO_2	EF CO	EF CH_4	EF SO_2
AF1	1702.01± 181.96	81.24 ± 8.90	1.49 ± 0.17	-
AF2	1676.80 ± 207.05	96.47 ± 12.80	1.96 ± 0.27	-
AF3	1708.20 ± 365.77	77.19 ± 19.15	1.56 ± 0.42	2.24 ± 0.69
AF4	1754.28 ± 202.28	48.46 ± 5.94	1.21 ± 0.15	2.30 ± 0.29
AF5	1678.80 ± 171.84	94.24 ± 9.73	2.51 ± 0.26	1.96 ± 0.24
Mean	1704.02	79.52	1.746	2.17
STDEV	31.32	19.22	0.50	0.18
CV	1.84	24.17	28.88	8.38

	Smoldering			
Fire	EF CO_2	EF CO	EF CH_4	EF SO_2
AF1	1609.54± 179.39	138.39 ± 15.96	2.46 ± 0.30	-
AF2	1636.98 ± 183.73	121.06 ± 13.99	2.39± 0.29	-
AF3	1606.58 ± 173.66	139.06± 15.55	3.16 ± 0.36	2.81 ± 0.76
AF4	1614.79 ± 194.90	134.02± 17.54	3.06 ± 0.41	6.11 ± 0.99
AF5	1611.10 ± 189.73	135.76 ± 17.28	3.406 ± 0.44	2.81 ± 0.38
Mean	1615.80	133.66	2.90	3.91
STDEV	12.21	7.33	0.45	1.91
CV	0.76	5.48	15.48	48.73

Table 7.8: Emission Ratios of the target species CO_2, CH_4, CO, NO_2 and SO_2 derived from this work (both those of the Australian field campaign in this chapter and those of the South African pilot study presented in Chapter 6) and a selection of those available in the literature for several fuel types and sampling/analysis methods. Note that (AB) OP FTIR denotes (airborne) open-path Fourier Transform Infra-red measurements, (AB) GC (airborne) gas chromatography and ChemAn is short for Chemiluminescence Analyser.

Study	$\mathbf{ER}_{\frac{CO}{CO_2}}$	$\mathbf{ER}_{\frac{CH_4}{CO_2}}$	$\mathbf{ER}_{\frac{CH_4}{CO}}$	$\mathbf{ER}_{\frac{NO_2}{CO_2}}$	$\mathbf{ER}_{\frac{NO_2}{CO}}$	$\mathbf{ER}_{\frac{SO_2}{CO_2}}$	$\mathbf{ER}_{\frac{SO_2}{CO}}$	Fuel Type	Sampling
This study Australia	0.082	0.0031	0.039			0.0009	0.014	Australian Savanna	OP FTIR
This study South Africa	0.017	0.0005	0.036	0.0007	0.0251	0.0002	0.014	African Savanna	OP FTIR
Ferek et al. (1998)	0.069	0.0069	0.124	-	-	-	-	Amazon /Cerrado	AB GC
Yokelson et al. (1999)	0.082		0.076	-	-	-	-	Pine	AB FTIR
Prasad et al. (2000)	0.124	-	-	0.0008	-	-	-	India Forest	GB Licor/ChemAn
Hobbs et al. (2003)	-	-	0.040	-	-	-	0.011	African Savanna	AB GC
Hobbs et al. (2003)	-	-	0.058	-	0.0254	-	-	African Savanna	AB FTIR
Pak et al. (2003)	0.021	0.0098	0.55	-	-	-	-	Tropical Vegetation	AB GC
Sinha et al. (2003)	0.072	-	0.039	-	-	0.0009	-	African Savanna	AB GC
Sinha et al. (2003)	0.064	-	0.053	0.002	-	-	-	African Savanna	AB FTIR
Shirai et al. (2003)	0.089	-	0.043	-	-	-	-	Aus Savanna	AB insitu
Wooster et al. (2011)	0.096	0.0043	0.046	-	-	-	-	African Savanna	OP FTIR

sampled was possibly emitted during predominately flaming combustion due to the same issue. The same theory applies to the low $\frac{CH_4}{CO_2}$ ratio for the South African pilot study, see Chapter 6 for a more detailed discussion on this.

As already mentioned, care needs to be taken when comparing emission ratios and emission factors from different studies due to sampling of aged and initial smoke. Hobbs *et al.* (2003) found that the ER $\frac{\Delta NO_2}{\Delta CO}$ decreased to around one third of its original value after approximately 40 minutes. However it is stated that this measurement should be viewed with care as all NO_2 downwind mixing ratios using the AFTIR were close to, or below the detection limit of the instrument. Also, NO_2 can react with OH to produce HNO_3. All the literature studies detailed in Table 7.8 describe air-borne sampling, with the exception of Prasad *et al.* (2000).

The $\frac{CO}{CO_2}$ ER from ground based OP-FTIR measurements from the Australian field campaign (0.082) falls close within the literature values of this ER for savannas (0.64-0.96), in particular the ER from Shirai *et al.* (2003) based on measurements from Australian savannas. However, equivalent ERs from pine and Amazon/Cerrado forests (0.082 and 0.069 respectively) are also within this range (Ferek *et al.*, 1998; Yokelson *et al.*, 1999). Pak *et al.* (2003) estimated the $\frac{CO}{CO_2}$ at a comparatively low 0.021, however this was from airborne sampling in Australia of smoke at around 2-5 km altitude from tropical fires in Africa and South America, hence the composition of this aged smoke (up to a few days old) is likely to be different to more fresh plumes. The highest $\frac{CO}{CO_2}$ ER is given by Prasad *et al.* (2000) from ground based sampling of tropical forests in India, suggesting that perhaps the sampling here was taken during lower burning efficiency. There is a discrepancy between the $\frac{CO}{CO_2}$ ERs derived from Sinha *et al.* (2003) using AFTIR and airborne gas chromatography (0.072 and 0.64 respectively) during the SAFARI 2000 field campaign. Although it is unlikely that the different methods sampled exactly the same smoke, this illustrates that even during the same fire there will be variations in estimated emissions.

Comparing the $\frac{CH_4}{CO_2}$ ER, the value derived here from the Australian savannas (0.031) is close to that of Wooster *et al.* (2011) from African savannas (0.0043), yet at least half of the

remaining ratios derived from biomass burning of other fuels. The $\frac{CH_4}{CO_2}$ ratio is not quoted in the literature very often as emissions of CH_4 correlate more with the emissions of CO.

For the $\frac{CH_4}{CO}$ ratio, the value from the Australian field campaign (0.039) is close to the equivalent ratio from the South African field campaign (0.036) and also within the range of the remaining ratios from savannas (between 0.40-0.058). Again, there is a variation between the $\frac{CH_4}{CO}$ ERs derived using airborne FTIR and gas chromatography from Sinha *et al.* (2003) (0.39 and 0.53 respectively). Hobbs *et al.* (2003) also made measurements during SAFARI 2000 using both airborne FTIR and gas chromatography, however sampling aged plumes, while Sinha *et al.* (2003) details sampling of initial smoke. The $\frac{CH_4}{CO_2}$ ER from Hobbs *et al.* (2003) again exhibits variation between the two sampling methods (0.040 and 0.058 for gas chromatography and AFTIR respectively). Also the ERs given by Hobbs *et al.* (2003) are larger than those quoted by Sinha *et al.* (2003). This can possibly be explained by the fact that CO gets removed from the plume as it travels long distances, hence the ER with respect to CO should increase with time (Pak *et al.*, 2003). The $\frac{CH_4}{CO_2}$ ERs for the other fuel types are consistently larger than those of savannas, highlighting the differences in emissions from different fuel types.

As mentioned in Chapter 6, there is a lack of data on SO_2 and NO_2 emissions, perhaps due to the relatively difficulty in measuring these gases within plumes. Hence it is not possible to make as comprehensive a comparison between literature values as with most of the other gases. Looking firstly at NO_2, its ER with respect to CO_2 derived during the South African pilot study (0.0007) is much less than that quoted by Sinha *et al.* (2003) via AFTIR of savanna fires. This could be due to the fact that airborne sampling tends to over estimate emissions from flaming combustion, such as NO_2. Yet the $\frac{NO_2}{CO}$ ratio from the pilot study (0.0251) is close to the equivalent value from Hobbs *et al.* (2003) derived too from AFTIR. Despite the difference in fuel type, the pilot study $\frac{NO_2}{CO_2}$ ER is close to that estimated by Prasad *et al.* (2000) from ground based sampling of Indian forest fires. The SO_2 ER with respect to CO_2 derived from the Australian field campaign (0.0009) is equal to that derived from Sinha *et al.* (2003) from African savannas but more that 4 times greater than that of

the pilot study (0.0002). Lastly, there is a good agreement between the $\frac{SO_2}{CO}$ ratio between those in Table 7.8, the values of this ER from the pilot study equal to the value from the Australian field campaign of this work (0.014) and close to that of Hobbs *et al.* (2003) from African savannas (0.011).

Table 7.9 lists the EF (gkg^{-1}) of the target species from numerous studies conducted in previous work from smoke emitted from fires of varying fuel types. As already noted in Chapter 6, the CO_2 EF from the pilot study is relatively high (1803 gkg^{-1}) compared to the other studies, mainly because the smoke sampled from these measurements was predominantly from flaming combustion. This is reflected in the high CO_2 EF and low CO and CH_4 EFs (19 and 0.33 gkg^{-1} respectively). See Chapter 6 for more on this.

The CO_2 EF derived from the Australian field campaign (1690 gkg^{-1}) is within the range of the equivalent EFs from savanna fires. However this range is quite variable, with the smallest CO_2 EF given by Shirai *et al.* (2003), 1613 gkg^{-1}, from Australian savanna smoke plumes and the greatest from Sinha *et al.* (2003) at 1706 gkg^{-1}. Shirai *et al.* (2003) estimated emissions from tropical savanna fires in northern Australia during the Biomass Burning and Lightening Experiment (BIBLE) phase B aircraft campaign. Samples were taken at approximately 3 km and 1.7 km over the source region and smoke could be of varying age. Sinha *et al.* (2003) however, made samples of smoke that were only a few minutes old, at approximately 500 m altitude. Therefore Sinha *et al.* (2003) is more likely to have sampled the fresh smoke that was injected into high altitudes during flaming combustion, hence a high CO_2 EF.

For the other fuel types, the CO_2 EFs vary in an inconsistent manner. For example Akagi *et al.* (2011) estimated the CO_2 EF for boreal forests as 1489 gkg^{-1}, whereas van Leeuwen and van der Werf (2011) gave a higher value of 1648 gkg^{-1}. Note that the emission factors of Akagi *et al.* (2011) are taken from various experiments from airborne, groundbased and laboratory measurements, hence they are an average of different measurement techniques. In contrast van Leeuwen and van der Werf (2011) estimated emission factors for savanna and grasslands, tropical forests and boreal forests based on weighted EF estimated *in situ* measurements and the GFED model framework. This shows that possibly using different methods to investigate emissions can lead to variability in the results. For tropical forests, the listed CO_2 EFs are less variable, all falling within the range of 1615-1677 gkg^{-1}, apart from that given by Christian *et al.* (2007), at a low 1343 gkg^{-1}, as part of the Tropical Forest and Fire Emissions Experiment (TROFFEE). TROFFEE was carried out in order to inves-

Table 7.9: *Emission Factors ($g.kg^{-1}$) of the target species CO_2, CH_4, CO, NO_2 and SO_2 derived from this work (both those of the Australian field campaign in this chapter and those of the South African pilot study presented in Chapter 6) and a selection of those available in the literature for several fuel types and sampling/analysis methods. Note that (AB) OP FTIR denotes (airborne) open-path Fourier Transform Infra-red measurements, (AB) GC (airborne) gas chromatography and ChemAn is short for Chemiluminescence Analyser. Note for Akagi et al. (2011) Emission factors are derived from airborne, groundbased and laboratory measurements. ChemAn short for Chemiluminescence Analyser*

Study	EF CO_2	EF CO	EF CH_4	EF SO_2	EF NO_2	Fuel Type	Sampling
This Study Australia	1691	88	1.90	2.23	-	-	OP
This Study South Africa	1803	19	0.33	0.52	1.32	African Savanna	OP FTIR
Wooster et al. (2011)	1665	101	2.5	-	-	African Savanna	AB FTIR
Sinha et al. (2003)	1700	68	1.7	0.43	-	African Savanna	AB GC
Sinha et al. (2003)	1706	69	2.2	-	-	African Savanna	AB
Shirai et al. (2003)	1613	88	2.22	-	-	African Savanna	FTIR
Akagi et al. (2011)	1686	63	1.94	0.48	-	Savanna	MIX
Akagi et al. (2011)	1643	93	5.07	0.40	-	Tropical Forest	MIX
Akagi et al. (2011)	1489	127	5.96	-	-	Boreal Forest	MIX
Zhang et al. (2008)	791	64	-	-	0.79	Rice Straw	Lab GC/ChemAn
Zhang et al. (2008)	1558	141	-	-	0.32	Wheat Straw	Lab GC/ChemAn
Zhang et al. (2008)	1262	115	-	0.43	0.43	Corn Straw	Lab GC/ChemAn
van Leeuwen and van der Werf (2011)	1647	68	2.8	-	-	Savannah Grasslands	GC
van Leeuwen and van der Werf (2011)	1626	82	6.6	-	-	Tropical Forests	
van Leeuwen and van der Werf (2011)	1648	95	4.8	-	-	Boreal Forests	
Sinha et al. (2004)	1705	73	1.4	0.22	-	Miombo Forests	AFTIR
Sinha et al. (2004)	1759	42	0.5	0.3	-	Dambo Grassland	GC
Yokelson et al. (2007)	1615	101	5.7	-	1.8	Brazilian Amazon	AFTIR
Yokelson et al. (2007)	1677	57	3.8	-	0.58	Global Tropical	GC
Yokelson et al. (2008)	1677	57	3.8	-	0.58	Global Tropical	FTIR LICOR
Christian et al. (2007)	1343	229	17	-	-	Global Tropical	LICOR

tigate emissions from vegetation fires in the tropics. Part of the campaign was carried out in the laboratory comparing the application of OP-FTIR, GC coupled with proton-transfer reaction mas spectrometry (GC-PTR-MS) on the analysis of emissions from numerous different types of tropical fuels. Field campaigns were carried out in Brazil, including both ground based and airborne sampling of vegetation fire plumes. These include PTR-MS and FTIR measurements (Yokelson et $al.$, 2007). The airborne EF derived using the AFTIR are given by Yokelson et $al.$ (2007), the equivalent ground-based by Christian et $al.$ (2007) and the laboratory by Yokelson et $al.$ (2008). Hence the low CO_2 EF of 1343 gkg^{-1} is likely to represent the smoldering emissions of the sampled fires. The field measurements have the advantage of measuring real fires, however they are not able to sample the whole of the fire. In particular, the ground based measurements are mainly of smoldering emissions. The smoke sampled by the airborne measurements consists of a mixture of emissions from flaming combustion and smoldering lofted emissions. In contrast, the laboratory experiments are able to sample the entire fire, however they do not include 'real' factors such as smoldering logs. In general, laboratory measurements sample emissions from foliage and twigs, ground based on large logs and airborne a mix of large and small sized fuels (Yokelson et $al.$, 2008). This explains the higher CO_2 emission factors of Yokelson et $al.$ (2007, 2008) at 1615 gkg^{-1} and 1677 gkg^{-1} respectively.

Sinha et $al.$ (2004) derived emission factors for various trace gases from two fires in Zambia, one Miombo woodland fire and another Dambo grassland fire during the SAFARI 2000 experiment. Airborne measurements were made with an AFTIR, SO_2 Teco fluorescence analyzer and canister samples for GC analysis. The CO_2 EFs for the Miombo forests and Dambo grasslands are 1705 gKg^{-1} and 1759 gkg^{-1} respectively. The lower EF from the Miombo forest fires maybe due to the greater smoldering combustion as the fuel type here will contain larger fuels compared to the grasslands that are made up of mainly easily combustible, fine fuels (Ferek et $al.$, 1998).

Looking at the emission factors derived from different types of straw by Zhang et $al.$ (2008), wheat straw produced the largest emission factors for CO_2 and CO and rice straw the least.

However the reverse was true for NO_2 (and for NO_x as a whole, not shown in Table 7.9. It is suggested that this difference could be attributed to the different regions in which the fuel types were plants (wheat and corn in North China and rice in South China), such different growing regions can effect the C and N content of the fuels. Moreover, the properties of the different fuel types, such as moisture, will effect how the fuel burns and hence the emissions.

With respect to the CO EFs, a similar pattern follows to that of the EF of CO_2. The EF from the pilot study is the lowest, at 19 gkg^{-1}, due to both a short sampling time and the predominantly flaming combustion emitted (see Chapter 6), corresponding to a high CO_2, EF. The same goes for the CH_4 EF for the pilot study, at 0.33 gkg^{-1} and by far the lowest of all the CH_4 EFs listed on Table 7.9. The CO EF derived from the Australian field campaign (88 gkg^{-1}) is within the range of the listed CO EFs for savannas, however again there is variation between these estimates, with the highest given by Wooster *et al.* (2011) at 101 gkg^{-1} and the lowest by Akagi *et al.* (2011) at 63 gkg^{-1}. This variation is probably due to the difference in sampling methods used to derive the EFs, for example Wooster *et al.* (2011) implements the same OP-FTIR methodology used in this work, hence it is likely that more of the emissions originate from smoldering combustion in contrast to e.g. Sinha *et al.* (2003) in which an AFTIR/GC was used, sampling more of the flaming emissions of a fire that move to higher altitudes and hence the EF of CO is smaller (68/69 gkg^{-1}) than that of Wooster *et al.* (2011). Note that there is not much variation however between the CO_2 and CO EFs derived from the AFTIR and GC by Sinha *et al.* (2003), with 1700 gkg^{-1} (AFTIR) and 1706 gkg^{-1} (GC) for CO_2 and 68 gkg^{-1} (AFTIR) and 69 gkg^{-1} (GC) for CO.

As is the case for CO_2, the CO EFs from the boreal forest fuel types given by Agaki *et al.* (2011) and van Leeuwen and van der Werf (2011) are not in close agreement (127 and 95 gkg^{-1} respectively). However they are negatively correlated with their equivalent CO_2 EFs, suggesting that the EFs derived from Akagi *et al.* (2011) represent more inefficient combustion than those given by van Leeuwen and van der Werf (2011). The most variation of the CO EFs for tropical forests is given by Yokelson *et al.* (2008), at 57 gkg^{-1} and Christian *et al.* (2007), at a much higher 229 gkg^{-1}, representing the laboratory and ground bases

measurements of the TROFFEE field campaign. This again shows how different sampling techniques can lead to varying results. Note that it is expected that from Christian *et al.* (2007) the CO_2 EF will be relatively high and CO EF relatively low due to the sampling of smoldering emissions that do not rise aloft. However, the laboratory measurements of Yokelson *et al.* (2008) have shown to have a higher CO_2, EF and lower CO EF than the equivalent EFs from the airborne measurements of Yokelson *et al.* (2008), despite generally airborne measurements sampling higher levels of flaming emissions.

The EFs of CH_4 representing savanna burning do not exhibit much variation (apart from that of the pilot study), all falling within range of 1.9-2.7 gkg^{-1}. The most variation for this species is between the tropical forest ecosystems, are discussed above, with the laboratory experiment of Yokelson *et al.* (2008) producing the smallest value (3.8 gkg^{-1}) and the ground based measurements from the same experiment, given by Christian *et al.* (2007) at a very high 17 gkg^{-1}. The CH_4 EFs given for boreal forests (5.96 and 4.8 gkg^{-1} respectively) do not show as much of a variation as with CO_2 and CO. The CH_4 EF for Dambo grassland (0.3 gkg^{-1}) given by Sinha *et al.* (2004) is relatively low, as is the corresponding CO EF (42 gkg^{-1}), again suggesting that for such fires the type of combustion is mainly flaming, due to fuel types that are able to burn at a high combustion efficiency. van Leeuwen and van der Werf (2011) also suggest that grass fuels in savannas favor flaming combustion as they have a larger surface to volume ratio, hence pyrolysis is easier and flaming combustion is dominant. Larger litter and plant stems that are found in forests are not as easily combusted and hence smoldering combustion is dominant. This is because it is easier to heat small density fuel types to ignition and hence they have a higher rate of heat production.

Looking at the EFs for SO_2 and NO_2, there is a gap in the literature for these species. From Table 7.9, it can be seen that all EFs for this species fall within the range 0.43-0.52 gkg^{-1}, including that from the pilot study. In contrast, the SO_2 EF derived from the Australian field campaign is up to 5 times greater, at 2.23 gkg^{-1}, greater than the corresponding CH_4 ratio. This suggesting that the SO_2 EF from the Australian field campaign could possibly over be overestimated. There is not much scope to compare NO_2 EFs as the few that

are listed are from varying fuel types.

7.5.4 Fluxes

The SO_2 and (where possible) NO_2 fluxes were calculated using the target species in plume vertical column amounts derived from the UV-DOAS spectra, the GPS distances and estimates of plume velocity derived from weather station measurements coupled with video imagery taken from above the fires using the helicopter. As in the pilot study described in Chapter 6, these flux rates were subsequently combined with the emission ratios of CO_2, CO and CH_4 to return their respective flux rates of the carbonaceous gases (Figure 7.30). Flux calculations from AF2 were omitted due to low column amounts of SO_2 and the inability to detect NO_2. For fire AF1, only the fluxes of SO_2 and NO_2 are given, as neither of these gases were able to be detected by the FTIR, hence the subsequent calculation of the carbon species fluxes were not possible.

From Figure 7.30, it can be seen that while fire AF3 exhibits a main peak in the middle of the fire when the smoke was most prominent and smaller peaks either side, fires AF4 and AF5 present less of a trend with not one but several main peaks. This can be related to the corresponding vertical column amounts of SO_2 and NO_2 for each fire, as shown in Figures 7.12, 7.13 and 7.14. Fire AF3 is the only fire that has a distinctive emission peaks of both gases in the middle of the fire. This follows on to the calculation of the fluxes, where the same flux emission peak is exhibited at around 10 minutes into the fire. This is not the case for the other fires, in particular fires AF4 and AF5. Again looking at Figures 7.12, 7.13 and 7.14, it can be seen that column amounts of SO_2 and NO_2 fluctuate throughout the duration of the fire, with no clear peaks. This contributes to the 'jagged' feature of the derived fluxes. At times for these fires there was GPS failure, at these points there was hence no 'distance' measurements for the collected spectra, resulting in comparatively less measurement points for the traverse where the GPS failure occurred and hence lower flux values at these traverses. This is also the case when the UV-DOAS spectra were saturated by high levels of incoming radiation.

The derived flux time series of NO_2 for fire AF1 does not exhibit significant raised values in the presence of the plume, compared with the equivalent SO_2 fluxes. This is due to the low pathlength amounts of NO_2 for this fire. Comparing the difference in flux rates between NO_2 and SO_2 for fire AF3, peak levels of SO_2 (270 $g.s^{-1}$) are almost double those of NO_2 (134 $g.s^{-1}$). The same ratio is held between the two gases for fire AF5, with fluxes for SO_2 and NO_2 reaching peaks at 156 and 76 $g.s^{-1}$ respectively. This relationship breaks down for fire AF4, as when the SO_2 flux time series reaches a peak of 439 $g.s^{-1}$, the NO_2 flux is only at 70 $g.s^{-1}$. This is because towards the end of the fire, the UV-DOAS spectra were at times saturated in the spectral region used to retrieve NO_2. Hence, for these points there does not exist any NO_2 pathlength amounts, resulting in lower levels of the NO_2 fluxes. The peak value of NO_2 for AF4 is over half of the SO_2 flux at that traverse, at 132 $g.s^{-1}$compared with 217 $g.s^{-1}$. Comparing fluxes between fires, AF4 reached the highest levels, despite AF3 column amounts of SO_2 reaching greater peak levels. This is because for fire AF4, the average estimated plume speed used was 17 $m.s^{-1}$, compared to 4-5 $m.s^{-1}$ used for the other fires. This is due to high wind speeds measured by the weather station at ground level. The SO_2 peak flux amount for AF3 is close to that of AF5. Despite the emission peaks of SO_2 being higher for AF3, outside of these peaks the SO_2 column amounts are greater for AF5 (see Figure 7.14). Looking at the derived fluxes of the carbonaceous species, peak values are high for all fires. For example for fire AF4, the peak flux rates of CO_2, CO and CH_4 are 335 $kg.s^{-1}$, 9 $kg.s^{-1}$ and 4.6 $kg.s^{-1}$ respectively.

It is noted that the flux rates for the carbon species described above, in particular those of CO_2, reach very high, perhaps unrealistic values. One possible reason for this the low SO_2 to CO_2 ER. In order to investigate this, this ratio was derived in an alternative way using the product below:

$$\frac{SO_2}{CO} \times \frac{CO}{CO_2}, \tag{7.2}$$

as both $\frac{SO_2}{CO}$ and $\frac{CO}{CO_2}$ have a stronger correlation compared to $\frac{SO_2}{CO_2}$. However for fires AF4 and AF5, Equation 7.5.4 was in fact equal to $\frac{SO_2}{CO_2}$ and for fire AF3 both values were close (0.001 for $\frac{SO_2}{CO_2}$ and 0.00092 for Equation 7.5.4. Hence the change in ratio made little or no difference. As there is not much information on the ERs of SO_2 it is difficult to make strong

comparisons with the ERs calculated here. EFs from Table 6.6 of SO_2 and CO_2 of Akagi *et al.* (2011) (from the savanna estimates) were used to estimate the SO_2 to CO_2, yielding a value of 0.0003, even smaller than that of this work. Another possible cause for the high flux estimates could be the too high an estimate of the SO_2 and NO_2 flux rates derived from the UV-DOAS. Again, apart from Oppenheimer *et al.,* (2004), there is not much information available in the literature of SO_2 and NO_2 fluxes emitted from biomass burning to compare the results here with.

Comparing the flux rates from the Australian field campaign with those from the South African fires, it can be seen that for the last two fires of South Africa, SF3 and SF4, fluxes reach beyond those in the Australian field campaign. For example NO_2 peaks at close to 500 g.s^{-1} for SF3 and SO_2 close to 600 g.s^{-1} for SF4. One reason for this could be the size of the burn plots of South Africa compared to those from the Australian field campaign. The plots of South Africa range between 71000-88000 m^2, whereas the Australian plots range between 44000-55000 m^2. The lower fluxes of SF1, SF2, AF1 and AF2 can be explained by low fuel loadings. The higher NO_2 fluxes of South Africa translate to higher fluxes for the carbon species as for this field campaign, the $\frac{NO_2}{CO_2}$ ratio was used due to the inability to detect SO_2 with the FTIR. For example CO_2 fluxes reach close to 800 kg.s^{-1} for SF3.

The FRP time series for fires AF3 and AF5 are shown in Figure 7.31 alongside the matching carbon fluxes. As stated in Chapter 5, the FRP time series has an error approximetly $\pm20\%$, coming from pixel level uncertainty and cooler parts of the fire remaining undetected due to a detection limit of 200^oC of the camera. The trace gas fluxes and the FRP time-series appear to follow the same trend, with peaks and troughs occurring at similar times. However the FRP series is made up of instantaneous measurements, whilst the fluxes are averages over each of the traverses, so there exists some discrepancies between the timing of the peaks and troughs. More importantly, the thermal radiation that makes up the FRP is essentially instantaneously measured by the MIR camera, whilst the smoke released at the same moments takes a finite amount of time to reach the DOAS, thus resulting in a temporal offset between the two measures. Note the dip in the FRP series of fire AF3 disagreeing

with the peak of the fluxes. This is explained by the obstruction of the FOV of the thermal camera by trees. Carbon fluxes reach close to 80 kg.s^{-1} for AF3 and 40 kg.s^{-1} for AF5. This compares with 10 kg.s^{-1}, 220 kg.s^{-1} and 170 kg.s^{-1} for SF2, SF3 and SF4 respectively. The FRP time series reach 12 MW and 60 MW for AF3 and AF5 respectively. In contrast, the maximum FRP from the South African fires reach much higher values, at 35 MW, 500 MW and 100 MW for fires SF2, SF3 and SF4 respectively. In particular notice the low FRP maximum of AF3 (12 MW) and carbon flux maximum (80 kg.s^{-1}). This discrepancy is probably attributed to the smaller measurement area of fire AF3. Initially the size burn plot was at was 1 hectare, marked by four corner fires at the edge of the plot. However the fire ultimately burnt an area around 4.5 hectors, but the measurement area for the thermal camera was probably kept to approximately 1 hectare.
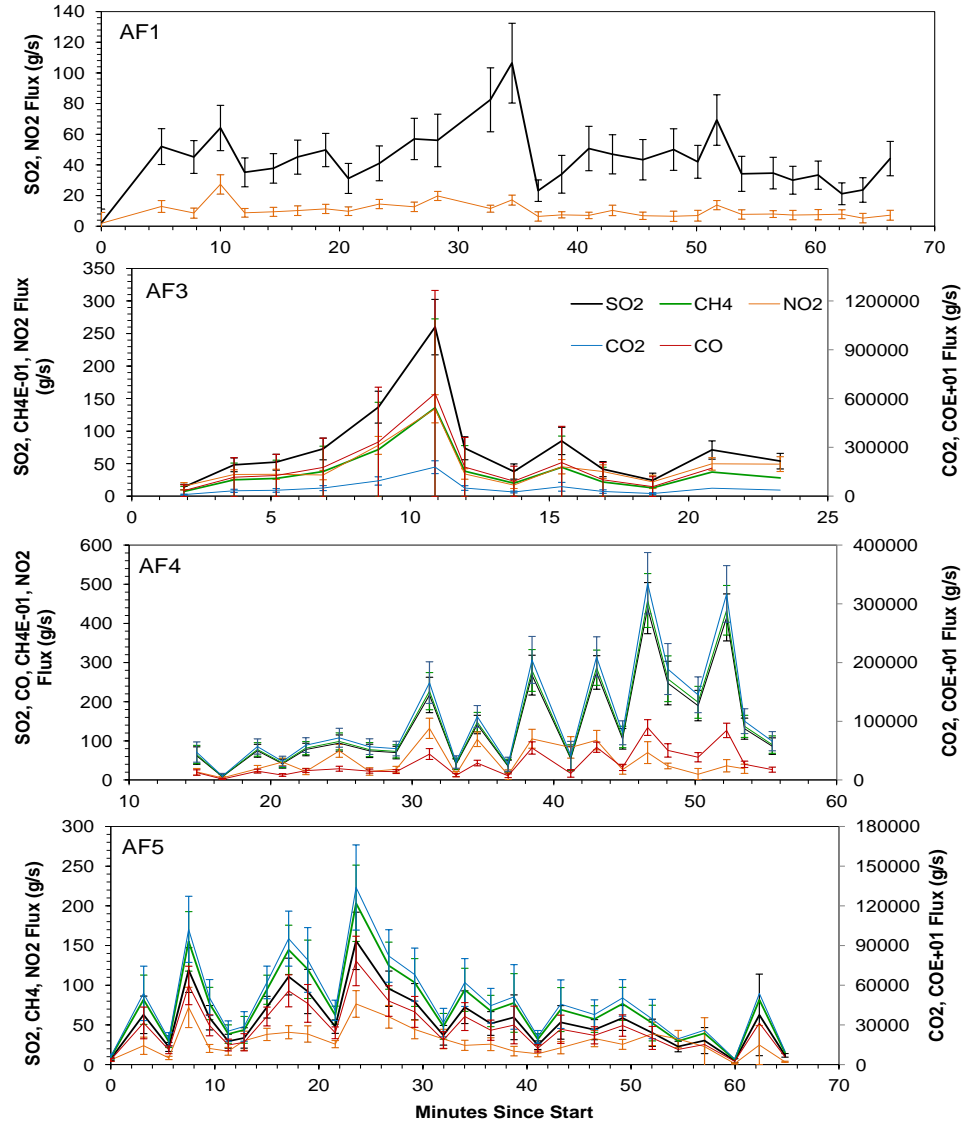
Figure 7.30: *The fluxes of SO_2, CO_2, CO and CH_4 for fires AF1, AF3, AF4 and AF5 from the Australian pilot study. The SO_2 and NO_2 flux for each fire was calculated using the pathlength averaged column amounts of SO_2 and NO_2 derived from the UV-DOAS spectra, shown in Figures 7.13 and 7.12. The emission ratios in Table 7.6 were applied to the SO_2 flux rate for each fire to calculate the flux rates of CO_2, CO and CH_4, as in Equation 6.6. Note that for fire AF1, only the NO_2 and SO_2 fluxes are shown as SO_2 was not able to be detected by the FTIR for this fire, due to low levels of smoke emitted by the fire. In addition, there are no fluxes at all for fire AF2 as the retrieved vertical column amounts of SO_2 and NO_2 by the UV-DOAS were of low values and exhibited high levels of noise, again due to the relatively low level of smoke emitted by this fire compared to the others.*
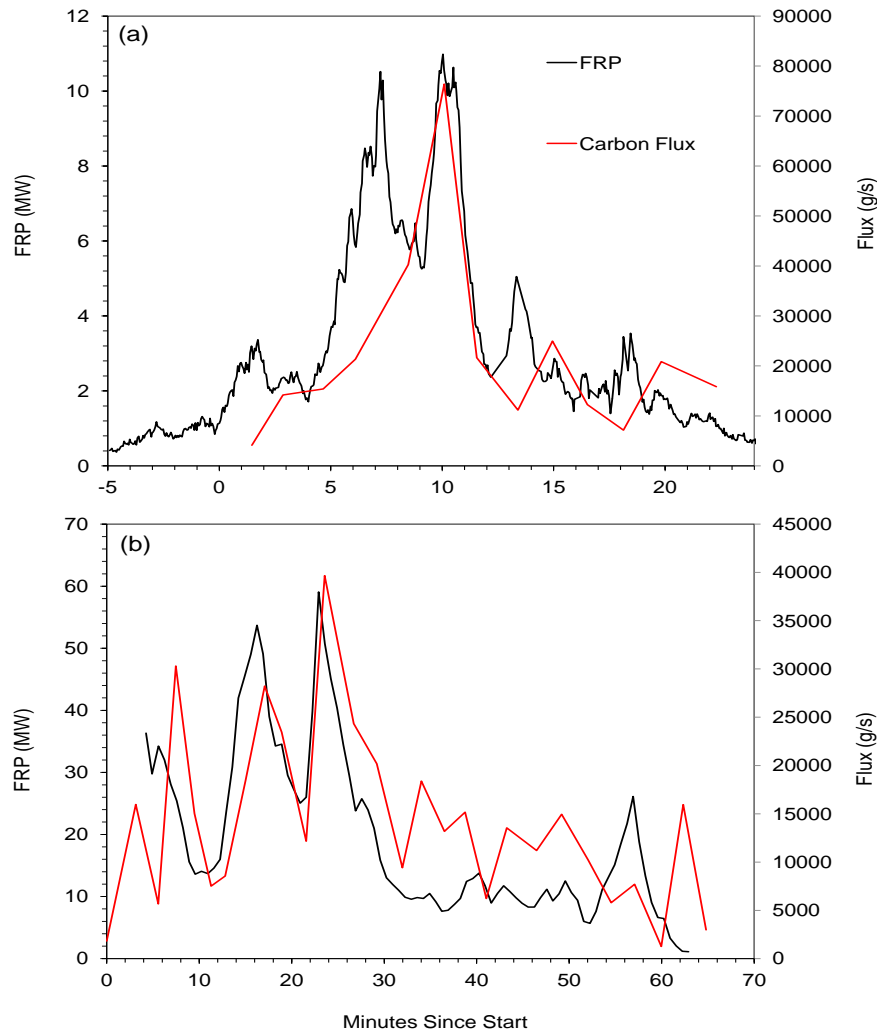
Figure 7.31: *The total carbon flux rates ($g.s^{-1}$ of the Australian fires (a) AF3 and (b) AF5 calculated by applying Equation ?? to the flux rates of CO_2, CO and CH_4 in Figure 7.30 (a) and (d). These are compared with the FRP time series (MW) of the same fires derived from the MIR thermal camera observations made in a helicopter above the fires, shown in black.*

7.6   Conclusion

This Chapter describes the deployment of the UV-DOAS and FTIR spectrometers during several managed tropical savanna burns in Arnhem Land, northern Australia. According to the methods detailed in Chapter 5, the UV-DOAS was implemented during the fire on a vehicle that was continuously traversing underneath the smoke plume throughout the dura-

tion of the burning, collecting UV spectra of scattered solar radiation. These spectra were then used to derive the vertical column amounts of NO_2 and SO_2 in the plume. For each of the fires, column amounts of NO_2 were significantly lower than SO_2, suggesting that the fuel in these types of ecosystems is comparatively lacking in levels of nitrogen. There was a relatively good agreement between the column amounts of the two gases within the fires. The strength of this agreement was higher when higher levels of smoke were emitted by the fires (AF3-AF5). For fires AF1-AF2, relatively less smoke was emitted, and hence column amounts were low and exhibited high levels of noise. This follows on from the results of the South African field campaign (presented in Chapter 5), in which low levels of smoke within a fire resulted in rather nosiey column amounts.

It was noted that there was some variability (for both gases) between retrieved column amounts of individual PT combinations from the spectra measured during a fire, bit not those measured using the gas cells. A suggested reason is any scattering or absorption caused by the particles present in the smoke plume.

The vertical column amounts calculated in this chapter from the Australian fires were compared with those from the previous two field campaigns of South Africa and Canada. As expected, due to both differences in fuel types, there were variations between results, particularly between the boreal forests in Canada and the savannas in Australia and South Africa, however there was some similarity between ratios of SO_2 to NO_2 from the Australian and South African fires.

The FTIR and IR source, as outlined in Chapter 6, were positioned by the burn plot, approximately 40 m apart, such that the smoke plume was able to fill the optical pathlength between the two instruments. IR spectra were collected and a non-linear least squares fitting forward model was applied to retrieve the mixing ratios of CO_2, CO, CH_4, and where possible SO_2 and NO_2, which were then used to calculate their emission ratios and emission factors. The MCE was also derived to investigate the variability of the emissions with respect to the different stages of combustion of the fire. The ERs and EFs derived here different with those

from the South African pilot study due to the short measurement time of the pilot study sampling and bias towards flaming combustion. When compared with ERs and EFs from the literature, it was found that there was general agreement with the corresponding work on savannas. However there did exist some variation between the literature, possibly due to the different sampling methods used to estimate the ERs and EFs.

The vertical column amounts of SO_2 and NO_2 from the UV-DOAS were coupled with estimates of plume velocity and GPS measurements to return the flux rates of these two gases. These were combined with the ERs derived from the FTIR measurements to estimate the target carbon species fluxes of fires. As was the case for the South African fires, the these fluxes reach very high values, possibly due to the low SO_2 (or NO_2) to CO_2 ERs, or high flux rates returned from the UV-DOAS measurements. For fires AF3 and AF5, the total carbon flux was compared with the FRP time series of the same fires derived with airborne MIR imagery. There was a good correlation between the two measurements, despite the fact that they were derived by two completely different methods. This gives confidence to these methods as both related to the fuel consumed by the fire, hence with further work and validation, they may be used to to give estimates on the total fuel consumed by a fire.

It was discussed in Chapter 6 about the potential usefulness of the EFs and ERs derived from the FTIR in creating a strong, constant database to be used in models to calculate emissions from biomass burning. The results in this chapter back up those in the pilot study. Hence there is the possibility of eliminating the inconsistencies of the current literature values of EFs and ERs by using the FTIR to collect in-plume spectra of open vegetation fires across the globe. Providing there is enough smoke, the FTIR can be deployed with the easy to use, portable, UV-DOAS to estimate carbon fluxes to assist in the modeling of carbon emissions from fires over time. The strong correlation of the derived carbon fluxes with the FRP provides strength to the use of the FRP method to estimate biomass emissions, as an alternative to Equation 1.7.

Chapter 8

Conclusion

Contents

8.1 Introduction

The overall aim of the work presented in this thesis was:

"To explore the use of portable ground-based Ultra-Violet Differential Optical Absorption Spectrometry (UV-DOAS) for deployment in vegetation fire assessment and smoke emission studies, including their ability to provide information on trace gas fluxes and their potential for validating variations in fuel consumption rate derived from thermal remote sensing methods during three field campaigns located in:"

In order to achieve this aim, three field campaigns were carried out, in Kruger National Park (South Africa), Banf National Park (Alberta, Canada) and Arnhem Land (Northern Territory), Australia. The UV-DOAS was deployed during several managed open vegetation fires in each field campaign. In addition to this, a Fourier Transform Infra-red (FTIR)

spectrometer was used during the South African and Australian field campaigns alongside the UV-DOAS spectrometer with objective to derive emissions ratios of carbonaceous gases to those gases also detectable in the UV, and then combine the measurements these two instruments.

As already explained in Chapter 1, biomass burning emissions play an important role in the impact of trace gases, in particular GHGs, on radiative processes in the atmosphere. There has been a great deal of research carried out in order to investigate such emissions over the last few decades since Seiler and Crutzen (1980) first highlighted the potential importance of tropical fire emissions to atmospheric chemistry and Earth's radiative budget. Currently the research is a mixture of laboratory work and ground-based and airborne field sampling, all of which have their advantages and disadvantages, however this difference in sampling methods introduces a difficulty in inter-comparisons between some of the research studies. Joint use of the UV-DOAS and FTIR spectrometers in the field potentially offers a new and relatively easy method to investigate emissions of biomass burning due to the easy to use nature of both instruments, the portability of the UV-DOAS and the ability of the FTIR to detect a wide range of gases within the smoke plume emitted from burning vegetation. Thus, there is scope to deploy these two instruments to a wide range of open vegetation fires in a wide range of ecosystems, allowing for strong comparisons of emissions from different fuel types.

The majority of the research carried out on the emissions of a particular species from biomass burning makes use of Equation 1.7 (Seiler and Crutzen, 1980), which requires knowledge of the emission factor of the species, the burnt area and fuel load of the fire in question and the combustion completeness of the fuel type. There is uncertainty associated with all of these variables, in particular the fuel load and combustion completeness (van der Werf et al., 2006). Results presented here demonstrate that the use of the UV-DOAS and the FTIR for the potential to build a consistent database of emission data to be used in emission models, eliminating the variation of the use of different methods and instruments. Building on the work of Kaufman *et al.* (1996), Wooster *et al.* (2005) proposed the use of fire radiative power

(FRP), which is directly related to the rate of biomass combustion (Wooster *et al.,* 2005), to replace the use of burnt area, combustion completeness and fuel load used in estimations of emissions, hence eliminating some of the uncertainty associated with these variables. Carbon flux rates derived in this work via the integration of measurements from the UV-DOAS and FTIR of the experimental burns have been compared with the FRP time series derived from MIR thermal camera imagery of the same fires in order to investigate the robustness of the use of FRP to estimate biomass combustion rates. This use of FRP is becoming more widespread, as the requirement for trace gas and aerosol emissions inputs into atmospheric modeling studies increases, including for real-time forecasting of atmospheric visibility, air quality and trace gas vertical column concentration (Kaiser *et al.,* 2011). Strong correlations between derived carbon fluxes and FRP rates give strength to the use of the FRP rate to estimate biomass burning emissions. Currently there has been no other validation of the use of the FRP in this way.

8.2 Assessment of Thesis Objectives

In order to address the aim given above, a number of objectives were set:

1. **Objective**: Inter-compare methods to estimate vertical column amounts of fire-emitted gases from UV-DOAS vegetation fire measurements (key expected species are sulphur dioxide and nitrogen dioxide; which have features in the UV spectral region).

This was investigated by deploying UV-DOAS spectrometry to collect measurements of smoke plumes produced during a series of open vegetation fires in three field campaigns conducted in Kruger National Park (South Africa), Banf National Park (Alberta, Canada) and Arnhem Land (Northern Territory, Australia). Two different retrieval methods were applied to a selection of the gas cell and fire plume spectra collected by the UV-DOAS instrument, in order to retrieve vertical column amounts of SO_2 and NO_2 from the analyses spectra. The two methods, the "DOAS forward model" and the 'empirical direct calibration method", are explained in detail in Chapter 3. It was found that the retrieved vertical column amounts from the DOAS forward model method could be much more variable from consecutively

timed spectra than those from the direct calibration method, in some cases varying in an unrealistic fashion It particular, the DOAS forward model method produced results that (i) could exhibit ambient (i.e. "out of plume") column amounts below zero, and (ii) showed relatively large fluctuations around the ambient baseline (between -10 to 10 ppmm for NO_2 and -50 to 50 ppmm for SO_2) and (ii) included unrealistically high column amounts from some spectra (> 1000 ppmm). The results from the direct calibration method did not exhibit these effects, in particular with column amounts never falling below zero and never showing such high and unrealistic column amounts as did the the "DOAS forward model" method. Therefore, due to its apparently greater robustness compared to the DOAS forward model method, the direct calibration method was subsequently used to retrieve the column amounts of SO_2 and NO_2 for each experimental burn analyzed in this work. When tested using the calibration gas cells of each species, the direct calibration method was always able to retrieve the true gas cell pathlength amount with approximately 95% accuracy.

In addition, it was found that within each fire, there was a good correlation with the column amounts of SO_2 and NO_2 providing there was enough smoke for retrievals of both species to be made. For fires in which the fuel loads of the burn plots were low, and hence not much smoke was emitted, there is a poor agreement between the target gases and retrieved column amounts generally show more variabilty. This suggests that the retrieval method is robust when it is able to measure high column amounts of the target gases, for example during measurements of the gas cells and high levels of smoke. However when not that much smoke is present in the optical path of the instrument, this robustness breaks down. Chapter 7 discusses the high fluctuations of both target gases around the baseline during ambient measurements. Hence it is necessary to determine the detection limit of this retrieval method for both gases, i.e. the lowest column amount that is detectable.

The column amounts were able to be used with plume velocity estimates and GPS location measurements to calculate the flux rates of the target gases during the South African and Australian field campaigns (see Objective 3). The experimental burns conducted in South Africa and Australia were two different types of savanna ecosystem. In contrast the

fires in Canada were conducted within the boreal forest, albeit only the UV-DOAS was able to be deployed there as the smoke from these fires was contained within a vertically lofted plume that did not lend itself to the OP-FTIR measurement approach described here. Nevertheless, the research has shown that the UV-DOAS method of measurement is applicable to fires showing these types of widely varying characteristics, allowing for the investigation of its potential to detect differences in emissions of SO_2 and NO_2 corresponding to different fire and fuel types. Chapter 5 details the analysis of the UV-DOAS data for the South African and Canadian field campaigns, while Chapter 6 provides results from the Australian field campaign. As expected, the SO_2 emission characteristics of the boreal forest fires were different to those of the savanna ecosystems, due to both fuel type and much higher fuel loads. SO_2 emissions from these fires were much larger than those of NO_2 by up to almost 500% which was not the case in South Africa or Australia. The literature confirms that that nitrogen levels in these are relatively lower than those of sulphur for these types of ecosystems. This is also the case for the tropical savannas of the Australian field campaign, which is shown in Chapter 7, where NO column amounts are consistently less than those of SO_2, and not detectable for the smaller fires.

2. **Objective**: Provide estimates of smoke trace gas emission ratios and emissions factors for vegetation fires, and assess the similarity and complementaries of UV-DOAS and FTIR-based systems.

This was investigated by deploying the FTIR and UV-DOAS systems together during the South African field campaign, described in Chapter 6, and the Australian field campaign described in Chapter 7. Although measurements were made only at the start of the fire, there was enough data collected to be able to determine the pathlength averaged mixing ratios of CO_2, CO and CH_4 and NO_2. Note that SO_2 was unable to be determined due to low levels of smoke, corresponding with the low column amounts of this gas from the UV-DOAS measurements.These mixing ratios were subsequently used to calculate the emission ratios and then emission factors of the measured species within the smoke plume. As NO_2 was able to be detected by within the FTIR and UV-DOAS spectra, the emission ratios between

the carbonaceous species and NO_2 were applied to the NO_2 flux rates calculated for each of the South African fires, in order to determine the flux rates of the target carbonaceous species (which comprise $> 95\%$ of the total carbon emitted in burns of this sort). For the pilot study in South Africa, although only emission ratios calculations from one fire were conducted due to a limited operation of the FTIR, and these were applied to the NO_2 fluxes of all the South African fires conducted in the same campaign, as fuel types and burning conditions were very similar across each.

Following on from the pilot study, improved FTIR measurements were obtained during the Australian field campaign, from which mixing ratios of CO_2, CO and CH_4 and SO_2 were retrieved from the IR spectra (Chapter 7). NO_2 was not able to be detected here however, possibly due to reportedly low levels of nitrogen found in this ecosystem. The retrieved mixing ratios were used to determine the emission ratios and emission factors using the same approach as the pilot study, which were then compared with those found in the literature (these are discussed below). The carbonaceous species flux rates of CO_2, CO and CH_4 were then able to be estimated by combining the SO_2 flux rates derived from the UV-DOAS spectra and the FTIR-derived emission ratios of the carbonaceous gases to SO_2. In summary, the pilot study in South Africa was used to investigate the key methods used to determine emissions ratios and fluxes from the data provided by the two instruments, and the methods by which these data could be combined to estimated carbonaceous species flux rates, which were then later applied to the more complete datasets collected during the Australian field campaign.

Comparisons were made between the emission ratios and emission factors derived in this work and those found in the literature, detailed in (Chapter 7). Regarding those from the South African pilot study, it appears that the IR spectral measurements were made of smoke emitted mainly during flaming combustion (that occurred close to the start of the burn). Hence values differed somewhat to those found in the literature, which tend to be reported as "whole fire" emissions ratios. The emission ratios and emission factors derived from the more complete data provided by the Australian field campaign were, however, generally in

line with those from savannas. However, it was found that even between different types of ecosystems there was variability in the emission ratios and emissions factors for the different species. This is very likely in part due to the difference in sampling methods, for example airborne vs. ground based field measurements. Airborne sampling tends to sampling smoke emitted more from flaming combustion which is injected to higher altitudes due to intense updrafts, whereas ground based sampling such as that used here (i.e. the OP-FTIR deployment), smoke from smoldering combustion is likely to be more dominant (Wooster et al., 2011). As different species tend to be emitted in different relative amounts during the different stages of combustion (Potter *et al.*, 2002), the derived emission ratios and factors may have some dependence on sampling method. Most current estimates of emission ratios and emission factors are derived from airborne sampling of recently emitted smoke. In addition, work has been carried out with measurements of large plumes that are a few days old. Such 'aged' smoke measurements also cannot be directly compared to those from fresh plumes, due to the chemical reactions that occur in the plume that cause variations in the amounts of gases and their chemical makeup over time.

Both NO_2 and SO_2 have rather weak absorption features in the IR spectral region used here, hence there needs to be a relatively large amount of these gases within the smoke plume for them to be reliably detected by the FTIR. There is also not much data available in the literature to compare the derived NO_2 to SO_2 emissions ratios to for savanna ecosystems, nor the ratios of other gases to either of these two. From what is available, the emission ratios presented in this work seem to be in line with those given in the literature, but the emission factors seem to be higher, for example the SO_2 to CO_2 ER (0.0009) derived in the Australian field campaign is equal to the only other equivalent emission ratio for savannas (Sinha *et al.*, 2003) however the SO_2 EF from the Australian fires is approximately up to 5 times those quoted in the literature.

3. **Objective**: To develop method to determine the flux of carbon from vegetation fires, based on UV-DOAS and FTIR measurement techniques, and use this to evaluate the efficacy of the variations in fuel consumption rate that can be derived from the Fire Radiative power

(FRP) approach.

Detection of either NO_2 or SO_2 in both the UV-DOAS and the FTIR spectra allows for the synergistic use of these data to estimate the flux rates of the key carbonaceous species (CO_2 CO and CH_4) emitted by the biomass burning event under study (via a combination of the FTIR-derived emission ratios of the carbonaceous species to either NO_2 or SO_2, and the DOAS-derived flux rates of this same gases). This procedure was possible for both the pilot study of South Africa, and for the Australian field campaign. To the authors knowledge, this is the first time that results derived from UV-DOAS and FTIR spectral measurements have been integrated in this way, and it appears that more research needs to be carried out to evaluate the efficacy of the technique. Currently, the flux estimates of the carbonaceous seem rather high, and when integrated over the duration of the fire provide estimates of total fuel consumption that sometimes appear higher that the likely amount of burnable fuel available. Note that the FRP method is expect to underestimate the carbon emitted by the fire to some extent, due to the failure of the thermal camera used to detect fire pixels with brightness temperatures below 200^oC. Nevertheless, it seems likely that the carbonaceous fluxes are overestimated. The high magnitude of these fluxes comes in part from the fact that the emission ratio of NO_2 (or SO_2) to CO_2 (as derived via the IR spectral) used in these calculations is very low (0.0007 for NO_2 and 0.0009 for SO_2) and thus the resulting CO_2 flux can be large even when the NO_2 (or SO_2) flux is quite small. However, from the limited information available in the literature, published ratios of NO_2 (or SO_2) to CO_2 do appear to be similarly low. Another potential source of the discrepancy could be that the estimated flux rates of NO_2 and SO_2, derived from the UV-DOAS measurements, are too high. Due to the lack of data in the literature on flux rates of these gases from burning in savanna fires, this is difficult to determine however. Despite the possibility that the absolute values of the derived carbonaceous fluxes are too high, it was still possible to use these trace gas fluxes as a comparative dataset to compare to the fire radiative power time series collected at the same fires.

The derived fluxes of CO_2, CO and CH_4 were used to derive the total carbon flux emitted by each of the fires and compared with the FRP time series derived from airborne IR

imaging from three fires in South Africa and two fires in Australia, presented in Chapters 6 and 7 respectively. Both the carbon flux and the FRP should theoretically vary with fuel consumption rate in a linear way, and indeed the matching C-flux and FRP measures for a fire exhibit approximately the same temporal pattern, i.e. with closely-timed peaks and troughs. Each data point on the FRP time series represents an instantaneous measurement made at a specific time, whilst each point on the flux rate time series represents an average of many measurements taken during each of the DOAS traverses. Hence, it cannot be expected that the C-flux and FRP time series will show exactly the same variations at exactly the same time. Nevertheless, the fact that both the C-flux and FRP time series follow the same general patterns does provide confidence to both methods, especially as both are derived from completely independent data sources.

8.3   Advancements Made in this Current Research

- Prior to this thesis, only Oppenheimer *et al.* (2004), has conducted a study involving the field deployment of a mini UV-DOAS system to investigate trace gas emissions from biomass burning. That study focused on the measurement of NO_2 from agricultural fires in Brazil. The current work is the only other known work in this specific area, the only one to target both SO_2 and NO_2, to apply the approach over multiple ecosystems and to inter compare performances. By traversing underneath the smoke plume released by the fires, cross sectional amounts of SO_2 and NO_2 in the plume were able to be derived from the UV spectra and then subsequently used to calculate flux rates via multiplication by the horizontal wind speed. This work has also presented for the first time, the integration of the UV-DOAS and FTIR spectrometer measurements to attempt to derive carbonaceous flux rates from open vegetation fire burns, via multiplication of the SO_2 and/or NO_2 fluxes by the corresponding emission ratios derived from the IR spectra. Flux calculations using the FTIR alone are not possible, as it is not able to scan across the plume cross section easily with the FTIR (i.e. only pathlengths along a path close to ground-level are possible). However the FTIR is able to detect carbon species, which do not have absorption features in the UV spectral region. The use of both instruments is therefore necessary to derive an

estimate of carbon flux.

- A retrieval method for SO_2 and NO_2 vertical column amounts from the UV-DOAS measurements based on the use of gas calibration cells has been shown to work well, provided there is substantial smoke in the measurement path to allow for the detection of SO_2 and NO_2. A detailed error budget has been calculated for these column amount measurements, and for the derived fluxes.

- In addition to the comparison of the direct calibration method and the forward model-based method for the purpose of retrieving vertical column amounts of SO_2 and NO_2 from the UV DOAS measurements, two similar forward models, the MALT (1996) and Burton (1998) approaches have been compared for their ability to derive mixing ratios of CO_2, CO, CH_4 and SO_2 from the IR spectra collected by the FTIR. Both methods have shown similar abilities to provide these measurements in the smoke polluted atmosphere of the biomass burning plumes.

- The FRP time series of several fires has been compared to the carbon flux derived using the trace gas fluxes. This is the first time such a comparison has been conducted. The strong similarities in the variations seen in both datasets provides confidence that both are driven largely by the same process, i.e. variations in fuel consumption rate; the carbon fluxes through the carbon released as smoke during the fire (assuming fuel burnt is approximately 50% carbon) and the FRP through the energy released by the fire, relating to fire intensity and hence fuel consumption.

8.4   Recommendations for Further Research

As detailed in Chapter 5, the method applied to estimate plume speed needed for the calculation of the trace gas flux rates in this research is very approximate. It is based mainly on estimating height from video footage taken above the fire via a helicopter. This estimate is then used with the log law and ground-based wind speeds to return a wind speed estimate at the plume heights. It has been noted in the past that where flux rates of SO_2 in volcanic plumes have been estimated using the UV-DOAS system, wind speed at plume height is the primary cause of uncertainty in the calculations. In the current study, the wind speed at

ground level was initially thought to be good enough to estimate the wind speed at height, and when it was realized that additional information was probably required this was after the time the field campaigns had already been carried out. Hence it was too late to provide additional measurements. Future field campaigns could use two UV-DOAS instruments in DUAL mode, in which two instruments are positioned underneath the plume such that their viewing axis is parallel. The column amounts of a given target gas are then retrieved from both instruments, and a correlation algorithm is used to determine how long it taken for the plume to get from the FOV of one instrument to the other. This is combined with the distance between the two instruments to derive plume velocity (Williams-Jones *et al.*, 2006; Boicu *et al.*, 2010). Another possibility is to deploy an airborne measurement device, such as a balloon, with an anemometer or other wind measurement device operating at height.

In the current work, the gases SO_2 or NO_2 have been used to link the UV-DOAS-determined flux rates with the FTIR derived emission ratios, in order to determine flux rates of the FTIR (but not UV-DOAS) detectable carbon species. SO_2 and NO_2 have strong absorption features in the UV, but not so strong in the IR. Hence, it can be difficult to derive emission ratios of these species from the IR spectra, particularly if there are low levels of smoke emitted by the fire. Formaldehyde (H_2CO) is another species that is detectable in both the UV and IR spectral regions. This gas has stronger absorption features in the IR compared to SO_2 or NO_2, hence there is the possibility to derive more stable ERs from this species that can be applied to its corresponding flux rate derived from the UV-DOAS. It would therefore make a good target species for use in this project. The problem with formaldehyde, however, is that it is a reactive gas, hence it is not possible to make gas cells containing a known quantity of this species as it will stick to the cell walls. As the direct calibration method relies on the use of gas cells, column amounts of H_2CO cannot be retrieved using this approach. The DOAS forward modeling retrieval method detailed in Chapter 3 does not explicitly rely on gas cells, so would be an approach potentially applicable for use with formaldehyde. For fire SF3 of the South African field campaign (Chapter 5) Figure 8.1 shows the retrieved column amounts of H_2CO, calculated using the DOAS forward model and the spectral fitting region of 310-320 nm. Note that SO_2 and O_3 were also fitted, along with

the ring spectrum. A moving average of 10 was implemented on the spectra before fitting. Retrieved values greater than 900 ppmm and less than -100 ppmm were removed from the time series as being unrealistic.
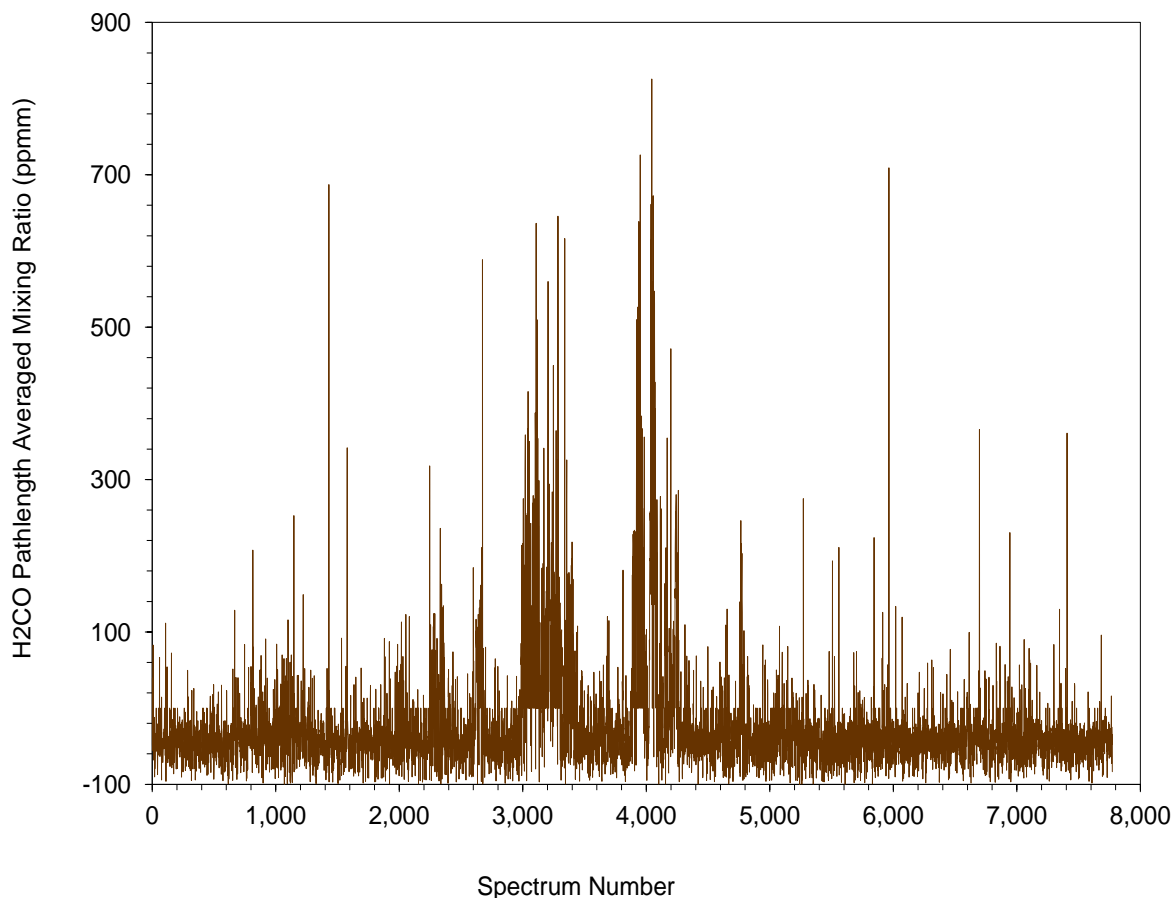
Figure 8.1: *The pathlength averaged column amounts of H_2CO derived for fire SF3 using the DOAS forward model, in the spectral fitting region of 310-320 nm. Note that SO_2 and O_3 were also included in the fit, along with the ring spectrum. A moving average of 10 was implemented on the spectra before they were fitted. Values greater than 900 ppmm and less than -100 ppmm were removed.*

The time series of H_2CO total column amounts shown in Figure 8.1 looks promising. The column amount peaks of H_2CO are the same position as those of SO_2 and NO_2 for the same fire (see Figure 5.25), signifying the presence of the plume. One thing to note is the negative column amounts outside of the plume. This has been a reoccurring feature with the DOAS

364

forward model method, in which returned column amounts fall below zero during ambient measurements, and perhaps even at times with low levels of smoke. Another thing to note is the high magnitude of the peaks of the time series of Figure 8.1, reaching up to 700 ppmm of H_2CO. Such values appear perhaps somewhat unrealistic, but as there are no gas cells for this species, it is impossible to validate this retrieval. Nevertheless it is still promising that the time series pattern of formaldehyde column amounts matches with that of NO_2 and SO_2, and also that it does not appear to exhibit much noise. For any future work, use of the DOAS forward model should be further explored for this use.

As detailed in Chapter 7, there is an issue with the individual PT (i.e. different wavelength) combinations retrieving different column amounts for the fire, however not for the gas cell spectra. A suggested reason for this is the effect of smoke particles in the plume, as these are present in the plume but not for the gas cell measurements. A point of future work is to simulate of the effect of scattering by such particles at UV wavelengths, e.g. using MODTRAN, and investigate their effect on the measured radiation signal and on the direct calibration method and the forward modeling method of trace gas retrieval. It is necessary to investigate the effect of scattering caused by particles in the plume on the absorption of the target gases and to quantify this effect.

During the analysis of the absorbance spectra, some absorbance features were noticed that existed in the fire plume spectra, but not the gas cell spectra. Once such feature is shown in Figure 8.2. Here it can be seen that at around 344 nm, there seems to be an absorbance feature, only present in the fire absorbance spectra, in the form of a peak and trough. This feature is stronger for CF1, in which the smoke plume was much larger than that of the South African fire. The difference between these peak and troughs was calculated from the absorbance spectra for all fire spectra of CF1 and SF3, shown in Figure 8.3.
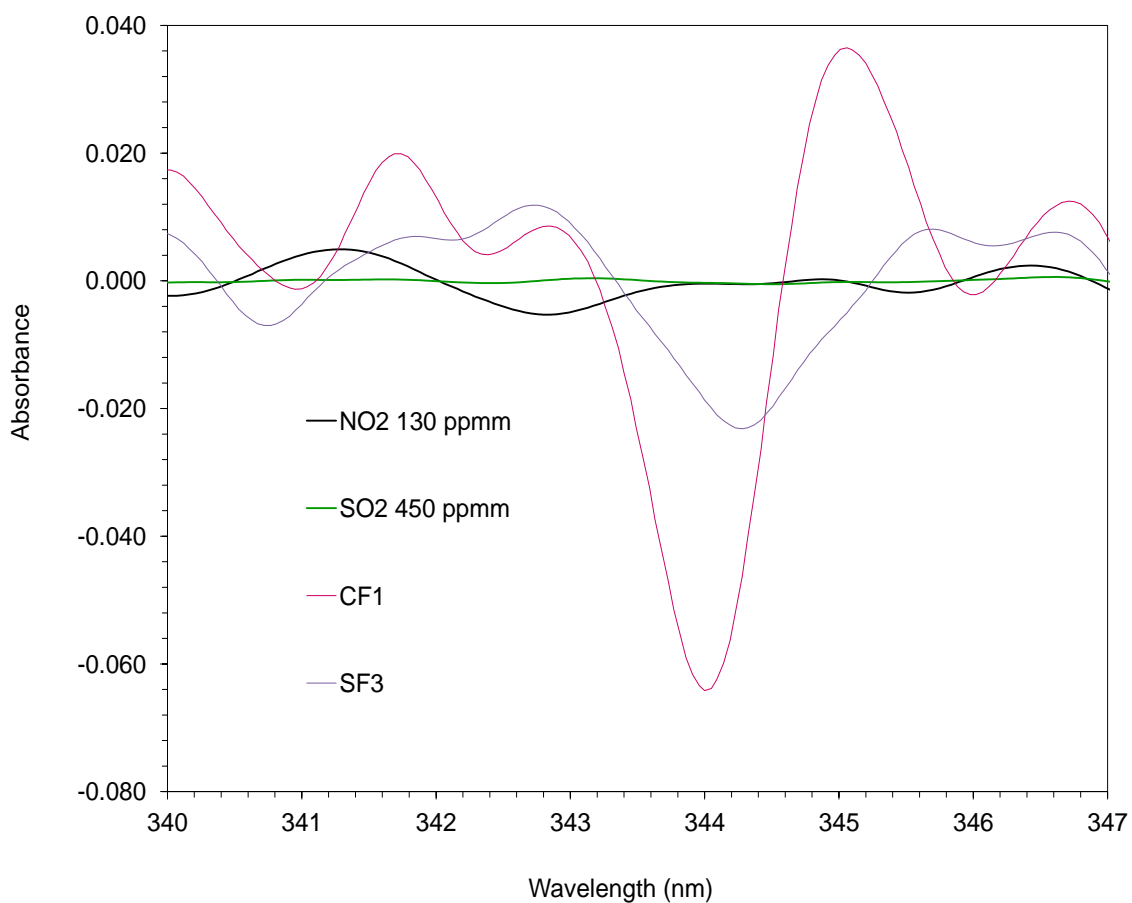
Figure 8.2: *The absorbances of an NO₂ gas cell (130 ppmm), SO₂ gas cell (450 ppmm), a fire spectrum for Canadian fire CF1 and South African fire SF3, showing a feature around 344 nm only present in the fire spectra.*
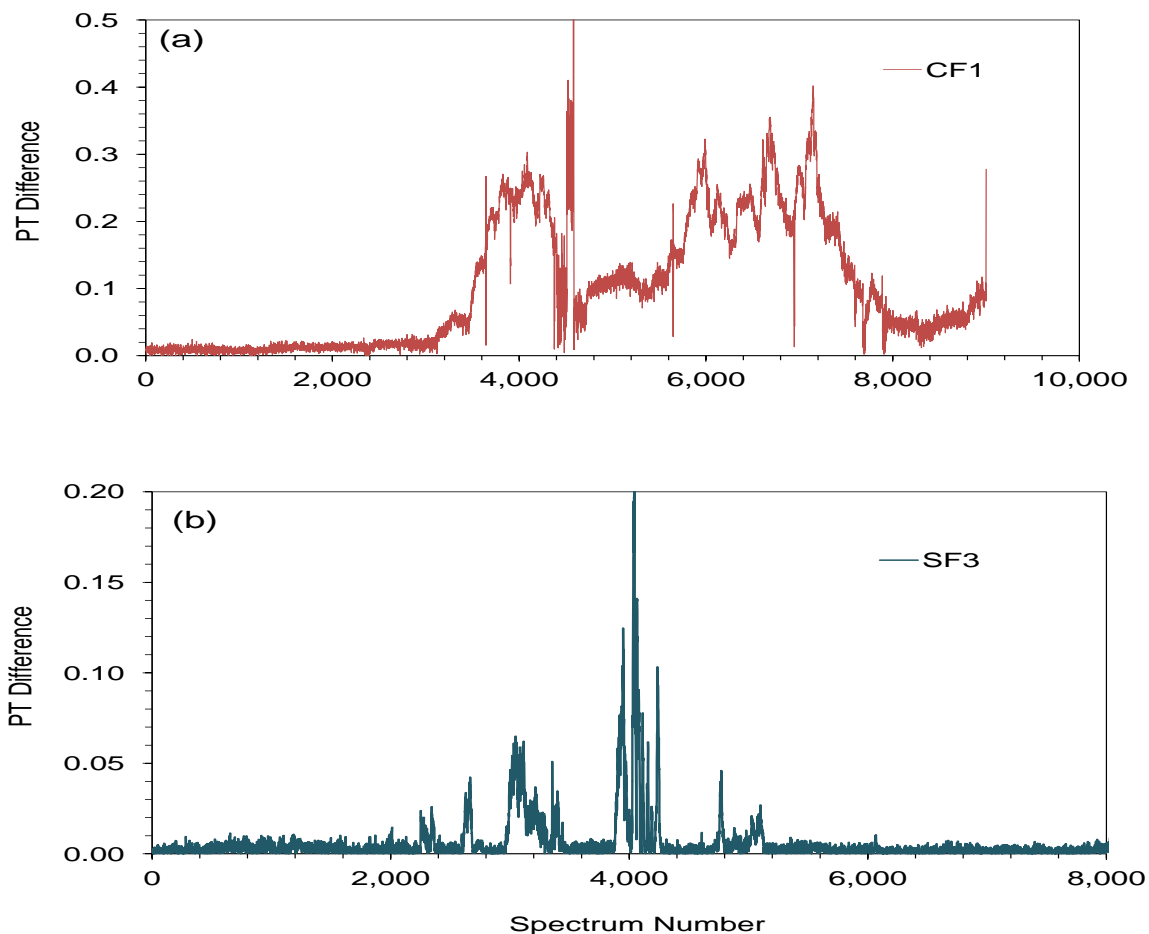
Figure 8.3: *The PT difference of the peak and trough feature shown in Figure 8.2 for the absorbance spectra of fire (a) CF1 and (b) SF3.*

Comparing Figure 8.3 with the retrieved pathlength column amounts of SO_2 and NO_2 of these fires shown in Figures 5.25 and 5.27, it is noted that the PT difference of this absorbance feature follows the same pattern as the column amounts, i.e increasing at the same time in the presence of the plume. Hence this absorption feature becomes more prominent in the presence of smoke. This could potentially be an absorption feature related to another (unconsidered) gas. Indeed, it is thought that H_2CO and HNO_2 have absorbance features around 344nm (Platt and Stutz, 2008), and so there is scope to investigate this further.

It can been noted that for the retrieved column amounts of NO_2 and SO_2 for all field campaigns, there is some fluctuation around the baseline for ambient baselines (around 10-30

ppmm) and quite nosiey retrievals for fires that emitted low levels of smoke. This suggests that the retrieval method is not very robust when it comes to low column amounts of the target gases. It would be interesting to find the detection limit, i.e the lowest amount of the target species that can accurately be retrieved by this method. This can be done by e.g. using a wider range of calibration cell measurements, down to low ppmm values, or by simulation modeling.

Chapter 9

Appendix

Contents

9.1 Introduction

In this current work, the link between the SO_2 and NO_2 flux rates and the FTIR derived emission ratios was presented in order to determine flux rates of the FTIR target carbon species (CO_2, CO and CH_4) emitted from the open vegetation fires of the field campaigns in South Africa and Australia. SO_2 and NO_2 have strong absorption features in the UV, however not as strong in the IR. Hence, it can be difficult to derive emission ratios of these species from the IR spectra, particularly if low levels of smoke are emitted by the fire. Formaldehyde (H_2CO) is another species that is detectable in both the UV and IR spectral regions. This gas has stronger absorption features in the IR compared to SO_2 or NO_2, allowing for the possibility to derive more stable ERs against CO_2, CO and CH_4, which can

subsequently be applied to the corresponding H_2CO flux rate derived from the UV DOAS. It would therefore make a useful target species for use in this project. The problem with formaldehyde, however, is that it is a reactive gas, hence it is not possible to make gas cells containing a known quantity of this species as it will stick to the cell walls. As the direct calibration method relies on the use of gas cells, column amounts of H_2CO cannot be retrieved using this approach. The DOAS forward model retrieval method detailed in Chapter 3 does not explicitly rely on gas cells, so would be an approach potentially applicable for use with formaldehyde.

After the main body of this work, investigations were carried out looking into the potential of the DOAS forward model in retrieving H_2CO and also HONO. Despite no available calibration gas cells for these species, they both have absorption features in the UV and IR, hence are potentially usefully in linking the DOAS derived flux rates with the FTIR derived emission ratios to estimate carbon fluxes. Vertical column amounts of H_2CO and HONO were retrieved from fires for all field campaigns, using the DOAS forward model presented in Chapter 3. The results from the largest fires are given below.

9.2 Vertical Column Amounts

H_2CO was retrieved in the spectral region of 314-321 nm, along with the cross sections of SO_2 and O_3 and the ring spectrum. HONO was retrieved within the region 330-337 nm, along with NO_2, O_3 and the ring spectrum. Retrievals of large absolute magnitudes were removed, as were results from spectra that were saturated by high levels of incoming light intensity.

Recall that for the retrievals of SO_2 and NO_2, the choice of wavelength region was determined by running the DOAS forward model and direct empirical method on the gas cell calibration spectra using a range of spectral fitting wavelength regions. The region which retrieved the vertical pathlength amounts closest to those of the actual gas cell and exhibited the least amount of noise was selected for the retrievals of the target gases on the fire spectra. As H_2CO and HONO calibration gas cells were not available at the time of measurement,

it was not possible to use this same method. Therefore, the retrieval region for the forward DOAS method for these two gases was selected based on which region produced realistic vertical column amounts with the least amount of noise. Note that there was not much difference between spectral regions in terms of the magnitude of the vertical pathlength column amounts, just noise levels.

Figures 9.1, 9.2 and 9.3 show the retrieved vertical column amounts of H_2CO and HONO from the Canadian, South African and Australian field campaigns. Vertical column amounts were averaged over 5 seconds for both CF1 and CF2 due to the extensive duration of both fires (just under 2 hours). Retrieved column amounts were averaged over 1 second for SF3, SF4 and AF3, whereas fires AF4 and AF5 were averaged over 2 seconds as they exhibited relatively more noise. This is consistent with the averaging used for the direct calibration method. Points where column amounts drop to zero represent instrument saturation, low levels of sunlight reaching the instrument due to the intensity of the smoke plume and failure of the non linear least squares fitting algorithm used in the DOAS forward model to converge. These points were removed from the time series for all vertical column amounts.
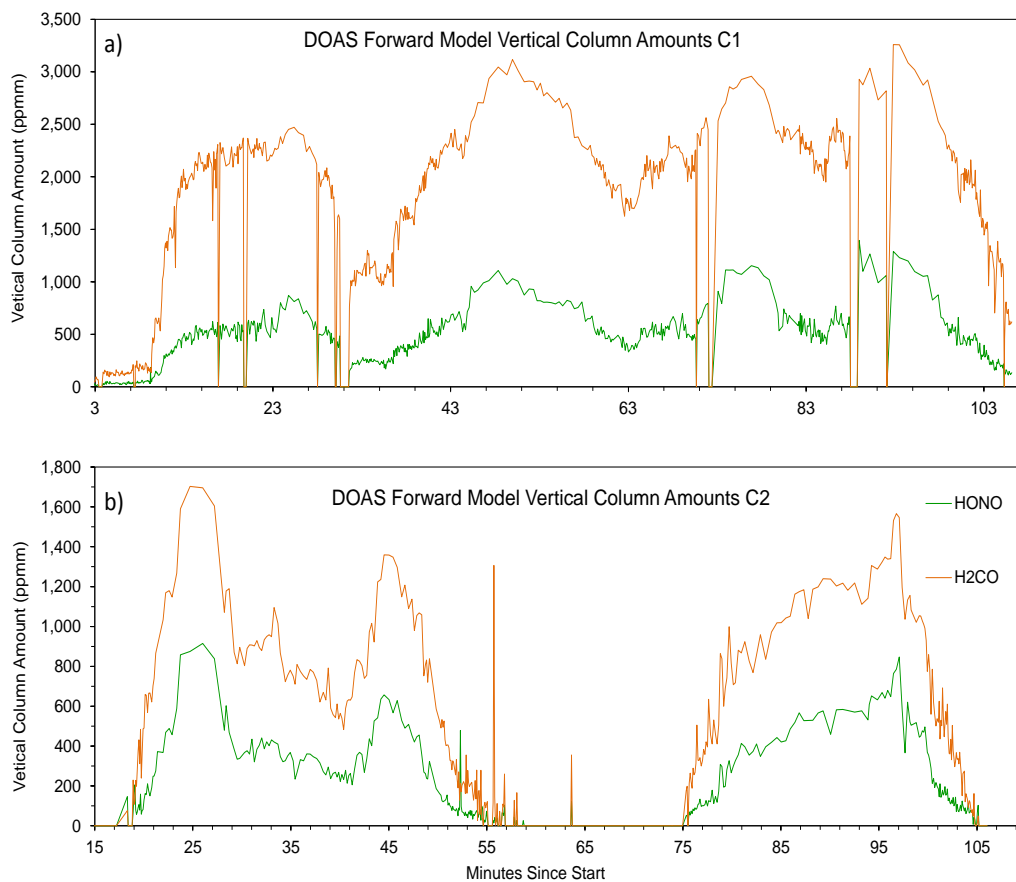
Figure 9.1: *H₂CO (orange) and HONO (green) vertical column amounts retrieved from the DOAS forward model using UV-DOAS smoke measurements made during the Canadian field campaign for fires CF1 (a) and CF2 (b)*

Note that spectra collected from fire CF1 exhibited particularly low levels of intensity, most likely due to the extensively thick smoke released from this fire. The plume for fire CF2 was also extensive, however the integration time for this fire was greater, resulting in a spectrum collected every 1-5 seconds, while in general spectra for fire CF1 were collected at a frequency of one per second. Hence the greater intensity of the CF2 spectra. See Chapter 5 for more on this.
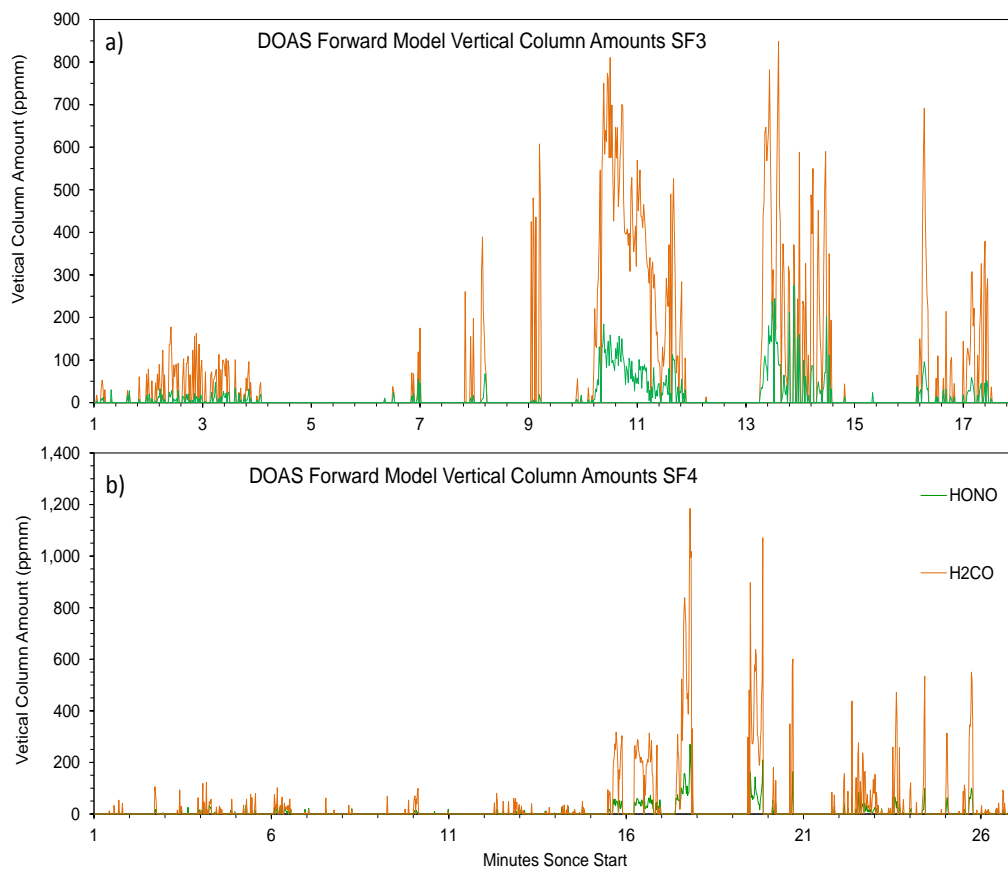
Figure 9.2: *H_2CO (orange) and HONO (green) vertical column amounts retrieved from the DOAS forward model using UV-DOAS smoke measurements made during the South African field campaign for fires SF3 (a) and SF4 (b)*
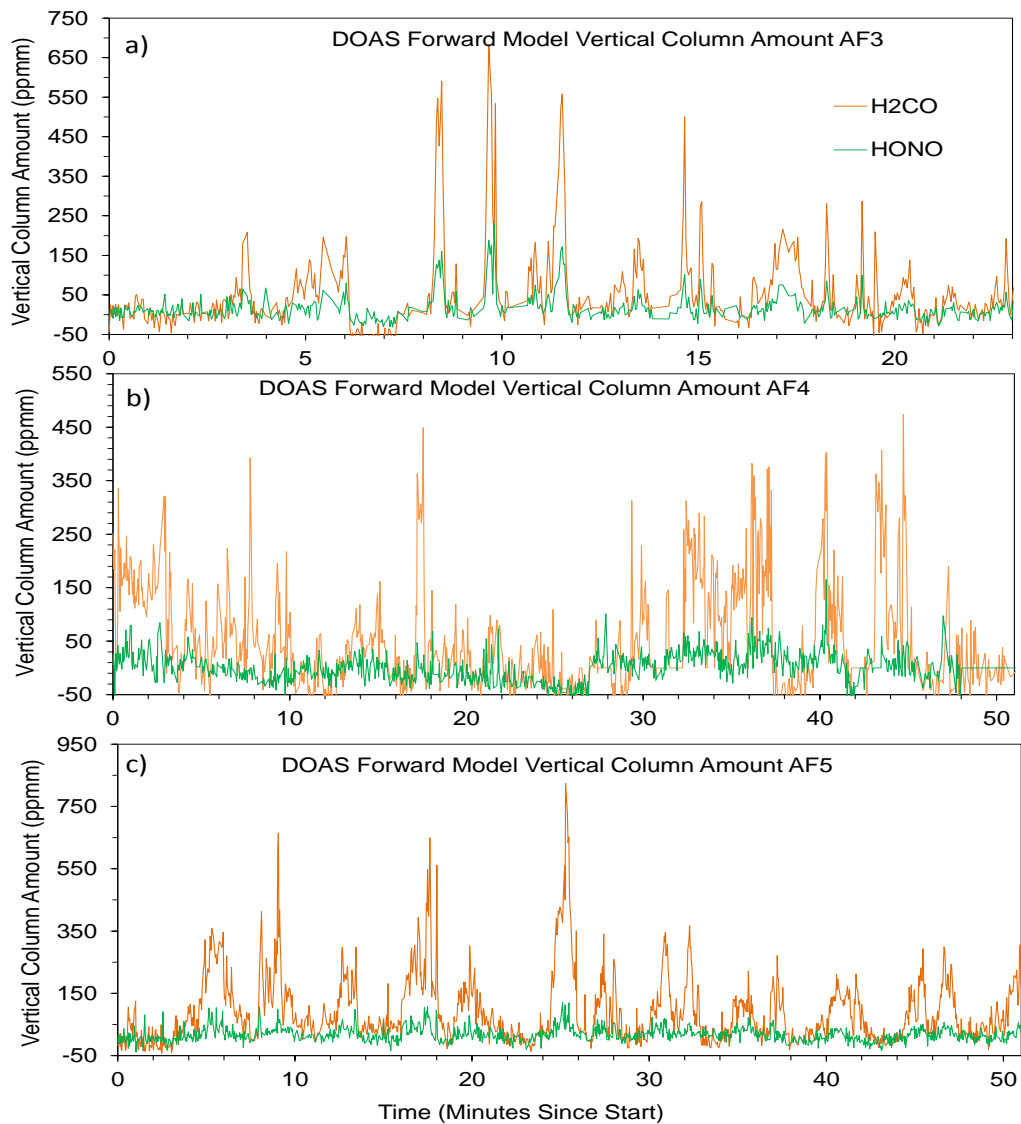
Figure 9.3: H_2CO (orange) and HONO (green) vertical column amounts retrieved from the DOAS forward model using UV-DOAS smoke measurements made during the Australian field campaign for fires AF3 (a), AF4 (b) and AF5 (c).

In general, both target gases peak at the same time for all fires with H_2CO being the dominant gas. Comparing the retrieved vertical column amounts from the DOAS forward model for each field site, H_2CO exhibits peak values approximately 3 times greater than those of HONO (≈ 3000 ppmm for CF1 and 1700 ppmm for CF2 compared with ≈ 1000 ppmm for CF1 and 800 ppmm for CF2 for HONO). If compared with the direct emprical method in Chapter 5, SO_2 vertical column amounts peak at ≈ 300 ppmm and 600 ppmm

for CF1 and CF2 respectively, while NO_2 at $\approx$ 150 ppmm for both fires. For the case of South Africa (Figure 9.2), again H_2CO is the dominant gas, with vertical column amounts reaching 900 ppmm for SF3 and 1200 ppmm for SF4. Maximum HONO column amounts for both SF3 and SF4 are close to 275 ppmm. This compares to peak amounts of SO_2 of $\approx$ 180 ppmm, and NO_2 amounts of 190 and 100 ppmm for SF3 and SF4 respectively (see Chapter 5). Finally, looking at the retrieved vertical column amounts from the Austrian field campaign (Figure 9.3), H_2CO peaks at 700 ppmm, 450 ppmm and 800 ppmm for fires AF3, AF4 and AF5 respectively, while HONO peaks at 170 ppmm and 80 ppmm for fires AF3 and AF4/AF5 respectively. This compares with peak amounts of SO_2 of 270 ppmm, 250 ppmm and 110 ppmm for AF3, AF4 and AF5 and 150 ppmm and 40 ppmm for fires AF3 and AF4/AF5 for NO_2. Note that in the case of the Australian fires, the retrieved vertical column amounts for NO_2 and HONO are very low, this could be attributed to fuel type.

This pattern of retrieved column amounts is linked with the fuel type burnt. From a study compiling emission factors from biomass burning Akagi *et al.* (2011) reported a H_2CO emission factor for open temperate forest fires of 2.27 g.kg^{-1} compared with a much smaller value of 0.52 g.kg^{-1} for HONO. This trend of high H_2CO emission factors is also presented in Simpson *et al.* (2011), were a value of 2.1 g.kg^{-1} is given for H_2CO for Canadian boreal forest fires compared with a HONO emission factor 1.03 g.kg^{-1}. Looking at the content of the fuel with respect to all the trace gases, it appears that there exists some discrepancies between studies. For example, Akagi *et al.* (2011) reported an emission factors for savanna fires of 0.48 $\pm$ 0.27 gkg^{-1} for SO_2, 0.20 gkg^{-1} for HONO and 0.73 $\pm$ 0.62 gkg^{-1} for H_2CO. This does not follow the same pattern as the emission trends given in this study, however note the large errors associated with the H_2CO and SO_2 emission factors. Also note that these emission factors were compiled from different studies using different sampling and analysis methods over numerous savanna environments. Andreae and Merlet (2001) reported a lower emission factor for H_2CO (0.26 $\pm$ 0.44 gkg^{-1}) compared with SO_2 (0.33 $\pm$ 0.16 gkg^{-1}) when investigating literature emissions from biomass burning. Sinha et al. (2003) presented emission factors of 0.43 $\pm$ 0.30 gkg^{-1} for SO_2 and 1.1 $\pm$ 0.38 gkg^{-1} for H_2CO using airborne sampling from savanna fires in southern Africa. Note the lack of NO_2 emission data from

this fuel type.

9.3　Flux Rates

In the earlier work of this thesis, flux rates were derived using estimates of plume speed based on estimated plume height from video footage recorded above the fire via a helicopter. This plume height estimate was then used with the log law and ground-based wind speeds to return wind speed estimates at plume height. In the current study, the wind speed at ground level was initially thought to be good enough to estimate the wind speed at plume height; however it was realized that additional information was probably required after the field campaigns. Hence it was too late to provide additional measurements. The method used was very rough, therefore for this additional work, the plume speed estimate is based on the wind speed collected at ground level. Future field campaigns could use two UV-DOAS instruments in DUAL mode, where two instruments are positioned underneath the plume with their viewing axis is parallel. The column amounts of a given target gas are then retrieved from both instruments, and a correlation algorithm is used to determine how long it has taken for the plume to get from the FOV of one instrument to the other. This is combined with the distance between the two instruments to derive plume velocity (Williams-Jones *et al.*, 2006; Boicu *et al.*, 2010). Another method to estimate plume speed is the deployment of an airborne measurement device, such as a balloon, with an anemometer or another wind measurement device operating at plume height. The additional inputs needed for the flux rate calculations follow the method detailed in Chapter 5

Figures 9.4 and 9.5 present the derived fluxes of the H_2CO and HONO using the vertical column amounts derived from DOAS forward model from the South African and Australian field campaign.
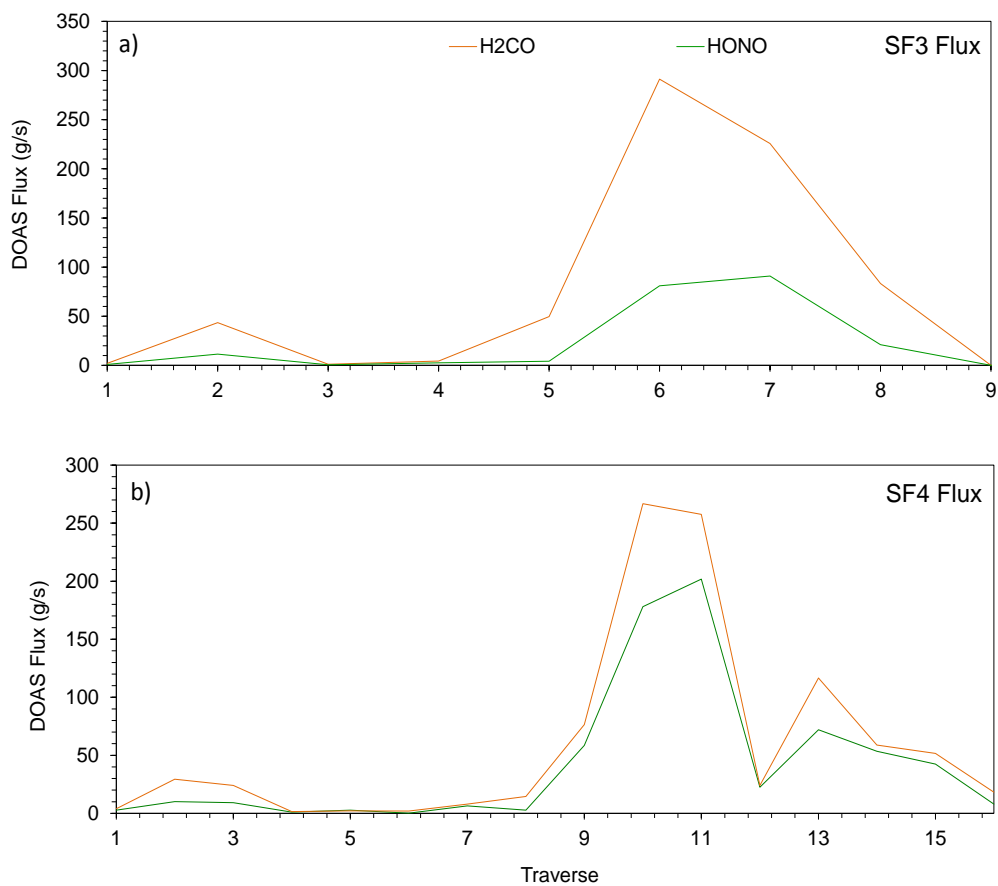
Figure 9.4: *H_2CO (orange) and HONO (green) fluxes (g/s) from South African fires SF3 (a) and SF4 (b) calculated using the vertical column amounts derived from the DOAS forward model.*
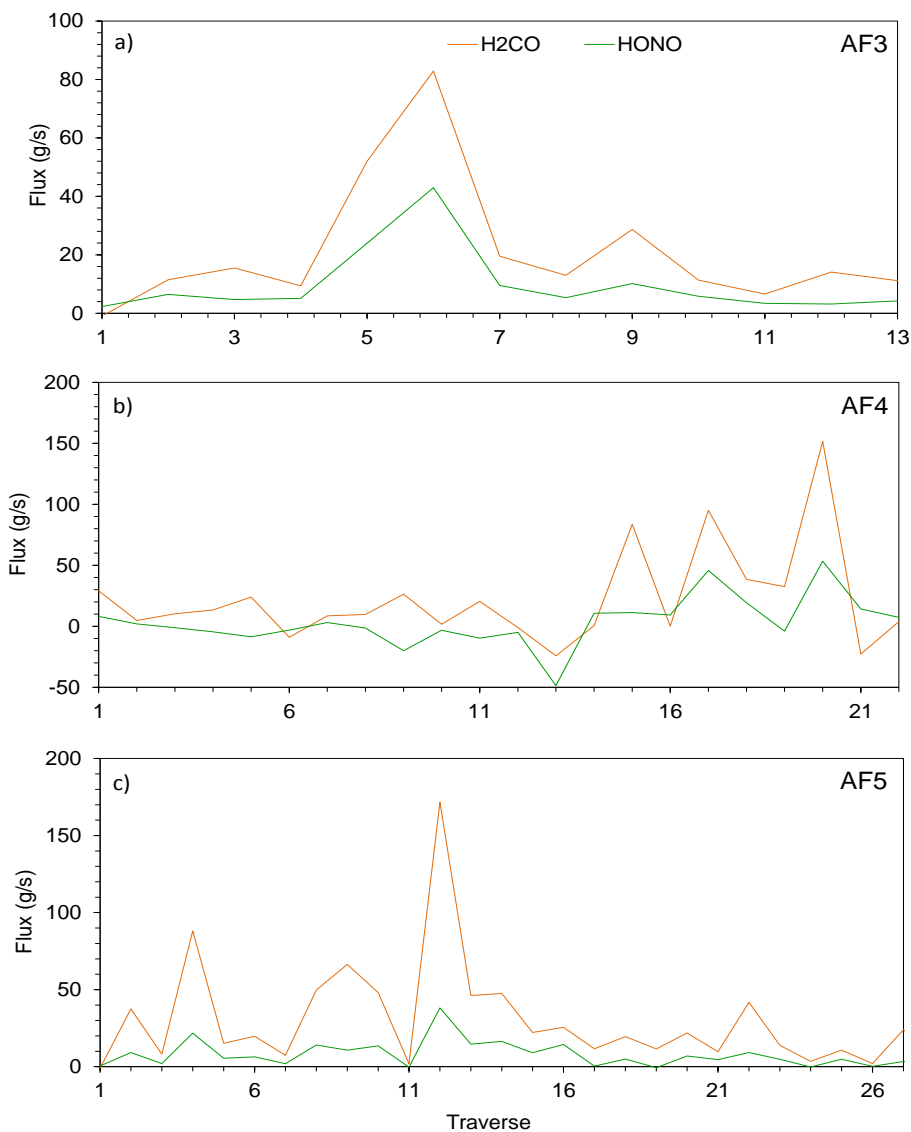
Figure 9.5: *H_2CO (orange) and HONO (green) fluxes (g/s) from the Australian fires fires AF3 (a), AF4 (b) and AF5 (c) calculated using the vertical column amounts derived from the DOAS forward model.*

In general, both gases follow the same emission pattern, apart from AF4, where HONO fluxes for this fire is noisey, due to the low vertcal column amounts seen in Figure 9.3.

9.4   FTIR horizontal pathlength amounts

Figure 9.6 shows the retrieved H_2CO horizontal pathlength amounts (ppm) for fires AF3 and AF5, using MALT, as in Chapter 6. The spectral range used for the retrieval was 2720-

2840 cm^{-1}. It was not possible to detect horizontal column amounts of HONO from MALT, perhaps due to the absorption features of this gas not being strong enough in the spectral range of the FTIR spectrometer and possibly given the pathlength amount of HONO present in the smoke plume of the fires sampled here.
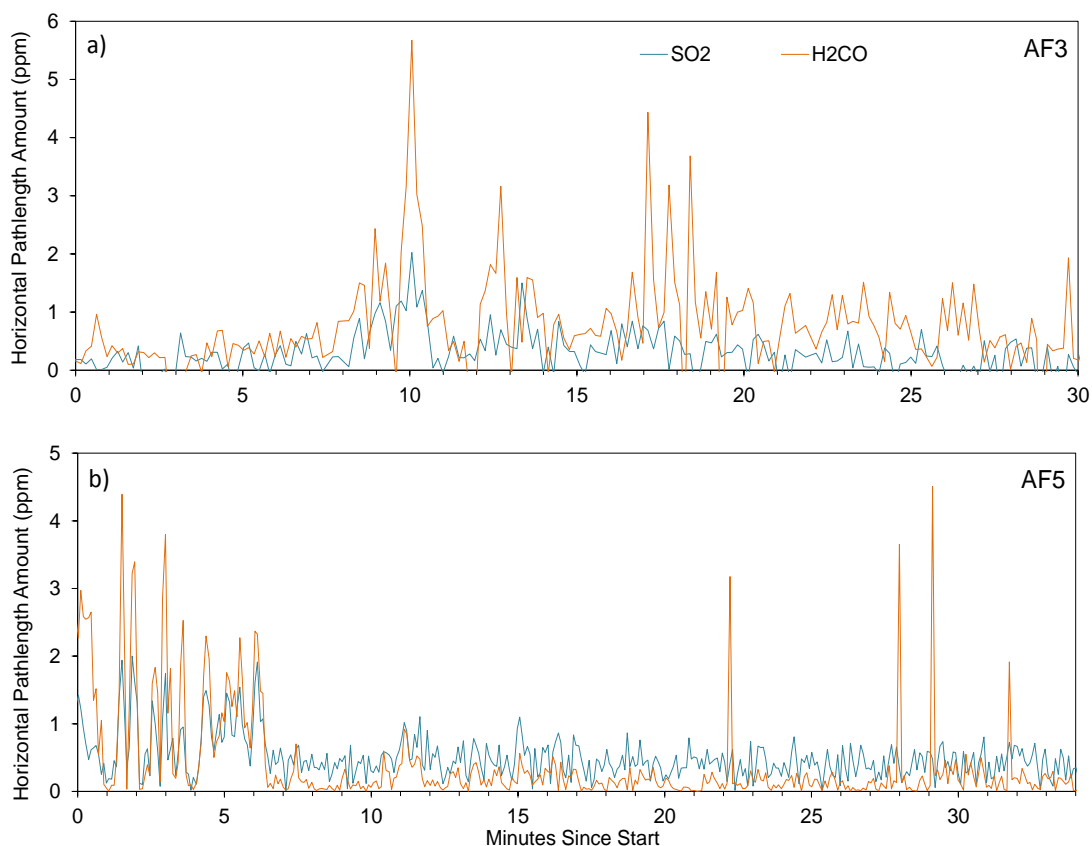
Figure 9.6: *Retrieved horizontal pathlength amounts of H$_2$CO (orange) and SO$_2$ (blue) for the Australian fires AF3 (a) and AF5 (b) using MALT.*

Also shown in Figure 9.6 are the retrieved horizontal pathlength amounts (ppm) of SO$_2$, used in this thesis to connect the DOAS flux rates with the FTIR retrieved carbon emissions. It can be seen that the pathlength amounts of H$_2$CO are at least double those of SO$_2$ during the main peak of the fires. This suggests that H$_2$CO could be a effective gas in linking the DOAS flux rates with the FTIR column amounts as the absorption features of this gas may be stronger than those of SO$_2$ in the target fitting regions available with the FTIR and/or there may be more of an abundance of this gas in the fuel.

Examples of the MALT fit for the target gases CO_2, CO, CH_4 and H_2CO are given in Figure 9.7 from one of the "during fire" spectra collected by the FTIR within the fitting region used for each of these gases. The figure presents the "during fire" measured spectrum (black) along with the fitted spectrum with the target gas included (pink) and without (green).
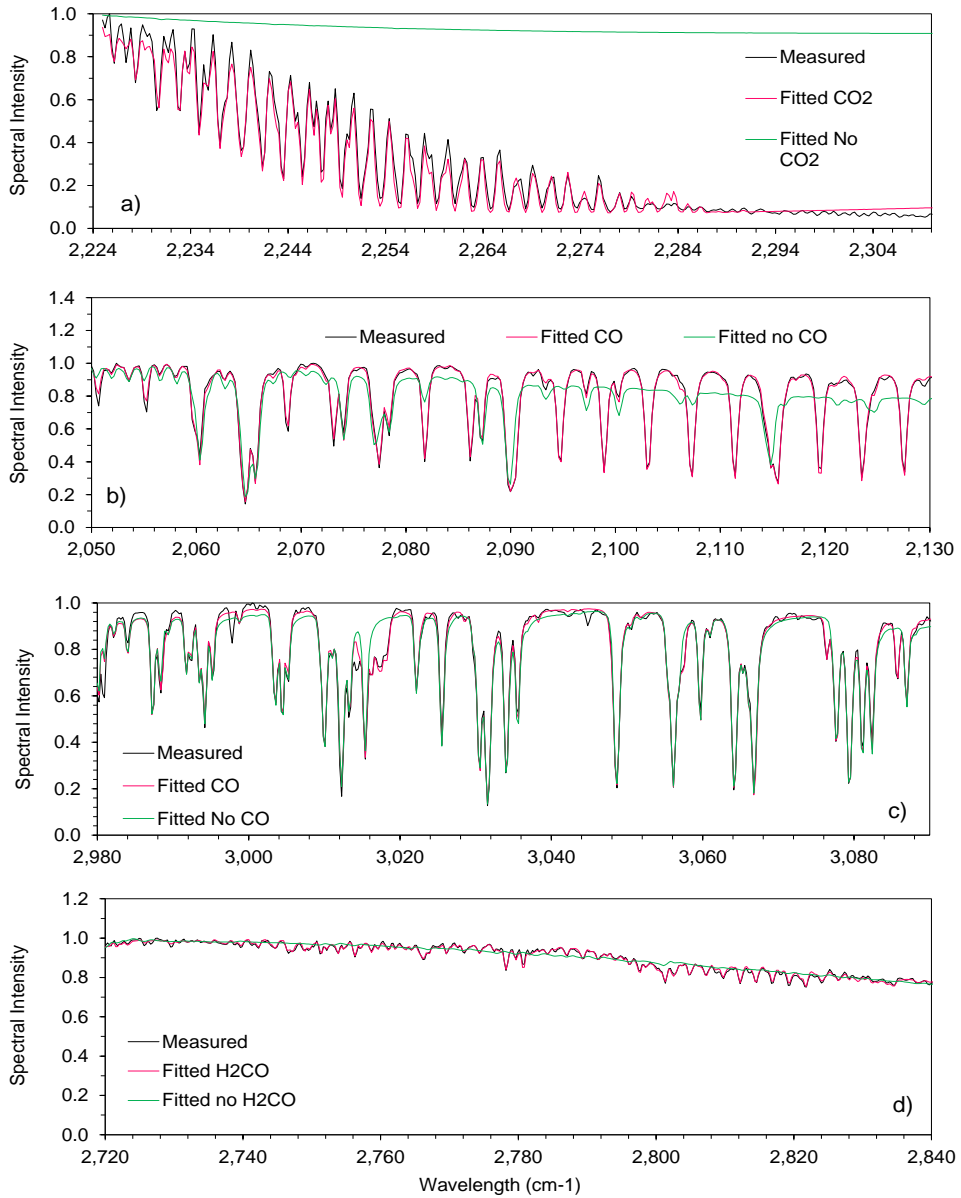
Figure 9.7: *An example of measured (black) and fitted spectra with (pink) and without (green) the target gases CO_2, CO, CH_4 and H_2CO in each of their respective spectral fitting windows.*

It can be seen that when each of the target gases is not included in the fit, the resulting modeled spectrum is smoother, i.e. the absorption features thought to be caused by the target gases are not being fitted, particularly for CO_2. This gives confidence that the gases are being fitted correctly.

9.5   Emission Ratios and Emission Factors

Emission Ratios of H_2CO with CO_2, CO and CH_4 were calculated for the Australian fires of AF3 and AF5 using the horizontal column amounts derived (Figure 9.8).
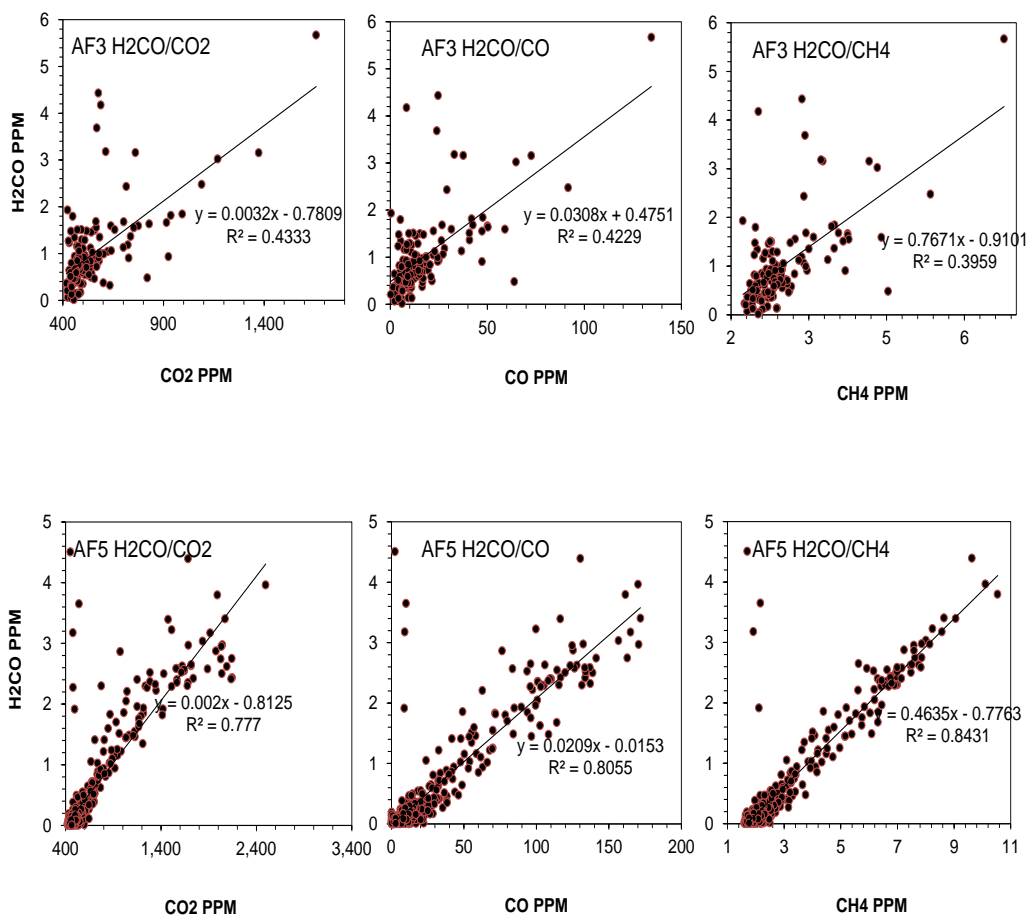
Figure 9.8: *Emission ratios of CO_2, CO and CH_4 against H_2CO, derived from the horizontal pathlength amounts of the respective gas species in the sampled smoke plumes of fires AF3 and AF5 from the Australian field campaign.*

Ideally, these need to be split into the flaming and smoldering phases of the fire using the MCE as some of the ratios seem to exhibit more than one slope. However, for now, the fire averaged ratios have been used. These ratios are used to link the flux rates of H_2CO derived from the DOAS vertical column amounts with the FTIR derived horizontal pathlength amounts of the carbon gases to estimate carbon fluxes (see below).

9.6 Carbon Fluxes

The carbon fluxes of the South African and Australian fires were estimated using the emission ratios derived from MALT and the H_2CO fluxes from the UV-DOAS measurements. All fluxes were calculated using estimations of plume velocity at ground level (unlike the previous work where log law was used for plume velocity at higher altitudes). The carbon fluxes were compared with the FRP time series retrieved from the thermal camera video. For the South African field campaign, the ERs were taken from Wooster *et al.* (2011), where the same methodology was carried with the OP-FTIR at field site as that of the PhD. Recall that only a short time from fire SF1 was sampled during the whole field campaign. Figures 9.9 and 9.10 present the comparison of the carbon fluxes with FRP for fires SF3, SF4, AF3 and AF5.
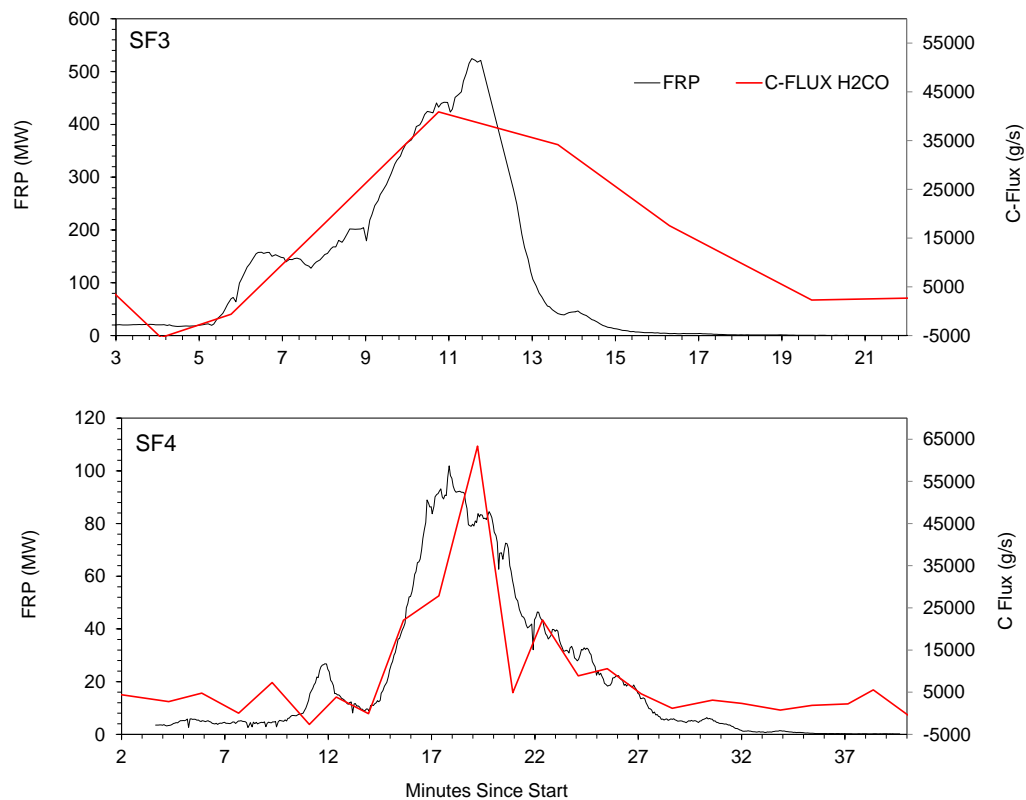
Figure 9.9: *The total carbon flux rates (g.s^{-1}) from the South African fires SF3 and SF4 in red and the FRP time series (mw) of the same fires derived from the MIR thermal camera observations made in a helicopter above the fires, shown in black.*
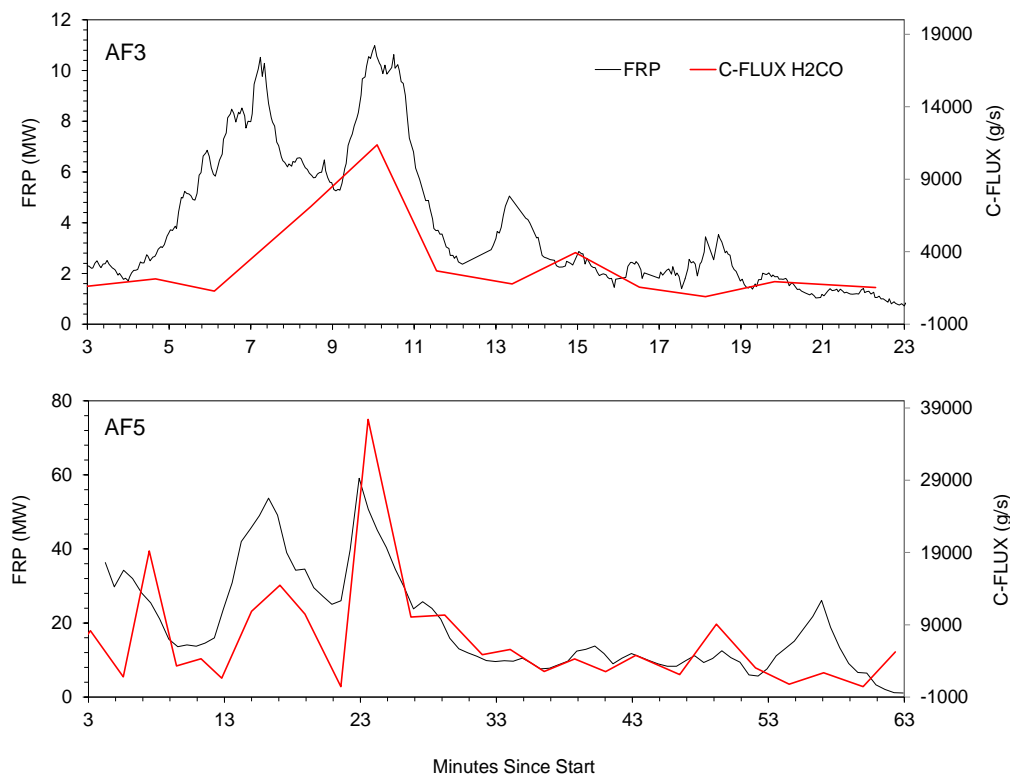
Figure 9.10: *The total carbon flux rates ($g.s^{-1}$) from the Australian fires AF4 and AF5 in red and the FRP time series (mw) of the same fires derived from the MIR thermal camera observations made in a helicopter above the fires, shown in black.*

The FRP and C-Fluxes follow the same trend of peaking within the same time space. Note that both time series will not peak at the exact same time as the FRP is a point measurement while the C-fluxes are averaged over each traverse. There is a discrepancy in trends of the C-flux and FRP for fire AF3, this is due to obstacle blocking the thermal camera used to derive the FRP, causing a dip in the time series during the fire.

9.7 Conclusion

It has been shown that both HONO and H_2CO can be retrieved from experimental open vegetation fires from the UV-DOAS spectra, providing there is sufficient smoke plume. Out of these two gases, H_2CO has the most potential for this work due to its ability to be retrieved from the FTIR spectra. The fact that H_2CO can be retrieved well in both the UV

and IR is a strong advantage. As it was seen in the thesis work, it was difficult at times to retrieve SO_2 and NO_2, particularly in the IR. As there is a considerable lack of emission data, particularly for NO_2 from boreal fires, it is difficult to compare and verify the results shown here, however there is some agreement with the current literature.

Additional work needs to be carried in terms of investigating ways to estimate plume speeds. It was decided to switch from the coarse method used in the PhD of estimating plume speed from aerial video recorded onboard a helicopter to wind speed estimated at ground level. With the former method, a maximum plume height was used, whereas in reality, measurements are made from the plume at varying heights, from ground level to maximum plume height.

Bibliography

Abel, S.J., Highwood, E.J., Haywood, J.M. and Stringer, M.A. (2005) The direct radiative effect of biomass burning aerosols over southern Africa. *Atmospheric Chemistry and Physics*, 5, 1999-2018.

Alberta Sustainable Development, Clean Water Area, Parks Canada, Yoho/Kootenay Lake Louise Field Unit, (2007), *Report:* Upper Saskatchewan Uit I Prescribed Burn Plan.

Akagi, S.K., Yokelson, R.J., Wiedinmyer, C., Alvarado, M.J., Reid, J.S., Karl, T., Crounse, J.D. and Wennberg, P.O. (2011) Emission factors for open and domestic biomass burning for use in atmospheric models. *Atmospheric Chemistry and Physics*, 11, 4039-4072.

Akinori, I. and Penner, J.E. (2004) Global estimates of biomass burning emissions based on satellite imagery for the year 2000. *Journal of Geophysical Research*, 109.

Amraoui, M., DaCamara, C.C. and Pereira, J.M.C. (2010) Detection and monitoring of African vegetation fires using MSG-SEVIRI imagery. *Remote Sensing of Environment*. 114(5), 1038-1052.

Andreae, M.O., Browell, E.V., Garstang, M., Gregory, G.L., Hariss, R.C., Hill, G.F., Jacob, D.J., Pereira, M.C., Sachse, G.W., Setzer, A.W., Silva Dias, P.L., Talbot,

R.W., Torres, A.L. and Wofsy, S.C. (1988) Biomass-burning emissions and associated haze layers over Amazonia. *Journal of Geophysical Research*, 93(D2), 1509-1527.

Andreae M.O. (1990) Biomass burning in the tropics: Impact on environmental quality and global climate. *Population and Environment*, 16, 268-291.

Andreae M.O. (1991) The influence of tropical biomass burning on climate and the atmospheric environment. *In* Oremland, R.S. ed. *Biogeochemistry of Global Change.* The United States: Chapman and Hall, 1993, 113-150.

Andreae, M.O., Anderson, B.E., Blake, D.R., Bradshaw, J.D., Collinsa, J.E., Gregory, G.L., Sachse, G.W. and M.C. Shipman. (1994) Influence of plumes from biomass burning on atmospheric chemistry over the equatorial and tropical South Atlantic during CITE 3. *Journal of Geophysical Research*, 99(D6), 12,793-12,808.

Andreae, M.O. (1996) Biomass burning: Its history, use, and distribution and its impact on the environmental quality and global climate. *In* Levine, J.S. ed. *Biomass Burning: Atmospheric, Climate and Biosperic Implications.* The United States: The MIT Press, 1996, 1-21

Andreae, M.O. and Merlet, P. (2001) Emission of trace gases and aerosols from biomass burning. *Global Biochemical Cycles*, 15(4), 955-966.

Ayra, S.P. (2001) *Introduction to Micrometeorology.* London: Academic Press.

Barrett, E.C. and Curtis, D.E. (1992) *Introduction to Environmental Remote Sensing.* Springer.

Biggs, R., Biggs, H.C., Dunne, T.T., Govender, N. and Potgieter, A.L.F. (2003) Experimental burn plot trial in Kruger National Park: history, experimental design

and suggestions for data analysis. *Koedoe: African Protected Area Conservation and Science*, 46(1).

Blake, N.J., Blake, D.R., Collins Jr, J.E., Sachse, G.W., Anderson, B.E., Brass, J.A., Riggan, P.J. and Rowland F.S (1996) Biomass burning emissions of atmospheric methyl halide and hydrocarbon gases in the south Atlantic region, *In* Levine, J.S. ed. *Biomass burning and Global Change, Biomass Burning in South America, Southeast Asia and Temperate and Boreal Ecosystems, and the Oil Fires of Kuwait.* Vol.2. The United States: The MIT Press, 1996, 575-595.

Blake, N.J., Blake, D.R., Wingenter, O.W., Barkley, C.S., McKenzie, L.M., Lopez, J.P., Simpson, I.J., Fuelberg, H.E., Sachse, G.W., Anderson, B.E., Gregory, G.L., Carrol, M.A., Albercook, G.M. and Rowland, F.S. (1999) Influence of southern hemispheric biomass burning on midtroposheric distributions of non methane hydrocarbons and selected halocarbons over the remote South Pacific. *Journal of Geophysical Research*, 104(D13), 16,213-16,232.

Bluth, G., Shannon, J., Watson, I., Prata, A. and Realmuto, V. (2007) Developement of an ultra-violet digital camera for volcanic SO_2 imaging. *Journal of Volcanology and Geothermal Research*, 177, 635-647.

Bobrowski, N., Hönninger, G., Lohberger, F. and U. Platt. (2004) IDOAS: A new monitoring technique to study the 2D distribution of volcanic gas emissions. *Journal of Volcanology and Geothermal Research.* 150, 329- 338.

Bogumil, K., Orphal, J. and Burrows, J. P. (2000) Temperature dependent absorption cross sections of O3, NO2, and other atmospheric trace gases measured with the SCIAMACHY spectrometer. *Proc. ERS - Envisat Symposium. Looking down at our Earth in the New Millennium, Gothenburg 16 - 20 October 2000.*

Burton, M.R. (1998) Remote sensing of the atmosphere using Fourier transform spectroscopy, PhD thesis, Department of Chemistry, University of Cambridge.

Castro, A.J., Lerma, A.M., Lopez, F., Guijarro, M., Diez, C., Hernando, C. and Madrigal, J. (2007) Open-path fourier transform infrared spectrometry characterization of low temperature combustion gases in biomass fuels. *Infrared Physics and Technology*, 51, 21-30.

Cofer III, W.R., Winstead, E.L., Stocks, B.J., Overlay, L.W., Goldammer, J.G., Cahoon, D.R. and Levine, J.S. (1996) Emissions from boreal forest fires: Are the atmospheric impacts underestimated? *In* Levine, J.S. ed. *Biomass burning and Global Change, Biomass Burning in South America, Southeast Asia and Temperate and Boreal Ecosystems, and the Oil Fires of Kuwait.* Vol.2. The United States: The MIT Press, 1996, 834-839.

Coheur, P.F., Clarisse, L., Turquety, S., Hurtmans, D. and Clerbaux, C. (2009) IASI measurements of reactive trace species in biomass burning plumes. *Atmospheric Chemistry and Physics*, 9, 5655-5667.

Consolidated Incinerator Facility (undated) *Combustion Principles; Study Guide*, ZIOITX92, Revision 02.

Cook, G.D. (2001) Effects of frequent fires and grazing on stable nitrogen isotope ratios in northern Australia. *Australian Ecology,* 26, 630-636.

Cortini, F. and Comeau, P.G. (2008) Evaluation of competative effects of green alder, willow and other tall shrubs on white spruce and lodgepole pine in Northern Alberta. *Forest Ecology and Management,* 255, 82-91.

Craine, J.M., Ballantyne, F., Peel, M., Zambatis, N.,Morrow, C. and Stock,

W.D. (2009) Grazing and landscape controls on nitrogen availability across 330 South African savanna sights. *Austral Ecology*, 34, 731-740.

Christian, T.J., Yokelson, R.J., Carvalho Jr., J.A., Griffith, D.W.T., Alvarado, E.C., Santos, J.C., Neto, T.G.S., Veras, C.A.G. and Hao, W.M. (2007) The tropical forest and fire emissions experiment: trace gases emitted by smouldering logs and dung from deforestation and pasture fires in Brazil. *Jounral of Geophysical Research*, 112.

Crutzen, P.J., Heidt, L.E., Krasnec, J.P., Pollock, W.H. and Seiler, W. (1979) Biomass burning as a source of atmosphere gases CO, H_2, N_2O, NO, CH_3CI and COS. *Nature*, 282, 253-256.

Dalton, M.P., Watson, I.M., Nadeau, P.A., Werner, C., Morrow, W. and Shannon, J.M. (2009) Assesment of the UV camera sulpher dioxide retrieval for point source plumes. *Journal of Volcanology and Geothermal Research*.

Davis, S.P., Abrams, M.C. and Brault, J.W. (2001) Fourier Transform Spectroscopy. *Academic Press Inc.*

Delmas, R., Lacaux, J.P. and Brocard, D. Determination of biomass burning emission factors: Methods and results. *Environmental Monitoring and Assesment*, 38, 181-204.

Department for Environment, Food and Rural Affairs (2007b) Wildlife and countryside, access to open countryside. DEFRA, United Kingdom.

Dhammapala, R., Claiborn, C., Jimenez, J., Corkill, J., Gullett, B., Simpson, C., and Paulsen, M. (2007) Emission factors of PAHs, methoxyphenols, levoglucosan, elemental carbon and organic carbon from simulated wheat and Kentycky bluegrass stubble burns. *Atmospheric Environment*, 41, 2660-2669.

Dozier, J. (1981) A method for satetellite identification of surface temperature fields of subpixel resolution. *Remote Sensing and the Environment.* 11, 221-229.

Dwyer, E., Gregoire, J.M. and Pereira, J.M. (2000) Climate and vegetation as driving factors in global fire activity. *In* J.L. Innes, M. Beniston and M.M. Verstraete, eds. *Biomass burning and its inter-relationships with the climate system.* Vol.3. The Netherlands: Kluwer Academic Publishers, 2000, 171-191.

Eckmann, T.C., Roberts, D.A. and Still, C.J. (2008) Using the muliple end-memeber spectral mixture analysis to retrieve subpixel fire properties from MODIS. *Remote Sensing and the Environment* 112, 3773-3783/

Edmonds, M., Herd, R.A. and Galle, B. (2003) Automated, high time-resolution measurements of SO_2 flux at Soufriere Hills Volcano, Montserrat. *Bulletin of Volcanology*, 65, 578-586.

Edwards, D.J. and Dudhia (1996), Reference forward model: High level algorithms definition, *ESA Doc*, PO-MA-OXF-GS-0004, Eur. Space Agency, Paris.

Elias, T., Sutton, J.A., Oppenheimer, C., Horton, K.A., Garbeil, H., Tsanev, V., McGonigle, A.J.S., Jones-Williams, G. (2005) Comparison of COSPEC and the two miniature ultraviolet spectrometer systems for SO_2 measurements using scattered sunlight. *Bulletin of Volcanology*, 68, 313-322.

European Commission: Joint Research Centre (2002) *Trace Gas Emission Estimation in Biomass Burning.* Italy: Institute of Environment and Sustainability, No.7/JRC-IES 16881-00.

Eva, H. and Lambin, E.F. (1998) Remote sensing of biomass burning in tropical

regions: Sampling issues and multisensor approach. *Remote Sensing of Environment*, 64(3), 292-315.

Ferek, R.J., Reid, J.S., Hobbs, Blake, D.R. and Liousse, C. (1998) Emission factors of hydrocarbons, halocarbons, trace gases and particles from biomass burning in Brazil. *Journal of Geophysical Research*, 103, 32107-32118.

Ferguson, S.A., Sandberg, D.V. and Ottamar, R. (2000) Modeling the effect of landuse changes on global biomass emissions. *In* J.L. Innes, M. Beniston and M.M. Verstraete, eds. *Biomass burning and its inter-relationships with the climate system.* Vol.3. The Netherlands: Kluwer Academic Publishers, 2000, 33-50.

Fiedler, V., Arnold, F., Ludmann, S., Minikin, A., Hamburger, T., Pirjola, L., Dornbrack, A. and Schlager, H. (2011) African biomass burning plumes over the Atlantic: Aircraft based measurements and implications for H_2SO_4 and HNO3 mediated smoke particle activation. *Atmospheric Chemistry and Physics*, 11, 2011.

Fishman, J. and Crutzen, P.J (1978) The origin of ozone in the troposphere. *Nature*, 274. 855-858.

Freeborn, P.H., Wooster, M.J., Hao, W.M., Ryan, C.A., Nordgren, B.L., Baker, S.P. and Ichoku, C. (2008) Relationships between energy release, fuel mass loss and trace gas aerosol emissions during laboratory biomass fires. *Journal Geophysical Research*, 113.

Garnett, M.H., Ineson, P., Stevenson, A.C. (2000) Effects of burning and grazing on carbon sequestration in a Pennine blanket bog, UK. *The Holocene*, 10,6 (2000) pp 729-736.

Garrett, J.R. (1992) *The Atmospheric Boundary Layer.* Cambridge University

Press, 316 pp.

Galle, B., Oppenheimer, C., Geyer, A., McGonigle, A.J.S., Edmonds, M. and Horrocks, L. (2002) A miniaturized ultraviolet spectrometer for remote sensing of SO_2 fluxes: a new tool for volcano surveillance. *Journal of Volcanology and Geothermal Research*, 119, 241-254.

Gellert, W., Kuestner, H., Hellwich, M. and Kaestner, H. (1977) *The VNR Encyclopedia of Mathematics.* New York: Van Nostrand.

Giglio, L and Kendall, J.D. (2001) Application of the Dozier retrieval to wildfire characterization. A sensitivity analysis. *Remote Sensing and the Environment* 77, 34-49.

Giglio, L., Csiszar, I. and Justice, C.O. (2006) Global distribution and seasonality of active fires as observed with the Terra and Aqua Moderate Resolution Imaging Spectroradiometer (MODIS) sensors. *Journal of Geophysical Research-Biogeosciences*, 111(G2).

Granier, C., Muller, J.R. and Brasseur, G. (2000) The impact of biomass burning on the global budget of ozone and ozone precursors. *In* J.L. Innes, M. Beniston and M.M. Verstraete, eds. *Biomass burning and its inter-relationships with the climate system.* Vol.3. The Netherlands: Kluwer Academic Publishers, 2000, 69-85.

Grant, C.C. and Scholes, M.C. (2006) The importance of nutrient hot-spots in the conservation and management of large wild mammalian herbivores in semi-arid savannas. *Biological Conservation,* 130, 426-437.

Graf, H.F., Li, Q. and Giorgetta, M.A. (2007) Volcanic effects on climate: Revisiting the mechanisms. *Atmospheric Chemistry and Physics,* 7, 4503-4511.

Griffith, D.W.T. (1996) Synthetic calibration and quantative analysis of gas-phase FTIR spectra. *Applied Spectroscopy*, 50, 59-70.

Griffith, D.W.T., Esler, M.B., Steele, P.L. and Reisinger, A. (2003) Non-linear least squares: high precision quantitative analysis of gas phase FTIR spectra presented at 2nd Intl. Conference on Advanced Vibrational Spectroscopy, Nottingham, 2003.

Grutter, M., Basaldud, R., Rivera, C., Harig, R., Junkerman, W., Caetano, E. and Delgado-Granados, H. (2008) SO2 emissions from Popocatepetl volcano: emission rates and plume imaging using optical remote sensing techniques. *Atmos. Chem. Phys.*, 8, 6655-6663.

Guyon P., Frank G.P., Welling M., Chand D., Artaxo P., Rizzo L., Nishioka G., Kolle O., Dias MAFS., Gatti LV., Cordova A.M. and Andreae M.O. (2005) Airborne measurements of trace gas and aerosol particle emissions from biomass burning in Amazonia. *Atmospheric Chemistry and Physics*, 5, 2989-3002.

Haaland, D.M. and Thomas, V.T. (1988) Partial least-squares methods for spectral analysis. 1. Relation to other quantitative calibration methods and the extraction of qualitative information. *Analytical Chemistry*, 60, 1193-1202.

Hager, S.A., Gerlach, T.M. and Wallace, P.J. (2008) Summit CO2 emission rates by the CO2/SO2 ratio method at Kilauea Volcano, Hawaii, during a period of sustained inflation. *Journal of Volcanology and Geothermal Research,* 177, 875-882.

Harder, J.W., Brault, J.W., Johnson, P.V. and Mount, G.H. (1997) Temperature dependant NO_2 cross sections at high spectral resolution. *Journal of Geophysical Research,* 102, 3861-3879.

Hendrick, F., Roozendael, M.V., Chipperfield, M.P., Dorf, M., Goutail, F., Yang, X., Fayt, C., Hermans, C., Pfeilsticker, K., Pommereau, J.P., Pyle, J.A., Theys, N. and De Mazière, M. (2007) Retrieval of stratospheric and tropospheric BrO profiles and columns using ground-based zenith-sky DOAS observations at Harestua, 60° N. *Atmospheric Chemistry and Physics*, 7, 4869-4885.

Hicks, B.B. (1975) A procedure for the formulation of bulk transfer coefficients over water. *Boundry-Layer Meteorology*, 8, 515-524.

Hobbs, P.V., Reid, J.S., Herring, J.A., Nance, J.D., Weiss, R.E., Ross, J.L., Hegg, D.A., Ottmar, R.D. and Liousse, C. (1996) Particle and trace-gas measurements in the smoke from prescribed burns of forest products in the Pacific-northwest. *In* Levine, J.S. ed. *Biomass burning and Global Change, Biomass Burning in South America, Southeast Asia and Temperate and Boreal Ecosystems, and the Oil Fires of Kuwait.* Vol.2. The United States: The MIT Press, 1996, 697-715.

Hobbs, P.V., Sinha, P., Yokelson, R.J., Christian, T.J., Blake, D.R., Gao, S., Kirchstetter, T.W., Novakov, T. and Pilewskie, P. (2003) Evolution of gases and particles from a savanna fire in South Africa. *Journal of Geophysical Research,* 108.

Hollas, M.J. (1998) *High Resolution Spectroscopy* 2nd ed. Chichester: John Wiley & Sons.

Hönningger, G., Friedeburg, C.V., Platt, U. (2004) Multi axis differential absorption spectroscopy (MAX-DOAS). *Atmospheric Chemistry and Physics*, 4, 231-254.

Horowitz, L., Walters, S., Mauzerall, D.L., Emmons, L.K., Rasch, P.J., Granier, C., Tie, X., Lamarque, J-F., Schultz, M.G., Tyndall, G.S., Orlando, J.J. and Brasseur, G.P. (2003) A global simulation of tropospheric ozone and related tracers: Description and evaluation of MOZART, version 2. *Journal of Geophysical Research*, 108(D24),

4784.

Horrocks, L.A. (2001) *Infrared Spectroscopy of Volcanic Gases at Masaya, Nicaragua.* Thesis (PhD). The Open University.

Jacobson, M.Z. (2004) The short-term cooling but long term global warming due to biomass burning. *American Meteorological Society*, 17, 2909-2926.

Jain, A.K., Tao, Z.N., Yang, X.J and Gillespie, C. (2006) Estimates of global biomass burning emissions for reactive greenhouse gases (CO, NMHCs, and NOx) and CO2. *Journal of Geophysical Research*, 111.

Jensen, J.R. (2007) *Remote Sensing of the Environment: An Earth Resource Perspective* 2nd Ed. Upper Saddle River, NJ: Prentice Hall.

Johnson, B.T., Osborne, S.R., Haywood, J.M. and Harrison, M.A.J. (2008) Aircraft measurements of biomass burning aerosol over West Africa during DABEX. *Journal of Geophysical Research*, 113.

Ichoku, C. and Kaufman, Y.J. (2005) A method to derive smoke emission rates from MODIS fire radiative energy measurements. *IEEE Trans. on Geosc. and Rem. Sens*, 43, 2636-2649.

Ichoku, C., Giglio, L., Wooster, M.J. and Remer, L.A. (2008) Global characterisation of biomass-burning patting erns using satellite measurements of fire radiative energy. *Remote Sensing of Environment*, 112, 2950-2962.

Innes, J.L.(2000) Biomass burning and climate: An introduction. *In* J.L. Innes, M. Beniston and M.M. Verstraete, eds. *Biomass burning and its inter-relationships with the climate system.* Vol.3. The Netherlands: Kluwer Academic Publishers, 2000,

1-13.

Ito, A. and Penner, J.E. (2004) Global estimates of biomass burning emissions based on satellite imagery for the year 2000. *Journal of Geophysical Research.* 109, D14S05.

Kahn, B.H., Fishbein, E., Nasiri L.S., Eldering, A., Fetzer, E.J., Garay, M.J., Lee, S.Y. (2007) The radiative consistency of the Atmospheric Infrared Sounder and Moderate Resolution Imaging Spectroradiometer cloud retrievals. *Journal of Geophysical Research*, 112.

Karl, T.G., Christian, T.J., Yokelson, R.J., Artaxo, P., Hao, W.M. and Guenther, A. The tropical forest and fire emissions experiment: method evaluation of volatile organic compound emissions measured by PTR-MS, FTIR and GC from tropical biomass burning. *Atmospheric Chemistry and Physics*, 7, 5883-5897.

Kaiser, J.W., Heil, A., Andreae, M.O., Benedetti, A., Chubarova, N., Jones, L., Morcrette, J.J., Razinger, M., Schultz, M.G., Suttie, M. and van der Werf, G.R. (2011) Biomass burning emissions estimated with a global fire assimilation system based on observed fire radiative power. *Biogeosciences Discussions.*

Kasischke, E.S., O'Neil, K., Bourgeau-Chavez, L.L. and French, N.H.F. (2000) Indirect and long term effects of fire on the boreal forest carbon budget. *In* J.L. Innes, M. Beniston and M.M. Verstraete, eds. *Biomass burning and its inter-relationships with the climate system.* Vol.3. The Netherlands: Kluwer Academic Publishers, 2000, 263-280.

Kaufman,, Y., Remer, L., Ottmar, R., Ward. D., Rong, L., Kleidman, R., Fraser, R., Flynn, L., McDougal D. and Shelton G. (1996) Relationship between remotely sensed fire intensity and rate of emission of smoke: Scar C experiment, in

Global Biomass Burning, edited by J. Levine, pp. 685-696. MIT Press, Cambridge Mass.

Kern, Christoph. (2009) Private communication.

Kirchhoff, V.W.J.H., De Oliveira, M.A. and Alvalá, P.C. (1996) Biomass burning effects on the distribution of atmospheric methane in brazil. *In* Levine, J.S. ed. *Biomass burning and Global Change, Biomass Burning in South America, Southeast Asia and Temperate and Boreal Ecosystems, and the Oil Fires of Kuwait.* Vol.2. The United States: The MIT Press, 1996, 595-598.

Koller, L.R. (1965) *Ultraviolet Radiation.* 2nd ed. United States of America: John Wiley & Sons.

Konstantinos D.G. (2005) *Overview of Binomial Filters* [Online]. Available from: http://www.cse.yorku.ca/ kosta/CompVis_Notes/binomial_filters.pdf Accessed March 2009.

Korontzi, S., Justice, C.O. and Scholes, R.L. (2003) Influence of timing and spatial extent of savanna fires in southern Africa on atmospheric emissions. *Journal of Arid Environments*, (2003), 92, 376-396.

Korontzi, S., Roy, D.P., Justice, C.O. and Ward, D.E. (2004) Modeling and sensitivity analysis of fire emissions in southern Africa during SAFARI 2000. *Remote Sensing of Environment*, 92, 255-275.

Kraus, S. (2006) *DOASIS A Framework Design for DOAS.* Germany: Shaker Verlag.

Kromer, T., Kessler M., Holst, B.K., Luther M., Gouda, E., Till W., Ibisch, P.L. and Vasquez, R. (1999) Checklist of Bolivian bromeliaceae with notes

Krotkov, N.A., McClure, B., Dickerson, R.R., Carn, S.A., Li, C., Bhartia, P.K., Yang, K., Kruegar, A.J., Li, Z., Levelt, P.F., Chen, H., Wang, P. and Lu, D. (2008) Validation of SO_2 retrievals from the ozone monitoring instrument over NE China. *Journal of Geophysical Research*, 113.

Langmann, B., Duncan, B., Texttor, C., Trentmann, J and van der Werf, G.R. (2009) Vegetation fire emissions and their impact on air pollution and climate.Atmospheric Environment, 43, 107-116.

Lauk, C. and Erb, K.H. (2009) Biomass consumed in anthropogenic vegetation fires: Global patterns and processes. *Ecological Economics*, 69, 328-334.

Lavorel, S., Flannigan, M.D., Lambin, E.F. and Scholes, M.C. (2006) Vulnerability of land systems to fire: Interactions among humans, climate, the atmosphere, and ecosystems. *Mitigation and Adaptation Strategies for Global Change*

Leigh, R. J. (2006) *A Concurrent MAX-DOAS system for the measurement of nitrogen dioxide and other trace species.* Thesis (PhD). University of Leicester.

Levenberg, K. (1944) A Method for the Solution of Certain Non-Linear Problems in Least Squares. *The Quarterly of Applied Mathematics* 2: 164-168.

Levine, J.S. (1994) Introduction. *In* Zepp, R.G. ed. *Climate-Biosphere Interactions: Biogenic Emissions and Environmental Effects of Climate Change.* New York: Wiley, 1994

Levine, J.S. (1996) Introduction. *In* Levine, J.S. ed. *Biomass burning and Global Change, Biomass Burning in South America, Southeast Asia and Temperate and Boreal Ecosystems, and the Oil Fires of Kuwait.* Vol.2. The United States: The MIT

Press, 1996.

Li, J., Savtchenko, A and Qin J. 2004. Digital imaging and gridding of AIRS visible/NIR data. *Geoscience and Remote Sensing Symposium.* 7, 4850-4853.

Li, A., Xie, P.H., Liu, C., Liu, J.G. and Liu, W.Q. (2007) A scanning multi-axis differential optical absorption spectroscopy system for measurement of tropospheric NO_2 in Beijing. *Chinese Physics Letters*, 24(10), 2859-2862.

Lillesland, T.M., Kiefer, R.W. and Chipman, J.W. (2007). *Remote sensing and image interpretation.* USA: John Willey and Sons.

Lobert, J.M., Scharffe, D.H., Hao W.M., Crutzen P.J. (1990) Importance of biomass burning in the atmosphere budgets of nitrogen-containing gases. *Nature*, 346, 552-554.

Marquard, D.W. (1963) An algorithm for least-squares estimation of non-linear parameters. *Journal of the Society for the Industrial and Applied Mathematics.* 11(2), 431-441.

Marley, N.A., Gaffney, J.S., Castro, T., Salcido, A. and Frederick, J. (2009) Measurements of aerosol absorption and scattering in Mexico City Metropolitan Area during the MILAGRO field campaign: a comparision of results from T0 and T1 sites. *Atmospheric Chemistry and Physics,* 9, 186-206.

McAteer, R.T.J. (2000) *Low Frequency Oscillations of the Solar Atmosphere.* Thesis (PhD). The Queen's University of Belfast.

McGonigle, A.J.S., Oppenheimer, C., Galle, B., Mather, T.A. and Pyle, D.M. (2002) Walking traverse and scanning DOAS measurements of volcanic gas emission

rates. *Geophysical Research Letters*, 29(20).

McGonigle, A.J.S., Oppenheimer, C., Hayes, A.R., Galle, B., Edmonds, M., Caltabiano, T., Salerno, G., Burton, M. and Mather, T.A. (2003) Sulphur dioxide fluxes from Mount Etna, Volcano and Stromboli measured with an automated scanning ultraviolet spectrometer. *Journal of Geophysical Research*, 108(B9).

McGonigle, A.J.S., Thomson, C.L., Tsanev, V.I. and Opprnheimer, C. (2004) A simple technique for measuring power station SO_2 and NO_2 emissions. *Atmospheric Environment*, 38, 21-25.

McGonigle, A.J.S. (2005) Volcano remote sensing with ground based spectroscopy. *Philosophical Transactions of the Royal Society.* 363, 2915-2929.

McGonigle, A.J.S., Inguaggiato, S., Aiuppa, A., Hayes, A.R. and Oppenheimer, C. (2005) Accurate measurement of volcanic SO_2 flux: Determination of plume transport speed and integrated SO_2 concentration with a single device. *Geochemistry Geophysics Geosystems*, 6(1).

McGonigle, A.J.S. (2007) Measurements of volcanic SO_2 fluxes with differential optical absorption spectroscopy. *Journal of Volcanology and Geothermal Research*, 162, 111-122.

McNaughton, S.J., Stronach, N.R.H. and Georgiadis, N.J. (1998) Combustion in natural fires and global emissions budgets. *Ecological Applications*, 8, 464-468.

Meyer, C.P., Cook, G.D., Reisen, F., Smith, T.E.L., Tattaris, M., Russel-Smith, J., Maier, S.W., Yates, C.P. and Wooster, M.J. (2012) Direct measurements of the seasonality of emission factors from savanna fires in northern Australia. *Journal of Geophysical Research: Atmospheres,* 117, D20.

Michael, C., Liousse, C., Gregoire, J.M., Tansey, K., Carmichael, G.R. and Woo, J.H. (2005) Biomass burning emission inventory from burnt area data given by the SPOT-Vegetation system in the frame of TRACE-P and ACE-Asia campaigns. *Journal of Geophysical Research*, 110(D9).

Millan, M. (1980) Remote sensing of air pollutants, a study of some atmospheric scattering effects. *Atmospheric Environment*, 14, 1241-1253.

Moffat, A. and Millan, M. (1971) The applications of optical correlation teqniques to the remote sensing of SO_2 plumes using sky light. *Atmospheric Environment*, 5, 677-690.

Mossmuller, H., Chakrabarty, R.K. and Arnott, W.P. (2009) Aerosol light absorption and its measurements: A review. *Journal of Quantative Spectrsocopy and Radiative Transfer*, 110, 844-878.

Mori, T. and Burton, M.R. (2006) The SO_2 camera: A simple, fast and cheap method for ground-based imaging of SO_2 in volcanic plumes. *Geophysical Research Letters*, 11.

Mori, T., Kazahaya, K., Oppenheimer, C., McGonigle, A.J.S., Tsanev, V., Olmos, R., Ohwada, M. and Shuto, T. (2006) Sulpher dioxide fluxes from the volcanoes of Hokkaido, Japan. *Journal of Volcanology and Geothermal Research*, 158, 235-243.

Muller, U., Kurte, R. and Heise, H.M. (1999) Investigation of photometric errors in FTIR-spectra obtained in open-path monitoring. *Journal of Molecular Structure*, 482-483, 539-544.

Nadeau, P.A. and Williams-Jones, G. (2008) Beyond COSPEC: Recent advances in SO_2 monitoring technology. *In* Stix, J., Williams-Jones, G. and Hickson, C. ed. *The*

COSPEC Cookbook: Making SO$_2$ gas measurements at active volcanoes, Proceedings of Volcanology, IAVCEI.

Nasholm, T., Ekblad, A., Nordin, A., Giesler, R., Hogberg, M. and Hogberg, P. (1998) Boreal forest plants take up organic nitrogen. *Nature*, 392, 914-916.

Nguyen, B.C., Mihalopoulos, N., Bonsang, B. and Putaud, J.P. (1991) Sulphur gas emissions from African savanna burning. *In* Oremland, R.S. ed. *Biogeochemistry of Global Change.* The United States: Chapman and Hall, 1993, 209-220.

Ogawa, M., and Yoshida, N. (2005) Nitrous oxide emission from the burning of agricultural residue. *Atmospheric Environement*, 19, 421-3429.

Oke, T.R. (1987) *Boundary Layers Climates.* Routledge

Oppenheimer, C., Tsanev, V.I., Allen, A.G., McGonigle, A.J.S., Cardoso, A.A., Paterlini, W. and Dias, C.D.M. (2004) NO$_2$ emissions from Agricultural burning in São Paulo, Brazil. *Environmental Science and Technology*, 38, 4557-4561.

Pak, B.C., Langenfelds, R.L., Young, S.A., Francey, R.J., Meyer, C.P., Kivlighon, L.M., Cooper, L.N., Dunse, B.L., Allison, C.E., Steele, L.P., albally, I.E. and Weeks, I.A. (2003) Measurements of biomass burning influences in the troposphere over southeast Australia during the SAFARI 2000 dry season campaign. *Journal of Geophysical Research,* 108(D3).

Parsons, D.A.B., Scholes, M.C., Scholes, R.J. and Levine, J.S. (1996) Biogenic NO emission from savanna soils as a function of fire regime, soil type, nitrogen and water status. *Journal of Geophysical Research,* 101, 23, 683.

Pekin, B.K., Boer, M.M., Macfarlane, C. and Grierson, P.F. (2009) Impacts of

increased fire frequency and aridity on eucalypt forest structure, biomass and composition in southwest Australia. *Forest Ecology and Management*, 258, 2136-2142.

Petersen, A.K., Warneke, T., Frankenberg, C., Bergamaschi, P., Gerbig, C., Notholt, J., Buchwitz, M., Schneising, O. and Schrems, O. (2010) First ground-based FTIR observations of methane in the inner tropics over several years. *Atmospheric Chemistry and Physics*, 10, 7231-7239.

Petron, G., Granier, C., Khattatov, B., Yudin, V., Lamarque, J.F., Emmons, L., Gille, J. and Edwards, D.P. (2004) Monthly CO surface source inventory based on the 2000-2001 MOPITT satellite data. *Geophysical Research Letters*, 31,

Pisano, J.T., Sauer, C.G., Robbins, J., Miller, J.W., Gamble, H. and Durbin T.D. (2003) A UV differential optical absorption spectrometer for the measurement of sulphur dioxide emissions from vehicles. *Measurement Science and Technology*, 14, 2089-2095.

Platt, U. (1994) Differential Optical Absorption Spectroscopy (DOAS). *In*: M. W. Sigrist, ed. *Air Monitoring by Spectroscopic Techniques.* Vol. 127. John Wiley & Sons, Inc, 1994, 27-84.

Platt, U. (2008) New possibilities for remote analysis of biomass-burning-plumes by DOAS. *in* W.M. Hao, ed. *Remote Sensing of Fire: Science and Application: The Proceedings of SPIE.* Vol.7089.

Platt, U. and Stutz, J. (2008) *Differential Optical Absorption Spectroscopy. Principles and Applications.* Germany: Springer.

Potter, C., Brooks-Genovese, V., Klooster, S. and Torregrosa, A. (2002) Biomass burning emissions of reactive gases estimated from satellite data analysis and ecosystem

modeling for the Brazilian Amazon region. *Journal of Geophysical Research*, 107, D20, 8056.

Prasad, R., Majumdar, N.B., Bhattacharya, P., Phukan, B.R. and Singh, S.P. (1999) Wood fuel trade in India. *Paper presented in the National Training Workshop on Wood fuel Trade in India*, Feb. 17-19, Indian Institute of Forest Management, Bhopal.

Prasad, K.V., Gupta, P.K., Sharma, C., Sarkar, A.K., Kant, Y., Badarinath, K.V.S., Rajagopal, T. and Mitra A.P. (2000) NO_x emissions from biomass burning of shifting cultivation areas from tropical deciduous forests of India-estimates from ground based measurements. *Atmospheric Environment* 34, 3271-3280.

Prasad, K.V., Kant, y., Gupta, P.K., Elvidge, C. and Badarinath, K.V.S. (2002) Biomass burning and related trace gas emissions from tropical dry deciduous forests of India: A study using DMSP-OLS data and ground-based measurements. *International Journal of Remote Sensing*, 23(14), 2837-2851.

Press, W.H., Teukolsky, S.A., Vetterling, W.T. and Flannery, B.P. (2007) *Numerical Recipes The Art of Scientific Computing.* 3rd ed. New York: Cambridge University Press.

Rao, C.N.R. (1961) *Ultra-violet and Visible Spectroscopy.* London: Butterworth & Co.

Rawes, M., Hobbs, R. (1979) Management of semi-natural blanket bog in the Northern Pennines. *Journal of Ecology*, 67(3), 789-807.

Reed, C.B. (1989) Linear least squares fits with errors in both coordinates. *Am. J. Phys*, 57, 642-646.

Richards, J.A. (1986) *Remote Sensing: Digital Image Analysis.* Springer-Verlag.

Riggan, P.J., Tissell, R.G., Lockwood, R.N., Brass, J.A., Pereira, J.A.R., Miranda, H.S., Miranda, A.C., Campos, T and Higgins, R. (2004) Remote measurement of energy and carbon flux from wildfires in Brazil. *Ecological Applications*, 14(3), 855-872.

Rivera, C., Sosa, G., Wohrnschimmel, H., de Foy, B., Johansson, M. and Galle, B. (2009) Tula industrial complex (Mexico) emissions of SO_2 and NO_2 during the MCMA 2006 field campaign using a mobile mini-DOAS system. *Atmos. Chem. Phys.*, 9, 6351-6361.

Roberts G., Wooster, M.J., Perry, G.L.W., Drake, N, Rebelo, L.M. and Diposito F. (2005) Retrieval of biomass combustion rates and totals from fire radiative power observations: Application to southern Africa using geostationary SEVIRI imagery. *Journal of Geophysical Research.* 110.

Rodgers, C.D. (2000) *Inverse methods of atmospheric sounding: Theory and practice.* Singapore: World Scientific Publishing Co. Ltd.

Rodriguez, L., Watson, I., Edmonds, M., Ryan, G., Hards, V., Oppenheimer, C. and Bluth, G. (2008) SO2 loss rates in the plume emitted by Soufriere Hills Volcano, Montserrat. *Nerc Open Research Archive.*

Romanya, J., Casals, P. and Vallejo V.R. (2001) Short-term effects of fire on soil nitrogen availabilty in Mediterranean grasslands and shrublands growing in old fields. *Ecological Management*, 147, 39-53.

Roocroft, T (a). *Bushwillow and Large-fruited Bushwillow*

Woodland   Gertenbach   Landscapes   3.   [Online].   Available   from: http://www.thekruger.com/gertenbach/gertenbach3.htm [Accessed March 2009].

Roocroft, T (b). *Lowveld Sour Bushveld of Pretoriuskop Gertenbach Landscapes 1.* [Online]. Available from: http://www.thekruger.com/gertenbach/gertenbach1.htm [Accessed March 2009].

Rose, D., Nowak, A., Achtert, P., Wiedensohler, A., Hu, M., Shao, M., Zhang, Y., Andreae, M.O. and Poschl, U. (2010) Cloud condensation nuclei in polluted air and biomass burning smoke near the mega-city Guangzhou, China-Part 1: Size resolved measurements and implications for the modeling of aerosol particle hygroscopicity and CNN activity. Atmospheric Chemistry and Physics, 10, 3365-3383.

Rothman, L.S., Gordon, I.E., Barbe, A., Benner, C.D., Bernath, P.F., Birk, M., Boudon, V., Brown, V., Camparague, A., Champion, J.P., Chance, K., Coudert, L.H., Dana, V., Devi, V.M., Fally, S., Flaud, J.M., Gamache, R.R., Goldman, A., Jacquemart, D., Kleiner, I., Lacome, N., Lafferty, W.J., Mandin, J.Y., Massie, S.T., Mikhailenko, S.N., Miller, C.E., Moazzen-Ahmadi, N., Naumenko, O.V., Nikitin, A.V., Orphal, J., Perevalov, V.I., Perrin, A., Predoi-Cross, A., Rinsland, C.P., Rotger, M., Simeekova, M., Smith, M.A.H., Sung, K., Tashkun, S.A., Tennyson, J., Toth, R.A., Vandaele, A.C. and Vander Auwera, J. (2009) The HITRAN 2008 molecular spectroscopic database. *Journal of Quantative Spectroscopy*, 110, 533-572.

Russel-Smith, J., Lucas, D., Gapindi, M., Gungunuka, B., Kapirigi, N., Namingum, G., Lucas, K., Giuliani, P. and Chaloupka, G. (1997) Aboriginal resource utilization and fire management practice in western Arnhem Land, monsoonal northern Australia: notes for prehistory, lessons for the future. *Human Ecology,* 25.

Russel-Smith, J., Ryan, P.G., Klessa, D., Waight, G. and Harwood, R. (1998) Fire regimes, fire-sensitive vegetation and fire management of the sandstone Arn-

hem Plateau, monsoonal northern Australia. *Journal of Applied Ecology,* 35(6), 829-846.

Salerno, G.G., Burton, M.R., Oppenheimer, C., Caltabiano, T., Randazzo, D., Bruno, N., Longo, V. (2009) Three years of SO$_2$ flux measurements of Mt. Etna using an automated UV scanner array: Comparison with conventional traverses and uncertainties in flux retrieval. *Journal of Volcanology and Geothermal Research*, 2009.0.013.

Schmidt, S. and Stewart, G.R. (2003) $\delta^{15}N$ values of tropical savanna and monsoon forest species reflect root specialisations and soil nitrogen status. *Ecosystems Ecology,* 134, 569-577.

Seiler, W. and Crutzen, P.J. (1980) Estimates of gross and net fluxes of carbon between the biosphere and the atmosphere from biomass burning. *Climatic Change* 2, 207-247.

Shirai, T., Blake, D.R., Meinardi, S., Rowland, F.S., Russel-Smith, J., Edwards, A., Kondo, Y., Koike, M., Kita, K., Machida, T., Takegawa, N., Nisha, N., Kawakami, S. and Ogawa, T. (2003) Emission estimates of selected volatile organic comounds from tropical savanna burning in northern Australia. *Jounral of Geophysical Research,* 108(D3).

Sinha, P., Hobbs, P.V., Yokelson, R.J., Bertschi, I.T., Blake, D.R., Simpson, I.J., Gao, S., Kirchstetter, T.W. and Novakov, T. (2003) Emissions of trace gases and particles from savanna fires in southern Africa. *Journal of Geophysical Research*, 108, D13.

Simpson, I.J., Akagi, S.K., Barletta, B., Blake, N.J., Choi, Y., Diskin, G.S., Fried, A., Fuelberg, H.E., Meinardi, S., Rowland, F.S., Vay, S.A., Weinheimer, A.J., Wennberg, P.O., Wieberg, P., Wisthaler, A., Yang, M., Yokelson, R.J. and Blake, D.R.

(2011) Boreal forest fire emissions in fresh Canadian smoke plumes: C1-C10 volatile organice compounds (VOCs), CO_2, CO, NO_2, NO, HCN and CH_3CN. *Atmospheric Chemistry and Physics,* 11, 6445-6463.

Sinha, P., Hobbs, P.V., Yokelson, R.J., Blake, D.R., Gao, S. and Kirchstetter, T.W. (2004) Emissions from Miombo woodland and Dambo grassland savanna fires. *Journal of Geophysical research*, 109.

Smith, T.E.L., Wooster, M.J., Tattaris, M. and Griffith, W.T. (2011) Absolute accuracy and sensitivity analysis of OP-FTIR retrievals of CO_2, CH_4 and CO over concentrations representative of "clean air" and "polluted plumes". *Atmospheric Measurement Techniques*, 4, 97-116.

Stott, P. (2000) Combustion in tropical biomass fires: a critical review. *Progress in Physical Geography*, 24(3), 355-377.

Stroppiana, D., Brivio, P.A. and Grégoire, J.M. (2000) Modelling the impact of vegetation fires, detected from NOAA-AVHRR data, on the tropospheric chemistry in Tropical Africa. *In* J.L. Innes, M. Beniston and M.M. Verstraete, eds. *Biomass burning and its inter-relationships with the climate system.* Vol.3. The Netherlands: Kluwer Academic Publishers, 2000, 193-213.

Stutz, J., Platt, U. (1992) Problems in using diode arrays for open path DOAS measurements of atmospheric species. *In* H.I. Schiff, U. Platt, eds. *Proceedings of the Europto series.* Optical Methods in Atmospheric Chemistry. 1715, 329-340.

Takegawa, N., Kondo, Y., Ko., M., Koike, M., Kita, K., Blake, D.R., Hu, W., Scott, C., Kawakami, S., Miyazaki, Y., Russell-Smith, J. and Ogawa, T. (2003) Photochemical production of O^3 in biomass burning plumes in the boundary layer over northern Australia. *Geophysical Research Letters,* 30, 1500.

Taylor, J.R. (1997) *Error Analysis: The study of uncertainties in physical measurements (2nd ed.)* Sausalito, CA: University of Science Books.

Theys, N., F., Roozendael, Hendrick, F., Fayt, C., Hermans, C., Baray, J.L., Goutail, F., Pommereau, J.P. and De Mazière, M. (2007) Retrieval of stratospheric and tropospheric BrO columns from multi-axis DOAS measurements at Reunion Island (21°, 56^oE) *Atmospheric Chemistry and Physics*, 7, 4733-4749.

Thomas, M. (1996) *Ultraviolet and Visible Spectroscopy.* 2nd ed. Chichester: John Wiley & Sons.

Tucker, G. (2003) Review of the impacts of heather and grassland burning in the uplands on soils, hydrology and biodiversity. *English Nature Research Report 550.*

University of Bremen. Cross section reference spectra library. Available from http://www.iup.physik.uni-bremen.de/gruppen/molspec/index.html [Accessed 2007].

van Leeuwen, T.T. and van der Werf, G.R. (2011) Spatial and temporal variability in the ratio of trace gases emitted from biomass burning. *Atmospheric Chemistry and Physics*, 11, 3611-3629.

van der Werf, G. R., Randerson, J. T., Giglio, L., Collatz, G. J., Kasibhatla, P. S. and Arellano, A. F., Jr. (2006) Interannual variability in global biomass burning emissions from 1997 to 2004. *Atmospheric Chemistry and Physics*, 6, 3423-3441.

van der Werf, G. R., Dempewolf, J., Trigg, S. N., Randerson, J. T., Kasibhatla, P. S., Gigliof, L., Murdiyarso, D., Peters, W., Morton, D. C., Collatz, G. J., Dolman, A. J. and DeFries, R. S. (2008) Climate regulation of fire emissions and deforestation in equatorial Asia. *PROCEEDINGS OF THE NATIONAL ACADEMY OF SCIENCES*

OF THE UNITED STATES OF AMERICA, 105, 20350-20355.

van der Werf, G. R., Morton, D. C., DeFries, R. S., Giglio, L., Randerson, J. T., Collatz, G. J. and Kasibhatla, P. S. (2009) Estimates of fire emissions from an active deforestation region in the southern Amazon based on satellite data and biogeochemical modeling. *Atmospheric Chemistry and Physics*, 6, 235-249.

van der Werf, G.R., Randerson, J.T., Giglio, L., Collatz, G.J., Mu, M., Kasibhatla, P.S., Morton, D.C., DeFries, R.S., Jin, Y. and van Leeuwen, T.T. (2010) Global fire emissions and the contribution of deforestation, savanna, forest, agricultural, and peat fires (1997-2009). *Atmospheric Chemistry and Physics*, 10, 11707-11735.

van der Werf, G.R., Randerson, J.T., Giglio, L., Collatz, G.J., Mu, M., Kasibhatla, P.S., Morton, D.C., DeFries, R.S., Jin, Y. and van Leeuwen, T.T. (2010) Global fire emissions and the contribution of deforestation, savanna, forest, agricultural and peat fires (1997-2009). Atmospheric Chemistry and Physics Discussions, 10, 16153-16230.

Vandaele, A.C., Hermans, C., Fayt, S., Fally, S., Carleer, M., Colin, R., M.F., Merienne and Jenouvrier, A. (2001) High resolution Fourier transform measurements of the NO_2 visible absorption cross-section: Temperature and pressure influences on its atmospheric detection, in: *IRS 2000 Current Problems in Atmospheric Radiation,* edited by W.L. smith and Y.M. Timofeyev, pp. 655-659, A. Deepak, Hampton, Va.

Vandaele, A.C., Hermans, C., Fally, S., Carleer, M., Colin, R., Merienne, M.F., Jenouvrier, A. and Coquart, B. (2002) High-resolution Fourier transform measurement of the NO_2 visible and near-infrared absorption cross sections: Temperature and pressure effects. *Journal of Geophysical Research,* 107.

Vandaele, A.C., Hermans, C., Fally, S., Carleer, M., Merienne, M.F., Jenouvrier,

A., Coquart, B. and Colin, R. (2003) Absorption cross-sections of NO_2: simulation of temperature and pressure effects. *Journal of Spectroscopy and Radiative Transfer,* 76, 373-391.

Verhoef, A., de Bruin, H.A.R. and van den Hurk, J.J.M. (1997) Some practical notes on the parameter kB^{-1} for sparse vegetation. *Journal of Applied Meteorology,* 36, 560-572.

Voight, S., Bogumil, K., Burrows, J.P. and Orphal, J. (2002) The temperature and pressure dependence of the absorption cross-sections of NO_2 in the 250-800 nm region measured by Fourier- transform spectroscopy. *Journal of Photochemistry and Photobiology,* 147, 1-7.

Wagner, T., Friedeburg, C.V., Frieβ, U., Sanghavi, S., Sinreich, R. and Platt, U. (2004) MAX-DOAS O_4 measurements: A new technique to derive information on atmospheric aerosols-Principles and information content. *Journal of Geophysical Research*, 109(D22).

Wagner, T., Beirle, S., Deutschmann, Eigemeier, E., Frankenberg, C., Grzegorski, M., Liu C., Marbach, T., Platt, U. and Penning de Vries, M. (2008) Monitoring of atmospheric trace gases, clouds, aerosols and surface properties from UV/vis/NIR satellite instruments. *Journal of Optics A: Pure and applied optics*, (10).

Wang, W.C., Yung, Y.L., Lacis, A.A., Mo, T. and Hansen, J.E (1976) Greenhouse effects due to man-made perturbations of trace gases. *Science*, 194(4266), 685-690.

Wang, Y.X. and McElroy, M.B. (2004) Asian emissions of CO and NO_x: Constraints from aircraft and Chinese station data. *Journal of Geophysical Research*, 109.

Ward, D.E. and Radke, L.F. (1993) Emissions measurements from vegetation fires: A comparative evaluation of methods and results. *In* P.J. Crutzen and J.G. Goldammer, eds. *Fire in the environment: the ecological, atmospheric and climate importance of vegetation fires.* Chichester: John Wiley, 1993, 1993, 53-76.

Weibring, P., Edner, H., Svanberg, S., Cecchi, G., Pantani, L., Ferrara, R. and Caltabiano, T. (1998) Monitoring of volcanic sulphur dioxide emissions using differential absorption lidar (DIAL), differential optical absorption spectroscopy (DOAS) and correlation spectroscopy (COSPEC). *Appl. Phys. B,* 67, 419-426.

Wiedinmyer, C., Quayle, B., Geron, C., Belote, A., McKenzie, D., Zhang, X., O'Neill, S. and Wynne, K.K. (2006) Estimating emissions from fires in North America for air quality modeling. *Atmospheric Environment*, 40, 3419-3432.

Williams-Jones, G., Horton, K., Elias, T., Garbeil, H., Mouginis-Mark, P., Sutton, A. and Harris, A. (2006) Accurately measuring volcanic plume velocity with multiple UV spectrometers. *Bulletin of Volcanology*, 68, 328-332.

Whitehead, P.J., Purdon, P., Russel-Smith, J., Cook, P.M. and Sutton, S. (2008) The management of climate change through prescribed savanna burning: Emerging contributions of Indigenous people in northern Australia. *Public Administration and Development,* 5, 374-385.

Wofsy, S.C. (1976) Interactions of CH_4 and CO in the earth's atmosphere. *Annual Review of Earth and Planetary Sciences*, 4, 441-469.

Worrall, F., Reed, M., Warburton, Jeff., Burt, T. (2003) Carbon budget for a British Upland peat catchment. *Science of the Total Environment*, 312,133-146.

Wooster, M.J. (2002) Small-scale experimental testing of fire radiative energy for

quantifying mass combusted in natural vegetation fires. *Geophysical Research Letters*, 29(21), 23-1-23-4.

Wooster, M.J., E., Oertel and Zhukov, B. (2003) Fire radiant energy for quantitative study of biomass burning: derivation from the BIRD experimental satellite and comparison to MODIS fire products. *Remote sensing of Environment* 86, 83-107.

Wooster, M.J., Roberts, G., Perry, G.L.W. and Kaufman, Y.J. (2005) Retrieval of biomass combustion rates and totals from fire radiative power observations: FRP derivation and calibration relationships between biomass burning and fire radiative energy release. *Journal of Geophysical Research* 110.

Wooster, M.J., Freeborn, P.H., Archibald, S., Oppenheimer, C., Roberts, G.J., Smith, T.E.L., Govender, N., Burton, M. and Palumbo, I. (2011) Field determination of biomass burning emission ratios and factors via open-path FTIR spectroscopy and fire radiative power assessment: headfire, backfire and residual smoldering combustion in African savannas. *Atmospheric Chemistry and Physics*, 11, 11591-11615.

Yan, X., Ohara, T. and Akimoto, H. (2006) Bottom-up estimates of biomass burning in mainland China. *Atmospheric Environment*, 40, 5262-5273.

Yellof, D.E., Labadz, J.C., Hunt, C.O. (2006) Causes of degradation and erosion of a blanket mire in the southern Pennines, UK. *Mires and Peat* 1(4).

Yokelson, R.J., Griffith, D.W.T and Ward, D.E. (1996) Open-path Fourier transform infrared studies of large-scale laboratory biomass fires. *Journal of Geophysical Research*, 101, 21067-21080.

Yokelson, R.J., Goode, J.G., Ward, D.E., Susott, R.A., Babbitt, R.E., Wade, D.D., Bertschi, I., Griffith, D.W.T. and Hao, W.M. (1999) Emissions of formaldehyde,

acetic acid, methanol and other trace gases from biomass fires in North Carolina measured by airborne Fourier transform infrared spectroscopy. *Journal of Geophysical Research,* 104, 30109-30126.

Yokelson, R. J., Artaxo, P. and Blake, D. R. (2007) The Tropical Forest and Fire Emissions Experiment: overview and airborne fire emission factor measurements. *Atmospheric Chemistry and Physics*, 7, 5175-5196.

Yokelson, R. J., hristian, T. J., Karl, T. G. and Guenther, A. (2008) The tropical forest and fire emissions experiment: laboratory fire measurements and synthesis of campaign data. *Atmospheric Chemistry and Physics*, 8, 3509-3527.

York, D. (1966) Least squares fitting of a straight line. *Can. J. Phys*, 44, 1079-1086.

Yue, W., Xu., J., Tan, W. and Xu, L. (2007) The relationship between land surface temperature and NDVI with remote sensing: application to Shanghai Landsat 7 ETM+data. *International Journal of Remote Sensing*, 28, 3205-3226.

Zhang, J.F. and Morawska, L. (2002) Combustion sources of particles: 2. Emission factors and measurement methods. *Chemosphere*, 49, 1059-1074.

Zhang, H., Ye, X., Cheng, T., Chen, J., Yang, X., Wang, L. and Zhang, R. (2008) A laboratory study of agricultural crop residue combustion in China: Emission factors and emission inventory. *Atmospheric Environment,* 42, 8432-8441.

Zhukov, B., Lorenz, E., Oertel, D., Wooster, M. and Roberts G. (2006) Spaceborne detection and characterization of fires during the bi-spectral infrared detection (BIRD) experimental small satellite mission (2001-2004). *Remote sensing of Environment.* 100, 29-51.